Modelling and optimisation of the Microflown

Promotiecommissie

Voorzitter:	Prof.dr. P.J. Gellings	Universiteit Twente
Secretaris	Prof.dr. P.J. Gellings	Universiteit Twente
Promotoren:	Prof.dr. M.C. Elwenspoek	Universiteit Twente
	Prof.dr.ir. W.F. Druyvesteyn	Universiteit Twente
Leden:	Dr.ir. G.J.M. Krijnen	Universiteit Twente
	Dr. V.B. Svetovoy	Yaroslavl University, Russia
	Prof.dr.ir. N.B. Roozen	Universiteit Eindhoven
	Prof.dr.ir. H. Tijdeman	Universiteit Twente
	Prof.dr. J. Müller	TU Hamburg-Harburg
	Prof.dr.ir. P.P.L. Regtien	Universiteit Twente

The research described in this thesis was carried out at the Transducers Science and Technology Group of the MESA$^+$ research institute, University of Twente, the Netherlands. It was performed within the framework of the STW project 'Micromachined Sound Intensity Sensors'.

Print: Océ Facility Services, Enschede

ISBN 90-365-2030-4

MODELLING AND OPTIMISATION OF THE MICROFLOWN

PROEFSCHRIFT

ter verkrijging van
de graad van doctor aan de Universiteit Twente,
op gezag van de rector magnificus,
prof.dr. F.A. van Vught,
volgens besluit van het College voor Promoties
in het openbaar te verdedigen
op vrijdag 16 april 2004 om 15.00 uur

door

Johannes Wilhelmus van Honschoten
geboren op 3 januari 1972
te Deventer

Dit proefschrift is goedgekeurd door de promotoren:

Prof.dr. M.C. Elwenspoek
Prof.dr.ir. W.F. Druyvesteyn

Aan mijn ouders

Contents

Chapter 1	**Introduction**	**1**
1.1	Sound intensity	2
1.2	The history of sound intensity measurements	4
1.3	The Microflown	6
1.4	Micromachined flow sensors	7
	1.4.1. The two wire principle	8
1.5	Thesis outline	8
1.6	References	12
Chapter 2	**Sound Intensity measurements**	**17**
2.1	Introduction	18
	2.1.1 Sound propagation	18
	2.1.2 Acoustic impedance	21
	2.1.3 Sound energy and sound intensity	22
2.2	Different methods to measure sound intensity	24
	2.2.1 The p-u measurement principle	25
	2.2.2 The p-p measurement principle	26
	2.2.3 The u-u measurement principle	29
2.3	Sound intensity determination in a reverberant room	31
	2.3.1 Two particle velocity sensors in a reverberant room: u-u principle 1	32
	2.3.2 Two particle velocity sensors in a reverberant room: u-u principle 2	34
2.4	Comparison of the different measurement principles	36
	2.4.1 Systematic errors in the p-p and u-u measurement techniques	36
	2.4.2 The one-dimensional p-u probe	38
	2.4.3 Comparison of the one-dimensional p-u probe to a p-p probe	38
	2.4.4 A three-dimensional ‘p-u probe’	43
	2.4.5 Near field sound intensity measurements	45
2.5	Summary and discussion	45
2.6	References	49
Chapter 3	**An analytic model of the particle velocity sensor**	**51**
3.1	Introduction	52
3.2	The temperature distribution around the wires	53
	3.2.1 The stationary situation	55
	3.2.2 Influence of an acoustic wave on the temperature profile	60
	3.2.3 The effect of the heat capacity of the sensors	65

3.3 Evaluation of the model 68
3.4 Comparison to experimental results 71
3.5 Conclusions 76
3.6 References 78

Chapter 4 Calibration of the particle velocity sensor in a tube 81
4.1 Introduction 82
4.2 The most common calibration methods for the particle velocity sensor 82
4.2.1 An anechoic environment 82
4.2.2 Time frame measurement in a long tube 83
4.2.3 Standing wave tube 85
4.2.4 Reverberant environment 86
4.2.5 Open window calibration 88
4.3 Relation between measured signal and reference pressure 88
4.4 The influence of viscothermal effects on the transfer function 93
4.5 The phase of the transfer function 95
4.6 Practical implications 97
4.7 Summary and conclusions 98
4.8 References 99

Chapter 5 Determination of the sensitivity behaviour by electronic characterisation 101
5.1 Introduction 102
5.2 Theory 102
5.2.1 The stationary temperature distribution 104
5.2.2 Analogy between acoustically and electrically induced disturbance 107
5.2.3 Implications for the electrical signals 110
5.2.4 A three-wire configuration 113
5.3 Experiments 113
5.4 Conclusions 116
5.5 References 118

Chapter 6 Towards a geometrical optimisation of the flow sensor 119
6.1 Introduction 120
6.2 The temperature as a three dimensional solution of the heat equation 120
6.3 The temperature difference due to the fluid velocity 122
6.4 The influence of the heat capacity of the wires 126
6.5 Geometrical optimisation 131
6.5.1 Analysis of the output signal 131
6.5.2 The low-frequency sensitivity 132

6.5.3 The frequency dependence of the sensitivity 134
6.5.4 Comparison to experimental characterisations 135
6.6 The three-wire configuration 137
6.6.1 The concept 137
6.6.2 Experimental characterisation of the three-wire device 139
6.6.3 An optimally performing device 140
6.7 Conclusions 142
6.8 References 144

Chapter 7 Noise reduction by means of a cross correlation technique 145
7.1 Introduction 146
7.2 Features of noise sources 146
7.3 Correlation function of stochastic signals 148
7.4 Measuring the noise spectral densities 151
7.5 Interpretation 153
7.6 An improvement of the signal to noise ratio 158
7.7 Conclusions 160
7.8 References 161

Chapter 8 An investigation of the low frequency noise of the Microflown 163
8.1 Introduction 164
8.2 Experimental observations 164
8.2.1 Method of approach 164
8.2.2 Variations of the sensors 165
8.2.3 The electronic measurement set-up 165
8.2.4 A heating cavity 168
8.2.5 Heating by electrical power dissipation 170
8.3 Processing of the experimental results 172
8.4 Theory 175
8.4.1 Introduction 175
8.4.2 A small perturbation of the temperature 176
8.4.3 Frequency distribution of the perturbation and of the temperature 179
8.4.4 Spectral density of voltage variations 181
8.4.5 Vibrations of the wire as a possible noise origin 183
8.5 Discussion 183
8.5.1 Noise due to the measurement set-up 183
8.5.2 The temperature and power dependence 184
8.5.3 The frequency dependence 186
8.5.4 Thermodynamic noise 187
8.5.5 Further research 187
8.6 References 189

Chapter 9 Discussion **191**
9.1 Summary 192
9.2 Discussion and conclusions 194
9.3 Outlook 197
9.3.1 Future research 197
9.3.2 Latest developments 200
9.4 References 205
Dankwoord **207**
Biografie **209**

Chapter 1

Introduction

Abstract

In this chapter a short introduction on the physical phenomena sound and sound intensity is given, and the Microflown and its working principle as a two-wire thermal flow sensor for acoustic measurements are briefly described. Additionally a concise, chapter-by-chapter overview of the complete thesis is presented.

1.1 Sound intensity

The physical phenomenon known as ‘sound’ in a medium essentially involves time-varying disturbances of the density of the matter from its equilibrium value. These local pressure changes are in most cases extremely small compared to the equilibrium value (typically of the order of 10^{-7}– 10^{-5} of this value) and accompanied by small vibrational movements of the particles in the medium. These elements in motion have speed, that for fluids (gases or liquids) is called the *particle velocity*. The frequency range of most interest of the involved audio-frequency vibrations, named the ‘audio-frequency range’, to which the human ear is sensitive, extends from about 20 Hz to 20 kHz.

Audio-frequency vibrations can also emerge in solids; they are then accompanied by sound in any fluid the solid material is in contact with. Acoustic vibrations in solids may propagate in many different waveforms, unlike sound in fluids, a phenomenon termed ‘structure-borne sound’.

Sound in a fluid depends for its existence upon two essential properties of the medium. First, the generation of pressure in response to a change in the volume available to a fixed mass of fluid, i.e. a change of density, and second, the existence of inertia; the characteristic of the medium to resist attempts to change its momentum.

Both the forces due to the local expansion of the fluid elements, and the accelerations of those elements, are related to the displacements of the particles from their averaged equilibrium positions. A sound wave is the result of this interaction, with disturbances propagating throughout the fluid, often to very large distances.

As fluid elements in motion have a certain velocity, they possess kinetic energy. In the regions of increasing density the pressure increases, so that, consequently, locally potential energy is stored. The potential and kinetic energies created by the action of the sound source on its surrounding medium are transported with the disturbance, and can only disappear through dissipative processes like fluid friction (viscosity), that are usually negligibly small for audio frequencies. Now, *sound intensity* is defined, as a measure of the rate of transport of the sum of these energies through the fluid, a vector quantity equal to the product of the sound

pressure and the associated fluid particle velocity vector. More explicitly, it is named sound power flux density [25].

Since the invention of the condenser microphone in the beginning of the twentieth century, it has been possible to measure, with increasing accuracy, the sound pressure. Why, however, is it then also important to be able to measure sound intensity, rather than sound pressure? The main reason is that sound intensity measurements enable the quantification of sound power generated by any one of several simultaneously operating sound sources, and thus facilitate the efficient and precise targeting and application of noise control measures. Besides, because of the fact that sound intensity is a vector quantity, possessing both magnitude and direction, while pressure is a scalar quantity having only a magnitude, the availability of accurate sound intensity measurements has important advantages. This vector characteristic allows the determination of the contribution to the total intensity of one steady sound source operating among many under normal operating conditions in the operating environment, so that no special-purpose test facilities that are often rather expensive are required. This distinction of the sound power output from individual sources in the presence of others can be considered as the major application of sound intensity measurement. The advantage of *in situ* measurement of sound intensity extends beyond this economic benefit, as many sound sources in practice are simply too big or heavy or too dangerous to be displaced. Besides, an *in situ* method based on the measurement of the sound pressure requires the microphones to be placed at a distance from the source larger than its maximum characteristic length, in which region noise of other interfering sources is comparable to that of the sound source. Reliable sound intensity measurements, however, can be performed at any distance.

Finally, measurements of the sound intensity allow an investigation of the distribution of the sound power flux radiated from a source over its surface, including vibrating partitions which separate adjacent spacers, so that the various regions may be placed in rank order. This has been seen to be very useful for the determination of automotive engine noise and in detecting weak regions in partitions.

The origination of practical and reliable sound intensity measurement can be considered as one of the most important developments in the acoustic technology

since the introduction of digital signal processing systems. Because of the importance of sound in our society it is of significance for equipment designers, manufacturers, users and acoustical engineers concerned with the control and reduction of noise. The importance of sound in every-day life is in the first place illustrated by, of course, our way of communication, but it can also offer a lot of pleasure in the form of music. Apart from the verbal communication, sound provides a valuable tool for acquiring and transferring information, as is shown by medical techniques like echoscopy and ultrasound imaging. However, the notorious inconveniences of sound are ubiquitous too, like for example the traffic noise, undesired sound production in engineering and the abundant noise near the airport.

1.2 The history of sound intensity measurements

The history of the measurements on sound intensity goes back to the nineteenth century, when Lord Rayleigh, a British physicist and mathematician, realised a system with a suspended disc of which the deflection is proportional to the particle velocity squared. In principle the intensity can thus be measured, but only for plane waves and besides the system is disturbed by random air movements. He investigated elaborately many acoustical phenomena, especially experimentally, but he also contributed significantly to a good descriptive and theoretic approach of sound. In 1877 ‘The Theory of Sound’ appeared [1].

The first patent for a device for the measurement of sound intensity or the sound energy flux in complex sound fields was granted to the American acoustician Olsen in 1932 [2, 3]. It was not until the early 1980s that the first commercial sound intensity measurement systems became available. The reason for this long delay can mainly be found in the technical difficulties to device a suitably stable and linear, wide frequency band transducer that converts reliably a fluid particle velocity into an electrical signal, and the problem of producing audio-frequency filters with identical phase responses. Several attempts were made to develop measurement systems with reasonable frequency ranges and a few theoretical analyses were presented [4-8]. Pioneering contributions in the area of

measurement of sound intensity radiated by complex sources were made by researchers in South Africa in the 1970s [9, 10] who used a combination of pressure and particle velocity microphones. A few years later the first commercially developed analogue sound intensity measurement systems became available. One of these was the Metravib instrument [11], a probe composed of three cheap Miniature electret microphones with variable microphone separation distance, and the Bruel & Kjær instrument [12] that employed high quality condenser microphones placed face-to-face.

In the 1970s, the combination of pressure microphones and particle velocity sensors was discarded in favour of a combination of two nominally identical microphones. Although some years later, however, a new form of velocity microphone based on the principle of convective Doppler shift of an ultrasonic beam was developed [13, 14], this has not become fully established yet.

The last decades the subjects of sound intensity, its measurement and the determination of both the sound pressure and the sound particle velocity have been thoroughly investigated. Research has been done on the errors that occur in measurements of sound intensity and particle velocity due to the influence of the used instrumentation [15-19], theoretic modelling and the three dimensional and directional description of sound fields in different environments [20-24], especially by Fahy [23, 25] and Jacobsen [16, 19, 20]. Since the 1990s, other applications of sound intensity measurement than the extensively investigated determination of the sound power flux developed rapidly, like the *in situ* determination of the acoustic impedance and the sound absorption properties and reflection properties of materials [26, 34, 35, 36]. Current research concentrates among others on the application in building acoustics, reduction of environmental and traffic noise, possibly by generating ‘anti-noise’ [41, 42], and imaging of acoustic sources by near-field microphone array techniques or acoustic holography [37, 38, 39, 40]. Both an overview of the current knowledge with respect to acoustic measurements and an entire theoretic description of sound and acoustic noise phenomena are found in [49, 50, 51].

Other present studies are involved with efficient algorithms for the solving of acoustic wave propagation problems [44, 45, 46]. Recently developed numerical techniques are used in the calculation of radiated sound fields. In addition, sound

fields in enclosed spaces may be efficiently predicted with the new algorithms. The techniques are validated with specially designed experiments, in which use is made of an array of pressure or particle velocity sensors. Acoustic sources can be localised by combining these experimental techniques and inverse numerical calculation processes.

1.3 The Microflown

The property of a sound wave to be characterised not only by pressure but also by a sound particle velocity, is exploited in the principle of the Microflown, a two-wire thermal flow sensor. The Microflown was invented in 1994 by Hans-Elias de Bree at the University of Twente. With this micromachined sensor, the particle velocity can be directly measured.

The Microflown consists of two closely spaced thin metallic wires of about 1 mm length and about 3 μm width. These resistive wires are electrically powered and heated to about 300 to 500 ºC, and they act as temperature sensors *and* as heaters. When a sound particle velocity or a fluid flow is present, the temperature distribution around these resistors is asymmetrically altered, and a temperature difference between the two wires occurs. Since the resistance of the wires is temperature dependent, their resistance difference quantifies the local flow or the particle velocity and this can be measured.

This thermal acoustic sensor, the Microflown, thus measures the sound particle velocity instead of the usually measured sound pressure. In 1997, De Bree received his Ph.D. on his work and research on the sensor, and in his thesis [26] the different general aspects of the Microflown are described. In this work, the required electronic circuits, the acoustic behaviour and the realisation and fabrication method of the sensor are dealt with, and a rough description of its operating principle is proposed as well.

The principle of a two-wire thermal flow sensor, sensitive to small fluid velocities, had also been investigated by B. Zehner in 1979 [33]. Zehner developed a model for a flow sensor of one or two heated wires in a channel and was able to calculate the response signal of the differential temperature to the fluid flow. The

dependence of the signal-to-noise ratio on different dimensions (channel depth, wire separation distance) were theoretically and experimentally investigated.
One year after de Bree had finished his Ph.D.-work, a company, 'Microflown Technologies BV', was founded by A. Koers and de Bree and obtained the legal rights for commercialisation of various Microflown based products. Since then, an increasing scientific and technical interest and a demand for this sensor have developed. By virtue of the company a practical probe, prepared and convenient for sound intensity and particle velocity measurements, including analysing system and software, now exists and a reliable supply of Microflowns has been established.

1.4 Micromachined flow sensors

The Microflown is termed a silicon microsensor [27], which means that it is fabricated by silicon micromachining, a reliable fabrication method of miniaturized systems derived from electronic integrated circuit fabrication technology in which etching techniques, thin film deposition and wafer bonding play an important role. Since two decades a dramatic development has been seen in the fabrication of silicon microsensors for sensing pressure, acceleration, temperature, angular rate and fluid flow, of which the Microflown is an evident example.
In general, micromachined flow sensors can be based on different measuring principles, like thermopiles [28], pyroelectric elements [29], pn-junctions [30], and optic effects [43], but the main principle is that of two or more heated wires in combination with the measurement of differential temperatures [31, 32].
The latter sensors, flow sensors based on a thermal principle, add some heat locally to the streaming fluid, and measure the resulting temperature distribution in the fluid close to or far away from the heater. The hydrodynamic concept that often plays an important role in thermal flow sensors, is the boundary layer. Close to the walls there is a region with large gradients in flow velocity. In the case of a heating element, also a thermal boundary layer builds op within this hydrodynamic boundary layer [27]. Since the dimensions of the boundary layer in comparison to

the geometries of the sensor are very important, the boundary layer phenomenon is very important for the design of many flow sensors. However, for the flow velocities and characteristic dimensions of the Microflown the associated Reynold's numbers are very low. This implies that there is no boundary layer playing a role; its thickness is much larger than the dimensions of the sensor.

1.4.1 The two wire principle

The two heated wires of the Microflown have both a heater and a sensor function; the upstream sensor wire cools down slightly more than the downstream sensor wire, leading to a small measurable temperature difference. See figure 1-1. In this way the Microflown is sensitive to a particle flow or a particle velocity, so that the sensor can be used both as a flow sensor and as a microphone. Together with a pressure microphone, a sound wave can thus fully be characterised.

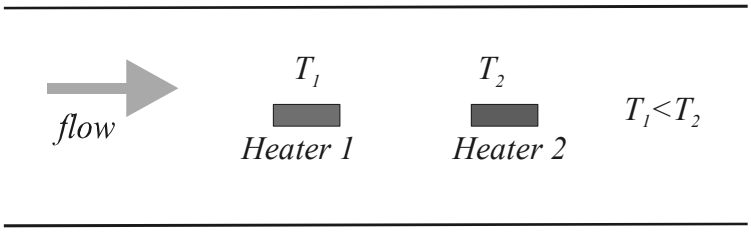

Figure 1-1: Schematic representation of the working principle of a thermal flow sensor.

This two-wire principle with two heated elements used to obtain a differential signal, is, for particle velocities of about 1 mm/s, essentially different from the single hot wire anemometer principle. The single wire anemometer principle is based on a temperature change of the wire due to the convection term. In the anemometry usually King's law, predicting a heat loss of a wire proportional to $\sqrt{v}$ [47], is applied. King's law can be used only for large Reynold's numbers, Re ~ 1, whereas for the Microflown Reynold's numbers are in the order of 10^{-3}. Due

to its differential principle, the Microflown is much more sensitive to low velocities, $v < ca.\ 10^{-3}$ m/s, than the anemometer. It was also noted in [47] that these very small velocities, $v < ca.$ 1 mm/s, cannot be resolved by an anemometer.

1.5 Thesis outline

This thesis aims to provide a better understanding of the sensor, the underlying physics and its frequency dependent acoustic behaviour. Consequently, a better performing device for the measurement of sound intensity in particular, and fluid flows in general, may be obtained. Further, the characterisation of the flow sensor, both acoustic and electronic, are described, and the noise properties of the sensor and the used materials under varying conditions are investigated.
The thesis is organised as shown below.

Chapter 2 deals with the different methods to measure sound intensity. First some introductorily elementary acoustic theory, especially on sound intensity, is treated. Sound intensity can be measured by various combinations of pressure microphones and/or particle velocity sensors, and the various measurement methods are described and mutually compared. It is shown that for both two- and three-dimensional sound intensity measurements a few measurement alternatives are available, each with their own advantages and disadvantages. In this respect, the use of a particle velocity sensor appears to be quite favourable.

Chapter 3 presents a general description of the Microflown that captures the behaviour of the two-wire thermal flow sensor when subject to a small flow or particle velocity. The approach is based on principal physical equations and an analytic model is developed that describes the physical processes that govern the sensor behaviour and determine its sensitivity. The frequency dependent behaviour of the sensitivity is analysed, in view of which two important characteristic frequencies are introduced.

Chapter 4 describes briefly the different aspects of the calibration of the particle velocity sensor. For characterisation of the sensor and quantitative determination of the sensitivity, it has to be calibrated. This is relatively easily and accurately done in a so-called standing wave tube, in which both the particle velocity sensor, a reference microphone and a loudspeaker are placed. The chapter exposes next the possible effects of the viscous and thermal properties of the air on the calibration measurements of the acoustic sensors.

Chapter 5 shows that, instead of the acoustic calibration described in the preceding chapter, an alternative characterisation method is also possible. A new and purely electronic calibration is proposed. It is shown that the sensor's sensitivity and frequency behaviour can be determined by connecting the sensor to an electronic set-up, which yields a more convenient method for determination of the device output response. A theory is developed that shows the geometry-independence of this approach; the electronic method can be applied for a wide range of thermal flow sensors, even for those consisting of more than two wires. The method is based on a general relation following from the heat transfer theory, which does not depend on the precise geometry of the sensor. Additionally, some experimental verifications of the theory for various thermal flow sensors of different geometries are treated in the chapter.

Chapter 6 is partially the application of the description that is developed in the third chapter. It describes the implementation into a software program, and since now a numeric model is involved instead of explicit analytic expressions, several assumptions and restrictions can be dropped. Since the model calculations can be performed numerically, they allow optimisation of the sensor by an investigation of the effect of different geometric and material parameters. The results of the theoretic model are compared with measured responses and a promising three-wire design is proposed.

Chapter 7 presents a method to reduce the noise level of the particle velocity sensor, if it is used for measurement of stationary signals; stationary sound intensity or particle velocity measurements. The method is based on the utilisation

of cross- instead of auto-correlation spectra of two of these sensors. The statistics involved with performing series of measurements are shortly described, and several experimental results are presented.

Chapter 8 treats the various aspects of the noise that occurs in acoustic measurements and that is even manifest in the measured output signal of a single heated wire. In particular attention is paid to the low-frequency $1/f$ noises, i.e. the class of $1/f^{\alpha}$ noises with $0.5 < \alpha < 2$. These are ubiquitous in many physical systems, especially in the spectral density of resistance fluctuations of metals. Experimental data for $1/f$ noise that is observed in measurements with heated wires, of different composition, are presented.

Chapter 9 comprises a summary of the thesis and the final conclusions. Besides some current and future applications are briefly described and some final remarks about further research are made.

1.6 References

1. J.W.S. Lord Rayleigh, 'The Theory of Sound', Vol. II, London, The Macmillan Company 2nd ed. (1896) (originally published in 1877).
2. I. Wolff, F. Massa, Direct measurement of sound energy density and sound energy flux in a complex sound field, *Journal of the Acoustic Society of America* 3 (1932) 317-318.
3. H.F. Olson, Field-type acoustic wattmeter, *Journal of the Audio Engineering Society* 22 (1974) 321-328.
4. J.H. Enns and F.A. Firestone, Sound power density fields, *Journal of the Acoustic Society of America* 14 (1942) 24-31
5. C.W. Clapp and F.A. Firestone, The acoustic wattmeter, an instrument for measuring sound energy flow, *Journal of the Acoustic Society of America* 13 (1941) 124-136.
6. R.H. Bolt and A.A. Petrauskas, An acoustic impedance meter for rapid field measurements, *Journal of the Acoustic Society of America* 15 (1943) 79(a).
7. S. Baker, Acoustic Intensity meter, *Journal of the Acoustic Society of America* 27 (1955) 269-273.
8. T.J. Schultz, Acoustic wattmeter, *Journal of the Acoustic Society of America* 28 (1956) 693-699.
9. J.F. Burger, G.J.J. van der Merwe, B.G. van Zyl and L. Joffe, Measurement of sound intensity applied to the determination of radiated sound power, *Journal of the Acoustic Society of America* 53 (1973) p. 1167-1168.
10. B.G. Van Zyl, and F. Anderson, Evaluation of the intensity method of sound power determination. *Journal of the Acoustic Society of America* 57 (1975) 682-686.
11. Intensimètre Acoustique INAC 201. Metravib, 64 chemin des Mouilles, BP 182, 69132 Ecully cedex, France.
12. O. Roth, A sound intensity real-time analyser, *Proceedings of Recent Developments in Acoustic Intensity Measurement*, ed. M. Bockhoff. Centre Technique des Industries Mécaniques, Senlis, France, p. 69-74.

13. S.A. Nordby and O.-H. Bjor, Measurement of sound intensity by use of a dual channel real-time analyzer and a special sound intensity microphone, *Proceedings of Inter-Noise 84*, ed. George C. Maling. Noise Control Foundation, New York, USA (1984) p. 1107-1109
14. O.-H. Bjor and H.J. Krystad, A velocity microphone for sound measurement, *Proceedings of the Autumn Conference 1982*, ed. Anon. Institute of Acoustics, Edinburgh (1982) p. B7.1-B7.5
15. .S. Cazzolato and C.H. Hansen, Errors in the measurement of acoustic energy density in one-dimensional sound fields, *Journal of Sound and Vibration* 236 (2000) 801-831.
16. F. Jacobsen and E.S. Olsen, The influence of microphone vents on the performance of sound intensity probes, *Applied Acoustics* 41 (1994) 25-45.
17. J.W. Parkins, S.D. Sommerfeldt and J. Tichy, Error analysis of a practical energy density sensor, *Journal of the Acoustical Society of America* 108, (2000) 211-222.
18. B.S. Cazzolato and C.H. Hansen, Errors arising from three-dimensional energy density sensing in one-dimensional sound fields, *Journal of Sound and Vibration* 236 (2000) 375-400.
19. F. Jacobsen, A note on finite difference estimation of acoustic particle velocity, *Journal of Sound and Vibration* (2002) 256(5), 849-859
20. F. Jacobsen, Active and reactive sound intensity in a reverberant sound field. *Journal of Sound and Vibration*, 143 (1990) 231-240
21. Y. Oshino and T. Arai, Sound intensity in the near field of sources, *Proceedings of the Symposium on Acoustic Intensity*, Tokyo (1987) 46-56
22. R.W. Guy and A. Abdou, A measurement system and method to investigate the directional characteristics of sound field in enclosures, *Noise Control Engineering Journal*, 42 (1994) 8-18
23. C.R. Fuller and F.J. Fahy, Characteristics of wave propagation and energy distribution in cylindrical shells filled with fluid, *Journal of Sound and Vibration*, 81 (1981) 501-518
24. R .Raangs, W.F. Druyvesteyn, H-H. de Bree, A novel two-dimensional sound particle velocity probe for source localization and free field measurements in a diffuse field, *Proceedings of Internoise* (2001).

25. F.J. Fahy, 'Sound Intensity', ISBN 0419198105, second edition (1995).
26. H.-E. de Bree, The Microflown, Ph.D.-thesis, ISBN 9036509262, (1997).
27. M.C. Elwenspoek, R. Wiegerink, 'Mechanical Microsensors', ISBN 3-540-67582-5 Springer-Verlag (2001).
28. D. Moser, R. Lenggenhager, H. Baltes, Silicon gas flow sensors using industrial CMOS and bipolar IC technology, *Sensors and Actuators, A* 25-27 (1991) 577-581.
29. H.Y. Hsieh, A. Spetz, J.N. Zemel, Pyroelectric anemometry: vector and swirl measurements, *Sensors and Actuators*, A 49 (1995) 141-147.
30. R. Kersjes, F. Liebscher, E. Spiegel, Y. Manoli, W. Mokwa, An invasive catheter flow sensor with on-chip CMOS readout electronics for the on-line determination of blood flow, *Sensors and Actuators, A* 54 (1996) 563-567.
31. H. Kuttner, G. Urban, A. Jachimowicz, F. Kohl, F. Olcaytug, P. Goiser, Microminiaturized thermistor arrays for temperature gradient, flow and perfusion measurements, *Sensors and Actuators* A 25-27 (1991) 641-645.
32. A. Glaninger, A. Jachimowicz, F.Kohl, R. Chabicovsky, G.Urban, Wide range semiconductor flow sensors, *Sensors and Actuators*, *A* 85 (2000) 139-146.
33. B. Zehner, Signal und Rausen beim Differential-Hitzdrahtanemometer, *Ph.D.-thesis*, Univ. of Karlsruhe, (1979).
34. F.J.M. van der Eerden, H-E. de Bree, H. Tijdeman, Experiments with a new acoustic particle velocity sensor in an impedance tube, *Sensors and Actuators* A 69 (1998) 126-133.
35. H. Schurer, Comparison of two methods for measurement of horn input impedance, *Proceedings of the 100th AES convention*, Copenhagen, (1996).
36. W.F. Druyvesteyn, H-H. de Bree, R. Raangs, Free field measurements in a reverberant room using the microflown sensors, *Proceedings of the ICA*, Rome (2001).
37. E.G. Williams, The nearfield acoustical holography (NAH) experimental method applied to vibration and radiation in light and heavy fluids, *Computers and Structures* 65, No 3 (1997) 323-335.
38. E.G. Williams and J.D. Maynard, Holographic imaging without the wavelength resolution limit, *Physical Review Letters* 45, (1980) 554-557.

39. J.C. Lee, Spherical Acoustic Holography of Low-Frequency Noise Sources, *Applied Acoustics* 48, No 1, (1996) 85-95.
40. I. Sakamoto, T. Tanaka, T. Miyake, Investigation of noise source identification accuracy by acoustic holography with model tires, *JSAE Review* 17, (1996) 191-212.
41. J. Krüger and P. Leistner, Noise Reduction with Actively Absorbing Silencers, *Applied Acoustics* 51 Issue 2 (1997) 113-120.
42. T. Berge, O. Kr. Ø. Pettersen, S. Sørsdal, Active cancellation of transformer noise: Field measurements, *Applied Acoustics* 23, Issue 4, (1988) 309-320.
43. R.I. Crickmore, S. H. Jack, D.B. Hann, C.A. Greated, Laser Doppler anemometry and the acousto-optic effect, *Optics and Laser Technology*, 31, (1999) 85-94.
44. W.M. Beltman, P.J.M. van der Hoogt, R.M.E.J. Spiering, H. Tijdeman, Implementation and experimental validation of a new viscothermal acoustic finite element for acousto-elastic problems, *Journal of Sound and Vibration* 216(1) (1998) 159-185.
45. W.M. Beltman, Viscothermal wave propagation including acousto-elastic interaction, part I: Theory, *Journal of Sound and Vibration* 227 (3) (1999) 555-586; and part II: Applications, *Journal of Sound and Vibration* 227 (3) (1999) 587-609.
46. T.G.H. Basten, P.J.M. van der Hoogt, R.M.E.J. Spiering, H. Tijdeman, On the acousto-elastic behaviour of double-wall panels with a viscothermal air layer, *Journal of Sound and Vibration* 243 (4) (2001) 699-719.
47. L.V. King, On the convection of heat from small cylinders in a stream of fluid (esp. Determination of the convection constants of small platinum wires with application to hot wire anemometry), *Proceedings of the Royal Society London* A 90 (1914) 563-..or 373-...
48. F. Kohl, A. Jachimowicz, J. Steurer, R. Glatz, J. Kuttner, D. Biacovsky, F. Olcaytug, G. Urban, A micromachined flow sensor for liquid and gaseous fluids, *Sensors and Actuators* A 41 (1994) 293-299.
49. A.D. Pierce, 'Acoustics, An introduction to its physical principles and applications', Acoustical Society of America, New York (1994).

50. D.A. Bies, C.H. Hansen, ‘Engineering Noise Control, Theory and Practice’, E&FN SPON, London (1996).
51. M. Heckl, H.A. Muller, ‘Taschenbuch der Technischen Akustik’, Springer, 2nd ed. (1995).

Chapter 2

Sound Intensity measurements

Abstract

To determine the time averaged sound intensity in a given point of the acoustic field, a few different principles can be applied, based on particle velocity sensors, pressure microphones or a combination of them. In this chapter different methods to measure the active sound intensity are described and mutually compared. Advantages and disadvantages of the varying methods are considered. The measurement principle that seems to be most favourable makes use of one pressure microphone and one particle velocity sensor. The advantage of this principle is that no pressure gradients or spatial derivatives of the particle velocity are involved. This so-called p-u probe is an affordable and practical measuring device for measuring several acoustic parameters, in particular (two dimensional) sound intensity. It can easily be extended to a three-dimensional probe, a microphone combined with three perpendicular particle velocity sensors, that measures the intensity as a vector quantity.

2.1 Introduction

2.1.1 Sound propagation[1]

The relationship between the variations in time and space of the physical quantities acoustic pressure, fluid density, and the quantities particle displacement, velocity and acceleration implies a propagation of the disturbances in the form of a wave through the medium. These local time-varying disturbances in the fluid density that propagate in the medium constitute the sound wave that can take various forms, depending upon the coordinate system used in its derivation. The pressure p and particle velocity u are dependent on each other, and their relationships can be rewritten into an expression for one dependent variable only. In general there is no exact solution of this equation, due to the complicated geometries of sources and boundaries. For understanding and approximate modelling of complicated physical systems, some limiting and simple examples are described. Special attention is paid to the particle velocity fields, since sound energy flow, or sound intensity, is produced by the interaction between sound pressure and particle velocity.

This well known 'wave equation', for example for the pressure, yields:

$$\nabla^2 p(r,t) - \frac{1}{c^2}\frac{\partial^2 p}{\partial t^2} = 0 \qquad (1.)$$

with c the sound velocity in the medium. Here $c^2 = \gamma P_0/\rho_0$, with P_0 the equilibrium (mean, static) pressure, ρ_0 the mean density of the medium and γ the ratio of specific heats of constant pressure and constant volume.

One of the limiting cases as a solution of the wave equation is the 'plane wave'. The sound field inside a long, uniform tube has, for frequencies for which the acoustic wavelength exceeds about half the peripheral length of the tube cross section, a particularly simple form. At any time t, each acoustic variable is uniform over any plane perpendicular to the tube axis, irrespective of the time dependence of the field. The governing homogeneous wave equation, Eq. (1.), is reduced to its one-dimensional form,

[1] For the introductorily elementary theory on sound use has been made of [5].

$$\frac{\partial^2 p}{\partial x^2}(r,t) - \frac{1}{c^2}\frac{\partial^2 p}{\partial t^2} = 0 \qquad (2.)$$

having the general solution

$$p(x,t) = f(t - x/c) + g(t + x/c) \qquad (3.)$$

in which f and g are functions depending on the spatial and temporal boundary conditions of the specific situation. They represent disturbances travelling at speed c in the positive-x and negative-x directions, respectively. Using the equation for the conservation of momentum in the x-direction,

$$\frac{\partial p}{\partial x} = -\rho_0 \frac{\partial u}{\partial t} \qquad (4.)$$

the associated particle velocity distribution is obtained as

$$u(x,t) = \frac{1}{\rho_0 c} f(t - x/c) - \frac{1}{\rho_0 c} g(t + x/c) \qquad (5.)$$

The quantity $\rho_0 c$ is termed the characteristic specific acoustic impedance of the fluid. It is seen from Eq.(5.) that the particle velocity can be deduced from the pressure, only if both the functions f and g are known.

A further idealisation, that appears to be very useful in many situations, is the plane *progressive* wave model in which only f or only g occurs. Although it describes a very unrealistic situation, it is a useful tool for the analysis of complex sound fields. For harmonically varying disturbances of frequency ω the pressure field can then be expressed in complex exponential form by

$$p(x,t) = p_0 e^{i(\omega t - kx)} \qquad (6.)$$

in which p_0 is a complex number, thus including a possible phase, and k represents the acoustic wavenumber $k = \omega/c$.

Another limiting situation is formed by a spherical wave, that can be found as a solution of the wave equation in a spherical coordinate system. The rectangular Cartesian coordinates are transformed into a radial coordinate r, an azimuthal angle θ and an angle of declination ϕ. For spherically symmetric fields, the θ- and ϕ-dependent terms disappear and the wave equation reads

$$\frac{\partial^2}{\partial r^2}(pr) - \frac{1}{c^2}\frac{\partial^2 (pr)}{\partial t^2} = 0 \qquad (7.)$$

It is easily seen that the general solution of Eq (7.) is

$$p(r,t) = \frac{1}{r} f(t - r/c) + \frac{1}{r} g(t + r/c) \tag{8.}$$

with f and g again functions depending on the boundary conditions. Since the function g represents a disturbance approaching the origin from infinity, it can usually be omitted, the term with f describes a disturbance that decreases in strength inversely with distance. Introducing now a harmonic time dependence, with a circular frequency ω, the pressure can be written in complex exponential form as

$$p(r,t) = \frac{A}{r} e^{i(\omega t - kr)} \tag{9.}$$

in which the factor in front, A, is complex and thus includes a possible phase.
The particle displacements, velocities and accelerations are in a radial direction. From the application of the momentum equation, Eq. (4.) that relates the pressure and radial particle velocity, for u_r can be written

$$u_r(r,t) = \frac{A}{\omega \rho_0 r}\left(k - \frac{i}{r}\right) e^{i(\omega t - kr)} = \frac{p(r,t)}{\rho_0 c}\left(1 - \frac{i}{kr}\right) \tag{10.}$$

In the first place it is seen that the phase relationship between pressure and particle velocity is dependent on the distance to the origin r, and second, two different regions can be distinguished: the near field, for which $kr << 1$, and the far field, with $kr >> 1$. In the near field, the particle velocity varies with distance as r^{-2}. In the far field, pressure and particle velocity are almost in phase and both vary as r^{-1}. Defining the time average of the product of two harmonically varying quantities represented by $a \cdot e^{i\omega t}$ and $b \cdot e^{i\omega t}$ over one period $2\pi/\omega$ as ½Re{ab*}, with * indicating the complex conjugate, it is seen from Eq.(10.) that

$$\overline{u_r^2} = \frac{\overline{p^2}}{(\rho_0 c)^2}\left(1 + (1/kr)^2\right) \tag{11.}$$

This means that, while the ratio of mean square particle velocity to mean square pressure is $(1/\rho_0 c)^2$ for plane waves, this ratio is approximately $(1/kr)^2$ larger in the near field. Similarly, the specific acoustic impedance, the ratio of the complex amplitudes of pressure and particle velocity of a harmonic acoustic field, is for this situation

$$z = \rho_0 c \frac{1 + i/kr}{1 + (1/kr)^2} \qquad (12.)$$

The imaginary component of this impedance becomes large positive in the near field, where $kr << 1$, the meaning of which we will see later (section 2.4.5).

In general, practical situations are more complicated than the described spherical and plane waves. However, the characteristic features of near fields and far fields remain the same. Fields produced by complicated spatial source distributions can be investigated by describing the source as a distribution of infinitely small elementary point sources with a certain phase. The resulting field is a superposition of the associated sound fields and can be expressed by the application of Green's functions. Eq.(9.) can be used as the 'free space' Green's function that involves a field originating from a spatially concentrated point source.

2.1.2 Acoustic impedance

The specific acoustic impedance at a point in a sound field is defined as the ratio of the complex amplitude of an individual frequency component of sound pressure at that point, to the complex amplitude of the associated component of particle velocity. Since it is a complex number it gives the magnitude and the phase of the ratio of the individual frequency components. The quantity is of importance for the description of energy flow in a sound field because the phase relationship between the pressure (a force-like quantity) and the fluid velocity indicates the effectiveness of their 'cooperation', in the same way that the power factor does for voltage and current in an electrical circuit.

Under free field conditions, the characteristic specific acoustic impedance z of the fluid is simple,

$$z = \rho_0 c \qquad (13.)$$

Since sound intensity probes measure both the pressure and particle velocity component (in the case of a two-microphone probe the latter is measured implicitly), they may be used to indicate the acoustic impedance anywhere in a sound field. For the determination of the sound absorption properties of material

surfaces, characterised by their surface normal specific acoustic impedance, this is very useful.

2.1.3 Sound energy and sound intensity

In elementary acoustic theory the fluid is assumed to be non-viscous, so that the only internal force is the pressure arising from the volumetric strain. Pressure is a manifestation of the rate of change of momentum of the gas molecules produced by their mutual interactions during random motion. Now, the kinetic energy of a fluid per unit volume, termed T, equals obviously $\frac{1}{2}\rho u^2$, with u the speed of the fluid particle motion, the particle velocity. The potential energy associated with volumetric strain of an elemental fluid volume is equal to the negative work done by the internal pressure on the surface of the elemental volume. Since the total volume change is given by the integral over the surface of the normal displacement of the surface, the potential energy U per unit volume V is given by

$$dU = -P(dV/V) \tag{14.}$$

The total pressure P is the sum of the equilibrium pressure P_0 and the acoustic pressure p. It can be shown [5] that the dominant contribution comes from p, so that Eq.(14.) becomes

$$dU = -p(dV/V) \tag{15.}$$

Using $dV/V = -d\rho/\rho$ and $p/(\rho-\rho_0) = c^2$, one sees that $d\rho = dp/c^2$ and with the small disturbance assumption $(\rho-\rho_0)/\rho_0 << 1$, Eq.(15.) becomes

$$dU = -pdp/\rho_0 c^2 \tag{16.}$$

Thus, the potential energy per unit volume is

$$U = p^2/2\rho_0 c^2 = p^2/2\gamma P_0 \tag{17.}$$

The total mechanical energy per unit volume associated with an acoustic disturbance, the ‘sound energy density’, is therefore

$$e = T + U = \frac{1}{2}\rho_0 u^2 + p^2/2\rho_0 c^2 \tag{18.}$$

The propagation of this sound energy is described by the physical quantity ‘sound intensity’. The vibrational potential and kinetic energies of the fluid elements in

the path of a transient sound wave are zero before a wave reaches them, and zero again after the wave has passed. Assuming no local transformation of energy into non-acoustic forms, the energy the fluid particles possess during their disturbance has clearly travelled onwards with the wave. In deriving an energy balance for a small region of fluid, some assumptions are made. Small dissipative forces are supposed to be negligible, no sources or sinks of heat or ork are present, and heat conduction can be neglected. The rate at which work is done on fluid on one side of an imaginary surface in the fluid, by the fluid on the other side, can then be written as the scalar product of the force vector $\vec{F}$ acting on that surface times the normal fluid particle velocity through that surface[2]. Equivalently, the rate of work W equals

$$\frac{dW}{dt} = \vec{F} \cdot \vec{u} = p\delta\vec{S} \cdot \vec{u} \tag{19.}$$

where $\delta\vec{S}$ is the elemental vector area which can be written as $\delta S\vec{n}$, with $\vec{n}$ the unit vector normal to the surface, directed into the fluid the force acts upon. The work rate per unit area thus becomes

$$\frac{dW}{dt} / \delta S = pu_n \tag{20.}$$

with $u_n = \vec{u} \cdot \vec{n}$ is the component of the particle velocity normal to the surface. The vector quantity $p\vec{u}$ is defined as the instantaneous sound intensity,

$$\vec{I}(\vec{r},t) = p\vec{u} \tag{21.}$$

In general, both the magnitude and direction of $\vec{I}(\vec{r},t)$ at any point $\vec{r}$ in space vary with time. From the definition, the dimension of sound intensity is energy per unit time per unit area: an energy transport through a surface. Similarly to the definition of the instantaneous sound intensity as the product of the instantaneous acoustic pressure and the instantaneous particle velocity, one can define the time-averaged (mean) sound intensity as

$$\vec{I}(\vec{r}) = \lim_{T\to\infty} \frac{1}{T}\int_0^T \vec{u}(\vec{r},t)\,p(\vec{r},t)dt\,. \tag{22.}$$

[2] In this thesis a vector quantity v is denoted by $\vec{v}$.

It has in general a real and imaginary part, termed respectively the active and reactive intensity.
Sound intensity measurements are useful, for example, for source localisation and the characterisation of a sound field due to one or more (correlated) sound sources. Moreover, they allow the quantification of sound power generated by any one of several simultaneously operating sound sources, and thus facilitate the efficient and precise targeting and application of noise control measures. Because of the fact that sound intensity is a vector quantity, possessing both magnitude and direction, while pressure is a scalar quantity, the availability of sound intensity measurements has important advantages. This vector characteristic enables the determination of the contribution to the total intensity by one steady sound source to the total acoustic field, so that no expensive special-purpose test facilities are required.

2.2 Different methods to measure sound intensity

For measurement of the active and reactive sound intensity, different methods can be distinguished [1,5]. In accordance with the definition of sound intensity as the product of acoustic pressure and particle velocity, an intensity measurement system should, in principle, consist of transducers of each of these two quantities. However, it is not always required to measure both quantities directly, and many current measurement systems implement an indirect transduction principle. Besides, in comparing different methods, the occurring errors and disturbing noise signals have to be treated with [1, 2, 3].
The main different measurement methods will be successively described here and mutually compared. Parts of the section are based on the work of Raangs [4] on the ‘three dimensional PU-probe’, the work of de Bree [9], and Druyvesteyn [4, 6-8]. Together with an investigation of literature about sound intensity measurements [5, 12-16], these form the basis of the overview presented here.
The method that will be seen to be the most appropriate and most adequate to determine the sound intensity is based on the use of one particle velocity sensor and one pressure microphone and is therefore called the ‘p-u method’.

The second, conventional, method, makes use of two microphones: the ‘p-p method’. If two microphones are used, only the projection of the sound intensity vector on the line connecting them is detected, so the method is one dimensional. For measurements in the other dimensions, a change of the orientation of the two sensors, or more microphones are required.
A third method makes use of two particle velocity sensors: the ‘u-u method’. Determination of the sound intensity component in the plane of, and perpendicular to the wires is possible, provided that the phase relation between pressure and particle velocity, or the acoustic impedance, is known.
All three methods are one-dimensional, so that sound intensity determination is possible in the plane of the sensors.

2.2.1 The p-u measurement principle

From Eq. (21.) follows obviously that the vector $\vec{I}$ can be directly determined from the measurement of both the acoustic pressure and the particle velocity (a vector quantity) at a point. The instantaneous sound intensity was defined as the product of the instantaneous acoustic pressure and the instantaneous particle velocity. Therefore, the two output signals from a probe comprising a combination of a pressure transducer and a particle velocity sensor can be multiplied together to give the time-dependent component of the intensity in the direction of the probe axis. The signal proportional to pressure may be directly multiplied by the signal proportional to the particle velocity component to produce an analogue of the instantaneous intensity component. If appropriate, this intensity signal can be time-averaged to obtain the mean (active) sound intensity component. The total vector $\vec{I}(t)$ can only be determined if three orthogonal components of the particle velocity can be simultaneously measured.

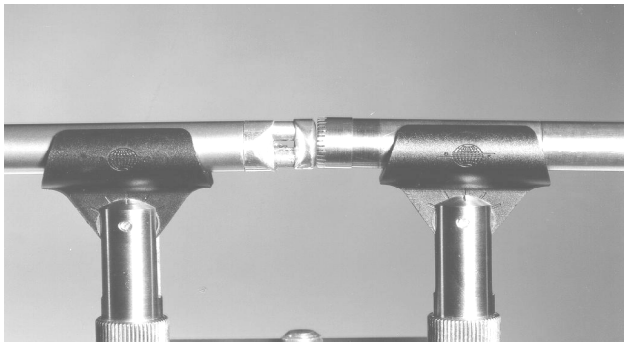

Figure 2-1: The first operational, one-dimensional, p-u probe, composed of a ½" Brüel & Kjær microphone and the Microflown, in 1997 [9].

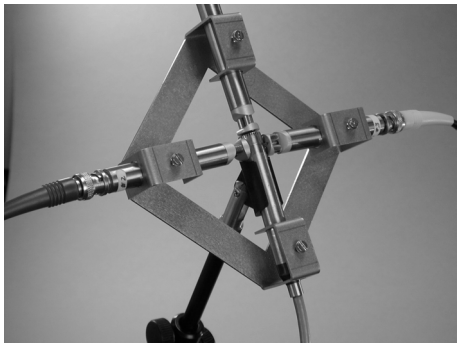

Figure 2-2: The '3D Ultimate Sound Probe', from Microflown Techn. BV. The three mutually perpendicular Microflowns, with the microphone in the middle are clearly visible.

If, however, only the mean intensity vector of a steady sound field is required, the results of sequential measurements of the three mean intensity components may be vectorially combined. Figure 2-1 is an illustration of a one-dimensional p-u probe, three-dimensional p-u probes are seen in figure 2-2 and 2-4.

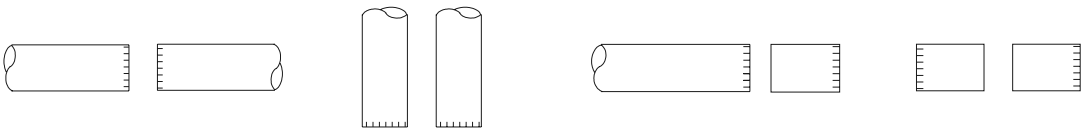

'face-to-face' *'side-by-side'* *'tandem'* *'back-to-back'*

Figure 2-3: Schematic p-p intensity probe configurations (from [5]).

2.2.2 The p-p measurement principle

The p-p probe is a sound intensity probe that consists of two closely spaced, identical microphones. These pressure transducers are placed close together in a support structure which is designed to minimise diffraction of the incident sound field. Usually the transducers are high quality condenser microphones for measurements in air (for underwater measurements piezo-electric hydrophones are

used). Most condenser microphone transducers take the form of short cylinders which may be associated in various configurations, like ‘face-to-face’, ‘side-by-side’, ‘tandem’ or ‘back-to-back’. See figure 2-3.

A pressure gradient can be measured in the direction parallel to the line between the acoustic centres of the microphones by employing a finite difference approximation to the local spatial gradient of the sound pressure.

From the difference between the measured pressures, one component of the pressure gradient is determined. According to the fluid momentum equation (see also Eq.(4.)) the component of the pressure gradient in any direction n is, in a small amplitude sound field, proportional to the time derivative of the particle velocity (the fluid particle acceleration) in that direction:

$$\rho_0 \frac{\partial u_n}{\partial t} = -\frac{\partial p}{\partial n}. \qquad (23.)$$

where $u_n(r, t)$ is the particle velocity in the direction n, and ρ_0 the fluid density.

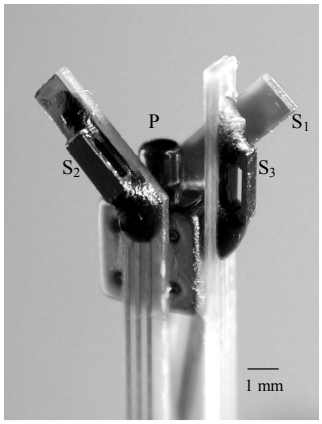

Figure 2-4: The three-dim. ‘PU-probe’ [4,9] from Microflown Techn., composed of a small microphone (P) and three velocity sensors (S_1, S_2, S_3) that measure perpendicular velocity directions

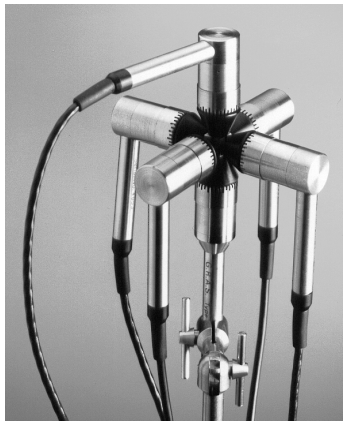

Figure 2-5: A three-dimensional ½’’ p-p probe consisting of three matched pairs of pressure microphones, type G.R.A.S.

Therefore the corresponding component of particle velocity follows from the time integral

$$u_n = -\frac{1}{\rho_0}\int_{-\infty}^{t}\frac{\partial p(\tau)}{\partial n}d\tau\,. \tag{24.}$$

which can be approximated by

$$u_n \approx -\frac{1}{\rho_0 d}\int_{-\infty}^{t}\big(p_1(\tau)-p_2(\tau)\big)d\tau\,. \tag{25.}$$

with d the distance separating the acoustic centres of the transducers, termed the 'separation distance'.

Since the pressure at the point midway between the transducers is approximated as

$$p(t) \approx \frac{1}{2}\big(p_1(t)+p_2(t)\big). \tag{26.}$$

the instantaneous intensity component in the direction n can be found from

$$I_n(t) \approx \frac{1}{2\rho_0 d}\big(p_1(t)+p_2(t)\big)\int_{-\infty}^{t}\big(p_1(\tau)-p_2(\tau)\big)d\tau\,. \tag{27.}$$

Equation (27.) may be variously implemented using sum, difference, integration and multiplication circuits. For a sound field that is temporally non-stationary, the explicit evaluation of $\bar{I}(t)$ is of importance and the full expression of (27.) is needed. Most sources, however, operate steadily and these sound fields can be considered to be stationary so that for the determination of the sound power of the source one is interested in the mean intensity. Time stationary signals $x(t)$ and $y(t)$ are such that the long-time averages $\overline{x(dx/dt)} = \overline{y(dy/dt)} = 0$ and $\overline{x(dy/dt)} = -\overline{y(dx/dt)}$. (The bar indicates the averaging over a time long compared to the time scale of fluctuations of $x(t)$ and $y(t)$.) One can write $\int p_1 d\tau$ as x and $\int p_2 d\tau$ as y, noting that $p_{1,2}$ is the time derivative of $\int p_{1,2} d\tau$. Substituting this in Eq. (27.) and taking then the time average of the thus obtained instantaneous intensity, we find for the mean (active) intensity component in the direction n

$$I(t) \approx -\frac{1}{\rho_0 d}\lim_{T\to\infty}\frac{1}{T}\int_0^T\left(p_1(t)\int_{-\infty}^{t}p_2(\tau)d\tau\right)dt\,. \tag{28.}$$

It is seen that the mean intensity in a time-stationary sound field can, in principle, be obtained from the product of the signal from one pressure transducer (microphone) and the integrated signal from another identical transducer in close proximity.

Figure 2-6: One dimensional sound intensity probe of Brüel & Kjær, consisting of two cylindrical pressure microphones, placed 'face to face', based on the p-p principle.

The standard, commercially available, sound intensity probe consists of two closely spaced, identical pressure microphones, which are placed 'face to face'. An example is seen in figure 2-6. A three-dimensional p-p probe is depicted in figure 2-5.

Using a dual channel audio analyser [19], the intensity is calculated from the multiplication of the measured pressure difference and the average pressure of the two sensors according to Eq. (27.). Although this probe works very adequately in most practical cases, some drawbacks of this probe [9, 20] can be mentioned. They are

- For different frequency ranges one should use different spacers (e.g. 12 mm for the frequency range 125 Hz < f < 5000 Hz and 50 mm for 31.5 Hz < f < 1250 Hz, with f the frequency [19]). Changing the spacers increases the measurement time.
- The properties of the two microphones, and especially the phase characteristics, should be equal. Therefore a pair of carefully matched microphones is used. (Brüel & Kjær supplies for example microphones with a phase matching of 0.3° accuracy [19].) Due to the phase mismatch, the probe is low frequency limited.
- The *reactivity* of a sound field defines the amount of reactive, or imaginary intensity, to the total intensity. The quality of the sound intensity measurement using the p-p method depends on this reactivity

of the sound field [5, 9]. The lower limit of the measurable bandwidth increases with the reactivity of the field.

- Since the p-p probe is relatively large, measurements in small cavities or cabinets are not possible.
- The sound intensity probe cannot be applied in the near field of a source, if the intensity is not constant along the probe.

2.2.3 The u-u measurement principle

The third method is based on a combination of two particle velocity sensors. Two of these sensors are placed close to each other, allowing the determination of both the sum (and the averaged value) and the difference of the particle velocities at their positions. In principle, the required pressure can be deduced from the divergence of the particle velocity according to the equation of mass conservation

$$\frac{\partial}{\partial t}\Delta\rho(\vec{r},t)+\rho_0\vec{\nabla}\cdot\vec{u}(\vec{r},t)=0 \tag{29.}$$

which can be rewritten, if the variation in density $\Delta\rho$ is considered to be proportional to the acoustic pressure p, as

$$\frac{\partial}{\partial t}p(\vec{r},t)-\rho_0 c^2\vec{\nabla}\cdot\vec{u}(\vec{r},t)=0 \tag{30.}$$

The sound pressure can then be calculated from

$$p=-\rho_0 c^2\int\frac{\partial u_x}{\partial x}+\frac{\partial u_y}{\partial y}+\frac{\partial u_z}{\partial z}dt \tag{31.}$$

To obtain the pressure, the space derivative of the vector $\vec{u}$ in three dimensions is therefore required.

With two closely spaced particle velocity probes of spacing Δx in the x-direction, with the separation distance much smaller than the wavelength, and particle velocity probes in the y- and z-direction, the pressure is determined as

$$\begin{aligned}p=&-\frac{\rho_0 c^2}{\Delta x}\int(u_x(x+\Delta x)-u_x(x))dt-\frac{\rho_0 c^2}{\Delta y}\int(u_y(y+\Delta y)-u_y(y))dt\\&-\frac{\rho_0 c^2}{\Delta z}\int(u_z(z+\Delta z)-u_z(z))dt\end{aligned} \tag{32.}$$

An electronic time integrating circuit is thus required in the measurement set up. See figure 2-7.

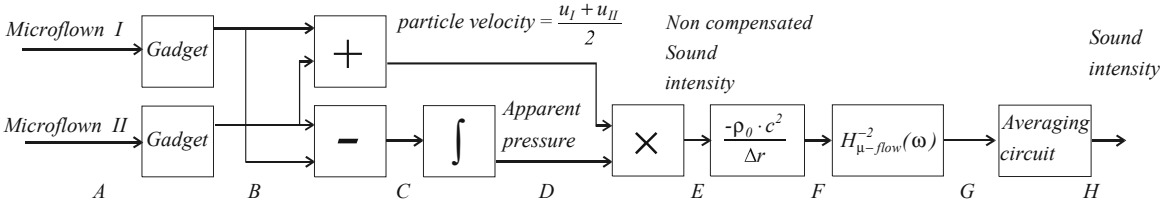

Figure 2-7: Block diagram to measure the sound intensity in one dimension r, from two particle velocity probes I and II, of separation distance Δr. The 'Gadget' symbolises the preamplifier, the transfer function of the used Microflown is measured to be $H_{\mu\text{-}flown}(\omega)$. (from [9])

For plane waves, when the 'far field' approximation is valid, the specific acoustic impedance is simply equal to $\rho_0 c$, and when the coordinate axes are chosen such that $\vec{u} = (u_x, 0, 0)$, *viz.* the sensors are positioned in the plane of and perpendicular to the propagation of the acoustic wave, only one particle velocity sensor suffices to determine both p, u and thus the sound intensity.

2.3 Sound intensity determination in a reverberant room

Sound intensity measurements are most easily performed under anechoic or 'free field' conditions, when there is no reverberant sound and the relation between pressure and particle velocity, the specific acoustic impedance, is known. The measurement of only one of the acoustic quantities allows quantification of the sound intensity. An anechoic environment is characterised by the absence of sound reflecting boundaries and since there is no reverberant sound field, one measures the free-field pressures and particle velocities. The specific acoustic impedance $z(r, t)$ in anechoic measurements is, for plane waves, very simple and real (Eq.(13.)), so

$$u_{anechoic} = \frac{p_{anechoic}}{\rho_0 c} \tag{33.}$$

Consequently, for plane waves the sound intensity can be expressed in both sound pressure and in the particle velocity:

$$I(t) = p(t)u(t) = \frac{p^2_{anechoic}(t)}{\rho_0 c} = \rho_0 c u^2_{anechoic}(t) \tag{34.}$$

In a reverberant room, however, the sound field is composed of the field of the direct sound wave, the diffuse (reverberant) sound field, and noise. A particle velocity or pressure sensor thus measures in principle the sum of all acoustic fields, although in general the physical quantity of interest is the sound intensity emitted by the source only. For a measurement of the sound intensity of a source of interest with the elimination of the reverberant field and possible noise, two different 'u-u methods', based on the use of a pair of particle velocity sensors and eventually a microphone, are possible. The methods will be denoted here as u-u principle 1 and u-u principle 2.

First, the correlation functions and correlation spectra of fluctuating signals have to be defined. The autocorrelation function of a signal $u(t)$ is defined here as

$$R_{uu}(\tau) = \lim_{T\to\infty} \frac{1}{T} \int_0^T u(t)u*(t+\tau)dt \tag{35.}$$

and the cross correlation function of a signal $u(t)$ and $p(t)$ as

$$R_{pu}(\tau) = \lim_{T\to\infty} \frac{1}{T} \int_0^T p(t)u*(t+\tau)dt \tag{36.}$$

so that by definition the mean intensity component in the direction of u is $R_{pu}(0)$. The distribution in frequency of the product of the u and u or the p and u components is given by the Fourier transform of the auto or cross correlation function:

$$G_{uu}(\omega) = \frac{1}{2\pi} \int_{-\infty}^{\infty} R_{uu}(\tau) e^{-i\omega\tau} d\tau \tag{37.}$$

and

$$G_{pu}(\omega) = \frac{1}{2\pi} \int_{-\infty}^{\infty} R_{pu}(\tau) e^{-i\omega\tau} d\tau \tag{38.}$$

Eqs. (37.) and (38.) give the autocorrelation spectrum (the auto spectral density) and the cross correlation spectrum (cross spectral density) respectively of the signals $u(t)$ and $p(t)$.

2.3.1 Two particle velocity sensors in a reverberant room: u-u principle 1.

The sound field in the reverberant room consists of a direct sound wave and the reverberant field (including possible acoustic noise), which we presume to be diffusive, *i.e*. the intensity is uniformly distributed over all directions. By using a particle velocity sensor in two perpendicular directions, both the particle velocity with and without (when measuring perpendicular to the source) the diffuse field are measured and the ratio between the direct and the diffuse sound field can be deduced. The direct particle velocity can thus be determined, and when a microphone is added, it becomes also possible to find the direct pressure. This provides all the information to determine the sound intensity. This measurement principle, in which the root mean square values of the free-field particle velocity in two directions (from two particle velocity sensors) and the free-field pressure are determined, is called 'u-u principle 1'.

Using the assumption of uniform spatial distribution of the reverberant sound field, the root mean square values of the free-field sound pressure and particle velocity can be measured [7, 8]. Furthermore the direct and reverberant sound field are assumed to be uncorrelated. With two mutually perpendicular particle velocity sensors the particle velocity in the direction of the direct sound wave and that in the perpendicular direction (from the diffuse sound field) are measured, from which the ratio of direct and reverberant sound follows. Using then the fact that due to the directional dependence of the sensitivity of the Microflown (the sensor sensitivity in the direction along angle θ is proportional to $\cos\theta$, as will be seen in the next chapter), only one third of the power of the diffuse field is measured by the sensor, it is seen that

$$u_{\parallel}^2 = u_{dir}^2 + \frac{1}{3}u_{rev}^2$$
$$u_{\perp}^2 = \frac{1}{3}u_{rev}^2 \tag{39.}$$

with $u_{\parallel}^2$ and $u_{\perp}^2$ representing the auto spectra of the particle velocities, measured in the direction of the direct sound wave and in the perpendicular direction, and u_{dir}^2, u_{rev}^2 the auto spectra due to the direct sound wave and the diffuse field respectively.

For the ratio of the direct field (the 'free field' sound) and the reverberant sound field thus follows

$$\frac{u_{dir}}{u_{rev}} = \sqrt{\frac{u_{\parallel}^2 - u_{\perp}^2}{3u_{\perp}^2}} \tag{40.}$$

and the direct sound field is calculated as

$$u_{dir} = \sqrt{u_{\parallel}^2 - u_{\perp}^2} \tag{41.}$$

Additionally to this u-u measurement, the pressure may be measured using a pressure transducer. (Strictly spoken, the method is not purely an 'u-u' measurement anymore when a microphone is added.) Generally the microphone is omni-directional so that the different pressures related to the direct and the reverberant field are measured equally sensitive (that is, independent of the angle of incidence), and thus $p^2 = p_{dir}^2 + p_{rev}^2$.

Since

$$\left(\frac{p_{dir}}{p_{rev}}\right)^2 = \left(\frac{u_{dir}}{u_{rev}}\right)^2 \tag{42.}$$

the root mean square value of the pressure of the direct sound field p_{dir} can be expressed in the measured total pressure p:

$$p_{dir} = \sqrt{\frac{p^2}{1 + \left(\frac{u_{rev}}{u_{dir}}\right)^2}} \tag{43.}$$

If the 'free field' condition for plane waves is satisfied, so that the specific acoustic impedance is equal to $\rho_0 c$, the (time averaged) sound intensity in a reverberant environment can then be calculated from both the free field particle velocity u_{dir} ('I_u') and the free field pressure p_{dir} ('I_p');

$$I_u = \rho_0 c u_{dir}^2 = \rho_0 c (u_{\parallel}^2 - u_{\perp}^2) \tag{44.}$$

$$I_p = \frac{p_{dir}^2}{\rho_0 c} = \frac{p^2}{\rho_0 c}\left(1 + \left(\frac{u_{rev}}{u_{dir}}\right)^2\right)^{-1} = \frac{p^2}{\rho_0 c}\left(1 + \left(\frac{3u_{\perp}^2}{u_{\parallel}^2 - u_{\perp}^2}\right)\right)^{-1} \tag{45.}$$

For purely diffuse reverberant sound fields that are not correlated with the sound source, the two measured values of the sound intensity are in principle equal.
This measurement principle, 'u-u principle 1', can also be used to calibrate a particle velocity sensor against a reference microphone in a reverberant sound field [6].

2.3.2 Two particle velocity sensors in a reverberant room: u-u principle 2.

A second, somewhat more extensive, method using two perpendicular particle velocity sensors in a reverberant sound field makes it also possible to calculate the angle of incidence in the plane of the sensors of the sound intensity. This measurement, 'u-u principle 2', makes use of both the auto correlation and the cross correlation spectra of the two particle velocity sensors (the Microflowns).
According to the definitions (37.) and (38.), the auto correlation spectra $G_{u_1u_1}$ and $G_{u_2u_2}$ and the cross correlation spectrum $G_{u_1u_2}$ of the two perpendicular sensors can be constituted, with which the direction ϕ (see figure 2-8) of the free field particle velocity (in the plane of the sensors) can be determined. One can write

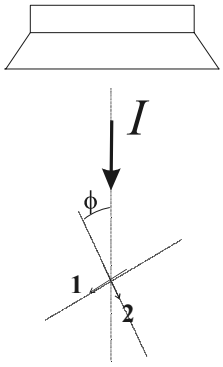

Figure 2-8: The measurement set up, consisting of the two mutually perpendicular particle velocity sensors and a loudspeaker. The orientations of the sensitivities are indicated by the arrows 1 and 2; the angle of incidence ϕ of the sound wave is defined here with respect to the sensitive direction of Microflown 1.

$$G_{u_1u_1} = u_{dir}^2 \sin^2\phi + \frac{1}{3}u_{rev}^2 \tag{46.}$$

$$G_{u_2u_2} = u_{dir}^2 \cos^2\phi + \frac{1}{3}u_{rev}^2 \tag{47.}$$

and

$$G_{u_1u_2} = u_{dir}^2 \cos\phi \sin\phi \tag{48.}$$

which can be solved for u_{dir}:

$$u_{dir}^2 = \sqrt{\left(G_{u_1u_1} - G_{u_2u_2}\right)^2 + 4G_{u_1u_2}^2} \tag{49.}$$

and for the angle ϕ:

$$\phi = \frac{1}{2}\arctan\left(\frac{2G_{u_1u_2}}{G_{u_2u_2} - G_{u_1u_1}}\right) \tag{50.}$$

On physical arguments ϕ has to be chosen such that $0 < \phi < \pi/2$.

Apart from the absolute value of the free field particle velocity, the particle velocity of the reverberant sound can be determined from these equations, Eqs. (46.)- (50.).

If, additionally, this particle velocity measurement is done in a plane perpendicular to the original plane of the sensors, the particle velocity as a full three-dimensional vector can be determined. From the thus found ratio between the values of the direct and the diffuse particle velocity vector, the direct pressure can be

determined from the measured total pressure in the sound field (if a pressure transducer is placed in the sound field too) since the ratios of direct and diffuse pressure and of the direct and diffuse particle velocity are equal. For plane waves, when the free field condition is satisfied, now follows from Eq. (49.):

$$I_u = \rho_0 c u_{dir}^2 = \rho_0 c \sqrt{\left(G_{u_1u_1} - G_{u_2u_2}\right)^2 + 4G_{u_1u_2}^2} \qquad (51.)$$

Measurement principle 2 can be considered as a more general method than principle 1, since the angle of incidence ϕ can also be determined. Determination of the sound field in the plane of the wires is possible if the phase relation between pressure and particle velocity, or the acoustic impedance, is known. However, for both u-u-measurements, principle 1 and principle 2, in general an additional pressure sensor is required to obtain the full sound intensity vector in the plane of the sensors. In principle, the additional pressure measurement can be performed in a different way, if the pressure is calculated from the divergence of the particle velocity as described in Eqs. (29.) to (32.), with closely spaced particle velocity probes in, in general, three dimensions and an electronic time integrating circuit (figure 2-7).

2.4 Comparison of the different measurement principles

2.4.1 Systematic errors in the p-p and u-u measurement techniques

The two described different techniques that are purely based on the sum and difference of two closely spaced sensors, i.e. the p-p measurement method and the u-u method in which the pressure is calculated from Eq.(31.) without the use of an additional pressure sensor, are subject to systematic errors which arise from the fact they involve approximations which are inherent in the transduction principle employed. That is to say, these errors arise from the approximations in Eqs. (25.), (26.), and (32.). These finite difference approximations, in which a gradient is approximated with a differential quotient, and the approximation of averaging the measured quantity (p or u) over the separation distance (Eq. (26.)), obviously lead to measurement errors. They are systematic errors, since they result directly from the principle of intensity measurement employed and not from imperfections in

the measurement systems; the instrumentation and measurement performance. The systematic errors are, however, functions of the type of field under investigation (e.g. a field from a plane progressive wave, an interference field or a point monopole field [5]) and of the orientations of the probe within the field. A thorough analysis of the systematic errors that are inherent in the p-p technique and a comparison of different p-p probes, are given in [5]. One of the conclusions is that for plane progressive waves, and plane wave interference fields, the condition for the normalized error in the estimated intensity $e(I)$ to be less than 5%, is that

$$e(I) < 5\% \text{ if } \quad kd < 0.55 \Leftrightarrow fd < 30 \tag{52.}$$

with d the separation distance of the sensors, k the wave number and f the frequency.

Other important errors and limitations in the finite difference estimation of the particle velocity, in which the phase is also of importance, are the instrumentation phase mismatch, the amplitude (sensitivity) mismatch, electrical noise, and in the case of the p-p method, the finite vent sensitivity of the microphones and interference of the microphones on the sound field. An investigation of these problems is given in [12]. The finite difference error in the measurement of the particle velocity has already been dealt with before in literature, in particular in sound intensity measurements, [15,16], and in the measurement of sound energy density in acoustic fields [15, 17, 18]. Even for one-dimensional fields the deduced expressions for errors are quite complicated [15].

2.4.2 The one-dimensional p-u probe

The main advantage of the p-u measurement method, based on the principle of determining the intensity from simultaneous measurement of both pressure and particle velocity, is that the above described errors due to the finite difference approximations do not occur. Using the p-u principle, no pressure gradients or spatial derivatives of the particle velocity are involved.

Besides, only one (usually expensive) microphone is required for the probe, and some of the disadvantages of the p-p probe mentioned can be eliminated. A one-

dimensional p-u probe was presented in figure 2-1 in which a ½" Brüel & Kjær pressure microphone together with the Microflown are shown. The particle velocity sensor is encapsulated such that it has an external configuration similar to the microphone. Both sensors can be positioned quite closely, thereby determining the pressure and particle velocity at almost the same point. Again using a dual channel analyser, the intensity is now calculated from the real part of the cross-spectrum of the microphone signal and the particle velocity signal.

2.4.3 Comparison of the one-dimensional p-u probe to a p-p probe

As mentioned, the calculation of the sound intensity using a p-p probe is very sensitive to a phase mismatch of the two pressure microphones, since the difference signal of the two sensors is required to obtain the particle velocity, Eq. (25.). A phase difference of 0.3º between the sensors is then considered to be large. However, such a phase difference can be neglected if, as in the p-u method, both the signal of the particle velocity sensor and the microphone are multiplied.
In advance, the reactivity index L_k. has to be defined here. It is defined as $L_k = L_I - L_p$, with L_I and L_p the intensity and pressure in dB with respect to 1 pW/m^2 and $2 \cdot 10^{-5}$ N/m^2, respectively. It is thus a measure of the difference between the sound intensity level of the source of interest and the total pressure level in the field due to all possible contributions, and is therefore a useful quantity for the validity of intensity measurements. The free-field condition is achieved when $L_k = 0$, thus $L_p = L_I$: this is the optimum situation to determine accurately the intensity. When L_k is large negative, the measured pressure (in dB) is much higher than the free-field pressure, so that the latter is difficult to be determined accurately. If the distance between sound source and intensity probe exceeds the reverberation distance (the distance to the source at which the direct field and reverberant field are equal), an accurate determination of the intensity becomes difficult. This is also the case when a high background noise level is present, when the sound field is directed in an oblique direction, or when the sound field consists of several uncorrelated contributions of equal strength.

A p-u probe consisting of a ½" Brüel & Kjær pressure microphone and a Microflown, and a p-p Brüel & Kjær intensity probe were compared in an experiment by Druyvesteyn and de Bree [20, 9]. With both probes, the intensity was measured and a dual Brüel & Kjær audio analyser was used for calculation of the intensity in 1/3 octave bands. In the case of the p-p probe the intensity can be found from the imaginary part of the cross spectrum between the two microphone signals; $I \propto Im(G_{p_1p_2})$. With the p-u probe, the intensity can be calculated in principle from the real part of the cross spectrum of the Microflown signal and the microphone signal, $I \propto Re(G_{pu})$.

However, there may be an extra phase difference between the p- and the u-signal, since the two sensors differ in physical behavior and the preamplifiers of the pressure microphone and particle velocity sensor are quite different. This phase difference can be determined in an acoustic experiment in an anechoic room with one sound source (a loudspeaker) and the p-u probe, that is connected to the dual channel audio analyser.

Some explorative experiments using two loudspeakers were performed. In the first experiment the two loudspeakers were positioned on one line, with the intensity probe in the middle, see figure 2-9A. The two loudspeakers were excited by two uncorrelated noise sources. When the excitation strength of the two loudspeakers are equal, the net energy flow should be zero, but both the pressure and the particle velocity level should be 3 dB higher than when one loudspeaker is excited.

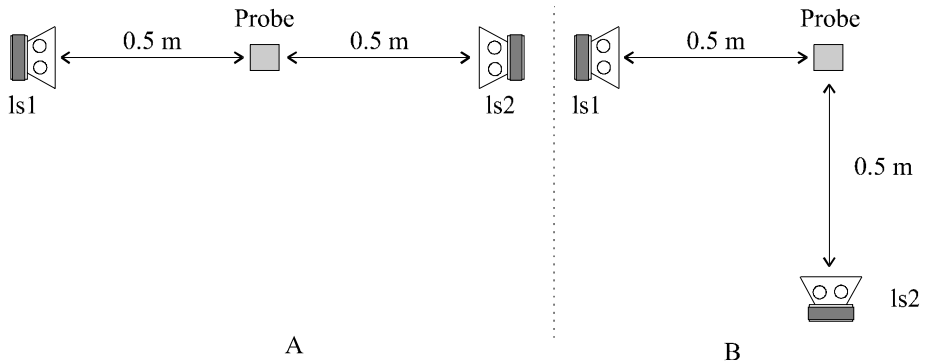

Figure 2-9: Measurement set-ups for comparison of the one-dimensional p-u probe and the p-p Brüel & Kjær intensity probe. A: the two loudspeakers are positioned in one line; B: the two loudspeakers in mutually perpendicular directions (from [9]).

To obtain a more negative reactivity index L_k, the same experiment was also performed in a reverberation room with a reverberation time of approximately 3 to 8 s. Next, in a second experiment the two loudspeakers were placed such that they generated noise in mutually perpendicular directions. For the intensity probe in the middle (see figure 2-9B) the contribution to the intensity from the second loudspeaker is theoretically zero. The loudspeakers were placed at a distance of 0.5 m to the sound intensity probe.

The intensity was measured for the configuration of figure 2-9A, both in an anechoic room and in a reverberant room, for 1/3 octave bands of 125, 315 and 3150 Hz. Some of the results (more are found in [9]) are presented in figure 2-10. The one-dimensional p-u probe was compared to a p-p probe with a separation distance between the microphones of 12 mm and a p-p probe with a spacing of 50 mm. In the experiment the two loudspeakers were excited to generate (uncorrelated) noise. The excitation of loudspeaker 1 (s_1) was kept constant, while that of loudspeaker 2 (s_2) was varied. The figures 2-10 show the measured relative intensity, measured by the different probes, as a function of $(s_2/s_1)^2$, with I_0 defined as the measured intensity when only loudspeaker s_1 is excited and loudspeaker s_2 is switched off.

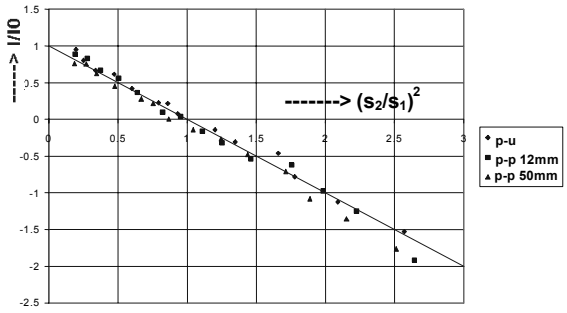

Figure 2-10a: Measurement performed in the anechoic room at 125 Hz in a 1/3 octave band. The theoretical prediction is shown by the line from (0,1) to (3,-2). Both the 12 mm and the 50 mm p-p probe behave as to be expected; the p-u probe performs well too.

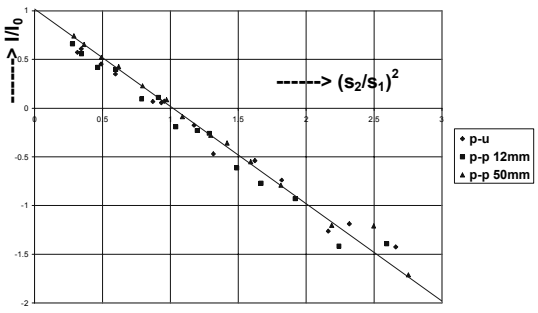

Figure 2-10b: Measurement performed in a reverberant room at 315 Hz in a 1/3 octave band. The theoretical prediction is shown by the line from (0,1) to (3,-2). Both the 12 mm and the 50 mm p-p probe behave as to be expected; the p-u probe performs well.

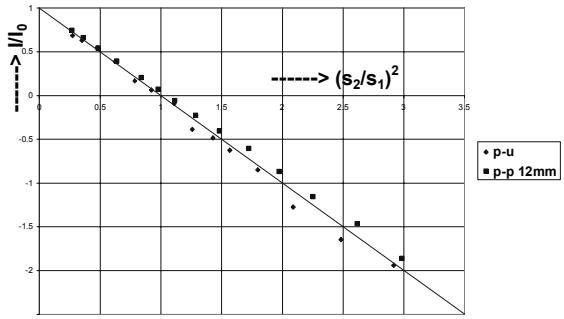

Figure 2-10c: Measurement performed in the anechoic room at 3150 Hz in a 1/3 octave band. At this high frequency the 50 mm p-p probe cannot be used. Both the 12 mm p-p probe and the p-u probe perform well.

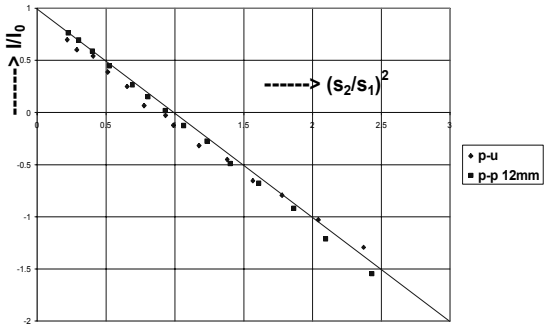

Figure 2-10d: Measurement performed in a reverberant room at 3150 Hz in a 1/3 octave band. The 50 mm p-p probe cannot be used at 3150 Hz. The other two probes are well performing.

The theoretically expected dependence is represented by the line, I/I_0 linearly dependent on $(s_2/s_1)^2$ with $I = 0$ for $s_1 = s_2$. The reactivity index for the experiments in the reverberation room for $s_2 = 0$ ($I = I_0$) was approximately $L_k = -7$ dB.

For the 1/3 octave bands with low center frequencies (below 1250 Hz) the p-u probe, the 12 mm and the 50 mm p-p probes can be used, but for higher frequencies the p-p probe with 50 mm separation distance cannot be used. At a frequency $f = 3$ kHz for example, the acoustic wavelength is roughly $\lambda \approx 10^{-1}$ m = 10 cm, so that a microphone separation distance of 5 cm is not negligible compared to the wavelength.

From the performed experiments it can be concluded that the experimental results show a satisfying correspondence to the theoretical predictions. It was seen however, see the figures 2-10e and 2-10f, that for sound intensity measurements in the reverberant room the p-p probe with 12 mm separation distance cannot adequately be applied for the low-frequency (125 Hz) octave bands. This is explained by the phase difference occurring across the two microphones, ca. 0.3°, together with the large reactivity index of $L_k = -7$ dB, so that a larger microphone separation distance is favourable.

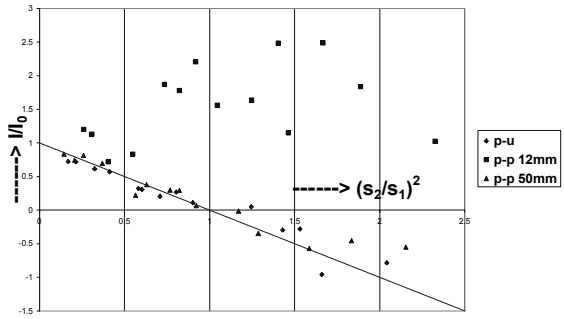

Figure 2-10e: Measurement performed in a reverberant room at 125 Hz in a 1/3 octave band. The figure shows well that, due to the large reactivity of the sound field, the 12 mm p-p probe cannot be used [9,20].

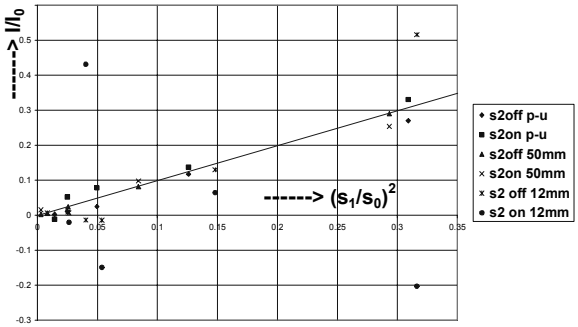

Figure 2-10f: Measurement result in the reverberant room, in the set-up of figure 3-5B, at 160 Hz, compared to the theoretical linear dependence. The 12 mm p-p probe performs poorly if loudspeaker 2 is switched off and even worse if it is switched on.

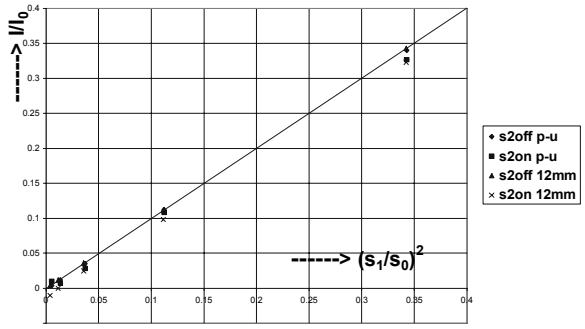

Figure 2-10g: Measurement result in the reverberant room, in the set-up of figure 3-5B at 2500 Hz, compared to the theoretical linear dependence. Both the 12 mm p-p and the p-u probe perform well [9,20].

For the configuration as sketched in figure 2-9B the measured intensity is expected to be independent of the excitation of loudspeaker 2, since the direct acoustic field and the direction of the intensity probe are perpendicular. The experiment was implemented as follows. The excitation levels of the loudspeakers were adjusted such that the pressures due to the two contributions measured at the microphone were equal, the level of loudspeaker 1 thereby defined as s_0. The measured intensity with loudspeaker 1 excited to this signal strength s_0 and loudspeaker 2

switched off was defined as I_0. Then the intensity I measured by the probe was measured as a function of the excitation of the first loudspeaker, s_1, both with loudspeaker 2 switched on and switched off.
The measurements were performed with the 12 mm p-p probe, the 50 mm p-p probe and the p-u probe, and the experimental results were compared to the theoretically expected linear dependence between (I/I_0) and $(s_1/s_0)^2$. For all investigated frequencies (the 1/3 octave bands at 160, 800 and 2500 Hz) the experimental 'p-u' results showed a satisfying correspondence to the linear relationship, see the figures 2-10e and 2-10f. As we see in these figures, the 12 mm p-p probe, however, does not perform well for the frequency octave band at 160 Hz. This is due to the fact that the phase difference of the microphones, as experimentally determined, is about 0.1-0.2°, in correspondence with the phase matching of these two sensors according to the specifications [19], 0.1-0.3°. Besides, for the frequencies higher than 2500 Hz, the 50 mm p-p probe cannot be used due to its too large separation distance. This is the reason that this probe is not shown in figure 2-10g.
An already noted disadvantage of the p-p probes thus appears: the microphone separation distance to be applied depends on the frequency range of interest while a too small separation distance is not favourable because of the phase mismatch of the two microphones.

2.4.4 A three dimensional 'p-u probe'

A three-dimensional particle velocity and pressure probe consists of three particle velocity sensors, Microflowns, positioned around a small pressure microphone. The particle velocity can be measured in three perpendicular directions, almost at the same place, close to the condenser microphone. See figure 2-4.
Using u-u measurement principle 1 or 2 with combinations of two particle velocity sensors in three perpendicular planes, together with the measurement of the sound pressure, the magnitude and direction of the intensity can be fully determined. A calibration method of this three-dimensional probe (figure 2-4), in a standing-wave-tube has to be performed for three directions. In chapter 4, a more extensive

description of the calibration in a standing wave tube and some illustrative results will be given.

A following step to the realisation of a three-dimensional p-u probe is a fully micromachined probe of three perpendicular particle velocity sensors, integrated on a single chip. To realise sensors in three directions in the two-dimensional, planar, wafer technology, a 'through-the-wafer' etching technique has been introduced. The two velocity directions defined as u_x and u_y in figure 2-11, lie in the wafer surface, while the u_z direction is obtained from two wires on the upper and lower side of the wafer. Currently (2003), this proposed solution for the measurement of three perpendicular velocities, is still under investigation.

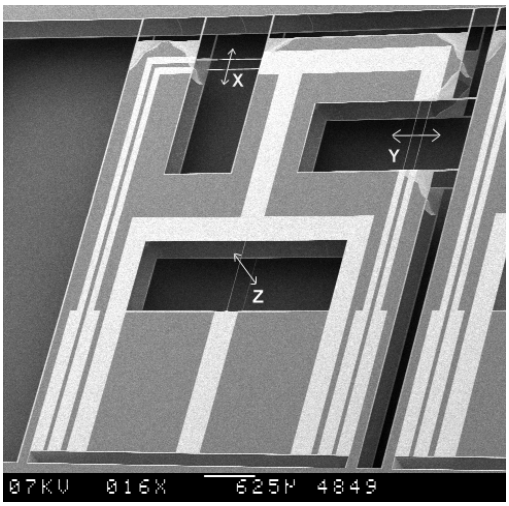

Figure 2-11: Integration of three mutually perpendicular Microflowns on a single chip, as realised by J.W. Berenschot, 1999 [9].

2.4.5 Near field sound intensity measurements

In section 2.1.1 it was seen that the ratio of mean square particle velocity and mean square pressure in the near field of an acoustic source essentially differs from that in the far field for plane waves. For a point source it was found that

$$\overline{u_r^2} = \frac{\overline{p^2}}{(\rho_0 c)^2}\left(1 + (1/kr)^2\right) \qquad (11.)$$

showing that, while the ratio of mean square particle velocity to mean square pressure is $(1/\rho_0 c)^2$ for plane waves, this ratio is approximately $(1/kr)^2$ larger in the near field. The specific acoustic impedance as given by Eq.(12.) on page 21 obtains a large imaginary component when $kr << 1$, that is, near to the source. In mechanical terms, the imaginary, or reactive component of the acoustic impedance, has the characteristic of inertia. This suggests that for $kr << 1$ some kinetic energy is stored in the near field, and not propagated to infinity. Clearly, this property is found for near fields of distributed sources in general, not only for purely spherical fields of ideal point sources.

For near field sound intensity measurements, principles that are based on the measuring of kinetic energy, i.e. particle velocities or flow, are therefore relatively favourable techniques compared to pressure measurements. The ratio of mean square particle velocity to mean square pressure exceeds the plane wave ratio by $(1/kr)^2$, which becomes large for both small wave numbers k (low frequencies) and for small distances to the source. This makes the u-u and p-u method preferable compared to the p-p measurement principles for sound intensity measurements in the near field region.

2.5 Summary and discussion

To determine the time averaged active (and reactive) sound intensity in a given point of an acoustic field, different measurement principles are possible. The p-p intensity probe, composed of two closely spaced pressure microphones, is based on the principle of deducing the particle velocity in the direction along the line connecting the acoustic points of the two sensors, from the pressure difference in this direction. This p-p measurement principle is widely used and yields (only) the component of the sound intensity in the direction along the probe; it is one-dimensional. Since the p-p probe is based on the determination of a pressure gradient, different microphone separations are required for different frequency ranges. Besides, a very good phase match between the sensors is required. The frequency bandwidth is limited by the phase mismatch of the microphones.

With another measurement method use is made of two mutually perpendicular particle velocity sensors: the u-u measurement principle. It is possible to obtain the

free field particle velocity, even in a reverberant sound field, from the two velocity sensors. Using the u-u principle 1, the particle velocities related to the free field and the reverberant sound field are deduced from the obtained signals of the sensor in the direction of the sound source and the sensor perpendicular to it. With u-u method 2, in which the auto spectrum and the cross correlation spectrum of the two sensors are determined, the sensors need not to be placed linear to and perpendicular to the sound source and it is also possible to determine this angle to the source. For both u-u methods the possibility exists to add a pressure microphone. This provides the additional required information to obtain the sound intensity in the plane of the sensors.

The preferable method is without doubt the p-u principle, it is the most direct and uncomplicated, and also most accurate method to determine the sound intensity.

The p-u intensity probe consists of a pressure microphone and a particle velocity sensor. Experiments with the different sensors have shown that the performance of this probe in acoustic measurements is similar to that of the p-p probe. An advantage of the p-u probe is that it is not necessary to use different spacers for the different frequency ranges, as is the case for p-p probes, so that one configuration suffices. Besides, no accurate matching of the sensors is necessary. Another advantage of the p-u probe is that its dimensions can be smaller, so that also near-field measurements can be performed. Combined with additional software, the p-u probe is an affordable and practical measuring device. Other acoustic parameters as the reactive intensity, the phase of the sound field, the energy density and the acoustic impedance can also easily be obtained from the particle velocity and pressure signals.

Moreover, in the near field, regions for which $kr << 1$, the ratio of particle velocity to pressure is relatively large; kinetic energy is stored in the near field. This means that for near field measurements methods based on the determination of the particle velocity have a relatively higher signal-to-noise ratio and are therefore favourable in comparison to p-p principles.

The main disadvantage is the calibration of the p-u probe. Since the two sensors detect different physical quantities it is not possible to use the same calibration method for both sensors unless the sound field is well known.

	p-p	u-u	p-u
accurateness (small errors)	-	-	+
affordability	-	+	+/-
appropriate for near field	-	+	+
large bandwidth	-	-	+
easy extension to three dim.	-	+/-	+
small size; convenience	-	+	+
simple calibration	+	+	-

Table 2-1: Comparison of the different principles, a 'p-p', 'u-u', and a 'p-u' probe, for sound intensity measurements.

An extension for three dimensional measurements leads to the three-dimensional p-u probe; a pressure microphone together with three perpendicular particle velocity sensors. Examples are seen in the figures 2-8 and 2-9. Such a probe provides all the information to determine the sound intensity as a vector, while only one, expensive, pressure microphone is needed. Besides it has, similar to the one dimensional p-u probe, the advantageous property that it can be positioned near a sound source for near field measurements. This configuration is preferable compared to a three-dimensional p-p probe that consists of six closely spaced sound pressure microphones (figure 2-5) and that is therefore rather expensive and due to the microphone separation distance in the three directions frequency limited. The three-dimensional p-u probe, on the contrary, is broad band. The magnitude and direction of the acoustic energy flow can be directly measured, even for non-stationary sound fields as from moving sources. From the obtained pressure and velocity vector, the total sound energy and the acoustic impedance can be determined as well.

For a concluding comparison between the three described measurement methods, the most relevant properties of the three probes with respect to sound intensity measurements, are mutually compared in table 2-1. The preference for the p-u principle is clear.

2.6 References

1. A.D. Pierce, 'Acoustics, An introduction to its physical principles and applications', Acoustical Society of America, New York (1994).
2. D.A. Bies, C.H. Hansen, 'Engineering Noise Control, Theory and Practice', E&FN SPON, London (1996).
3. M. Heckl, H.A. Muller, 'Taschenbuch der Technischen Akustik', Springer, 2nd ed. (1995).
4. R. Raangs, W.F. Druyvesteyn, Sound source localization using sound intensity measured by a three dimensional PU-probe, *Proceedings of the 112th AES Convention*, Munchen (2002).
5. F. J. Fahy, 'Sound Intensity', ISBN 0419198105, 2nd ed. (1995).
6. R. Raangs, W.F. Druyvesteyn, H-E. de Bree, A low-cost Intensity Probe, *Proceedings of the 110th AES Convention*, Amsterdam (2001).
7. R .Raangs, W.F. Druyvesteyn, H-E. de Bree, A novel two-dimensional sound particle velocity probe for source localization and free field measurements in a diffuse field, *Proceedings of the Internoise Conference* (2001).
8. W.F. Druyvesteyn, H-E. de Bree, R. Raangs, Free field measurements in a reverberant room using the microflown sensors, *Proceedings of the ICA*, Rome (2001).
9. H.-E. de Bree, 'The Microflown', ISBN 9036515793, Amsterdam, The Netherlands (2001).
10. J.W. van Honschoten, H-E. de Bree, F.J.M. van der Eerden, G.J.M. Krijnen, The influence of viscothermal effects on calibration measurements in a tube, *Proceedings of the 109th AES Convention*, Los Angeles (2000) 5182-5191.
11. F.J.M. van der Eerden, H-E. de Bree, H. Tijdeman, Experiments with a new acoustic particle velocity sensor in an impedance tube, *Sensors and Actuators* A 69 (1998) 126-133.
12. F. Jacobsen, A note on finite difference estimation of acoustic particle velocity, *Journal of Sound and Vibration* 256 (5), (2002) 849-859.

13. I. Wolff, F. Massa, Use of pressure gradient microphones for acoustical measurements, *Journal of the Acoustic Society of America* 4 (1993) 217-234.
14. R.K. Cook, P.A. Schade, New method of measuring the total energy density of sound waves, *Proceedings of Inter-Noise 74*, Washington (1974) 101-106.
15. B.S. Cazzolato and C.H. Hansen, Errors in the measurement of acoustic energy density in one-dimensional sound fields, *Journal of Sound and Vibration* 236 (2000) 801-831.
16. F. Jacobsen and E.S. Olsen, The influence of microphone vents on the performance of sound intensity probes, *Applied Acoustics* 41, (1994) 25-45.
17. J.W. Parkins, S.D. Sommerfeldt and J. Tichy, Error analysis of a practical energy density sensor, *Journal of the Acoustical Society of America* 108 (2000) 211-222.
18. B.S. Cazzolato and C.H. Hansen, Errors arising from three-dimensional energy density sensing in one-dimensional sound fields, *Journal of Sound and Vibration* 236 (2000) 375-400.
19. Brüel and Kjaer, Techical Review no. 3,4 (1982), 4 (1985), 4 (1986), 1 (1996).
20. W.F. Druyvesteyn and H.-E. de Bree, A new sound intensity probe; comparison to the Brüel and Kjær p-p probe, *Journal of the Audio Engineering Society*, Vol.48, no. 1/2 (2000).

Chapter 3

An analytic model of the particle velocity sensor

Abstract

This chapter treats an analytical model describing the physical processes that govern the behaviour of the Microflown and determine its sensitivity. The temperature distribution around the two heated wires is calculated. Forced convection by an acoustic wave causes a small, asymmetrical, perturbation to this temperature profile, so that a temperature difference between the two wires occurs. This temperature difference, to which the sensitivity is proportional, is calculated with perturbation theory. Subsequently the frequency dependent behaviour of the sensitivity can be analysed; it is shown that there are two important corner frequencies, the first related to the time constant of heat diffusion, the second related to the heat capacity of the heaters. Especially for small wire separations, the developed analysis appears to be in good agreement with experimental results.

3.1 Introduction

The sensor that is the main subject of this thesis, the Microflown, is an acoustic sensor based on a thermal principle [1]. Since its invention in 1994 [2], it is mostly used for measurement purposes, like one dimensional and three dimensional sound intensity measurements [3, 4, 5, 6], measurements of the acoustic impedance [7, 8] and the pressure [9]. The particle velocity sensor is also used as an 'add-on' microphone for professional recording purposes [14]. This is because the Microflown is, contrary to pressure gradient microphones, comparatively sensitive to low frequency sound waves. A particle velocity sensor with a wide measurable frequency spectrum can be obtained by a combination of a Microflown and a so-called 'pressure gradient' microphone, it has a 'figure-of-eight' polar pattern of the sensitivity. The Microflown is used as well for measuring DC flows [10], and can be used as a mass flow sensor [17, 18, 19]. Sound-energy determination and three-dimensional impulse response measurements with this sensor are under investigation.

The sensor itself consists of two closely spaced (*ca*. 100 μm) thin wires of silicon nitride, similar to [16], with an electrically conducting platinum pattern on top of them. A SEM photograph of a Microflown is depicted in figure 2-1.

Dimensions of the two wires are $1000 \times 10 \times 0.5$ μm ($l \times w \times h$). The metal pattern is used as heater *and* as temperature sensor, by using its temperature dependent resistance. The silicon nitride layer is used as a mechanical support for the platinum resistor patterns. The sensors are powered by an electrical current, and heated to an operational temperature between 200ºC and 500ºC.

When a particle velocity is present, the temperature distribution around the resistors is asymmetrically altered, and a temperature difference between the two wires occurs. In a first order approximation, this temperature difference of the two wires is proportional to the particle velocity, and since the resistance of the heated wires increases with their temperature, it can be electronically measured.

Due to heat diffusion effects in the fluid and the thermal mass of the wires, the thermal response of the wires decreases with increasing frequencies. The Microflown therefore exhibits a decrease of sensitivity with increasing frequencies.

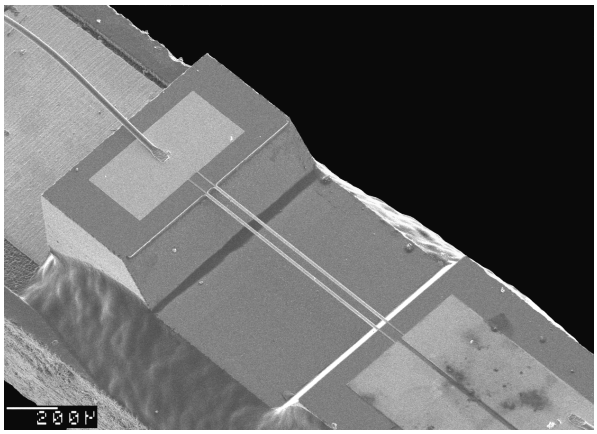

Figure 3-1: SEM Photo of a bridge type Microflown. At the top of the sample a wire-bond is visible. The sample is glued on a printed circuit board; the glue is seen at the lower left side of the picture.

3.2 The temperature distribution around the wires

A detailed three dimensional model of the device was developed a few years ago [12]. In that model, the final expression for the sensitivity was obtained by calculating a multiple sum of a definite function. Though the sums converge rather fast, this result is not very convenient for engineers designing the Microflown for specific applications. Significant progress achieved in the Microflown technology since then has allowed to simplify the model. First, the wire width was reduced to 2 μm and its thickness became 100 nm for the platinum layer and 200 nm for the silicon nitride support. These sizes are much smaller than all the other dimensions. Therefore, in most cases one can consider the wire as a one dimensional object except for those situations in which the width or thickness of the wire plays an essential role. Second, the technology has offered the possibility to make the wires longer so that a two dimensional approach is a good approximation for the real device. Third, in many cases the surrounding surfaces are far from the wires, so that we can consider them as free standing.

Our aim here is to get a relatively simple explicit expression for the sensor sensitivity, which has a sufficient precision for engineering applications.

In the model to be developed the device consists of two infinitely long heaters of width L and thickness h, separated by a distance a, which is much larger than L or

h. We will neglect the transverse wire dimensions everywhere where it does not bring any physical contradictions. For example, the expression for the heater temperature is divergent in the limit $L \to 0$. In this case a simple way to take into account the finite wire width will be proposed. The wire width and thickness are also important when the effect of the thermal mass of the wire is considered.

A certain particle velocity with amplitude v is assumed as the signal to be measured. The possible discrepancy between the velocity of an undisturbed (free field) sound wave and the particle velocity at the position of the sensor is not taken into account. Although it can be expected that the wires slightly influence the velocity profile around them, the measured velocity v nearby the wires is supposed to be proportional to the particle velocity. This is posed only as a convention, in view of the fact that generally the sensor has to be calibrated due to the more significant influence of the package gain.

It should be stressed that the device is operating at velocities very small in comparison with those typical for the hot wire anemometry. The Microflown is able to measure particle velocities as small as 50 nm/s [23]. A sound pressure of 1 Pa (94 dB) corresponds to a velocity v = 2.2 mm/s, while anemometers lose their sensitivity at velocities of about $v \sim 1$ cm/s [21, 24].

The heated wires cause a temperature distribution of the air around them. This undisturbed temperature profile, not yet influenced by an acoustical wave, is calculated first. Subsequently this profile is used as a starting point for the calculation of the temperature difference of the heaters that occurs when a flow is applied, by addition of a perturbation to the original temperature profile.

In section 3.2.1 the stationary temperature distribution is calculated, so that in 3.2.2 the influence of an acoustic wave can be analysed as a perturbation to this function, and in section 3.2.3 the effect of the finite heat capacity of the sensors on the frequency behaviour is taken into account.

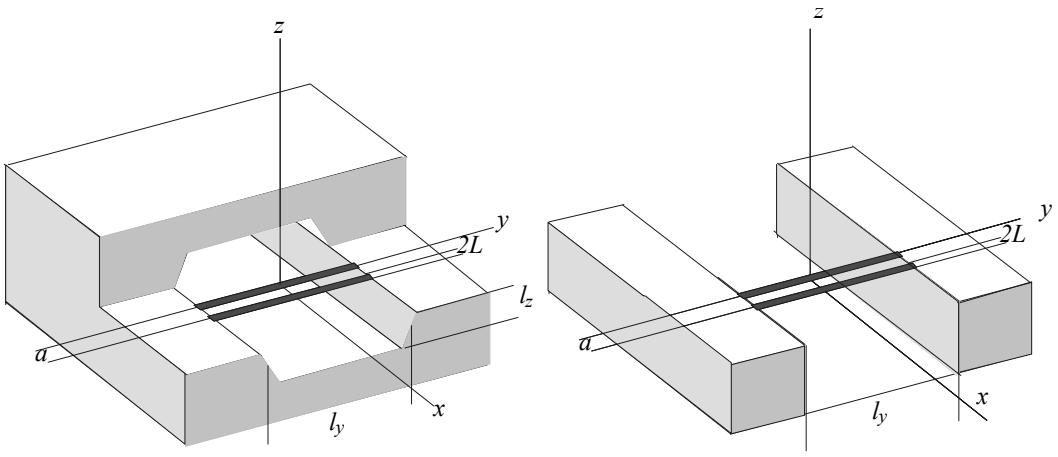

Figure 3-2: Geometry of the sensor used in the analysis. Left: geometry used in the previous model [12]; right: geometry analysed in this chapter, without walls above and under the heaters.

3.2.1 The stationary situation

The temperature profile around the heaters in the two-wire realisation of the Microflown is adequately described in [12] for the configuration of the channel with fixed walls in the positive and negative *y*- and *z*-direction (see figure 3-2). The distribution of the temperature in the situation in which the fluid (*i.c.* the air) is in rest was shown to be a good starting point to describe the temperature change due to a sound wave. From the temperature difference between the heated wires the sensitivity of the sensor was deduced. In [12], both unperturbed and perturbed temperature profiles are written as a Fourier series, as expansions in harmonics.
In this paper a configuration is assumed in which no walls in the *y*- or *z*-direction are present, and a theory is developed to find an analytical expression for the temperature difference between the wires and so for the sensitivity of the sensor.
The stationary heat transport equation for this geometry reads

$$-\nabla(k\nabla T) = Q, \qquad (1.)$$

where $k = k(T)$ represents the heat conductivity of the medium, and Q is the amount of heat generated per unit time and volume.
Suppose first that the heater is infinitely long in the *y*-direction (l_y much larger than all other dimensions) and infinitely thin in the *x* and *z*-directions. Since the

total power is P, and the power per unit of length is P/l_y for the heat source one can write:

$$Q = \frac{P}{l_y}\delta(x)\delta(z), \tag{2.}$$

where the δ-functions appear at the heater position. Since the length l_y is large and the temperature along this direction is assumed to be constant, the problem is reduced to a two dimensional one and therefore becomes simpler than the model based on the expansion in harmonics as presented in [12].

Additionally we will assume that k is independent of T. For high wire temperatures (400-500 ^{0}C) this assumption is true with a precision of approximately 10 %. This can be considered as an acceptable precision for engineering purposes. In this case equation (1.) is simplified as

$$(\partial_x^2 + \partial_z^2)T = -\frac{P}{l_y k}\delta(x)\delta(z) \tag{3.}$$

The general solution of this equation is

$$T(r) = -\frac{P}{2\pi k l_y}\ln\frac{r}{r_0}, \quad r = \sqrt{x^2 + z^2}, \tag{4.}$$

where r_0 is an arbitrary constant. We are searching for the solution that is finite in the origin, r = 0, and goes to zero at infinity. Obviously, Eq. (4) shows divergencies in both of these limits. The divergency in the origin has a clear physical meaning: we did not take into account the finite width of the wire. It can be easily taken into consideration in the way as will be described below. The divergency at infinity reflects the two dimensional nature of the problem; there is no physical system that is exactly two dimensional. At large distances this logarithmic behaviour should be changed due to the finite length of the wire. The question is to what extend one can use the solution (4.) and what is the value of r_0.

The answer is that Eq.(4.) describes the behaviour of a real three dimensional system with so called logarithmic precision. Let us note first that the arbitrary constant r_0 has to be proportional to the only length scale l_y (current sensors have $l_y \approx 1500$ μm). Then the logarithmic precision means that our solution is true while

$$\left|\ln\left(\frac{r}{l_y}\right)\right| >> 1. \tag{5.}$$

We are interested in the temperature distribution on distances of the order of 100 μm (the separation between the wires), therefore, the logarithmic precision is only 40 %; not very good. Fortunately there is a possibility to improve the solution accuracy.

One can find the exact solution of the three dimensional problem with the geometry shown in figure 3-2 (right) and see how it can be approximated by Eq.(4.). The three dimensional problem with the cold walls at $y = \pm l_y/2$ can be solved similar to that as was described in [12]. We are looking for a solution as an expansion in harmonics

$$\begin{aligned} T(x,y,z) &= \sum_{n=0}^{\infty} T_n(x,z)\cos\left(2\lambda_n y / l_y\right) \\ \lambda_n &= \frac{\pi}{2}(2n+1). \end{aligned} \tag{6.}$$

In this way the boundary conditions on the walls will be satisfied (for a physical discussion see [12]). For the amplitudes $T_n(x, z)$ we will find an equation similar to (3.) but with an additional term

$$(\partial_x^2 + \partial_z^2)T_n - \left(\frac{2\lambda_n}{l_y}\right)^2 T_n = -\frac{2(-1)^n}{\lambda_n}\frac{P}{l_y k}\delta(x)\delta(z) \tag{7.}$$

It can be solved by making a two dimensional Fourier transform to find

$$T_n(r) = \frac{P}{2\pi k l_y}\frac{2(-1)^n}{\lambda_n} K_0\left(\frac{2\lambda_n r}{l_y}\right), \tag{8.}$$

where $K_0(x)$ is the modified Bessel function of the second kind. It can be substituted in Eq. (6.) to get the three dimensional temperature distribution. This distribution is rather flat in the y-direction changing only nearby the walls [12]. In the limit $r \to 0$ it behaves as

$$T(x,0,z) = -\frac{P}{2\pi k l_y}\left(\ln\left(r / l_y\right) - \gamma - 2\ln\Gamma(3/4) + \frac{3}{2}\ln\pi\right) \tag{9.}$$

where $\gamma = 0.577$ is the Euler constant and $\Gamma(x)$ is the gamma-function. The function (9.) behaves exactly as the solution of the two dimensional problem (4.)

with the only difference that the constant r_0 has a definite value: $r_0/l_y = 0.480$. A comparison of the temperature distributions given by the exact solution of the three dimensional problem (6.) and (8.), and that given by Eq.(4.) is presented in figure 3-3 by the solid and dashed lines, respectively. One sees that the approximation is very good up to $r/l_y \leq 0.2$. This distances range covers all the practical needs.

This is the most important conclusion from the analysis above because, as we will see later, for the calculation of the sensor sensitivity we have to know the gradient of the stationary temperature distribution but not the temperature itself. However, this gradient does not depend on the parameter r_0 at all.

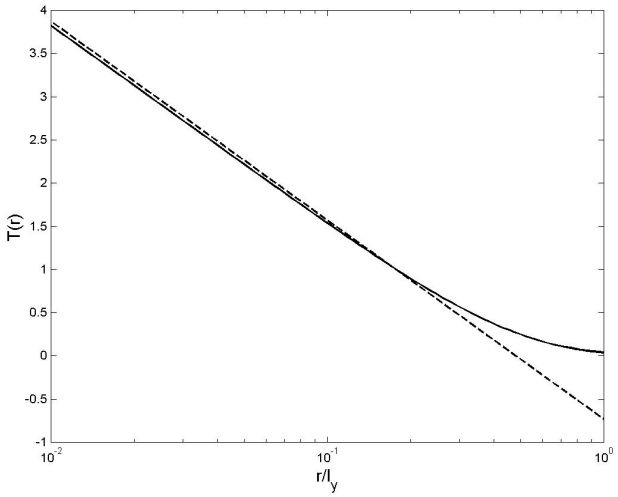

Figure 3-3 The temperature distribution given by the exact solution of the three dimensional problem, Eqs. (6.) and (7.), (solid line) compared to the approximation of Eq. (4.) (dashed line).

We justified the use of the two dimensional solution and indicated the upper limit on the distance from the wire where the two dimensional approximation is still applicable. Now let us discuss the divergency at $r \rightarrow 0$. Due to this divergency Eq.(4.) does not allow to calculate the temperature of the wire itself. It is since we neglected the wire width. One can easily take into account the finite width of the wire in the following way. We can distribute the point-like sources in the x-direction on the wire in such a way that the boundary condition is fulfilled: the temperature on the wire is constant. It gives an integral equation for the source

distribution function. However, since the wire is narrow, there is a much simpler approximate way. For a narrow wire any distribution can be changed by the averaged one over the wire width. This approximation will be good while the temperature change on the wire is small in comparison with the temperature itself. For the wires as narrow as 2 μm it is obviously the case. In a mathematical language this physical picture can be formulated as

$$T(x,z) = -\frac{P}{2\pi k l_y}\frac{1}{2L}\int_{-L}^{L} \ln\frac{\sqrt{(x-x')^2+z^2}}{r_0}dx' \qquad (10.)$$

At distances much larger than the wire width, $|x|$, $|z| >> L$ it coincides with (4.), but on the wire itself it gives the finite temperature

$$T(0,0) = -\frac{P}{2\pi k l_y}\left(\ln(L/r_0)-1\right) \qquad (11.)$$

The temperature distribution will be used as the basis for the following. The integral in (10.) can be found explicitly but it is not very informative since the point of interest is the temperature gradient but not the temperature itself. So we leave the integral in its original form for a while. During the calculation of the temperature profile above, only one heater was considered, see Eq.(3.). Due to the linearity of the heat equation the solution for T is a sum of two solutions, each for only one source, one source at $x = 0$, the other one at $x = a$. The new solution for T is therefore not fundamentally different from Eq.(4).

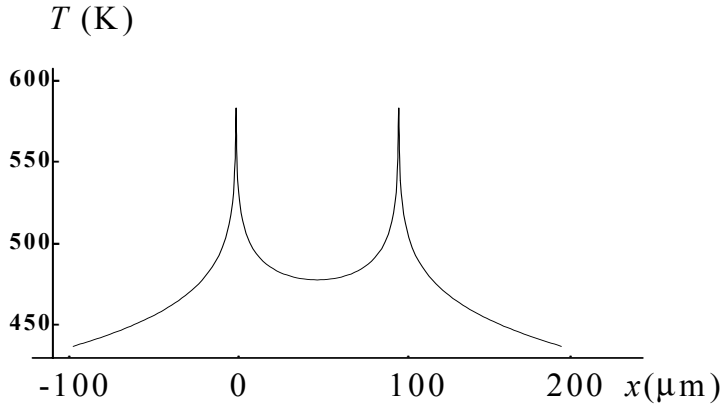

Figure 3-4. Temperature distribution around the two sensors in a stationary situation. The heaters are located at x=0 and x=100 μm, the dissipated power is assumed to be 10 mW.

It can be written, for example, in the form $T_{total}(x)=T_{left\ heater}(x)+T_{right\ heater}(x)$, where $T_{right\ heater}(x)= T(x\text{-}a)$ and $T_{left\ heater}(x)=T(x)$.

For the situation of two heaters at a mutual distance of 100 μm, a length l_y of 1.5 mm and a dissipated power of 10 mW, the temperature distribution is shown in figure 3-4. On the scale of the figure, no difference can be distinguished between the exact solution (Eqs. (6.) and (8.)) and the two dimensional approximation.

3.2.2 Influence of an acoustic wave on the temperature profile

If the gas in the channel is moving, the temperature can be found from the full heat equation

$$\rho c_p\left(\partial_t T+\vec{v}\cdot\vec{\nabla}T\right)-k\nabla^2 T=Q, \qquad (12.)$$

where $\vec{v}$ is the gas velocity , ρ and c_p are the density and heat capacity of the gas, respectively, the heat power density Q is defined as before by Eq. (2.). The convective term $\vec{v}\vec{\nabla}T$ is responsible for the differential signal from the device, which constitutes the main concern of this chapter.

The free convection is not significant in our case (as it is in many microsystem applications). Free convection becomes important when the Grashof number (Gr) is larger than 1000 [25], but in our situation $Gr < 1$.[1]

Let us consider two competing processes: the heat diffusion defined by the heat diffusion coefficient $D = k/\rho c_p \approx 1.9\cdot10^{-5}$ m^2/s (air) and the forced convection defined by the velocity magnitude v = 4 mm/s (it corresponds to a very high acoustic pressure of 100 dB). Due to the diffusion the time to travel for a particle from one wire to the other is l^2/D, due to the forced convection this time will be l/v. Comparing these times yields

[1] The Grashof number is defined as

$$Gr=\frac{g\beta\Delta T l^3}{\nu^2},$$

where g is the gravity acceleration, β the gas thermal expansion coefficient, ν the kinematic viscosity, ΔT the temperature change, and l is a characteristic length. For the Microflown the characteristic length is small: l~100 µm, and therefore $Gr \le 1$.

$$\frac{v}{D/l} << 1 \qquad (13.)$$

because the diffusion velocity $D/l \approx 0.2$ m/s is large in comparison with v. This means that the temperature profile due to the heat conductivity is formed comparatively fast; the contribution of the convection is small so that the convective term in Eq. (12.) can be treated as a perturbation. Therefore, we can consider the temperature as $T+\delta T$, where the first term is the temperature in still air that was found in the previous section and δT is the temperature correction caused by convection. For this correction one finds from (12.) the following equation

$$\partial_t \delta T - D\nabla^2 \delta T = -v\partial_x T, \qquad (14.)$$

where it has been assumed explicitly that the gas is moving only in the x-direction, $\vec{v} = (v,0,0)$.

Since the velocity is supposed to be directed along the channel, $\vec{v} = (v,0,0)$ the product $v\partial_x T$ appears at the right-hand side of Eq.(14.).

For arbitrary direction of the velocity $\vec{v}$ in the plane of the wires, one should substitute instead of v the magnitude of the dot product $\vec{v}\cdot\vec{n}$, with $\vec{n}$ the vector normal to the wires in the plane of the wires ($|\vec{n}| = 1$), which is equal to $|\vec{v}|\cos\phi$. Here ϕ defines the angle between the vectors $\vec{v}$ and $\vec{n}$. (This causes the 'cos ϕ'-dependence of the sensitivity, which directionality is often referred to as a 'figure-of-eight' [1].)

First, we will consider the case of one heater. Generalisation to the case of two heaters is straightforward since the equation is linear. At the right hand side one has to substitute the temperature distribution for the stationary problem (10.). It was already noted that the gradient $\partial_x T$ does not depend on the parameter r_0. Equation (14.) has to be solved at the boundary condition $\delta T \to 0$ at large distances from the wires.

In acoustic applications the periodic signals are of main interest and a particle velocity in the sound wave is therefore considered in the form of a harmonic signal $v = v_0\, exp(i2\pi ft)$ with a frequency f. The temperature correction is then also harmonic in time: $\delta T = \delta T(x,z)\, exp(i2\pi ft)$, with the amplitude $\delta T(x,z)$ depending only on the coordinates. This amplitude can be found from

$$i2\pi f\delta T - D(\partial_x^2 + \partial_z^2)\delta T = -v_0\partial_x T \qquad (15.)$$

with the boundary conditions $\delta T \to 0$ at infinity.

An important comment has to be made at this point. The temperature (10.) is a symmetric function of x with respect to the sensor position x=0. Therefore, the temperature gradient in (15.) is an antisymmetric function. This means that in first order the wire temperature does not change due to the gas flow. For the Microflown this is not a problem because of the presence of the other wire at $x = a$ that will feel the presence of the heat flux from the first one. It seems, however, a contradiction to the hot wire anemometry. Actually there is no contrariety. If one would calculate the second order correction to the temperature it would be defined by the term $-v_0\partial_x\delta T$, which is symmetric in x. The wire temperature changes therefore as v^2. It was already stressed that at small gas velocities the anemometer loses its resolution. It works perfectly well at large Reynolds numbers, Re>>1 when there is a thin boundary layer around the wire. In that case the heat transfer coefficient is proportional to$\sqrt{Re} \sim \sqrt{v}$. However, the Microflown operates in the range Re << 1, where the boundary layer does not exist (formally it is larger than the device size). At this condition the heat transfer coefficient does not depend on the velocity at all in the first order approximation [22]. This dependence appears only as $Re^2 \sim v^2$ in full agreement with our conclusion.

Equation (15.) can be solved using a Fourier transform over the z coordinate

$$\overline{\delta T}(x,q) = \int_{-\infty}^{\infty} \delta T(x,z)e^{iqz}dz. \qquad (16.)$$

The right hand side in (15.) is transformed accordingly, using the stationary temperature distribution (4.). For the x-dependence of the Fourier amplitude one finds

$$\overline{\delta T}'' - K^2\overline{\delta T} = -\frac{v}{D}\frac{P}{2kl_y}sign(x)e^{-q|x|}, \qquad K = \sqrt{q^2 + i2\pi f/D}. \qquad (17.)$$

Here a prime denotes a derivative to x and q should be interpreted as the absolute value $|q|$. The solution of this equation that is continuous at x = 0, together with its derivative, and goes to zero at infinity, is

$$\delta\bar{T}(x,q) = -i\frac{v}{2\pi f}\frac{P}{2kl_y}sign(x)\left(e^{-q|x|} - e^{-K|x|}\right). \qquad (18.)$$

The expression is antisymmetric due to the presence of the sign-function.

To find the z-dependence of the temperature correction, the inverse Fourier transform has to be found. Analytically, this is not possible. However, it should be realised that the only place of interest for $\delta T(x,z)$ is at $z = 0$: the wire can be at an arbitrary x position but its z-coordinate is zero. In this case the inverse transform can be found analytically. If one heated wire is at the position $x = 0$ and the other at $x = a$ then the influence of the first one to the second changes its temperature by $\delta T(a,0)$. However, the second heater also influences the first one and due to the antisymmetry its temperature changes with $-\delta T(a,0)$. The device measures the differential signal, which is proportional to the difference between the temperatures of the wires. As stated above, the total function for the temperature T consists of two terms of the form (9), like $T_{left\ heater}$ and $T_{right\ heater}$, with one term shifted over a distance a. The behaviour of $T(x)$ as a sum of two functions is illustrated by figure 3-5a and 3-5b.

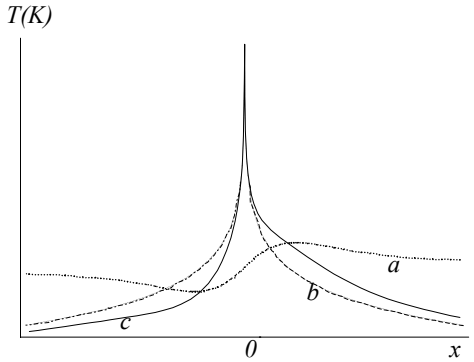

Figure 3-5a: The original, unperturbed, temperature profile of one heater vs. x (b), the perturbation δT(x) due to convection (a) and the sum of both (c).

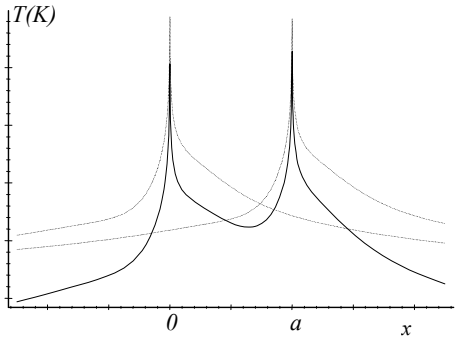

Figure 3-5b: Temperature due to convection vs. x for two heaters at a mutual distance a, as a sum of two single temperature functions.

The temperature difference between the wires can be expressed in the form

$$\Delta T = 2\delta T(a,0) = e^{i2\pi f}\frac{2v}{D/a}\frac{P}{2\pi kl_y}\frac{1}{i\bar{f}}\left[1 - \sqrt{i\bar{f}}K_1\left(\sqrt{i\bar{f}}\right)\right], \qquad (19.)$$

with $K_1(x)$ the modified Bessel function of the second kind, and in which the dimensionless frequency has been introduced as

$$\bar{f} = \frac{f}{f_D}, \quad f_D = \frac{D}{2\pi a^2}. \tag{20.}$$

The frequency f_D is called the thermal diffusion frequency. Of course, only the real part of ΔT has a physical meaning.

For large $\bar{f}$, the term with the Bessel function decreases exponentially, and the amplitude of ΔT decreases as $1/\bar{f}$. For small $\bar{f}$, i.e. $\bar{f} << 1$ or $f << f_D$, the behaviour of the Bessel function is as

$$\sqrt{i\bar{f}}\,K_1(\sqrt{i\bar{f}}) = 1 + \frac{i\bar{f}}{2}\left(\ln\frac{\sqrt{i\bar{f}}}{2} + \gamma - \frac{1}{2}\right) \tag{21.}$$

and again a divergency problem emerges: ΔT diverges logarithmically in the zero frequency limit. The problem is connected with the two dimensional nature of the model again. It should be stressed that the reason for this divergency is not connected with the finite wire width, which can be safely kept zero; the problem appears due to the small q range (large distances). To avoid the problem, we once more have to return to the real three dimensional world. As can be seen from the expansion (6.), there is a smallest wave number along the y-direction, which is $q_0 = \pi/l_y$. The larger values of n in (6.) are not important because they are integrated out in two dimensions, but the first one is of principal importance. It is easy to see that to take q_0 into account, q and K in (17.) should be changed into

$$q \to \sqrt{q_0^2 + q^2}, \quad K \to \sqrt{q_0^2 + q^2 + i2\pi f / D}. \tag{22.}$$

Then the final expression for the temperature difference can be written as

$$\Delta T = 2\delta T(a,0) =$$
$$= e^{i2\pi f}\,\frac{2v}{D/a}\,\frac{P}{2\pi k l_y}\,\frac{1}{i\bar{f}}\left[\alpha K_1(\alpha) - \sqrt{\alpha^2 + i\bar{f}}\,K_1\left(\sqrt{\alpha^2 + i\bar{f}}\right)\right], \tag{23.}$$

$$\alpha = \pi\frac{a}{l_y}.$$

This expression is finite at zero frequency. For small α, the Bessel functions in Eq. (23.) can be expanded in α, and the limit for $f \to 0$ can be calculated. The difference between the wire temperatures in this case is

$$\Delta T(f=0) = e^{i2\pi f}\,\frac{2v}{D/a}\,\frac{P}{4\pi k l_y}\left(\ln\left(\pi a/2l_y\right)+\gamma\right) \qquad (24.)$$

This result defines the Microflown sensitivity to a constant gas flow. For applications Eq. (24.) must be used carefully since it is actually an expression with logarithmic precision and therefore can be not very precise. Furthermore, it works only at very low frequencies, which are not too interesting for acoustical applications. To be precise, as follows from (23.), the limit of (24.) is true for frequencies

$$f < \frac{\pi D}{4l_y^2}$$

which is about 7 Hz for the current device dimensions.
In the opposite limit one can use Eq. (19.) that is not restricted by the logarithmic precision. For acoustic applications therefore, the formula (19.) should be adequate.

3.2.3 The effect of the heat capacity of the sensors

The next step in the approach is to take into consideration the heat capacity of the sensors. The effect of this heat capacity becomes important for increasing frequencies. In Eq. (12.) an additional term appears with respect to this effect, so

$$\begin{aligned}&(\rho c_p)_{air}(\partial_t T + v\cdot\nabla T)\\ &+ Lh(\rho c_p)_{sensor}\left(\delta(x)+\delta(x+a)\right)\delta(z)\partial_t T - \nabla(k\nabla T) = Q\end{aligned} \qquad (25.)$$

Here h is the thickness of the wire, ρ represents the density and c_p the heat capacity of the fluid (the air) or the sensor.
The heated wire consists of a layer of silicon nitride of about 200 nm thickness, and a platinum (or chromium/platinum) wire of ca. 100 nm on it. The products ρc_p of both materials are of the same order of magnitude too: $(\rho c_p)_{Pt} \approx 2.85\cdot10^6$ Jm^{-3}K^{-1}; $(\rho c_p)_{SiNi} \approx 1.66\cdot10^6$ Jm^{-3}K^{-1}. This means that in order to calculate the specific value of $h(\rho c_p)_{sensor}$ in the equation, one should take the sum of both products $h_{Pt}\cdot(\rho c_p)_{Pt}$ and $h_{SiNi}\,(\rho c_p)_{SiNi}$. For air the similar product is tree orders of magnitude smaller, $(\rho c_p)_{air} \approx 1.3\cdot10^3$ Jm^{-3}K^{-1}.

If, again, a small perturbation δT is added to this equation, the same approach as to Eq. (12.) leads to

$$\begin{aligned}&\partial_t \delta T - D\nabla^2 \delta T \\ &= -v\partial_x T - Lh\frac{(\rho c_p)_{sensor}}{(\rho c_p)_{air}}(\delta(x)+\delta(x-a))\delta(z)\partial_t \delta T\end{aligned} \tag{26.}$$

if the two beams of the two-wire device are at $x = 0$ and $x = a$. After the Fourier transform from $\delta T(x,z)$ to $\delta\bar{T}(x,q)$, this can be written as

$$\begin{aligned}&\delta\bar{T}''(x,q) - K^2\delta\bar{T}(x,q) \\ &= \frac{v}{D}\partial_x \bar{T}(x,q) + i\frac{f}{f_{hc}}[\delta T(0,0)\delta(x) + \delta T(a,0)\delta(x-a)]\,.\end{aligned} \tag{27.}$$

Note that the coefficients near the δ-functions are not the Fourier amplitudes but the original temperature corrections at the wire positions. The second corner frequency f_{hc} has been introduced in (27.) as

$$f_{hc} = \frac{D}{2\pi Lh}\frac{(\rho c_p)_{air}}{(\rho c_p)_{sensor}} \approx 3000\ Hz\,. \tag{28.}$$

The numerical value is given for room temperature. However, the device operates at quite high temperatures and the change of the air density around the wire cannot be neglected. The frequency f_{hc} will be scaled with temperature as the ratio of room and wire temperatures, T_r/T_w.

Equation (27.) can be solved in the following way. Consider first one wire located at $x = 0$ (no term with $\delta(x\text{-}a)$ in (27.)). The contribution from the other wire can be added later just shifting the wire position to $x = a$. The term with the δ-function on the right hand side changes the boundary conditions at $x = 0$: instead of the continuity of the function and its derivative, the δ-function demands a finite discontinuity of the derivative

$$\delta\bar{T}'\big|_+ - \delta\bar{T}'\big|_- = i\frac{f}{f_{hc}}\delta T(0,0) \equiv C\,. \tag{29.}$$

The derivative jump C is an unknown constant. One can find the solution of Eq. (27.) expressed via this constant. It is given by the same function (18.) plus an additional term:

$$\delta\bar{T}(x,q) = -i\frac{v}{2\pi f}\frac{P}{2kl_y}sign(x)\left(e^{-q|x|} - e^{-K|x|}\right) + \frac{C}{2K}e^{-K|x|}. \qquad (30.)$$

The inverse Fourier transform of this expression at $z = 0$ can be found explicitly

$$\delta T(x,0) = \frac{vx}{D}\frac{P}{2\pi kl_y}\frac{1}{i\bar{f}_x}\left[1 - \sqrt{i\bar{f}_x}K_1\left(\sqrt{i\bar{f}_x}\right)\right] + \frac{C}{2\pi}K_0\left(\sqrt{i\bar{f}_x}\right), \qquad (31.)$$

$$\bar{f}_x = \frac{2\pi f x^2}{D},$$

where the x-dependent dimensionless frequency f_x has been introduced. It is interesting to note that the δ-term gives a change of the temperature of the wire itself due to the finite heat capacity, so, that $\delta T(0,0)$ is not zero any more. Of course, direct application of Eq.(31.)) gives an infinite value for $\delta T(0,0)$, but we already know how to deal with it: one has to average first the temperature correction over the wire width and then substitute $x = 0$. This procedure is equivalent to the change

$$\bar{f}_x(x \to 0) \to \bar{f}_L = 2\pi f L^2 / D.$$

If we take now into account the second wire at $x = a$ too, the solution of Eq. (27.) will be composed of two functions of the form (31.), one of them shifted over a distance a, as we have seen before, and expressed via the constant C'. This constant is defined similar to the definition of C, and corresponds to the discontinuity of the derivative on the other wire at $x = a$:

$$\delta\bar{T}'\big|_{a+} - \delta\bar{T}'\big|_{a-} = i\frac{f}{f_{hc}}\delta T(a,0) \equiv C'. \qquad (32.)$$

To find these unknown constants, C, and C' for the jump on the other wire, one should find the temperature correction produced by both wires. This is the sum of the two single solutions: $\delta T_{total}(x,0) = \delta T(x,0) + \delta T(x-a,0)$ and it is expressed via C and C'. In this function δT_{total}, we substitute, one by one, $x = 0$ and $x = a$. In the first case the correction will be proportional to C, in the second one to C'. In this way we obtain two linear equations for the unknown constants. Solving them gives $C = -C'$, and the final result for the difference between the wire temperatures becomes

$$\Delta T = e^{i2\pi f}\,\frac{2v}{D/a}\,\frac{P}{2\pi k l_y}\times \\ \frac{1}{i\bar{f}_a}\,\frac{1-\sqrt{i\bar{f}_a}\,K_1\left(\sqrt{i\bar{f}_a}\right)}{1-i\frac{f}{f_{hc}}\left[K_0\left(\sqrt{i\bar{f}_L}\right)-K_0\left(\sqrt{i\bar{f}_a}\right)\right]}. \qquad (33.)$$

This is the final analytic expression to which the sensor sensitivity is proportional. The dimensionless frequencies here $\bar{f}_a, \bar{f}_L$ are defined as $\bar{f}_x$ in (31.) for $x = a$ and $x = L$, respectively. Eq. (33.) differs from (19.) only by the dominator, which takes into account the finite heat capacity of the sensor wires. For small frequencies, $f << f_{hc}$, (33.) coincides with (19.) but at higher frequencies it leads to an additional suppression of the sensitivity.

3.3 Evaluation of the model

With the original temperature profile around the heaters expressed by Eq.(10.), the perturbation δT as a function of x, and the temperature difference between the wires ΔT can thus be explicitly calculated (Eq. (33.)).

This expression, that also takes into account the finite heat capacity of the wires, is only slightly different from Eq. (19.) that is an antisymmetric function: $\delta T(x) = -\delta T(-x)$. The deviance from pure antisymmetry of the final expression Eq. (33.) is generally only small and is due to the finite heat capacity of the wires.

To visualise the temperature of the fluid around the sensors, it is useful to plot both the unperturbed and the altered temperature as a function of x. The unperturbed function has approximately a 'ln(x)'-behaviour, see also figure 3-5a, and for one heater this is indicated by the dotted line (line *b*) in figure 3-5a. Using the expression for $\delta T(x)$, the altered temperature function due to a given velocity term v, looks like the dashed line (line *a*) in figure 3-5. Note that, due to the fact that the temperature correction is (almost) an antisymmetric function in x, the correction to the temperature at the heater itself is in a first-order approximation zero. Because of this asymmetry, the averaged value over the width of the heater around $x = 0$ is 0; the used perturbation theory predicts *no* change of the temperature at the heater due to flow when there is only one wire.

For the two wires, the function is composed of the sum of both single temperature functions, which result is represented by the line in figure 3-5b. It is seen that in this situation the temperatures of both heaters *do* change due to the flow; the asymmetry of the function yields a temperature difference between the heaters. In this respect the Microflown is essentially different from a single hot wire anemometer ('SHWA') [15]: the measured temperature difference –and thus the output signal- occurs only by virtue of the fact that there are two wires. For the involved low velocities, the temperature decrease of only one wire of the Microflown, if there would be only one, is in first-order approximation zero. The single hot wire anemometer principle is based on a temperature change of the wire due to the convection term, and in the anemometry often King's law, predicting a heat loss of a wire proportional to $\sqrt{v}$ [20], is applied. King's law can be used only for large Reynolds numbers, Re > 1, whereas for the Microflown Reynolds numbers are in the order of 10^{-3}. Due to its two-wire principle, the Microflown is much more sensitive to low velocities, $v < ca.\ 10^{-3}$ m/s, than the anemometer. It was also noted in [21] that these very small velocities, $v < ca.$ 1 mm/s, cannot be resolved by an anemometer.

The behaviour of expression (19.) for the temperature difference between the wires bares resemblance with that of a first order (low pass filter) function, although it is evident that these functions are not equal. For frequencies small compared to the thermal diffusion frequency f_D, the function is constant (independent of frequency), for frequencies much higher than this frequency the function is inversely proportional to the frequency; see figure 3-6. Nevertheless, there is a large region around the thermal diffusion frequency f_D, for which the function slowly decreases (on a logarithmic scale): although the thermal frequency is an important scale factor in the expression for ΔT, it does not equal the corner frequency of a corresponding first order transition. For the interpretation of experimentally obtained sensitivity curves, it is useful to fit these curves in an optimisation procedure. It is then convenient to approximate the function (19.) by a first order function $H(f)$ (a 'low pass filter') for which $|H(f)| = \frac{\Delta T(0)}{\sqrt{1+(f/f_d)^2}}$, with corner frequency f_d and a magnitude $\Delta T(0)$ at $f = 0$. The value $\Delta T(0)$ represents the temperature difference at low-frequency ($f \to 0$), while f_d is proportional to the

thermal frequency f_D of the original curve (Eq. (20.)). Frequency f_d differs only by a scale factor from f_D: in defining the dimensionless frequency $f_D = D/2\pi a^2$, only D and a^2 are of real importance, the scale factor in front can be chosen arbitrarily. The theoretical value of $S(0)$, i.e. the sensitivity for 'steady' flow (f = 0) was calculated as in expression (24.). In principle, this function can easily be optimised for a to find the optimum mutual wire distance. However, it should be realised that (24.) was obtained from an expansion of the Bessel functions in α ($\alpha = a\pi/l_z$). It is therefore only an approximation, valid for small α. Differentiating with respect to a and setting equal to zero gives

$$a_{opt} = \frac{2l_y}{\pi} e^{-(1+\gamma)} \approx 0.13 l_y \qquad (34.)$$

Since this value for a implies that α is almost out of the allowed range, Eq. (34.) can be used only as a crude approximation.

If next the influence of the heat capacity of the wires is also taken into account, the total frequency response of a Microflown can be approximated by:

$$|\Delta T| = \Delta T(0) \frac{1}{\sqrt{1 + f^2 / f_{hc}^2}} \frac{1}{\sqrt{1 + f^2 / f_d^2}} \qquad (35.)$$

with f_{hc} the heat capacity corner frequency. This expression is useful when comparing experimentally obtained sensitivity curves to theory. Three important components of the sensitivity curve can be distinguished: the low frequency sensitivity, the frequency dependence with respect to the thermal diffusion between the wires and the frequency dependence caused by the thermal capacity of the sensors. Note that in all these parts, $\Delta T(0)$, f_D and f_{hc}, the thermal diffusion coefficient D occurs. Due to the temperature dependence of D, they are therefore all temperature dependent.

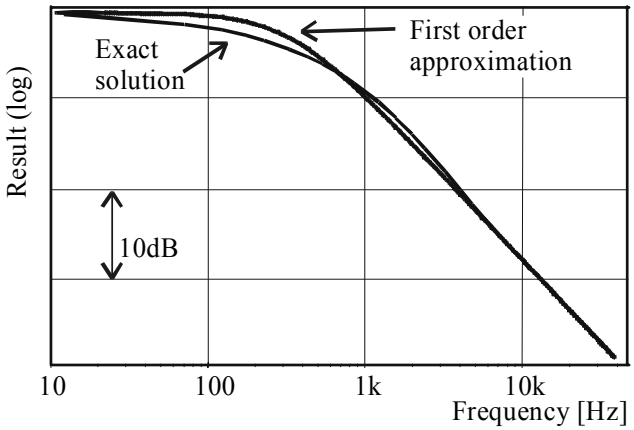

Figure 3-6: Comparison of the output signal, proportional to ΔT, as calculated from Eq.(19.), to the corresponding first order function. In Eq.(19.), a=300 μm and D=7.7·10^{-5} m^{2}s^{-1} at T=600 K due to the temperature dependence of D.

With the determination of $\Delta T(0)$, f_D, and f_{hc} by fitting the measured sensitivity functions of the sensors, the sensors can thus be well characterised for typical operation conditions.

3.4 Comparison to experimental results

For an experimental investigation of the sensitivity of various sensors, Microflowns of varying mutual wire distance a, width L and length l_y were designed. Having designed first the different masks for the required wafers, we started the process with the deposition of a 200 nm thick layer of silicon nitride on which an adhesion layer of 10 nm chromium and a 90 nm thick platinum layer was deposited by sputtering. Then it was patterned by lift off. Subsequently the silicon nitride was etched by reactive ion etching, *RIE*, followed by anistropic etching in KOH to etch the beams free. This underetching was achieved by a slight misalignment of the mask. (See also [1]).

The measurements of the Microflowns were performed in a ‘standing wave tube’. This is a long tube with at one side a sound source generating a broad frequency spectrum, and at the other side a reflecting cross section with a reference microphone in it. In the tube standing wave patterns occur. Somewhere along this standing wave tube a Microflown is placed, so that from the ratio between the

signals of the reference microphone and the Microflown the sensitivity of the latter can be deduced [1,8,11]. This calibration method is more extensively described in chapter 4. For frequencies above 4 kHz, up to about 20 kHz, both sensors have to be utilised in an anechoic room, since the standing wave tube cannot be used anymore for frequencies higher than, depending on its precise geometry, ca. 4 kHz.

For an investigation of the mutual variance in sensitivity of sensors of the same geometry, and the errors due to the measurement set-up, at first several sensors of exactly the same geometry were successively measured. From these results it could be concluded that the compound reproducibility of measurements and fabrication technology was better than 2 %.

The parameters to be varied in the experiments were chosen to be the following dimensions of the sensor: the width L, the mutual wire distance a and the wire length l_y. The dimensions were independently varied.

Comparing Microflowns with wire lengths of 0.5; 1.0; 1.5 and 3.0 mm showed that l_y is not of significant influence on the sensitivity, which is in accordance with what is theoretically expected.

Next, the influence of the mutual wire distance a on the low frequency sensitivity and the characteristic frequency f_d was investigated. Therefore, different sensors, with a varying from 30, 60, 90, up to 700 μm have been measured in the standing wave tube. From the ratio of the output signal and the sensitivity of the reference microphone, the sensitivity curves were obtained. These were compared to the model calculations of the sensitivity for the concerned parameter values, Eq. (33.). Two representative results for both magnitude and phase of the sensitivity, for wire separations a = 50 μm and a = 150 μm, are shown in figure 3-7. The theoretical curves are depicted by the lines, these are obtained from the explicit calculation of expression (33.).

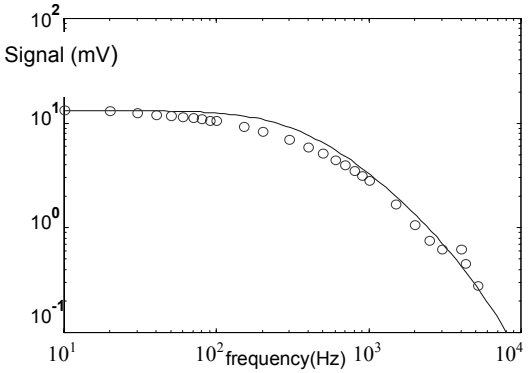

Figure 3-7a: Magnitude of the experimentally determined sensitivity of a Microflown with a = 50 μm, l_y=1 mm, L = 2 μm, and P = 12 mW (dots), compared to the calculated curve according to Eq. (33.) (line).

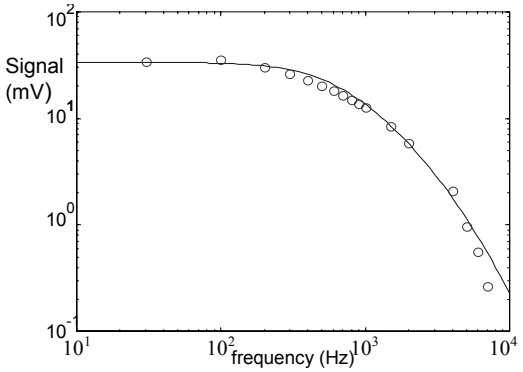

Figure 3-7c: Magnitude of the experimentally determined sensitivity of a Microflown with a = 150 μm, l_y=1 mm, L = 2 μm, and P = 12 mW (dots), compared to the calculated curve according to Eq. (33.) (line).

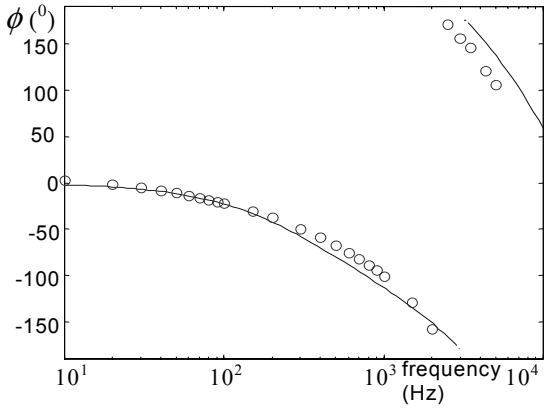

Figure 3-7b: Phase of the experimentally determined sensitivity of a Microflown with a = 50 μm, l_y=1 mm, L = 2 μm, and P = 12 mW (dots), compared to the calculated curve according to Eq. (33.) (line).

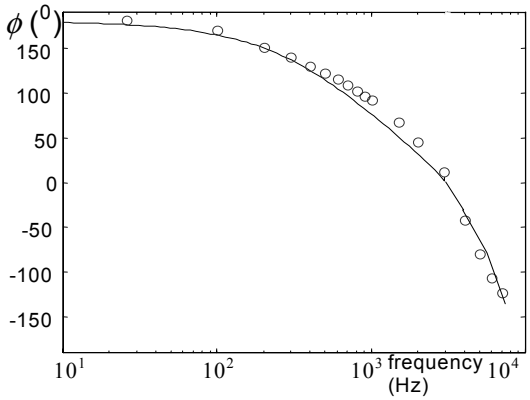

Figure 3-7d: Phase of the experimentally determined sensitivity of a Microflown with a = 150 μm, l_y=1 mm, L = 2 μm, and P = 12 mW (dots), compared to the calculated curve according to Eq. (33.) (line).

The signal of the sensor, that is the output voltage u_0, is proportional to the temperature difference ΔT (from Eq. (33.)) according to the relation [1, 12]

$$u_0 = \frac{U_0}{2}\vartheta\Delta T \tag{36.}$$

with U_0 the applied voltage over the sensor wires and θ the temperature coefficient of the resistance, that was measured to be $\theta = 3.0\cdot10^{-3}\ \mathrm{K}^{-1}$. The applied voltage by the source was $U_0 = 10$ V.

For each geometry, the output signal u_0 as a function of frequency, and f_d and f_{hc} are thus calculated. It is seen that the experimentally obtained points and the calculated curves correspond rather well, without any fitting parameters.

The measured output voltage functions of all sensors were approximated by the product of two 'first-order' functions, Eq. (35.) to find $\Delta T(0)$, f_D and f_{hc} . In figure 3-8 the low frequency sensitivity $S(0)$, the output voltage per m/s, is plotted as a function of a. For comparison, the calculated value according to Eq. (24.) and (36.) is depicted too. As stated before, the deduced expression (24.) is only an approximation, and only valid for $\pi a/l_y$ small. However, the calculated optimum $a_{opt} = 130$ μm is in satisfactory correspondence with the experimental results.

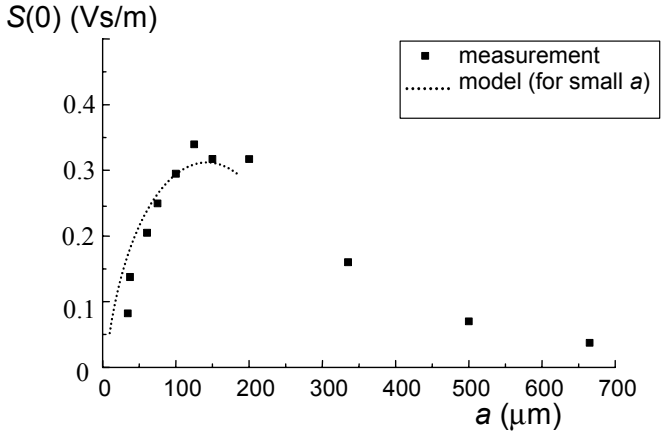

Figure 3-8: Magnitude of the low frequency sensitivity (determined from the output signal at ca. 10 Hz), as a function of mutual wire distance a. Dissipated power P=16 mW, l_y=1 mm. The calculated value of S(0) according to Eq.(24.), valid for small a, is shown by the dotted line.

The wire width L and wire separation a of the various sensors were independently varied. From the approximations of the measured sensitivity functions the two corner frequencies could then be obtained. A very precise determination of the first characteristic frequency f_d becomes difficult for small a (in which case f_d becomes large, above ca. 5 kHz), since the other corner frequency $f_{hc} \approx 3$ kHz (for $L = 2$ μm) then dominates the sensitivity function. For f_d and f_{hc} of about the same magnitude, both values cannot very well be discriminated. The heat capacity corner frequency is inversely proportional to the thermal mass of the sensor (Eq.(28.)), that means $f_{hc} \sim L^{-1}$. The experimentally obtained corner frequencies f_{hc} are shown in figure 3-9 as a function of the inverse of the wire width, together with the theoretical proportionality. The theoretical line is calculated for the used material parameters and dimensions of the sensor wire. For $L = 2$ μm, a value of $f_{hc} \approx 3.6$ kHz was found, which is not too far from the calculated value $f_{hc} \approx 3$ kHz (Eq.(28.)) for this geometry.

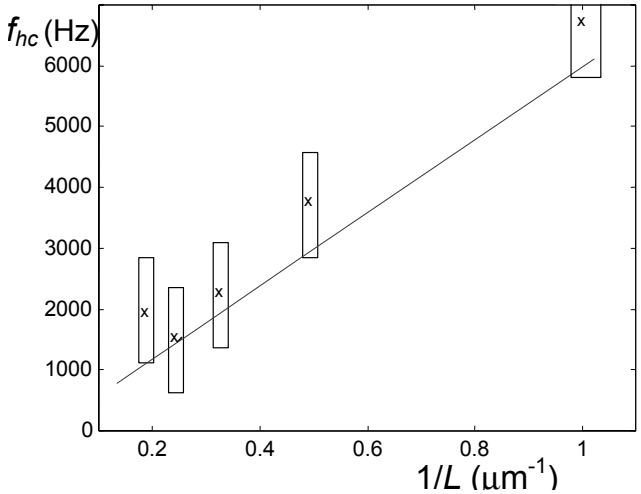

Figure 3-9: The corner frequency f_{hc} due to the heat capacity, as a function of the inverse of the wire width, L^{-1}. The line shows the calculated value for a 200 nm thick silicon nitride beam with a 100 nm thick platinum layer of 1 mm length.

Next, in figure 3-10 the corner frequencies f_d are depicted. As can be expected from Eq. (20.), f_d should be proportional to a^{-2}, which line is also shown. Due to the difficulty to distinguish two separate, different, first order functions the errors

in f_{hc} *and* f_d can be relatively large for some fits. The correspondence between theory and experiment seems nevertheless sufficient, for both corner frequencies.

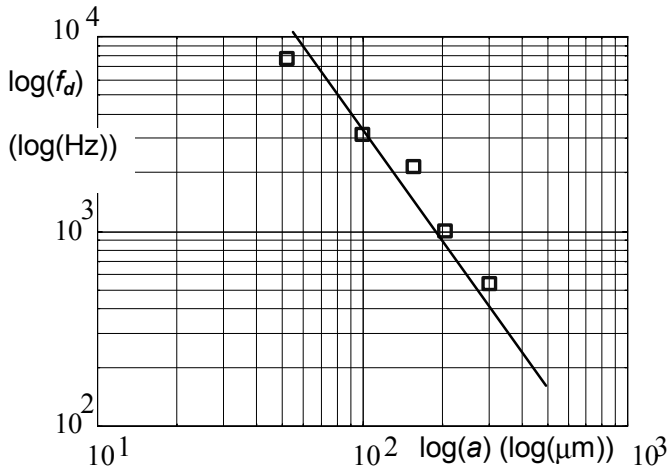

Figure 3-10: Characteristic frequency f_d of the fitted sensitivity curves, as a function of the distance between the sensing wires, plotted logarithmically. The line shows the theoretical dependence $f_d \propto a^{-2}$.

3.5 Conclusions

For a reliable description of the behaviour of the Microflown, and to deduce an expression for the sensitivity of the flow sensor as a function of frequency, geometrical and material parameters, an analytical model was developed. This was done by a calculation of the temperature distribution around the two heated wires and the perturbation due to the forced convection by an acoustic wave. It was seen that the wires' resulting temperature difference can be calculated using the perturbation theory. In this way we could analyse the frequency dependent behaviour of the output signal. In the sensitivity function, two important characteristic frequencies are found. The shape of the function is mainly determined by the first characteristic frequency; the 'thermal frequency'. It is proportional to the quotient D/a^2, with D the heat diffusion coefficient of the fluid (generally the air) and a the mutual distance between the wires. The dependence of the first characteristic frequency on a, namely $f_d \sim a^{-2}$, has been verified in

experiments. The experimentally obtained values of this characteristic frequency are found to be in satisfactory correspondence to the model.

Second, the heat capacity of the heaters causes an additional 'first order' frequency dependence. The corresponding corner frequency depends on D, the geometry of the heated wires and of course on the thermal masses of the sensor material and the fluid. For the used heaters in the experiment, the theoretical value of this corner frequency can be calculated as f_{hc} = 3 kHz for L = 2 μm. Both the experimentally found magnitude and the dependence on the wire width of the corner frequency f_{hc} are in acceptable agreement with the theory.

Another very important parameter of the sensitivity function is its magnitude for steady ('DC') flows, $S(0)$. From the developed theory this value can be calculated explicitly, although the deduced expression is an approximation and valid only for small a. The dependence of $S(0)$ on a and also the thus calculated optimum a_{opt} are experimentally confirmed.

Concluding, all characteristic parameters of the frequency dependent sensitivity of the Microflown, found in measurements, correspond both qualitatively and quantitatively well to the model; the developed analysis was confirmed by experimental results and seems to give a reliable description. This offers the possibility of an optimisation of the sensor as described in chapter 6.

3.6 References

1 H-E. de Bree, P.J. Leussink, M.T. Korthorst, H.V. Jansen, T.S.J. Lammerink, M.C. Elwenspoek, The Microflown: a novel device measuring acoustical flows, Sensors and Actuators A 54 (1996) 552-557.

2 H-E. de Bree, T.S.J. Lammerink, M.C. Elwenspoek, J.H.J. Fluitman, Patent PCT/NL95/00220, Use of a fluid flow measuring device as a microphone and system comprising such a microphone.

3 W.F. Druyvesteyn, H-E. de Bree, A new sound intensity probe; comparison to the Bruel & Kjaer p-p probe, *Journal of the Audio Engineering Society* 48 (2000) No. 1/2 (Jan./ Febr.).

4 W.F. Druyvesteyn, H-E. de Bree, M.C. Elwenspoek, A new acoustic measurement probe; the Microflown, *IOA London* (1999).

5 H-E. de Bree, W.F. Druyvesteyn, E. Berenschot, M.C. Elwenspoek, Three-dimensional sound intensity measurements using microflown particle velocity sensors, *Proceedings of MEMS*, Orlando (1999).

6 H-E. de Bree, W.F. Druyvesteyn, M.C. Elwenspoek, Realisation and calibration of a novel half inch p-u sound intensity probe, *Proceedings of the 106th AES Convention*, Munchen (1999).

7 H. Schurer, Comparison of two methods for measurement of horn input impedance, *Proceedings of the 100th AES convention*, Copenhagen (1996).

8 F J.M. van der Eerden, H-E. de Bree, H. Tijdeman, Experiments with a new acoustic particle velocity sensor in an impedance tube, *Sensors and Actuators* A 69, (1998) 126-133.

9 H-E. de Bree, T. Korthorst, P.J. Leussink, H.V. Jansen, M.C. Elwenspoek, A method to measure apparent acoustic pressure, flow gradient and acoustic

intensity using two micro machined flow microphones, *Proceedings of Eurosensors X*, Leuven (1996).

10 H-E. de Bree, H.V. Jansen, T.S.J. Lammerink, G.J.M. Krijnen, M.C. Elwenspoek, Bi-directional fast flow sensor with a large dynamic range, *Journal of Micromechanics* 9 (1999) 186-189.

11 W.F. Druyvesteyn, H-E. de Bree, Intensity measurements in various rooms / a new intensity probe, *Proceedings of the 16th ICA and 135th ASA meeting*; Vol. 4, 2827-2828. (1998).

12 V.B. Svetovoy, I.A. Winter, Model of the μ-flown microphone, *Sensors and Actuators* A 86 (2000), 171-181.

13 M.R. Spiegel, 'Advanced Calculus' (1974).

14 H-E. de Bree, Add-on Microflown for a high-end pressure gradient microphone, *Proceedings of the 109th AES Convention*, no 5181(2000).

15 C.G. Lomas, 'Fundamentals of hot wire anemometry', Cambridge University Press, Cambridge, (1986).

16 R.G. Johnson, R.E. Higashi, A highly sensitive silicon chip microtransducer for air flow and differential pressure applications, *Sensors and Actuators* A 11, (1987) 63-72.

17 C. Yang, H. Søeberg, Monolithic flow sensor for measuring milliliter per minute flow, *Sensors and Actuators* A, 33 (1992) 143-153.

18 K. Petersen, High precision, high performance mass-flow sensor with integrated laminar flow micro-channels, *Sensors and Actuators* A (1985) 361-363.

19 G.B. Hocker, A microtransducer for air flow and differential pressure sensing applications, *Micromachining and micropackaging of transducers* (1985) 207-214.

20 L.V. King, On the convection of heat from small cylinders in a stream of fluid (esp. Determination of the convection constants of small platinum wires with application to hot wire anemometry), *Proceedings of the Royal Society London* A, 90 (1914), 563-.., or 373-..

21 F. Kohl, A. Jachimowicz, J. Steurer, R. Glatz, J. Kuttner, D. Biacovsky, F. Olcaytug, G. Urban, A micromachined flow sensor for liquid and gaseous fluids, *Sensors and Actuators* A, 41 (1994), 293-299.

22 L.D. Landau, Fluid Mechanics (L.D. Landau, E.M. Lifschitz, Course of Theoretical Physics Vol. 6), ISBN 0750627670 (1987).

23 H-E. De Bree, 'The Microflown', ISBN 9036515793, Amsterdam, The Netherlands (2001).

24 www.processcontrolscorp.com/thermal.htm;www.kurz-instruments.com/a6.pdf

25 J.P. Holman, 'Heat Transfer' 9th ed., ISBN 0072406550 (MacGregor and Emery) (2002)

Chapter 4

Calibration of the particle velocity sensor in a tube

Abstract

To determine the frequency response of the Microflown, several calibration measurements are available. Of all the alternatives, the most common calibration methods are the anechoic calibration of the sensor, the time frame method in a long tube and the standing wave tube. For a frequency range of 20 Hz – 4 kHz, the standing wave tube is most favourable. In this chapter, the limits of validity of this method are analysed. The effects of the viscous and thermal properties of the fluid (normally the air) are considered. It is shown, both theoretically and experimentally, that for a broad frequency spectrum these viscothermal effects on the calibration are relatively small.

4.1 Introduction

The behaviour of the particle velocity sensor is well described by means of the frequency response of the sensor, that is, the magnitude and the phase of the sensitivity of the particle velocity sensor for a broad frequency spectrum. Various calibration methods are available to determine this frequency response, each with its own advantages and disadvantages. In default of reference particle velocity microphones, the main concern calibrating a particle velocity sensor is involved with the realization of a well-known particle velocity imposed on the probe. This problem is overcome by measuring the sound pressure in a configuration of well-defined specific acoustic impedance. This is mostly realized by one of the three approaches: placing the sensor and the reference microphone into an anechoic room, placing them into a long tube using time frame measurements, or into a standing wave tube. Due to the relatively small size, low cost and wide bandwidth of the latter, this method is often favourable. Therefore, we analyse in more detail the possible effects of the viscous and thermal properties of the air (damping) in the tube on the calibration results.

4.2 The most common calibration methods for the particle velocity sensor

In this paragraph a short overview of possible methods for calibration of the particle velocity sensor is given, while a more extensive description can be found in [1, 2]. The most important methods to determine magnitude and phase of the sensitivity function of the sensor are the anechoic room, the long calibration tube, the (relatively short) standing wave tube, the calibration in a reverberant environment or the ‘open window’ calibration’.

4.2.1 An anechoic environment

The anechoic room is a chamber with fully sound absorbing and therefore non-reflecting walls. Due to the absence of sound reflections, the free field situation is approximated. Into the room a simple sound source is placed. Using a common

pressure microphone, the sound pressure can be accurately measured. The particle velocity can then be determined once the specific acoustic impedance $z(r)$ is known. The impedance for a spherical sound wave, at normal conditions (room temperature) is given by

$$z(r) \equiv \frac{p(r,t)}{u_r(r,t)} = \rho_0 c_0 \left(\frac{ikr}{ikr+1} \right) \qquad (1.)$$

with $k = \omega/c$ the wave number, ρ_0 and c_0 the air density and the velocity of sound in the air at room temperature and r the distance to the source. Obviously, for $kr >> 1$, the specific acoustic impedance is real and constant,

$$z(r) = \rho_0 c_0 \qquad (2.)$$

So for acoustic sensors that are located far from the source, the calibration becomes relatively simple. The calibration in the anechoic room is a, although rather expensive, quite practical and very reliable. It can be used in a bandwidth from 50 Hz to 20 kHz. Since it is very difficult to absorb low frequency sound waves, most anechoic rooms cannot be used for frequencies below this 50 Hz. Anechoic chambers that are appropriate for frequencies down to 50 Hz have sound absorbers of one or two meters thickness, and are therefore large (*ca.* 10 m cubed). For the frequency range higher than 1 kHz, anechoic rooms can be designed smaller; a 10 cm thick sound absorbing layer and a volume of about 1 m^3. (For $f >$ 1 kHz, kr becomes (much) larger than 1 for a 50 cm distance to the source.) Figure 4-8 shows, besides some other calibration measurements, also an anechoic calibration result. Due to uniform spherical spreading of the sound intensity, sound levels in anechoic rooms are considerably lower than in sound tubes.

4.2.2 Time frame measurement in a long tube

An inexpensive solution to approach free field measuring conditions is measuring in a long tube by means of time frame measurements. An illustration of the long tube measurement set up is shown in figure 4-1a. Frequency bandwidths to be measured in a long tube are typically 100 Hz – 2.5 kHz. The specific acoustic impedance of a tube without reflections at the end is equal to the free field impedance, $z = \rho_o c_o$, Eq. (2). A sine burst is generated by a loudspeaker and a measurement can be performed before a reflection returns (the tube can still be

considered to be infinitely long). For a reliable measurement, at least ten periods have to be measured. For a long tube, with l the distance from particle velocity sensor and microphone to the tube end, the lowest measurable frequency is thus

$$f_{min} = \frac{10c_0}{2l} \tag{3.}$$

Above a cut-off frequency f_c, the characteristic impedance is changed due to the occurrence of standing waves perpendicular to the propagation direction. It has been found that this cut off frequency is given by

$$f_{cut\ off} = \frac{c_0}{1.71d} \tag{4.}$$

with d the tube diameter.

An acoustic burst of certain frequency generated by the loudspeaker provides one point for the phase and one for the amplitude of the sensitivity function of the sensor. It takes about 30 s. for a sound wave to vanish, after that time a subsequent point in the frequency spectrum can be determined. In a frequency range from 100 Hz – 2.5 kHz, usually about 400 measurements are performed. A characteristic measurement result is shown in figure 4-1b. The time delay of both signals is well visible and it is observed that after the first reflection, sound pressure signal and particle velocity signal are in antiphase.

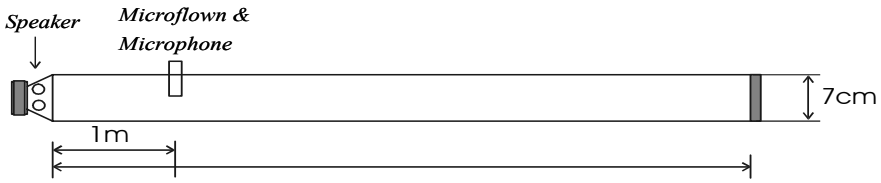

Figure 4-1a: A 40 m long tube is used to calibrate the particle velocity sensor in a frequency range from 100 Hz to 2.5 kHz (from [1]).

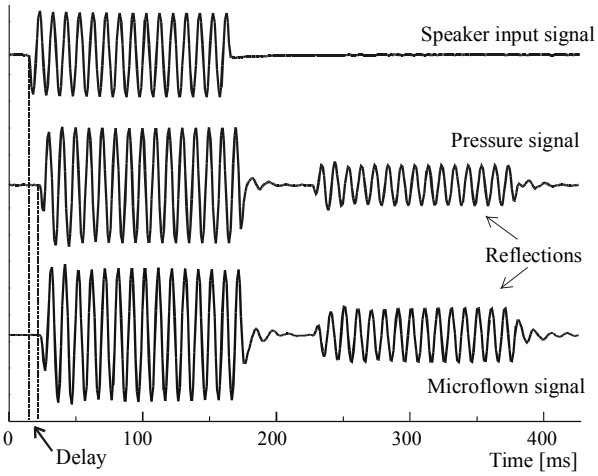

Figure 4-1b: A typical calibration measurement in the standing wave tube, for a certain frequency. To obtain the sensitivity curve of the sensor, the total frequency bandwidth has to be scanned. (from [1])

4.2.3 Standing wave tube

A standing wave tube is generally, due to its relatively small size and low cost, the most favourable calibration method for a particle velocity sensor [1]. The tube is rigidly terminated with a sound reflecting end so that standing waves occur, a reference microphone at one end and a loudspeaker or vibrating piston that generates a broad frequency spectrum at the other. In the tube the sensor to be investigated is placed. See figure 4-2. By the use of two standing wave tubes of different lengths and diameters, a bandwidth of 10 Hz to about 7 kHz can be achieved.

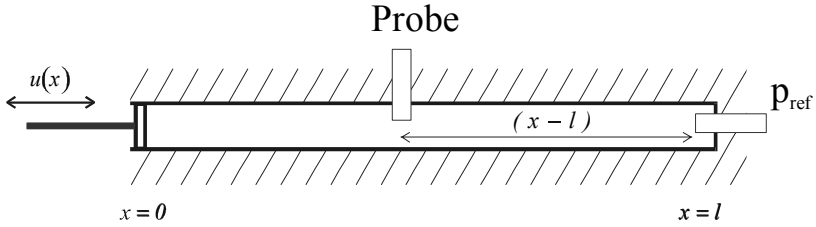

Figure 4-2: A standing wave tube, rigidly terminated at x = l, in which the fluid is driven by a vibrating piston at x = 0.

For frequencies lower than the cut-off frequency (Eq. (4.)), harmonic excitation of the piston or a loudspeaker generates a sound wave in the tube for which the plane

wave approximation is allowed. In the ideal situation, the solution of the wave equation is a superposition of the complex pressures associated with the plane waves travelling in the positive and in the negative direction,

$$p(x) = Ae^{-ikx} + Be^{ikx} \tag{5.}$$

in which A and B are arbitrary complex numbers. Using the conservation of momentum, $\frac{\partial p}{\partial x} = -\rho \frac{\partial u}{\partial t}$, the associated particle velocity of this solution is

$$u(x) = \frac{A}{\rho_0 c} e^{-ikx} - \frac{B}{\rho_0 c} e^{ikx} \tag{6.}$$

With the boundary conditions that the particle velocity is zero at $x = l$, and equal to amplitude u_0 at the piston or loudspeaker: $u(0) = u_0$, the constants A and B are easily determined so that

$$p(x) = -i\rho_0 c u_0 \frac{\cos k(l-x)}{\sin kl} \qquad u(x) = u_0 \frac{\sin k(l-x)}{\sin kl} \tag{7.}$$

and the specific acoustic impedance along the tube reads

$$z(x) = -i\rho_0 c \cot(k(l-x)) \tag{8.}$$

This cotangent-dependence of the acoustic impedance is rather inconvenient for calibration and it is more suitable to put a reference microphone at the rigid end of the tube where the sound pressure attains its maximum value $p_{ref}(l) = p_{ref,\,0}$. The particle velocity at the place of the sensor $u(x)$ can be related to the reference sound pressure at the end of the tube:

$$\frac{u(x)}{p_{ref}(l)} = \frac{i}{\rho_0 c} \sin(k(l-x)) \tag{9.}$$

It is thus seen that the particle velocity and reference sound pressure have a phase shift of $\pi/2$.

4.2.4 Reverberant environment

In a reverberant environment sound of a single sound source is reflected by the various boundaries, which produces the diffuse sound field. Calibration of the particle velocity is possible together with a reference pressure sensor and by measurements of the particle velocity sensor in the direction of the direct sound

wave combined with measurements of the velocity in the perpendicular direction. It is then possible to determine the ratio of the direct sound field (u_{dir}), and the reverberant or diffuse sound field (u_{rev}). Due to the angular dependence of the sensitivity, the 'cos θ directivity' (the polar pattern of the sensitivity is a so-called figure of eight, see [1, 2, 5]), only one third of the power in the diffuse sound field is measured. With $u_{\parallel}^2$ and $u_{\perp}^2$ the auto spectra of the measured particle velocities in the direction of the sound source and perpendicular to that, respectively, it is seen that

$$\begin{aligned} u_{\parallel}^2 &= u_{dir}^2 + \tfrac{1}{3} u_{rev}^2 \\ u_{\perp}^2 &= \tfrac{1}{3} u_{rev}^2 \end{aligned} \tag{10.}$$

so that

$$\frac{u_{dir}}{u_{rev}} = \sqrt{\frac{u_{\parallel}^2 - u_{\perp}^2}{3u_{\perp}^2}} \tag{11.}$$

A reference microphone with an omnidirectional sensitivity measures the autospectrum of the pressure p^2 :

$$p^2 = p_{rev}^2 + p_{rev}^2 \tag{12.}$$

assumed that the reverberant sound field is uniformly diffuse.

Using the relations

$$\left(\frac{p_{dir}}{p_{rev}}\right)^2 = \left(\frac{u_{dir}}{u_{rev}}\right)^2, \tag{13.}$$

and

$$p_{dir} = \sqrt{\frac{p^2}{1 + \left(\frac{u_{rev}}{u_{dir}}\right)^2}} \tag{14.}$$

the particle velocity sensor can be calibrated with respect to the reference microphone. (This is related to 'u-u-principle 1' as described in the second chapter).

4.2.5 Open window calibration

In [1] it was shown that even an open window calibration, that is, a series of calibration measurements with a sound source in a room and the probe placed just outside an open window provided remarkably reliable results. In this way a setting is created without any reflections and thus the anechoic conditions are well approximated.

4.3 Relation between measured signal and reference pressure

Because of the importance of the calibration method in a standing wave tube, for both very low frequencies and for high frequencies, the possible influence of viscous and thermal effects on the calibration have to be analysed. Using the set up as shown in figure 4-2, the frequency dependent 'transfer' function $\frac{u}{p_{ref}}$ that provides the relevant information about the sensitivity of the particle velocity sensor can be determined. However, this ratio can be influenced by viscous and thermal effects of the gas (usually the air) in the tube. To investigate these influences, the coefficients related to the viscous and thermal effects are considered in the equations for the wave propagation.

The propagation of sound waves with viscothermal effects has been extensively studied in literature. The propagation in tubes was investigated by Kirchhoff and Rayleigh [10]. In fluid dynamics, the phenomenon, especially the steady-state situation, was dealt with by [11-14], and also in acoustics several papers on the subject have been presented [15, 16]. Up to date, there is a large variety of models. Tijdeman [6] and Beltman [7] give an overview of the different analytic solutions presented in literature. It is shown there that the viscothermal propagation is governed by a number of dimensionless parameters. The two most important parameters are the shear wave number and the reduced frequency. Beltman [7] shows that the various models in acoustics can be grouped into three main categories. The essential points in these models are the pressure gradient across layer thickness or tube cross-section, and the incorporation of effects such as compressibility and thermal conductivity. The most extensive model is based on

the complete solution of the principle Navier-Stokes equations, taking into account all terms. A second model introduces some simplifications in the basic equations but the pressure gradient is accounted for. The simplest model, the low reduced frequency model, assumes a constant pressure across the layer thickness or tube cross-section and takes into account the effects of inertia, viscosity, compressibility and thermal conductivity.

For the current situation of the calibration of the particle velocity sensor in the standing wave tube, the wave propagation is considered from a standard acoustical point of view and the viscothermal properties will cause only small effects. The principal approach of Zwikker and Kosten [17], in which the shear wave number and the reduced frequency play an important role, is well applicable. Using the Zwikker and Kosten theory, the problem of convected viscothermal acoustic equations in a narrow tube can be simplified [17, 18]. This theory treats viscosity and thermal conductivity effects separately, within complex density and complex compressibility functions. The sound pressure is essentially constant through each cross section, and the excess density and sound pressure (when scaled by the equilibrium density and pressure of air, respectively) are comparable in magnitude. These last two observations are assumed to apply to uniform tubes having arbitrary cross-sectional shape, and a generalised theory of sound propagation in narrow and wide tubes is then derived. The two-dimensional wave equation that results can be used to describe the variation of either particle velocity or excess temperature over a cross section. Complex density and compressibility functions, propagation constants, and characteristic impedances can then be calculated. Here, the results of this theory for a tube of circular cross section are applied.

For harmonic excitation at frequencies below the cut off frequency, for which the plane wave approximation is justified, the solution that satisfies the wave equation is given by a superposition of the complex pressures associated with a plane wave propagating in the positive and in the negative direction. The situation is then purely one-dimensional and the acoustic pressure can be expressed as

$$p(x,t) = (\overline{p}_A e^{\Gamma kx} + \overline{p}_B e^{-\Gamma kx}) e^{i\omega t} \tag{15.}$$

in which Γ represents the propagation coefficient and $\overline{p}_A$ and $\overline{p}_B$ are the complex amplitudes of the forward and backward propagating waves. Assuming that the

pressure is constant across the tube cross-section and taking now into account the effects of inertia, compressibility, viscosity and thermal conductivity of the fluid, the Zwikker and Kosten theory gives for the complex propagation coefficient Γ reads for a cylindrical tube

$$\Gamma = \sqrt{\frac{\gamma}{n(s\sigma)} \frac{J_0(i\sqrt{i}\cdot s)}{J_2(i\sqrt{i}\cdot s)}} \tag{16.}$$

with n a coefficient that depends on the fluid and the flow profile, and characterises the thermodynamic processes in the tube:

$$n = \left(1 + \frac{\gamma - 1}{\gamma} \frac{J_0(i\sqrt{i}\cdot s\sigma)}{J_2(i\sqrt{i}\cdot s\sigma)}\right)^{-1} \tag{17.}$$

Here J_0 and J_2 are the zeroth and second Bessel function of the first kind, respectively, $\gamma = C_p / C_v$ the ratio of specific heats, $s = R_e \sqrt{\frac{\omega \rho_0}{\mu}}$ the shear wave number, and $\sigma^2 = \frac{\mu C_p}{\lambda}$ the Prandtl number. R_e represents the equivalent radius of the tube, $R_e = 2 \times \frac{area}{perimeter}$. ($\rho_0$, μ, and λ are respectively the density, dynamic viscosity and the thermal conductivity coefficient of the gas.)

An important parameter in these models is the shear wave number s, which is a measure for the ratio of the inertial and viscous effects of the fluid. A small shear wave number indicates the dominance of the viscous effects, in which case the velocity distribution over the cross section of the tube approaches a Poisseuille flow, whereas a large shear wave number, when the inertia of the fluid is dominant, corresponds to a plane wave profile. In physical terms the shear wave number represents the ratio between the characteristic length scale (the layer thickness or, in this case, the tube radius) and the boundary layer thickness. A second important parameter is the reduced frequency, which is a measure of the ratio between this length scale and the acoustic wavelength. Both γ and σ depend only on the material properties of the gas.

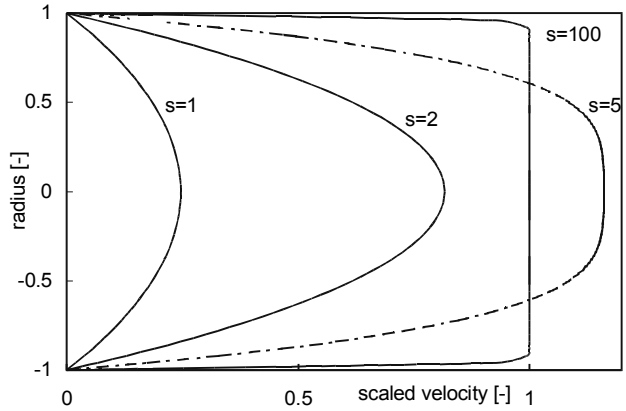

Figure 4-3: The particle velocity profile in the tube as a function of the shear wave number s.

For s << 1, a tube is called 'narrow', for s >> 1 it is said to be 'wide'. For wide tubes, Eq.(16) can be approximated by the solution of Kirchhoff:

$$\Gamma = i + \frac{1+i}{\sqrt{2}}\left(\frac{\gamma - 1 + \sigma}{s\sigma}\right) \tag{18.}$$

If the viscous and thermal effects can be neglected, $\Gamma = i$, but in general the propagation coefficient has the form $\Gamma_{re} + i\,\Gamma_{im}$: the attenuation of the wave is determined by Γ_{re} and its phase velocity equals c_0/Γ_{im}.

To determine now the transfer function $\frac{u}{p_{ref}}$, an expression for $u(x)$ at the place of the sensor is needed. Using Eq. (15.) and applying as before the equation of momentum conservation, one finds for the particle velocity

$$u(x,t) = \frac{-i}{\Gamma \rho_0 c_0}(\overline{p}_A e^{\Gamma k x} - \overline{p}_B e^{-\Gamma k x}) e^{i\omega t} \tag{19.}$$

The reference microphone is located at the end of the tube $x = l$, so $p_{ref} = p(l)$. Using the definition for the dimensionless acoustic impedance ζ at $x = l$,

$$\zeta = \frac{1}{\rho_0 c_0}\frac{p(l)}{u(l)} \tag{20.}$$

and the boundary condition at $x = 0$,

$$p(0) = p_0 \tag{21.}$$

the amplitudes of the forward and backward travelling waves, $\overline{p}_A$ and $\overline{p}_B$, can be derived.

For the required transfer function it is then found that

$$\frac{u}{p_{ref}} = \frac{1}{\rho_0 c_0}\left(\frac{\cosh \Gamma kL}{\zeta} + \frac{i \sinh \Gamma kL}{\Gamma}\right) \qquad (22.)$$

with L the distance between the place of the sensor x and the end of the tube l; $L = l - x$.

For an acoustically hard wall at the end $x = l$ of the tube (which is the case), $\zeta = \infty$. If additionally the viscous and thermal effects can be neglected, the function is simplified to $\frac{u}{p_{ref}} = \frac{i}{\rho_0 c_0} \sin kL$. In this situation, the measured transfer function is only determined by the sensitivity characteristics of the sensor under investigation, and the thus obtained frequency dependent curve unravels therefore the behaviour of the particle velocity sensor. With negligible viscothermal influences, the phase shift between pressure and particle velocity oscillates between $\pi/2$ and $-\pi/2$, and the distance between the maximum and minimum points of the function is determined by $L/c = (l - x)/c$, when plotted as a function of frequency. Varying the place of the sensor along the tube changes the distance between the tops. This is illustrated by the following experiment for the calibration of a particle velocity sensor. In a standing wave tube of 98 cm length and 9 cm diameter, a particle velocity sensor (a ½" ICP Microflown, for specifications see [1]) and a reference microphone (a ½" pressure microphone, GRAS 26AC) are fixed. To avoid a mechanical transfer function between the loudspeaker and the sound probes, the loudspeaker was not mounted rigidly to the tube. For frequencies at the minima of the transfer functions, calibration of the sensor is not possible. To overcome this problem, the tube is used in two ways: the reference microphone can be mounted on both sides of the tube. Due to the asymmetries in the tube, the distance $(l - x)$ is varied by reversing the position of the reference microphone and the loudspeaker. It is varied between $(l - x) = 20$ cm and 55 cm. The obtained frequency curves are plotted together in figure 4-4.

The phase difference between u and p_{ref} for both situations is depicted in the figures 4-5a and 4-5b.

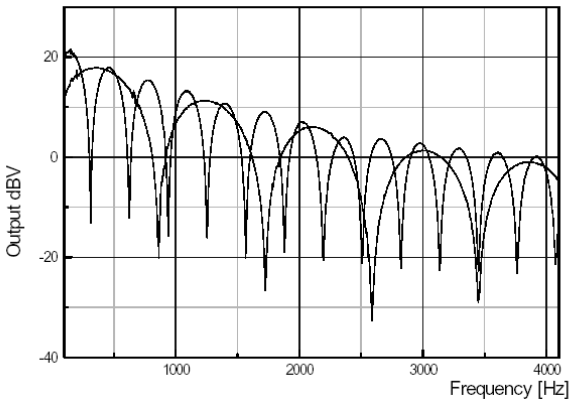

Figure 4-4: Amplitude response of a particle velocity sensor (½"ICP Microflown). The transfer function u/p_{ref} is depicted as a function of frequency for both (l-x) = 20 cm and 55 cm (the positions of the reference microphone and the loudspeaker are changed). See also figure 4-5.

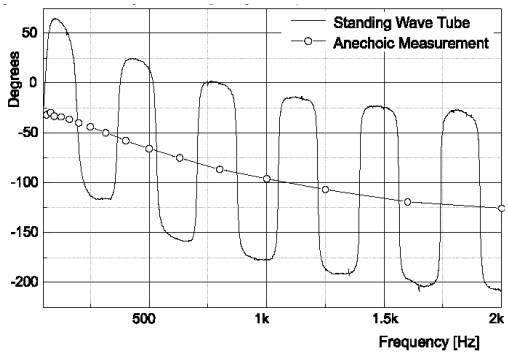

Figure 4-5a: Phase difference between u and p_{ref} for L=55 cm. The solid line represents the standing wave tube measurements, the line with circles has been measured in the anechoic room.

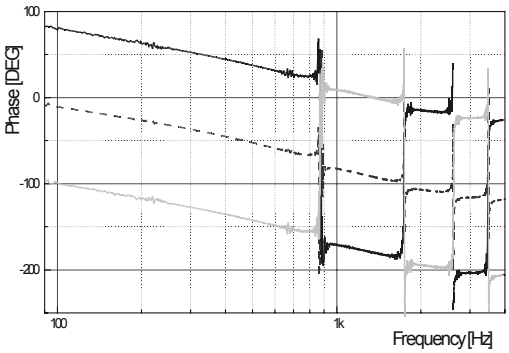

Figure 4-5b: Phase difference between u and p_{ref} for L=20 cm. The solid line and the grey line are successively obtained by rotating the sensor 180^0. The dotted line is the averaged value.

4.4 The influence of viscothermal effects on the transfer function

Using the approximation of Kirchhoff, Eq. (18.), the propagation coefficient can be separated in a real and imaginary part, for which can be written

$$\Gamma_{re} = \frac{\delta}{\sqrt{\omega}}$$
$$\Gamma_{im} = 1 + \frac{\delta}{\sqrt{\omega}} \tag{23.}$$

with

$$\delta = \frac{1}{2}\sqrt{2}\left(\frac{\gamma - 1 + \sigma}{R_e}\right)\sqrt{\frac{\lambda}{\rho_0 C_p}} \tag{24.}$$

Setting again $\zeta(l) = \infty$, the modulus of the transfer function, M, then becomes

$$|M(\omega)| = \frac{1}{\rho_0 c_0}\left|\frac{i\sinh\Gamma kL}{\Gamma}\right| =$$
$$= \frac{1}{\rho_0 c_0}\sqrt{\frac{\cos^2(\Gamma_{im}\frac{\omega L}{c})\sinh^2(\Gamma_{re}\frac{\omega L}{c}) + \sin^2(\Gamma_{im}\frac{\omega L}{c})\cosh^2(\Gamma_{re}\frac{\omega L}{c})}{\Gamma_{re}^2 + \Gamma_{im}^2}} \tag{25.}$$

For negligibly small δ, this expression is of course reduced to $\frac{u}{p_{ref}} = \frac{i}{\rho_0 c_0}\sin\frac{\omega L}{c}$, with maximum points at frequencies $\omega = n\frac{\pi c}{2L}$, when plotted as a function of frequency. These points will be slightly shifted when δ increases. Realistic values for the material parameters are σ = 0.845, C_p = 1.0·10^3 J·kg^{-1} K^{-1}, γ = 1.4, a gas density ρ_0 = 1.2 kg·m^{-3}, thermal conductivity λ = 24·10^{-3} W·m^{-1}K^{-1} and dynamic viscosity μ = 17.1·10^{-6} Pa·s. As follows from the equations, the possible influence of viscothermal effects is inversely proportional to the tube diameter. Assuming now the quite small tube diameter of 12 mm, Eq.(25.) can be evaluated. The deviation of the obtained function with respect to the ideal value $1/\rho_0 c_0$ in dB (defined as $20\cdot^{10}\log \rho_0 c_0 M$) is plotted as a function of frequency in figure 4-6a. The figure shows that even for this small radius R_e, the deviation on the logarithmic scale is little. Even in the low frequency region f ~10 Hz, the error does not exceed 1 dB, which is from acoustic point of view not very much.

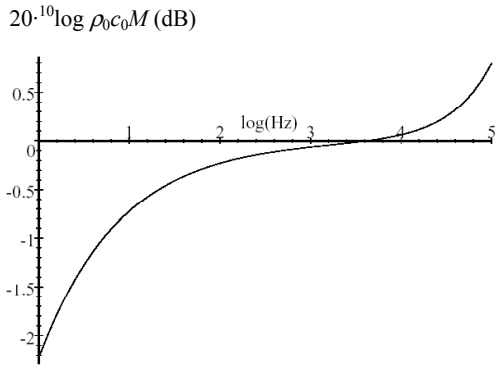

Figure 4-6a: Deviation of the modulus of the transfer function $M = u/p_{ref}$ with respect to the ideal value $1/\rho_0 c_0$ in dB, for R_e = 6 mm. (γ = 1.4, σ = 0.845, $C_p = 1.0 \cdot 10^3$ J·kg^{-1}K^{-1}, $\lambda = 24 \cdot 10^{-3}$ W·m^{-1}K^{-1}, $\mu = 17.1 \cdot 10^{-6}$ Pa·s)

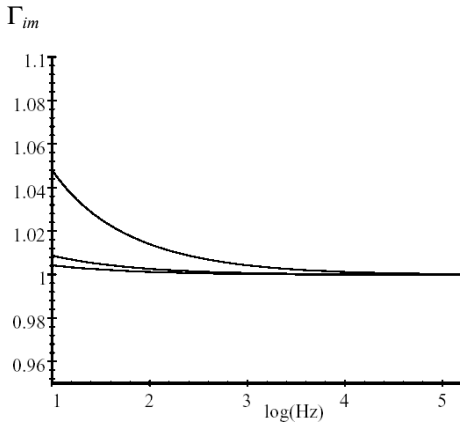

Figure 4-6b: Imaginary part of the propagation constant, Γ_{im}, for tube radii of 1 cm (upper curve), 5 and 10 cm (lower curve).

For parameter values for which there is a significant effect, i.e. small radius R_e, small frequency ω, and large Prandtl number σ^2 the condition $s >> 1$ is not satisfied so that the Kirchhoff approximation cannot be applied. Using the original expressions Eq.(16.) and (17.) and the mentioned gas parameters the propagation constant was calculated for tube radii of 1, 5 and 10 cm, leading to figure 4-6b.

4.5 The phase of the transfer function

It is obvious that the viscous and thermal properties of the air may influence the phase of the transfer function as well. For negligible viscothermal effects, $\Gamma = i$ and the phase ϕ between u and p_{ref} is $\pm \pi/2$. This phase shift between $\pi/2$ and $-\pi/2$ occurs at the frequencies $\omega/\omega_0 = n$ (n integer) with $\omega_0 = \pi c/L$. Small deviations from this value appear for $\Gamma_{re} > 0$, so that the phase is

$$\phi_{u,p} = \arctan \frac{\mathrm{Im}(i/\Gamma \sinh \Gamma kL)}{\mathrm{Re}(i/\Gamma \sinh \Gamma kL)} \qquad (26.)$$

To visualise the influence of Γ_{re} on the phase, the behaviour of ϕ is plotted as a function of frequency in figure 4-7 for different values of δ in Eq. (23.). The phase (Eq. (26.)) is evaluated for $\delta = 1 \cdot s^{-1/2}$ and $\delta = 10^{-1} \cdot s^{-1/2}$. It is seen that, with increasing δ, the phase characteristic deviates more from the ideal curve as can be observed from its smoothed shape, and the points of changing sign of ϕ being shifted slightly to the left. For small δ and ω/ω_0 large, this frequency shift can be approximated by $\Delta\omega = -\delta\sqrt{\omega_0}$ [19]. In the figure, the integer values $n = \omega/\omega_0$ are chosen sufficiently large. The frequency shift of the curve in figure 4-7 is practically invisibly small and the fluid parameters or tube dimensions have to be chosen almost unrealistically to allow the frequency shift to be experimentally observable. The smoothed (rounded) shape however, is well observed as is illustrated in figure 4-5.

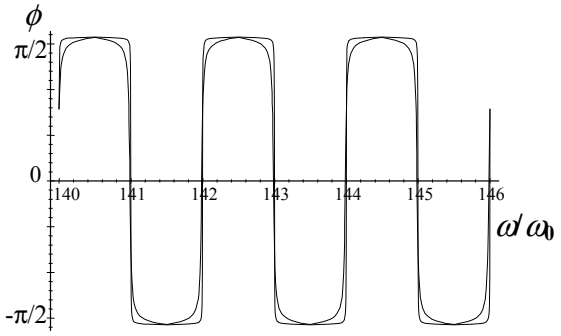

Figure 4-7: Phase of the transfer function u/p_{ref} as a function of $n = \omega/\omega_0$ with $\omega_0 = \pi c/L$, for $\delta = 1 \cdot s^{-1/2}$ and $\delta = 10^{-1} \cdot s^{-1/2}$. The points where ϕ changes sign are slightly shifted to the left, with $\Delta\omega = -\delta\sqrt{\omega_0}$.

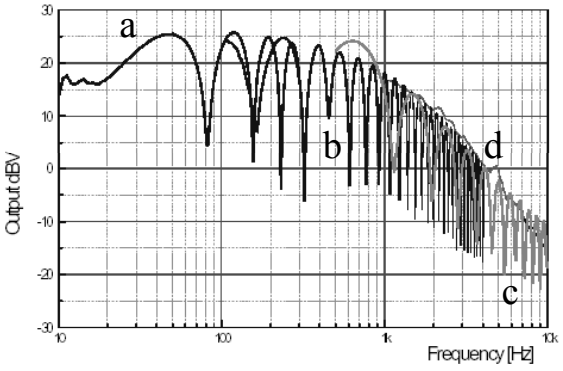

*Figure 4-8: Measured transfer function of the particle velocity sensor in different tubes, compared to that measured in the anechoic room. **a**: a large standing wave tube (L= 8 m, R_e=16 cm) for 20 Hz – 1 kHz, **b**: a short standing wave tube (L= 75 cm, R_e=4.5 cm) for 100 Hz – 4 kHz, **c**: short tube for 500 Hz- 10 kHz, **d** : an anechoic room (1 m^3) for 1 kHz – 12 kHz.*

Viscothermal effects will be partially responsible for this smoothed phase characteristic measured in the standing wave tube. Obviously, the effect of the

smoothening of the phase characteristic becomes more dominant for increasing δ, *i.e.* for larger viscosity and damping.

4.6 Practical implications

From the above analysis some consequences can be deduced for an accurate calibration measurement in which the viscothermal effects are reduced. Most parameters, like the gas density ρ_0, the thermal conductivity λ and parameter γ can hardly be influenced. One can, however, choose the (equivalent) radius R_e of the tube rather large. In particular for low frequency calibrations, a minimum limitation for the tube radius can be obtained. Since the propagation factor appears in the form ΓkL in the numerator of the transfer function, it is also important to choose the length L not too large. On the other hand, L should be larger than 1/8 of the wavelength for an accurate acoustic measurement, so $L/c \geq 1/8f$, and a rule of thumb is that the total tube length must be twice as large. Concluding, some practical implications for the possible dimensions of the calibration set-up can be deduced. Since the cut-off frequency for a tube of diameter d ($d = 2R_e$) equals $f_c = 0.59\ c/d$, the chosen diameter determines the maximum frequency that can be measured as well. A diameter of 15 cm, for example, implies a maximum frequency of about 1.3 kHz. Practical values that can be opted for are: a tube of 8 meters in length (in which $L \approx 4$ m) and 15 cm in diameter for a bandwidth of 10 Hz up to 1 kHz. In a bandwidth of 100 Hz to 4 kHz, a tube of 1 meter length and diameter 4 cm is used. For the calibration of the Microflown in a bandwidth 500 Hz – 10 kHz, a 40 cm long tube with a diameter of 12 mm is preferable.

With these guidances, calibration measurements were performed in standing wave tubes of different lengths and diameters. The results were compared to the calibration of the particle velocity sensor in the anechoic room. In the latter set-up, viscothermal effects can be practically neglected. The measurement results are shown together in figure 4-8. For a bandwidth of 10 Hz to 1 kHz, we used a 8 meter long tube with $d = 15$ cm; for the frequency range 100 Hz to 4 kHz length and diameter were 90 cm and 4 cm respectively; for 500 Hz to 16 kHz the length was 60 cm and the diameter 12 mm. The arch-shapes of the curves are due to the

sin or *sinh*-functions in the transfer function, only the maximum points are relevant for the sensitivity. The other curve in figure 4-8 is the obtained sensitivity in the anechoic room. It is seen that for frequencies above 2 kHz, the standing wave tube give a small overestimation compared to the anechoic results. In principle, this may be caused due to the described viscothermal effects. However, as stated above, these viscothermal effects in the tube can only be responsible for small deviations. Over all, the different curves fit satisfactory well to each other.

4.7 Summary and conclusions

It was shown that, among the various available calibration methods for the particle velocity sensor, the standing wave tube is generally most favourable. The tube is a simple and convenient set-up and tubes can be used for a broad frequency spectrum. We analysed the viscous and thermodynamic effects due to the fluid properties on this calibration. Many aspects of viscothermal effects have already been extensively studied and described in literature. We found that, generally, these effects turn out to be relatively small, even for low frequencies, the frequencies for which the Microflown is particularly useful and accurate.

The transfer function for the sensitivity of the sensor was deduced, in which the propagation factor Γ, that represents the viscothermal effects, was included. To reduce the influence of the thermal and viscous effects on the calibration in the tube, the shear wave number s and the Prandtl number (σ^2) should be chosen large, which imposes a rather large (~15 cm) tube radius for low frequencies. For frequencies up to 10 kHz, a radius of 12 mm is appropriate. Second, the length of the tube should be taken as small as possible, provided that the quotient L/c remains larger than the frequency ω to be measured.

Although the viscothermal effects on the modulus of the transfer function are small, they are well visible in the shape of the phase characteristic. These influences were experimentally observed.

It was experimentally shown that the different calibrations in various tubes and that in an anechoic room fit well to each other.

4.8 References

1. H.-E. de Bree, 'The Microflown', The Netherlands, ISBN 9036515793 (2001).
2. H.-E. de Bree, The Microflown, Ph.D. thesis, ISBN 9036509262, University of Twente (1997).
3. H.-E. de Bree, W.F. Druyvesteyn, M.C. Elwenspoek, Realization and calibration of a novel half inch p-u sound intensity probe, *Proceedings of the 106th AES Convention*, Munchen (1999).
4. J.Y. Chung, D.A. Blaser, Transfer function method of measuring in-duct acoustic properties, I. Theory, *Journal of the Acoustic Society of America* 68 (3) (1980) 907-913.
5. H.-E. de Bree, P.J. Leussink, M.T. Korthorst, H.V. Jansen, T.S.J. Lammerink, M.C. Elwenspoek, The Microflown, a novel device measuring acoustical flows, *Sensors and Actuators* A 54 (1996) 552-557.
6. H. Tijdeman, On the propagation of sound waves in cylindrical tubes, *Journal of Sound and Vibration* 39 (1) (1975) 1-33.
7. W.M. Beltman, Viscothermal wave propagation including acousto-elastic interaction, part I: theory, *Journal of Sound and Vibration* 227 (3) (1999) 555-586.
8. V.B. Svetovoy, I.A. Winter, Model of the Microflown microphone, *Sensors and Actuators* A 86 (2000) 171-181.
9. F.J.M. van der Eerden, H-E. de Bree, H. Tijdeman, Experiments with a new acoustic particle velocity sensor in an impedance tube, *Sensors and Actuators* A 69 (1998) 126-133.
10. J.W.S. Rayleigh, 'The theory of sound', Vol. II, New York; Dover, second revised edition (1945).
11. V. Ramamurthy, U.S. Rao, The steady streaming generated by a *vibrating* plate parallel to a fixed plate in a dusty fluid, *Fluid Dynamics Research* 2 (1987) 47-63.

12. C.Y. Wang and B. Drachman, The steady streaming generated by a vibrating plate parallel to a fixed plate, *Applied Scientific Research* 39 (1982) 55-68.
13. N. Rott, The influence of heat conduction on acoustic streaming, *Journal of Applied Mathematics and Physics* 25 (1974) 417.
14. P. Merkli and H. Thomann, Transition to turbulence in oscillating pipe flow, *Journal of Fluid Mechanics* 68 (1975) 567-575.
15. G. Maidenik, Energy dissipation associated with gas-pumping in structural joints, *Journal of the Acoustical Society of America* 40 (1966) 1064-1072.
16. E.E. Ungar and J.R. Carbonell, On panel vibration damping due to structural joints, *AIAA Journal* 4 (1966) 1385-1390.
17. C. Zwikker, *Sound Absorbing Materials*, chapter 2 (1949).
18. H.S. Roh, W.P. Arnott, J.M. Sabatier, R. Raspett, Measurement and calculation of acoustic propagation constants in arrays of small air-filled rectangular tubes, *Journal of the Acoustical Society of America* 89 (6) (1991) 2617-2624.

Chapter 5

Determination of the sensitivity behaviour by electronic characterisation

Abstract

In the foregoing chapter a purely acoustic calibration method of the flow sensor was treated. The Microflown was then characterised acoustically, in a standing wave tube with a sound source and a reference microphone. In this chapter it is shown that the sensor's sensitivity and frequency behaviour can be determined electronically as well, and an electronic method for determination of the device output response, which is more convenient, is therefore presented. The method is not only less complicated, it also makes it possible to cover easily the entire acoustic frequency spectral range. The principle is shown to be geometry independent, it can be applied for a wide range of thermal flow sensors, even for those consisting of more than two wires. The method is based on a general relation following from the heat transfer theory. This relation does not depend on the precise geometry of the sensor. The theory is experimentally verified for various thermal flow sensors of different geometries, up to approximately 10 kHz, and a good correspondence between measurements and theory is found.

5.1 Introduction

As illustrated by the preceding chapter, the sensitivity of the Microflown is generally determined in an acoustic set-up. In this calibration, use is made of merely acoustic principles, and the sensor response to sound or gas flow. This chapter presents and describes an electronic method, instead of this acoustic method, for determination of the device sensitivity.

From physical principles and similarities between the governing equations, it can be proven that from electronic measurements only, the acoustic behaviour can be deduced. The deduction of the sensitivity of the sensor, the output response due to a gas flow or particle velocity, is based on the heat diffusion equation for the temperature near the wires, as was described in chapter 3. To the stationary temperature distribution around the sensor wires, a temperature perturbation is applied by a small convection term. Now, in an electronic set-up, an alteration of the stationary temperature profile is achieved by the electronic heating of one of the wires, causing both wires to change in temperature. These temperature changes provide the required information to deduce the acoustic response.

Since the method is geometry-independent, it can be applied very generally. This means that for *all* types of thermal flow sensors consisting of more than one wire and based on the principle of temperature gradient measurement [3, 4, 5, 6], the electronic method can be used to deduce the response of the sensor to fluid flows, for both AC- and DC-flows.

5.2 Theory

We will show that the sensitivity of the Microflown to acoustic signals can be found by using electrical measurements only. The relationship between its sensitivity and the impedances of the two wires exists for very general assumptions about the system. The first assumption for this system is that the heat transfer in the device can be described by the linear heat equation. Since the heat conductivity of air depends on temperature, this assumption restricts the power dissipated in the wires, as the wire temperature should stay below approximately 500 K [1]. The second assumption is that the wire width and thickness are much

smaller then all the other geometrical parameters characterising the Microflown. This is true for all current Microflowns used in applications, and many flow sensors.

Devices of different design are in practical use. The channel can be closed, half-open, or open (with free standing wires). See also figure 3-2. One can find an analytical solution for the temperature distribution for a rectangular channel [1] or for free standing wires, as we did in chapter 3 and [2]. In the general case of an arbitrary channel cross section one can find the solution of the heat equation in terms of unknown eigenvalues and eigenfunctions describing the temperature distribution in the channel cross section.

The statement to be proven here is that the relation between the acoustic sensitivity and the impedances of the wires does *not* depend on the unknown eigenvalues and eigenfunctions and so it has a very general character. It will be proven that the background temperature, the correction to it due to time-dependent particle velocity (sound wave) and that due to a time varying power in a wire, all can be expressed via the same Green's function. This property is true if the wires can be considered as thin. The reason is that all these values are the solution of the same heat equation with the same boundary conditions. In this way one can deduce a relationship between the acoustic sensitivity and the wires' electrical impedances as a function of the wires' positions. Such a relation is not very helpful in practical sense but the specific symmetry of the heat equation allows us to relate the derivative of the Green's function to sensor position with the integral over frequency from this function. In this way the acoustic sensitivity at frequency f is connected with the electrical transfer function of the device averaged over the frequency band from 0 to a given frequency f.

The basic description of the sensor has been developed in detail in chapter 3. The problem was solved there for a geometry with free standing wires, but the proposed method is still valid for a rectangular channel, and much more general geometries. Here we will follow the description of that chapter and adopt the same notations.

5.2.1 The stationary temperature distribution

Let us consider first the stationary temperature distribution in the channel of the Microflown when the gas inside does not move. The coordinate system is chosen as shown in figure 5-1 with the *x*-axis along the channel.

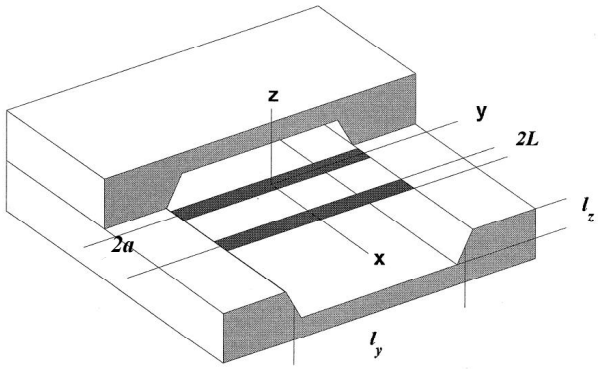

Figure 5-1: Geometry of the sensor used in the analysis.

The wires, of length l_y, are directed along the *y*-direction. The distance between the wires is *2a*; one of them is located at $x = a$ and the other one at $x = -a$. If both of them are heated with a constant power *P* and there is no gas flow, then the temperature distribution *T(x,y,z)* is found from the stationary heat equation:

$$-k\nabla^2 T = \frac{P}{l_y}[\delta(x-a)+\delta(x+a)]\delta(z). \qquad (1.)$$

where $\delta(x)$ is the Dirac delta function.

According to our assumptions in (1) the heat conductivity *k* was supposed not to depend on temperature and because the wires are thin and narrow the heat sources on the right-hand side can be described by δ-functions. Note that the power is distributed homogeneously along *y* and the temperature is determined by the power per unit wire length.

It is convenient to introduce the dimensionless coordinates and parameters

$$\xi = \frac{x}{l}, \quad \eta = \frac{y}{l}, \quad \zeta = \frac{z}{l}, \quad \xi_1 = \frac{a}{l}, \quad \xi_0 = \frac{L}{l}, \qquad (2.)$$

where *l* is any characteristic size of the channel cross section and *L* is half the width of the wire. In the dimensionless coordinates the equation (1) will get the form

$$\left(\partial_{\xi}^{2} + \nabla_{\perp}^{2}\right)T = -\frac{P}{kl_{y}}[\delta(\xi - \xi_{1}) + \delta(\xi + \xi_{1})]\delta(\zeta), \tag{3.}$$

where $\nabla^2_{\perp}=\partial^2_{\eta}+\partial^2_{\zeta}$ is the transverse Laplace operator.

At the channel walls, the temperature obeys homogeneous boundary conditions, for example, $T = T_0$. Because the device walls are made of silicon, which has a heat conductivity k_{Si} much larger then the air conductivity k, we can take the walls to be at the environment temperature T_r (room temperature). Even in the situation that the wire is in contact with the silicon substrate it was proven [1] that only a small part of the heat flux escapes via this contact and that the main heat flux goes via the air. Therefore, even in the contact points the same boundary conditions hold. The situation that there are no walls in any direction can be considered as a wall at infinity where the same condition ($T = T_0$) is true. Eq. (3.) is linear and one can redefine the temperature $T \rightarrow T - T_0$ in such a way that the boundary condition is reduced to $T = 0$ at the channel walls.

One can define the set of functions $\psi_n(\eta,\zeta)$ which obey the boundary conditions and are the eigenfunctions of the transverse Laplace operator:

$$\nabla_{\perp}^{2}\psi_{n}(\eta,\zeta) = -\lambda_{n}^{2}\psi_{n}(\eta,\zeta) \tag{4.}$$

with corresponding eigenvalues λ^2_n. Here the index n is actually a multi-index comprising two numbers (n,m) since Eq.(4.) is two dimensional. These numbers do not need to be integer; one or both of them can be continuous if the problem described by Eq.(4.) has a continuous spectrum. There is no necessity to have explicit expressions for the functions $\psi_n(\eta,\zeta)$ and the values λ^2_n, it is quite sufficient to know that the functions can be chosen orthogonal:

$$\int d\eta d\zeta \psi_{n}\psi_{m} = \delta_{nm}. \tag{5.}$$

Here δ_{nm} is the product of Kronecker symbols if both components of the multi index are integer; one or both of the symbols have to be changed by the δ-function if one or both of these components are continuous.

The solution of Eq.(3.) can be found by expanding the temperature on these functions ψ_n:

$$T(\xi,\eta,\zeta) = \sum_{n} T_{n}(\xi)\psi_{n}(\eta,\zeta) \tag{6.}$$

If one or both components of the multi-index are continuous then the corresponding summation has to be changed by an integral. Using then the orthogonality condition (5.) one can find the equation for the components $T_n(\xi)$:

$$\partial_\xi^2 T_n - \lambda_n^2 T_n = -\frac{P}{kl_y} A_n \left[\delta(\xi - \xi_1) + \delta(\xi + \xi_1)\right], \qquad (7.)$$

where the constants A_n are $A_n = \int d\eta \psi_n(\eta, 0)$.

The solution of Eq.(7.) should obey the boundary conditions at both ends of the channel $T_n \to 0$ when $\xi \to \pm\infty$. This solution can be easily found as

$$T_n(\xi) = \frac{P}{kl_y} \frac{A_n}{2\lambda_n} \left[\exp\left(-\lambda_n |\xi - \xi_1|\right) + \exp\left(-\lambda_n |\xi + \xi_1|\right)\right]. \qquad (8.)$$

One can substitute it into Eq.(6.) to get the final result for the temperature distribution. Note that actually we have not solved the heat equation because the functions ψ_n and the values of λ_n have not been specified. However, Eq.(8.) is everything that is needed to connect the acoustical sensitivity of the sensor with the electrical measurements.

One important detail should now be mentioned. If one would like to find the heater temperature, for example at $\xi = \xi_1$, one fails because the sum in (6.) will diverge. This is because at large n the eigenvalues λ_n are proportional to n but the coefficients A_n can be n-independent. Then the sum in (6.) will be logarithmically diverging. It is quite clear why this divergence appears. It results from the approximation that the wire can be considered as infinitely thin. There is an easy way to avoid this problem without any significant complication of the mathematics. One should average the temperature over the heater width in the place where it is located. For example, if one intends to calculate the heater temperature at $\xi = \xi_1$ one can average only the first term in (8.) in the range $\xi_1 - \xi_0 < \xi < \xi_1 + \xi_0$ because the second term does not bring any trouble and is safely converging due to the presence of the exponent. The averaging then gives us

$$\overline{T}_n(\xi_1) = \frac{P}{kl_y} A_n \left[\frac{1 - \exp(-\lambda_n \xi_0)}{2\lambda_n^2 \xi_0} + \frac{\exp\left(-\lambda_n |\xi + \xi_1|\right)}{2\lambda_n}\right].$$

Comparing it with (8.) at $\xi = \xi_1$ a simple rule to avoid the divergence problem can be deduced. In the place where the divergence is possible the following substitution has to be made:

$$\frac{1}{\lambda_n} \to \frac{1-\exp(-\lambda_n \xi_0)}{\lambda_n^2 \xi_0}. \tag{9.}$$

This change allows taking into account the final width of the wire and makes the sum in (6.) convergent. Indeed, at $\lambda_n\xi_0<<1$ the right hand side of (9.) coincides with the left hand side but at large n it behaves as $1/\lambda_n^2$ providing the sum in (6.) to be convergent.

5.2.2 Analogy between acoustically and electrically induced disturbance

Now one can consider the situation that the gas in the channel is flowing along the channel with some velocity $v(t)$ defined by a sound wave. This movement breaks the symmetry in the temperature distribution due to the convection process. The sound velocity is typically small in comparison with the heat diffusion velocity $D/l \sim 0.1$ m/s, where $D = k/\rho c_p \approx 1.9\cdot10^{-5}$ m^2/s is the heat diffusion coefficient for air. For this reason the convection introduces only a small correction δT^a to the temperature distribution, and we can proceed in the same way as we did in chapter 3. The correction δT^a can be found from the nonstationary heat equation when the convective term is considered as a perturbation

$$\partial_t \delta T^a - D\nabla^2 \delta T^a = -v(t)\partial_x T. \tag{10.}$$

For the electrical characterisation of the device suppose that both wires are heated by a constant power P, but that one of the heaters, for example at $x = a$, is powered additionally by a small AC component $\delta P(t)<< P$. We are interested in the correction to the sensor's temperature δT^e due to this additional AC power. It can be found from the following equation:

$$\partial_t \delta T^e - D\nabla^2 \delta T^e = \frac{\delta P(t)}{l_y}\frac{1}{\rho c_p}\delta(x-a)\delta(z). \tag{11.}$$

Of course, the equations (10.) and (11.) are the same but the sources on the right hand side, which define the solutions, are quite different. In the acoustic case a source is distributed along the channel axis but in the electric case the source is located on the wire. When the sources are different the solutions will also differ.

However, because the unperturbed temperature T obeys the heat equation for both situations, in the limit of small perturbations, it is possible to connect δT^a and δT^e. Consider the case of a harmonically in time varying sound wave and an AC power

$$v(t) = v\exp(i\omega t), \quad \delta P(t) = \delta P \exp(i\omega t) \tag{12.}$$

with the corresponding frequency $f = \omega/2\pi$. Introducing the dimensionless coordinates and frequency

$$\overline{f} = \frac{\omega l^2}{D} \tag{13.}$$

one gets instead of (10.) and (11.)

$$\nabla^2 \delta T^a - i\overline{f}\delta T^a = -\frac{v}{v_0}\partial_\xi T,$$
$$\nabla^2 \delta T^e - i\overline{f}\delta T^e = \frac{\delta P}{kl_y}\delta(\xi - \xi_1)\delta(\zeta),$$

where $v_0 = D/l$ represents the diffusion velocity. The temperature correction obeys the same boundary conditions as the temperature itself: it disappears on the channel walls and is going to zero at $\xi \to \pm\infty$. Therefore, we can expand δT (acoustic or electric) in the same eigenfunctions ψ_n:

$$\delta T(\xi, \eta, \zeta) = \sum_n \delta T_n(\xi)\psi_n(\eta, \zeta). \tag{14.}$$

Substituting it into the equations above one finds

$$\partial_\xi^2 \delta T_n^a - K_n^2 \delta T_n^a = \frac{v}{v_0} A_n \partial_\xi T_n,$$
$$\partial_\xi^2 \delta T_n^e - K_n^2 \delta T_n^e = -\frac{\delta P}{kl_y} A_n \delta(\xi - \xi_1), \tag{15.}$$

where $K_n^2 = \lambda_n^2 + i\overline{f}$.

To see the correspondence between δT^a and δT^e it will be convenient to write the solutions via the same Green's function $G_n(f, \xi\text{-}\xi')$ which, by definition, obeys the equation

$$\partial_\xi^2 G_n(f, \xi - \xi') - K_n^2 G_n(f, \xi - \xi') = \delta(\xi - \xi'). \tag{16.}$$

It has a well-known solution

$$G_n(f,\xi-\xi') = -\frac{1}{2K_n}\exp\left(-K_n|\xi-\xi'|\right). \tag{17.}$$

Using this function the solution of the equations (15.) can be written then as follows

$$\begin{aligned}\delta T_n^a &= \frac{v}{v_0}A_n\int_{-\infty}^{\infty}d\xi' G_n(f,\xi-\xi')\partial_{\xi'}T_n(\xi'),\\ \delta T_n^e &= -\frac{\delta P}{kl_y}A_n G_n(f,\xi-\xi_1).\end{aligned} \tag{18.}$$

The unperturbed temperature distribution $T_n(\xi)$ given by (8.) can also be represented via the same Green's function but then taken at zero frequency:

$$T_n(\xi) = -\frac{P}{kl_y}A_n\left[G_n(0,\xi-\xi_1)+G_n(0,\xi+\xi_1)\right]. \tag{19.}$$

Using only general properties of the Green's function we can transform the integral in (18.) to the form:

$$\begin{aligned}i\bar{f}\delta T_n^a = \frac{v}{v_0}\frac{P}{kl_y}A_n\partial_\xi\{\ &G_n(0,\xi-\xi_1)+G_n(0,\xi+\xi_1)\\ &-G_n(f,\xi-\xi_1)-G_n(f,\xi+\xi_1)\ \}\end{aligned} \tag{20.}$$

Now it is seen that the acoustic and electric corrections to the temperature are really related to each other. However, there is no direct proportionality between δT^a and δT^e. Moreover, δT^a depends on the derivative on ξ, which we are not able to control. The actual precise relation comes from a specific property of the Green's function for the heat equation

$$\partial_\xi\left[G_n(f,\xi-\xi')-G_n(0,\xi-\xi')\right] = \frac{i}{2}(\xi-\xi')\int_0^{\bar{f}}d\bar{f}\,G_n(f,\xi-\xi') \tag{21.}$$

which can be checked directly with the help of (17.). In this way a general relation can be deduced, connecting the temperature response of the Microflown to an acoustic wave with the Green's function, which, on its turn, is proportional to the temperature response to the electric signal:

$$\delta I_n^a = -\frac{v}{2v_0}\frac{P}{kl_y}A_n\frac{1}{f}\int_0^f df\left[(\xi-\xi_1)G_n(f,\xi-\xi_1)+(\xi+\xi_1)G_n(f,\xi+\xi_1)\right]. \tag{22.}$$

This relation is true for any point along the channel.

For practical purposes one is interested in the temperatures of the sensors, that are located at $z = 0$ and $x = a$ or $x = -a$. Additionally, since the sensor resistances are really important, the temperatures have to be averaged over the wire length. Now these averaged temperatures are denoted as ΔT_1 and ΔT_2 for the sensors located at $x = a$ and $x = -a$, respectively. Using (14.), (18.), and (22.) for the mean wire temperatures characterised electrically or acoustically one finds

$$\begin{aligned} \Delta T_1^e &= -\frac{\delta P}{k l_y}\sum_n \frac{l}{l_y} A_n^2 G_n(f,0), \quad \Delta T_2^e = -\frac{\delta P}{k l_y}\sum_n \frac{l}{l_y} A_n^2 G_n(f,2\xi_1), \\ \Delta T_1^a &= -\Delta T_2^a = -\frac{v}{v_0}\frac{P}{k l_y}\frac{\xi_1}{f}\int_0^f df \sum_n \frac{l}{l_y} A_n^2 G_n(f,2\xi_1). \end{aligned} \tag{23.}$$

Therefore the final relation between the averaged sensor temperatures in the acoustical and electrical characterisation becomes obvious

$$\Delta T_1^a = \frac{v}{v_0}\frac{P}{\delta P}\frac{\xi_1}{f}\int_0^f df\, \Delta T_2^e . \tag{24.}$$

It shows that the acoustical response at a frequency f is proportional to the electrical response averaged over the frequency range from 0 to f. This is a nontrivial and unobvious relation that will be true for any device as long as the wires are thin and the temperature dependence of the heat conductivity can be neglected (linear heat equation). For thin wires it was natural to suppose that their heat capacity is not important, but in reality it can become relevant at high frequencies. The method to take this finite heat capacity into account has been proposed in chapter 3 and it can also be applied to the problem of the electrical characterisation of the device. However, it is not the purpose of this chapter to discuss this aspect of the problem now.

5.2.3 Implications for the electrical signals

In practical applications the voltage of a wire is often easily measured, and in the electrical characterisation one measures the voltage of the wire(s) as a function of frequency. For this reason the relation (24.) has to be expressed via directly

measured values. The voltage is connected with the current I flowing via the sensor by Ohm's law:

$$U = I R_0 \left[1 + \alpha T(P)\right], \tag{25.}$$

where R_0 is the sensor resistance at room temperature, α is the temperature coefficient, and $T(P)$ is the sensor temperature above the room temperature at a given power $P=U \cdot I$. When the device is operating as an acoustic sensor a stabilised voltage source U_0 is used and the signal u^a is recorded as indicated in figure 5-2.

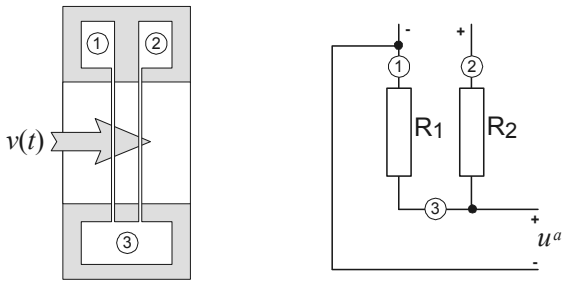

Figure 5-2: Electrical scheme of the Microflown, operating acoustically; $R_1=R_2=R$, u^a is the output signal.

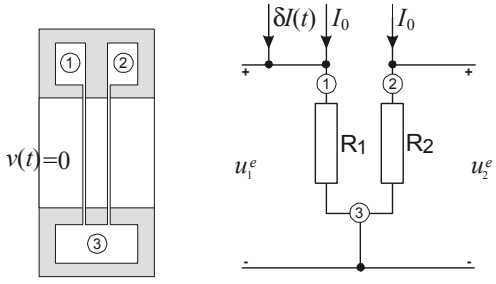

Figure 5-3: Scheme of the set up used in the electrical characterisation. Now v(t)=0 (compare with figure 5-2) and the additional current is δI(t).

In this case the temperature change of the sensor is related to the external influence: the acoustic wave. If the wave has a frequency f then the signal on this frequency can be written as

$$u^a = \frac{U_0}{2} \alpha \frac{R_0}{R} \Delta T_1^a, \tag{26.}$$

where ΔT^a_1 is defined at operating power $P=U_0^2/R$ and R is the sensor resistance at operating temperature.

In the case of the electrical characterisation a stabilised DC current I_0 is flowing through each wire, while an additional AC component flows through wire 1 ($x=a$). The resulting current for the wire 1 can be written as $I = I_0+\delta I \cos(\omega t)$. The amplitude of the AC component δI can always be chosen small not to complicate the analysis. Neglecting then the higher order terms of AC components, the additional oscillating power in the wire can be represented as

$$\delta P = u_1^e I_0 + U_0 \delta I\,, \tag{27.}$$

where $U_0=U(I_0)$ is the DC component of the voltage. The AC voltage measured on wire 1 can be written then using the Ohm law

$$u_1^e = R\delta I + \alpha R_0 I_0 \Delta T_1^e\,.$$

Since the sensor temperature is proportional to δP, we can express the AC voltage on wire 1 as

$$u_1^e = \delta I R \cdot \frac{1+S_1}{1-S_1}, \quad S_1 = -\alpha \frac{R_0}{R}\frac{P_0}{kl_y}\sum_n \frac{l}{l_y} A_n^2 G_n(f,0). \tag{28.}$$

Here P_0 represents the DC power. Wire 2 is powered with only a DC current and the AC voltage on this wire will be

$$u_2^e = \alpha I_0 R_0 \Delta T_2^e\,.$$

The temperature correction is again proportional to the amplitude of the oscillating δP, which can be found from (27). Thus one can find

$$u_2^e = \delta I R \cdot \frac{2S_2}{1-S_1}, \quad S_2 = -\alpha \frac{R_0}{R}\frac{P_0}{kl_y}\sum_n \frac{l}{l_y} A_n^2 G_n(f,2\xi_1). \tag{29.}$$

Using the basic relation (24.) one can express now the acoustic signal (26.) via the electric signals (28.) and (29.)

$$u^a = \left(\frac{U_0}{2}\right)\frac{va}{D}\cdot\frac{1}{f}\int_0^f df\,\frac{u_2^e}{\delta I R + u_1^e}. \tag{30.}$$

This is the final relation we have been looking for. It contains only one geometrical parameter of the device, the mutual wire distance a, and only one medium parameter, the fluid characteristic D. All the other parameters are electrical, and well defined.

The electrical characterisations of the device gives the values $u^e_{1,2}$ as functions of frequency. To obtain the acoustic signal the integral in (30.) should be calculated numerically. To do this one needs to extrapolate the integrand to smallest frequencies, which are not accessible in the measurements. The low frequency behaviour of $u^e_{1,2}$ is easy to investigate analysing the Green's function (17.) in the limit $f \to 0$. This analysis gives

$$F(f) = \frac{u_2^e}{\delta I R + u_1^e} \to (A + iBf) \quad \text{at } f \to 0\,,$$

where A and B are some constants. If the experimental cut-off frequency is f_0, then

$$\int_0^{f_0} df\ F(f) = f_0\left[\operatorname{Re} F(f_0) + \frac{i}{2}\operatorname{Im} F(f_0)\right]. \qquad (31.)$$

This relation defines the extrapolation procedure and so the problem can be considered as completely solved.

5.2.4 A three-wire configuration

A different geometry of the acoustic flow sensor can be realised with three instead of two wires. In this configuration, the central wire acts as heater, while the other two wires, in which a relatively low power is dissipated, act as sensing wires.

This sensor-heater-sensor ('SHS'-) configuration will be described in detail in the next chapter. In that chapter we will see that this probe has an improved performance, and that an approximately two times higher low frequency sensitivity than in a two-wire situation can be attained, if in the central heated wire approximately 85% of the total power is dissipated. Since most of the power is dissipated in the central heater, that does not act as a sensor, the two sensing wires have a relatively low temperature and therefore a relatively low noise level. Following a similar approach as above, Eqs. (15.)-(24.), it can be deduced that, in this three-wire situation, the acoustical response of one wire can again, similarly, be expressed in the electrical responses of this wire to the additional powering of the other two wires. Both of the other two wires have to be powered apart, independently. For the three-wire thermal flow sensors, with arbitrary powers in the different wires, this means that principally the problem is also solved.

5.3 Experiments

In the experimental set-up both wires of the (two-wire) sensor were connected as shown in figure 5-4. The two wires were powered using a stabilised DC-current I_0. Using the current source, the frequency of the additional current δI was varied in a broad frequency range while both the voltage of wire A (resistance R_1) and wire B (resistance R_2) were recorded, using a lock-in amplifier. Using Eq.(30.), the

predicted acoustic sensitivity as a function of frequency was determined. The low experimental cut-off frequency was taken as 10 Hz. From this numerical procedure, the predicted acoustic response of the sensor was found to be as the graphs plotted in figure 5-5.

The dissipated DC power in each wire was set to be 10 mW, by adjusting the constant current I_0 through wire A and B. The additional oscillating current δI through wire A was chosen to be $\delta I = 0.01 I_0$. The electronic responses of wires A and B were recorded using a lock-in amplifier. Both amplitude and phase were recorded in a frequency range 10 Hz-10 kHz.

Besides, the sensitivity was determined acoustically, in a 'standing wave tube'. From the ratio between the output signals of the reference microphone and the Microflown, the sensitivity of the latter was deduced.

The described set-up and experimental approach was used for several sensors. As we know from chapter 3, the dimensions of the sensor, in particular the mutual wire distance and the etch depth (the distance to the channel surface, l_z), determine the precise frequency behaviour of the sensitivity function. To investigate these effects and to verify the geometry-independence of the correspondence between electronic and acoustic behaviour, four Microflowns of different geometry were analysed. The sensors had a wire length l_y of 1 mm, and the mutual distance $2a$ between the wires varied from 50, 100 to 300 μm. The etch depth of the channel, i.e. the vertical distance l_z to the heat sink, varied between 40 and 240 μm.

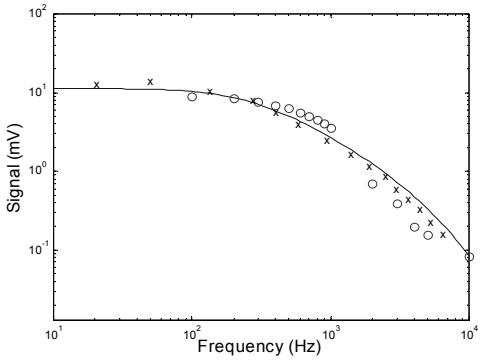

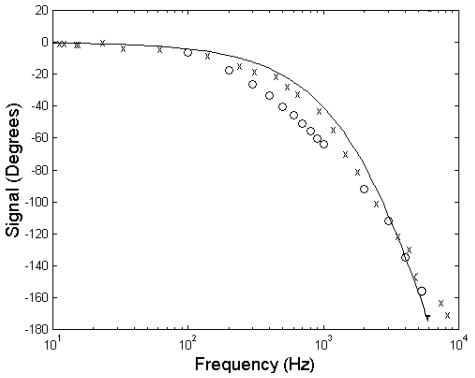

Figure 5-4a: Electrically determined points (x) of the sensitivity and the acoustically measured points (o), together with the theoretical prediction, using model calculations (line), for 'device 1': l_z=40 μm; 2a=100 μm; R_1=3274 Ω; R_2=3620 Ω. Left: amplitude of the response, right: the phase.

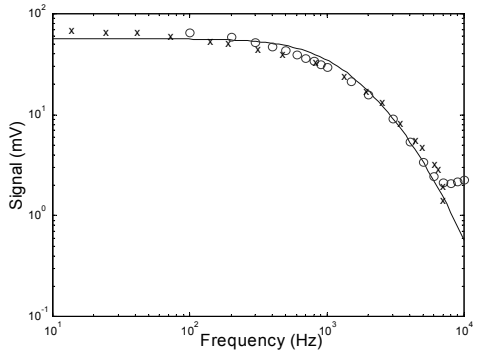

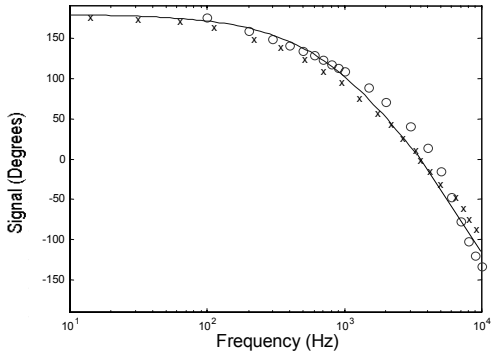

Figure 5-4b: As figure 5-4a, for 'device 2': etch depth l_z=240 μm; mutual wire distance 2a=50 μm; wire resistances R_1=3425 Ω;R_2=3464 Ω.

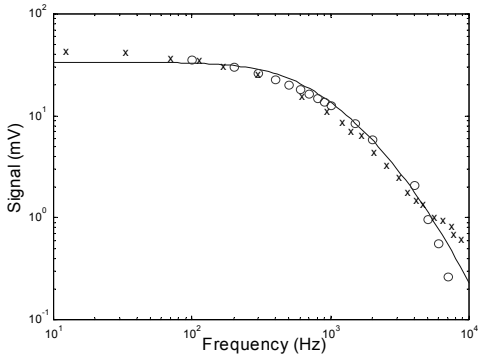

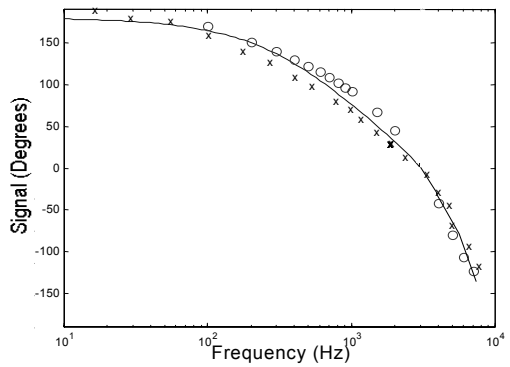

Figure 5-4c: As figure 5-4a, for 'device 3': etch depth l_z=240 μm; mutual wire distance 2a=100 μm; wire resistances R_1=2920 Ω; R_2=2875 Ω.

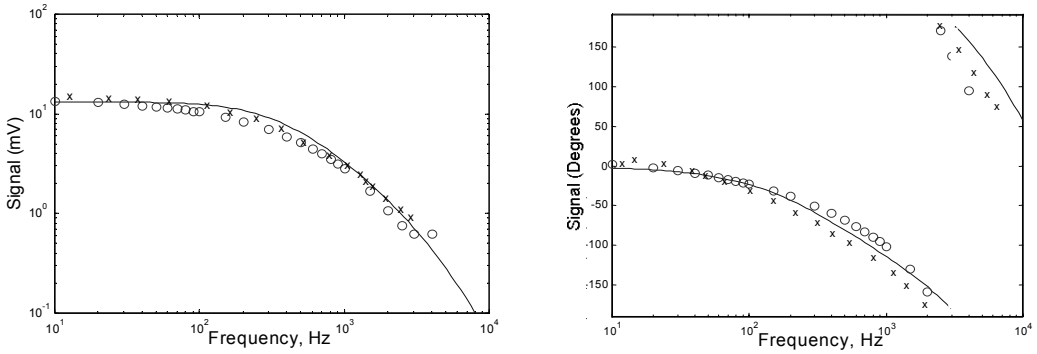

Figure 5-4d: As figure 5-4a, for 'device 4': etch depth l_z=240 μm; mutual wire distance 2a=300μm; wire resistances R_1=1411 Ω; R_2=1414 Ω.

Figure 5-4 shows the electronically obtained results (the crosses), together with the acoustic sensitivity of the sensor as measured in the standing-wave-tube (circles). Additionally, the acoustic sensitivity is theoretically determined from the model of chapter 3 that calculates the sensor output for a given sensor geometry. Experiment and theory were compared for these four different geometries.

From these figures it can be concluded that there is a satisfying correspondence between the electrically determined measurement points of the sensor sensitivity and the acoustically determined sensitivity (determined in the standing wave tube). Besides they can be well related to the theoretical prediction for the output signal for the different geometries. Nevertheless small deviations are observed for high frequencies. These deviances may be explained by the finite heat capacities of the sensor wires, that have not been taken into account in the described approach.

5.4 Conclusions

An electrical characterisation method for the sensitivity of the Microflown was presented. In conclusion, it is shown that the new calibration method is a more convenient and less complicated method than the acoustic calibration of the Microflown using e.g. a standing wave tube. We proved from physical principles and correspondences in physical equations that this method yields all the required information to deduce the sensor's acoustic response from electronically obtained

information. The strength of the theoretical description and prediction of the acoustic response lies in the fact that it is very general and independent of the precise geometry of the sensor. It can be shown that for a three-wire configuration the method can be applied as well. This means that both two- and three-wire thermal flow sensors can be electrically characterised. The theory has been experimentally verified for various geometrically different two-wire Microflown up to approximately 10 kHz, and a good correspondence between measurements and theory was found.

5.5 References

1. V.B. Svetovoy, I.A. Winter, Model of the Microflown microphone, *Sensors and Actuators* A 86 (2000) 171-181.
2. J.W. van Honschoten, G.J.M. Krijnen, V.B. Svetovoy, H-E. de Bree, M.C. Elwenspoek, Optimization of a two-wire thermal sensor for flow and sound measurements, *Proceedings of MEMS,* Switzerland (2001).
3. H. Kuttner, G. Urban, A. Jachimowicz, F. Kohl, F. Olcaytug, P.Goiser, Microminiaturized thermistor arrays for temperature gradient, flow and perfusion measurements, *Sensors and Actuators* A 25-27 (1991) 641-645.
4. A. Glaninger, A. Jachimowicz, F. Kohl, R. Chabicovsky, G.Urban, Wide range semiconductor flow sensors, *Sensors and Actuators* A 85 (2000) 139-146.
5. K. Hirata, M. Esashi, Stainless steel-based integrated mass-flow controller for reactive and corrosive gases, *Sensors and Actuators* A 3200, (2002).
6. T.S.J. Lammerink, N.R. Tas, M.C. Elwenspoek, J.H.J. Fluitman, Microliquid flow sensor, *Sensors and Actuators* A (1993) 45-50.

Chapter 6

Towards a geometrical optimisation of the flow sensor

Abstract

In this chapter we proceed with the model of the Microflown as described in chapter 3. The theory is now implemented into a numeric program, so that several assumptions and restrictions for the deduction of the analytic model can be dropped. The implementation of the numeric model into a software program allows for extensive calculations on the influence of varying sensor dimensions on the sensitivity. Consequently, improved devices could be fabricated, and also Microflowns with a new geometry consisting of three wires, instead of the usual two, of which the central wire is relatively most heated. These are the best performing sensors up to date with a frequency range attending over 5 kHz and signal-to-noise ratios improved by 10 dB to more than 20 dB over previous designs.

6.1 Introduction

In the second chapter a model of the particle velocity sensor was developed, in order to deduce an explicit analytic expression of the sensitivity. Particularly for engineering applications it is useful to obtain such a compact expression. Even more important, the deduction gives insight into the physics of the sensor behaviour. However, the analytic deduction was possible by virtue of the reduction of the problem to a two-dimensional one. Now, we release this restriction and take into account the finite length of the wires. Starting from the same basic equation, the heat diffusion equation, and following the same approach of the perturbation theory, we try to find a three-dimensional solution for the temperature difference. This will be written in the form of a double series, an expansion in orthonormal eigenfunctions.

This representation in the form of a series allows for the implementation into a software program, in which the dimensions of the sensor and material parameters can easily be varied and investigated.

6.2 The temperature as a three dimensional solution of the heat equation

To find the temperature distribution around the wires, the stationary heat diffusion equation is a good starting point as seen in chapter 3. It reads

$$-\nabla(k\nabla T) = Q \tag{1.}$$

where k represents the thermal conductivity of the fluid, which is in principle a function of temperature, $k = k(T)$, and Q the heat produced by a heater per unit of time and volume.

We use the geometry as defined in figure 6-1, with the width of the heater equal to $2L$, and l_y the wire length. Contrary to what was done in chapter 3, we now take into account the finite channel depth of $2l_z$: the surfaces at $z = l_z$ and $z = -l_z$ behave as cold walls. If the power P is assumed to be produced homogeneously along the heater, Q can be written as

$$Q(x, y, z) = \frac{P}{2Ll_y} F(x)\delta(z) \tag{2.}$$

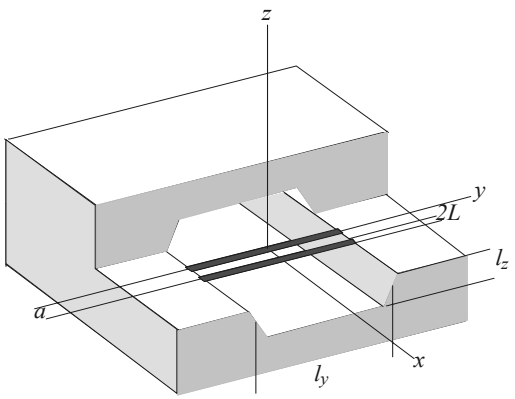

Figure 6-1: Model geometry of the sensor used in this chapter, with cold surfaces at $z = \pm l_z$ above and under the heaters.

At first we analyse the situation of only a single heater. Due to the linearity of the equations the solution for two wires is just the superposition of two single solutions (see also section 3.2.1). This heater is positioned along the *y*-axis, its thickness in the *z*-direction is assumed to be very small and the *x*-coordinates of the heat source obey the function $F(x)$, with

$$\begin{aligned} F(x) &= 0 \ \ for \ |x| > L \ ; \\ F(x) &= 1 \ \ for \ |x| < L \end{aligned} \tag{3.}$$

Assuming that the thermal conductivity k does not depend on the temperature, which is justified if the temperature gradients are not too high [1], the heat equation becomes linear and yields

$$(\partial_x^2 + \partial_y^2 + \partial_z^2)T = -\frac{P}{2l_y kL} F(x)\delta(z) \tag{4.}$$

To simplify this equation further, the function $F(x)$ is changed into a δ-function as well: if the width $2L$ is not too large, $F(x)/2L$ can be replaced by $\delta(x)$.
Introducing the normalised variables $\xi = x/l_z$; $\eta = 2y/l_y$; $\zeta = z/l_z$, where l_z is half of the channel height, changes the equation into

$$(\partial_\xi^2 + (\frac{2l_z}{l_y})^2 \partial_\eta^2 + \partial_\zeta^2)T = -\frac{Pl_z^2}{l_y k}\delta(x)\delta(z) = -\frac{P}{l_y k}\delta(\xi)\delta(\zeta) \tag{5.}$$

Taking into account that the solution should obey the boundary conditions that it is zero at the channel surfaces at $z = \pm l_z$ and at $y = \pm l_y/2$, we write $T(\xi,\eta,\zeta)$ as an expansion in the orthonormal eigenfunctions in η and ζ, the harmonics,

$$T(\xi,\eta,\zeta)=\sum_{nm=0}^{\infty}T_{nm}(\xi)\cos(\lambda_n\zeta)\cos(\lambda_m\eta),$$
$$\lambda_n=\frac{\pi}{2}(2n+1) \tag{6.}$$

Substituting this expansion into Eq.(5.), and taking into account the boundary conditions and the matching condition at $\zeta = 0$, gives for $T_{nm}(\xi)$:

$$T_{nm}(\xi)=\frac{T_0(-1)^m}{\lambda_m\sigma_{nm}}e^{-\sigma_{nm}|\xi|}$$
$$T_0=\frac{P}{kl_y},\sigma_{nm}=\sqrt{\lambda_n^2+(2l_z/l_y)^2\lambda_m^2} \tag{7.}$$

6.3 The temperature difference due to the fluid velocity

A temperature difference between the two heated wires occurs when there is a flow of the fluid (the gas) in the channel. In order to calculate this temperature difference due to the presence of a small forced convection term concerning the velocity v, we can consider this convection term in the heat diffusion equation as a perturbation to the stationary temperature profile of the wire.

In the case of a moving gas in the channel, the heat equation for the temperature becomes

$$\rho c_p(\partial_t T+v\nabla T)-\nabla(k\nabla T)=Q \tag{8.}$$

with v the gas (or fluid) velocity, c_p the heat capacity of the gas at constant pressure and the heat power density Q defined as before (Eq.(39.)).

If the temperature gradients are not too high so that the inhomogeneities of the heat conduction coefficient k can be neglected again, and when the gas velocities are relatively small, the solution of Eq.(8.) consists of the temperature from Eq.(7.), plus a small correction δT proportional to v. This correction, or perturbation term, δT, obeys the nonhomogeneous equation

$$\partial_t\delta T-D\nabla^2\delta T=-v\partial_x T \tag{9.}$$

with $D = k/\rho c_p$, the thermal heat diffusion coefficient.

Since the velocity is supposed to be directed along the channel, in the x-direction, $\vec{v} = (v,0,0)$ and the product $v\partial_x T$ appears at the right-hand side of Eq.(9.).

The amplitude of the acoustic wave, the particle velocity, depends on the fluid parameters, in particular the density, and is thus temperature dependent, so that it cannot be considered to be constant along the sensor. For a harmonically varying wave in the sensor with a velocity v corresponding to an acoustic pressure δp at room temperature T_r, one can write in good approximation

$$v(\xi,\eta,\zeta,t) = v_0 \frac{T(\xi,\eta,\zeta)}{T_r} e^{i\omega t}$$
$$v_0 = \frac{\delta p}{\rho(T_r)c} \qquad (10.)$$

with $\rho(T_r)c$ the acoustic impedance z at room temperature T_r, z = 448 kg/m^{2}s. For the latter relation between velocity and pressure, the 'free field' condition was assumed to be met. Since the expression for v in Eq. (10.) in this form does not obey the boundary conditions, namely it does not vanish on the channel walls[1], it should be modified into an expansion in harmonics in ζ and in η:

$$v(\xi,\eta,\zeta,t) = e^{i\omega t} \sum_{nm}^{\infty} v_{nm}(\xi)\cos(\lambda_m \eta)\cos(\lambda_n \zeta) \qquad (11.)$$

of which the amplitudes $v_{nm}(\xi)$ still have to be determined. The involved Reynold's numbers are very low (Re $\leq 10^{-3}$), so that for a rectangular channel and a fully developed flow the velocity distribution is parabolic [12] and can be approximated by only the first harmonic. Therefore, an adequate expression for the velocity becomes [1]

$$v(\xi,\eta,\zeta,t) = v_0 \frac{T(\xi,\eta,\zeta)}{T_r} e^{i\omega t} \cos(\frac{\pi}{2}\eta)\cos(\frac{\pi}{2}\zeta) \qquad (12.)$$

which clearly shows the position and temperature dependence of the particle velocity within the sensor.

The stationary temperature distribution (v = 0) in the channel is found from the heat equation, Eq. (5). In order to simplify the calculations, they are performed at first for the situation of only one wire at $\xi = 0$. Afterwards, the solutions for T and

[1] The assumption that on the channel walls $\eta = \pm 1$, $\zeta = \pm 1$, $v = 0$, is called the 'no-slip condition' [11, 12].

for δT can be easily shifted to $\xi = +\xi_1$ resp. $\xi = -\xi_1$. (For a sensor with a wire separation a, $\xi_1 = a/2l_z$.)

For the temperature one can write as before the expansion in harmonics from Eq. (6.), with $T_n(\xi)$ as in Eq. (7.). The correction term δT is found from Eq. (9.), which, for harmonic oscillations in time of the form $\delta T = \delta T(\xi,\eta,\zeta)\, e^{i\omega t}$, becomes

$$i\omega\delta T - D\nabla^2\delta T = -v\partial_x T \tag{13.}$$

Scaling to dimensionless variables changes this into

$$(\partial_\xi^2 + (\frac{2l_z}{l_y})^2\partial_\eta^2 + \partial_\zeta^2)\delta T - i\omega\frac{l_z^2}{D}\delta T = -\frac{v}{\bar{v}}\partial_\xi T, \quad \text{with} \quad \bar{v} \equiv \frac{D}{l_z} \tag{14.}$$

The thermal diffusion constant D depends on the temperature via the fluid density ρ. It also depends on the temperature via $k(T)$ and $c_p(T)$, but these temperature dependences are small compared to the temperature dependence of ρ. The fluid velocity is not constant within the sensor either, since it is temperature dependent too (Eq.(12.)). Nevertheless, in the ratio $v/\bar{v}$ the temperature dependence disappears so that one can take as a good approximation for the velocity $v_0 e^{i\omega t}\cos(\frac{\pi}{2}\eta)\cos(\frac{\pi}{2}\zeta)$, and use D at room temperature.

For the correction term δT, a double expansion similar to that for T can be made. It is

$$\begin{aligned} &\delta T(\xi,\zeta,\eta) = \sum_{n,m=0}^{\infty}\delta T_{nm}(\xi)\cos(\lambda_n\zeta)\cos(\lambda_m\eta), \\ &\lambda_n = \frac{\pi}{2}(2n+1) \end{aligned} \tag{15.}$$

Using the expansion for $\delta T(\xi)$, Eq. (15.), then

$$\delta T_{nm}'' - \sigma_{nm}^2\delta T_{nm} - i\frac{\omega l_z^2}{D}\delta T_{nm} = \frac{v_0}{\bar{v}}\partial_\xi T_{nm}(\xi) \tag{16.}$$

with the notation $\delta T'' \equiv \frac{\partial^2 T}{\partial\xi^2}$. To be fully correct, one should take for v_0 in Eq.(16.) the full expansion in harmonics, $\sum_{i,j=0}^{\infty} v_{ij}\cos(\lambda_i\eta)\cos(\lambda_j\zeta)$,or at least, for a parabolic flow profile, the first coefficient of this series, $v_0\cos(\frac{\pi}{2}\eta)\cos(\frac{\pi}{2}\zeta)$, as in

Eq.(12.). For each δT_{nm}, the velocity term in the right hand side of Eq.(16.) will thus contain a summation over i and j. In [1] this total summation was evaluated explicitly, and from the calculation there it was concluded that if the full expansion of v is replaced by the single value v_0 (actually corresponding to a uniform velocity distribution), the result changes less than 1 %. Therefore, we apply this simplification and set $v(\xi,\eta,\zeta) = v_0$.

Since Eq. (7.) gives $T_{nm}(\xi) = \frac{T_0(-1)^m}{\lambda_m \sigma_{nm}} e^{-\sigma_{nm}|\xi|}$; $T_0 = \frac{P}{kl_y}$, this can be substituted and the equation for $\delta T_{nm}(\xi)$ becomes

$$\delta T_{nm}'' - K_{nm}^2 \delta T_{nm} = -sign(\xi)\frac{v_0}{\bar{v}}\frac{(-1)^m}{\lambda_m} T_0 e^{-\sigma_{nm}|\xi|} \tag{17.}$$

with

$$K_{nm}^2 = \sigma_{nm}^2 + i\frac{\omega l_z^2}{D}$$

Define the frequency $\bar{f}$:

$$\bar{f} \equiv \frac{\omega l_z^2}{D} \longrightarrow K_{nm}^2 = \sigma_{nm}^2 + i\bar{f}$$

The total solution of this nonhomogeneous equation is the sum of the solution of the homogeneous equation and a particular solution of the nonhomogeneous one, taking into account the matching condition at $\xi = 0$ and the boundary conditions for $\delta T(\xi)$.

A solution of the nonhomogeneous equation is found as

$$\delta T_{nm}^{nonh.}(\xi) = sign(\xi)\frac{1}{i\bar{f}}\frac{v_0}{\bar{v}}\frac{(-1)^m}{\lambda_m} T_0 e^{-\sigma_{nm}|\xi|} \tag{18.}$$

And for the homogeneous equation yields:

$$\delta T_{mn}^{hom.}(\xi) = \begin{cases} Ae^{-K_{nm}\xi}, \xi > 0 \\ Be^{K_{nm}\xi}, \xi < 0 \end{cases} \tag{19.}$$

with A and B constants to be determined from the matching conditions for δT_{nm} and δT_{nm}' at $\xi = 0$. The matching condition $\lim_{\xi\downarrow 0} \delta T_{nm}(\xi) = \lim_{\xi\uparrow 0} \delta T_{nm}(\xi)$ gives:

$$A - B = -\frac{2(-1)^m}{if\lambda_m}\frac{v_0}{\bar{v}}T_0,$$

and from $\lim_{\xi\downarrow 0} \delta T_{nm}'(\xi) = \lim_{\xi\uparrow 0} \delta T_{nm}'(\xi)$ it is seen that $A = -B$.

For the total solution for δT_{nm}, (there is still one heated wire as heat source, positioned at $x = 0$) one can therefore write

$$\delta T_{nm}(\xi) = sign(\xi)\frac{1}{if}\frac{v_0}{\bar{v}}\frac{(-1)^m}{\lambda_m}T_0(e^{-\sigma_{nm}|\xi|} - e^{-K_{nm}|\xi|}) \tag{20.}$$

If there are now two wires, symmetrically positioned at $\xi = -\xi_1$ and $\xi = \xi_1$, the expression becomes

$$\begin{aligned}\delta T_{nm}(\xi) = {} & sign(\xi - \xi_1)\frac{1}{if}\frac{v_0}{\bar{v}}\frac{(-1)^m}{\lambda_m}T_0(e^{-\sigma_{nm}|\xi-\xi_1|} - e^{-K_{nm}|\xi-\xi_1|}) + \\ & + sign(\xi + \xi_1)\frac{1}{if}\frac{v_0}{\bar{v}}\frac{(-1)^m}{\lambda_m}T_0(e^{-\sigma_{nm}|\xi+\xi_1|} - e^{-K_{nm}|\xi+\xi_1|})\end{aligned} \tag{21.}$$

The temperature difference between the two wires at $\xi = -\xi_1$ and $\xi = \xi_1$ is therefore given by

$$\Delta T_{velocity} = \sum_{n,m=0}^{\infty} \delta T_{nm}(\xi_1) - \delta T_{nm}(-\xi_1) = \sum_{n,m=0}^{\infty} \frac{2}{if}\frac{v_0}{\bar{v}}\frac{(-1)^m}{\lambda_m}T_0(e^{-2\sigma_{nm}\xi_1} - e^{-2K_{nm}\xi_1}) \tag{22.}$$

6.4 The influence of the heat capacity of the wires

When the heat capacities of the two wires cannot be neglected and their finite values has to be taken into account, an additional term will appear in the heat diffusion equation. Eq. (9.) becomes then

$$\partial_t \delta T - D\nabla^2 \delta T = -v\partial_x T + H(z)\frac{(\rho c_p)_{sensor}}{(\rho c_p)_{air}}(F(x-a)\partial_t \delta T + F(x+a)\partial_t \delta T) \tag{23.}$$

with

$$\begin{aligned} & H(z) = 0 \ for \ |z| > \tfrac{h}{2}; \\ & H(z) = 1 \ for \ |z| < \tfrac{h}{2} \end{aligned} \tag{24.}$$

in which h represents the thickness of the wires, and $F(x)$ as defined in Eq.(3.).
For small h, the step function $H(z)$ can be replaced by $h\delta(z)$, so that the equation can be written as, in normalised variables,

$$\begin{aligned}&\nabla^2_{\xi,\zeta}\delta T - i\bar{f}\partial_t \delta T = \\ &\frac{v_0}{\bar{v}}\partial_\xi T - i\delta(\zeta)\bar{f}\frac{h}{l_z}\frac{(\rho c_p)_{sensor}}{(\rho c_p)_{air}}(F(\xi-\xi_1)\delta T + F(\xi+\xi_1)\delta T)\end{aligned} \tag{25.}$$

To replace the ratio $\frac{h}{l_z}\frac{(\rho c_p)_{sensor}}{(\rho c_p)_{air}}$ in the right-hand side of the equation, the following parameter can be introduced:

$$\beta = \frac{h}{l_z}\frac{(\rho c_p)_{sensor}}{(\rho c_p)_{air}} \tag{26.}$$

In normalised variables the wire width is $2\xi_0 \equiv 2L/l_z$. For small wire widths, one can let $\xi_0 \to 0$, and since $\lim_{\xi_0 \downarrow 0} F(\xi-\xi_1) = 2\xi_0\delta(\xi-\xi_1)$, the equation in normalised variables becomes

$$\begin{aligned}&\delta T_{nm}'' - K^2_{nm}\delta T = \\ &\frac{v_0}{\bar{v}}T_{nm}' - 2i\beta\xi_0\bar{f}\left(\sum_{j,k=0}^{\infty}\delta T_{jk}(\xi_1)\delta(\xi-\xi_1) + \sum_{j,k=0}^{\infty}\delta T_{jk}(-\xi_1)\delta(\xi+\xi_1)\right)\end{aligned} \tag{27.}$$

This is a differential equation for δT_{nm}, with in the right hand side the expressions $\sum_{j,k=0}^{\infty}\delta T_{jk}(\xi_1)$ and $\sum_{j,k=0}^{\infty}\delta T_{jk}(-\xi_1)$. These expressions however, are not variables but have just a certain (but still unknown) value. They are therefore written as:

$$\begin{aligned}&\sum_{j,k=0}^{\infty}\delta T_{jk}(\xi_1) \equiv q; \\ &\sum_{j,k=0}^{\infty}\delta T_{jk}(-\xi_1) \equiv -q\end{aligned} \tag{28.}$$

The following equation should therefore be solved

$$\delta T_{nm}'' - K^2_{nm}\delta T_{nm} = \frac{v_0}{\bar{v}}T_{nm}' - 2i\beta\xi_0\bar{f}q\big(\delta(\xi-\xi_1) - \delta(\xi+\xi_1)\big) \tag{29.}$$

which is done by solving first the (inhomogeneous) equation without the terms with the δ-functions , and then using these δ-functions to determine the additional conditions for the derivative δT_{nm}'.

Because of symmetry, we can restrict ourselves to the values $\xi > 0$. In the range $0 < \xi < \xi_1$, the solution of the homogeneous equation reads $\delta T_{nm}(x) = A \sinh(K_{nm}\xi)$, for $\xi > \xi_1$ it is $\delta T_{nm}(x) = B\, e^{-K_{nm}\xi}$, with A and B constants to be determined. For the inhomogeneous equation we try a solution of the form

$$\delta T_{nm}^{\ inhom} = C T_{nm}' \tag{30.}$$

and inserting this form into Eq.(29.), it is seen that the constant C should equal

$$C = -\frac{v_0}{\bar{v}}\frac{1}{i\bar{f}}.$$

So the expression for δT_n becomes

$$\begin{aligned} \delta T_{nm} &= A\sinh K_{nm}\xi - \frac{v_0}{\bar{v}}\frac{T_{nm}'}{i\bar{f}}, \quad 0 < \xi < \xi_1 \\ \delta T_{nm} &= Be^{-K_{nm}\xi} - \frac{v_0}{\bar{v}}\frac{T_{nm}'}{i\bar{f}}, \qquad \xi > \xi_1 \end{aligned} \tag{31.}$$

in which the constants A and B still have to be determined. This can be done using the two requirements for δT_{nm}:

¹) $\delta T_{nm}\big|_{\xi\downarrow\xi_1} = \delta T_{nm}\big|_{\xi\uparrow\xi_1}$, and ²) $\delta T_{nm}'\big|_{\xi\downarrow\xi_1} - \delta T_{nm}'\big|_{\xi\uparrow\xi_1} = -2i\beta\xi_0\bar{f}q$.

The first condition gives:

$$A\sinh K_{nm}\xi_1 - Be^{-K_{nm}\xi_1} = -\frac{v_0}{\bar{v}}\frac{1}{i\bar{f}}(\delta T_{nm}'\big|_{\xi\downarrow\xi_1} - \delta T_{nm}'\big|_{\xi\uparrow\xi_1}) = \frac{v_0}{\bar{v}}\frac{1}{i\bar{f}}\frac{P}{kl_y} \tag{32.}$$

and from the second condition follows:

$$\begin{aligned} &-K_{nm}Be^{-K_{nm}\xi_1} - \frac{v_0}{\bar{v}}\frac{1}{i\bar{f}}\delta T_{nm}''\big|_{\xi\downarrow\xi_1} \\ &-(K_{nm}A\cosh K_{nm}\xi_1 - \frac{v_0}{\bar{v}}\frac{1}{i\bar{f}}\delta T_{nm}''\big|_{\xi\uparrow\xi_1}) = -2i\beta\xi_0\bar{f}q \end{aligned} \tag{33.}$$

If we make the definitions

$$\begin{aligned} &\gamma \equiv 2i\beta\xi_0\bar{f}; \\ &c \equiv \frac{v_0}{\bar{v}}T_0 \end{aligned} \tag{34.}$$

then Eq. (32.) and (33.) can be combined to find A and B:

$$A = (\frac{\gamma q}{K_{nm}} + \frac{c}{i\bar{f}})e^{-K_{nm}\xi_1}; \quad B = \frac{\gamma q}{K_{nm}} \sinh K_{nm}\xi_1 - \frac{c}{i\bar{f}} \cosh K_{nm}\xi_1 \tag{35.}$$

Using these values for A and B in Eq. (31), the value of δT_{nm} in $\xi = \xi_1$ is found as

$$\delta T_{nm}(\xi_1) = (\frac{\gamma q}{K_{nm}} + \frac{c}{i\bar{f}})e^{-K_{nm}\xi_1} \sinh K_{nm}\xi - \frac{v_0}{\bar{v}} \frac{T_{nm}'(\xi_1)}{i\bar{f}} \tag{36.}$$

and since $T_{nm}(\xi) = \frac{(-1)^m}{\lambda_m} \frac{T_0}{\sigma_{nm}} (e^{-\sigma_{nm}|\xi-\xi_1|} + e^{-\sigma_{nm}|\xi+\xi_1|})$ (with T_0 from Eq.(7.)), one can calculate $\lim_{\xi \uparrow \xi_1} T_{nm}'(\xi) = -2\frac{(-1)^m}{\lambda_m} T_0 e^{-\sigma_{nm}\xi_1} \sinh \lambda_{nm}\xi_1$, so that for the value δT_{nm} in $\xi = \xi_1$, which still depends on parameter q, can be written:

$$\begin{aligned} \delta T_{nm}(\xi_1, q) = \frac{c}{i\bar{f}} (e^{-2K_{nm}\xi_1} \sinh K_{nm}\xi_1 - 2\frac{(-1)^m}{\lambda_m} e^{-\sigma_{nm}\xi_1} \sinh \sigma_{nm}\xi_1) + \\ + \frac{\gamma q}{K_{nm}} e^{-K_{nm}\xi_1} \sinh K_{nm}\xi_1 \end{aligned} \tag{37.}$$

With the definition of q,

$$q = \sum_{n,m=0}^{\infty} \delta T_{nm}(\xi_1, q) \tag{28.}$$

now only an equation for q rests, which can be solved.

Solving the equation for q with the expression for $\delta T_{nm}(\xi_1,q)$ gives for q:

$$q = \delta T(\xi_1) = \frac{c}{i\bar{f}} \frac{\sum_{n,m=0}^{\infty} 1 - e^{-2K_{nm}\xi_1} - 2\frac{(-1)^m}{\lambda_m}(1 - e^{-2\sigma_{nm}\xi_1})}{1 - \frac{\gamma}{2} \sum_{n,m=0}^{\infty} \frac{1 - e^{-2K_{nm}\xi_1}}{K_{nm}}} \tag{38.}$$

The summation in the denumerator diverges, due to the infinitely small wire width. If we take here into account the finite width of the wire, by averaging over the width $2\xi_0$, the expression for q becomes

$$q = \frac{c}{i\bar{f}} \frac{\sum_{n,m=0}^{\infty} 1 - e^{-2K_{nm}\xi_1} - 2\frac{(-1)^m}{\lambda_m}(1 - e^{-2\sigma_{nm}\xi_1})}{1 - \frac{\gamma}{2} \sum_{n,m=0}^{\infty} \frac{1}{K_{nm}} (1 - \frac{1}{2K_{nm}\xi_0} e^{-2K_{nm}\xi_1} \sinh 2K_{nm}\xi_0)} \tag{39.}$$

The output signal of the operating Microflown, when it is exposed to acoustic waves or fluid flows, is a voltage. This output voltage results from a resistance difference between the two wires that is caused by the temperature difference between the wires. For small temperature variations, the resistance change of a wire is in good approximation linearly proportional to its temperature change: if the resistance at a certain temperature T_0 is defined as R_0, then the resistance at a temperature T, $R(T)$, is

$$R(T) = R_0(1+\alpha(T-T_0)) \tag{40.}$$

in which α represents the resistance temperature coefficient in K^{-1}.

The temperature difference due to flow between two wires at $\xi = \xi_1$ and $\xi = -\xi_1$, ΔT, is equal to: $\Delta T = \delta T(\xi_1) - \delta T(-\xi_1) = 2\delta T(\xi_1)$. The differential output voltage, which is usually amplified and then measured, is directly related to the resistance variation ΔR of one wire. The voltage source applies a voltage u_0 over both wires in series so that the voltage drop over one heater is $u_0/2$.

The temperature correction at the wire $\delta T(\xi_1)$ is certainly not constant along the wire length. For calculating the corresponding resistance change of the wire, averaging over the wire length would be required, so that the resistance difference between the two wires is

$$\Delta R = 2\alpha R_0 \sum_{n,m=0}^{\infty} \frac{1}{2}\int_{-1}^{1} \delta T_{nm}(\xi_1)\cos\lambda_m \eta d\eta \tag{41.}$$

which is simply

$$\Delta R = 2\alpha R_0 \sum_{n,m=0}^{\infty} \delta T_{nm}(\xi_1)\frac{(-1)^m}{\lambda_m} \tag{42.}$$

with $\delta T(\xi_1)$ from Eq.(39.).

Sometimes, a set-up is used in which only the thermal change of one wire is taken as signal, therefore $\delta T(\xi_1)$. If however both wires are applied and the temperature difference between these two is used, then $\Delta T = \delta T(\xi_1) - \delta T(-\xi_1) = 2\delta T(\xi_1)$, and the measured output voltage is

$$\delta u = \frac{u_0}{2}\frac{\Delta R}{R_{op.temp}} = \frac{u_0 \alpha R_0}{R_{op.temp}} \sum_{n,m=0}^{\infty} \delta T_{nm}(\xi_1)\frac{(-1)^m}{\lambda_m} \tag{43.}$$

with $R_{op\ temp}$ the resistance of one wire at the operating temperature, and $\delta T_{nm}(\xi_1)$ from Eq.(39.).

6.5 Geometrical optimisation

6.5.1 Analysis of the output signal

In acoustic calibration measurements, this δu (Eq.(43.)) as a function of frequency, $\delta u(\omega)$, is measured. As we have already seen in the third chapter, the function can be characterised by its two main properties when plotted double logarithmically: the low-frequency absolute value, i.e. the intersection with the vertical axis, and a characteristic frequency determining where the function falls off. Both the low-frequency sensitivity and the corner frequency should be as high as possible. Therefore, our purpose is to optimise the expression (43.).

From a dimensional analysis on the dependence of δu on the different parameters, using the Buckingham Pi Theorem [2], follows that δu can be written as a function of mutually independent variables. Since many independent parameters like α and R_0, can be considered as constants, on which the dependence of δu is trivial, we can analyse the behaviour of δu as a function of dimensionless parameters. These dimensionless parameters are the normalised frequency $f/(D/2\pi l_z^2)$, and the geometrical variables a/l_z and l_z/l_y. Additionally, the ratio P/l_y, the power per unit length, is an important scale factor.

To investigate the behaviour as a function of l_z, l_y, and a for very low frequencies or frequency zero, we can let $f \downarrow 0$ and calculate $\lim_{f\downarrow 0} \delta u(a, a/l_z, P/l_y)$. Note that K_{nm} in the expression for $\delta T_{nm}(\xi_1)$ in Eq. (43.) is a function of f. Moreover, writing δu as a function of these variables allows an investigation of the behaviour for $l_z \to \infty$. This is of great importance since many of the current devices do not have a channel surface acting as heat sink above the wires, but only free space.

All the factors that do not depend on geometrical parameters are taken together and we introduce $C_0 = \dfrac{\alpha R_0 u_0 v_0}{R_{op.temp} k}$.

$$\lim_{f\downarrow 0} \delta u = C_0 a \frac{P}{l_y} \Phi(\frac{a}{l_z}) \qquad (44.)$$

The explicit form of Φ can be determined from evaluation of the expression (43.), in which $\delta T_{nm}(\xi_1)$ is found from Eq.(37.), with substituted in it q from Eq.(39.). The scaled variables ξ_1 and $\bar{f}$ now have to be written in the original dimensions. For convenience of the reader the final summation is not shown here explicitly, and this last step of the approach is only mentioned.

It is noted that both the parameters a and a/l_z appear in Eq.(44.); one can also make a different choice for the set of mutually independent variables, with P/l_y and the combination a/l_y and l_z/l_y.

Apart from the optimisation of the (low-frequency) output signal δu, it is important to consider the 'signal-to-noise' (*S/N*) ratio of the output. This signal to noise ratio is the actual quantity to be maximised. This is achieved by increasing δu and simultaneously lowering the noise, in particular the resistance noise. For this Johnson or Nyquist noise [3, 4] the voltage fluctuations of a resistor R at absolute temperature T in a frequency interval Δf obey

$$\langle V_{noise}^2 \rangle_{(f, f+\Delta f)} = (4kTR)\Delta f \qquad (45.)$$

with k the Boltzmann constant. Since the wire resistance of the sensor is also temperature dependent (Eq.(40.)), noise increases with the wire temperature.

First we concentrate on the optimisation of the low frequency sensitivity $\lim_{f\downarrow 0} \delta u$, or $S(f=0)$ (in V per m/s particle velocity), and of the frequency behaviour of the sensitivity function, in the next section attention is paid to the aspects of (resistance) noise as well.

6.5.2 The low-frequency sensitivity

Using a mathematic software program, a script that calculates explicitly expression (43.), with the various parameters (such as the wire length l_y, the mutual distance a, the etch depth l_z, the power and the wire resistance) as input variables, was written. Considering the relevant mutually independent variables in expression (44.), we varied subsequently a/l_z, P/l_y and l_z/l_y. In this approach other

parameters as D, α and u_0 that appear in the factor C_0 in front of the expression (44.) are not taken into account, since these are not geometry dependent and δu is simply proportional to C_0. In the calculations, the lengths l_z and l_y are characteristic values; the script evaluated explicitly the temperature and its correction as expansions in harmonics (as in Eqs. (6.), (15.) with eigenfunctions in two dimensions, y and z) with the boundary conditions that T and δT are zero at $z = l_z$ and $y = l_y$.

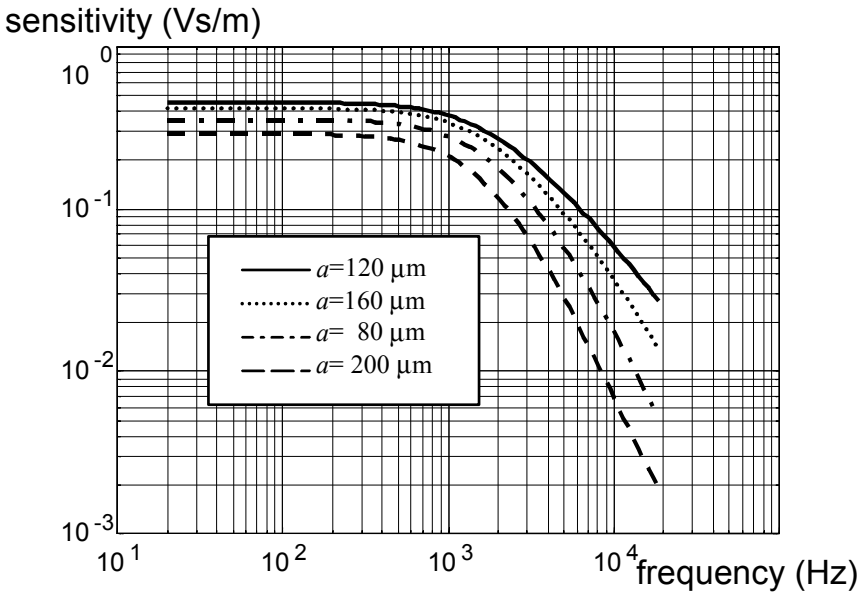

Figure 6-2: Numerically calculated sensitivity according to the model, for varying mutual wire distance a. The etch depth is l_z=200 µm; wire length l_y=500 µm, P =45 mW and R_0=2.0 kΩ.

Keeping the power per unit length, P/l_y constant, the sensitivity as a function of frequency was calculated. Some of these calculated sensitivity curves are plotted in figure 6-2. This figure shows some representative functions for different parameters. The output signal is expressed in V per m/s particle velocity. For given etch depth l_z, it is seen that there is an optimum value for a, for which the low-frequency sensitivity $S_{f=0}$, the intersection of the curve with the vertical axis, is maximal. Besides, the value of a determines the first characteristic frequency. As we have seen in chapter 3 this characteristic frequency equals for very large l_z, when the wires can be considered to be in free space, $f_D = D/2\pi a^2$.

To find the value of the ratio a/l_z for which $S_{f=0}$ is maximal, the expression for δu, Eq.(44), should be optimised for a/l_z. It can be seen that this value is independent of l_y, and the optimal ratio was calculated to be approximately $(a/l_z)_{opt} \approx 0.3$. In figure 6-3 the calculated low-frequency sensitivity as a function of this quotient a/l_z is plotted. From the figure it is concluded that for given l_z, an optimum value for a exists, but we see from the calculations that for given a, the sensitivity $S(f = 0)$ monotonously increases with l_z up to $l_z=l_y$.

So, the influence of the ratio l_z/l_y on the low frequency sensitivity was investigated. As one sees from the curve in figure 6-4, for ratios l_z/l_y above approximately 0.6, the sensitivity does not increase significantly.

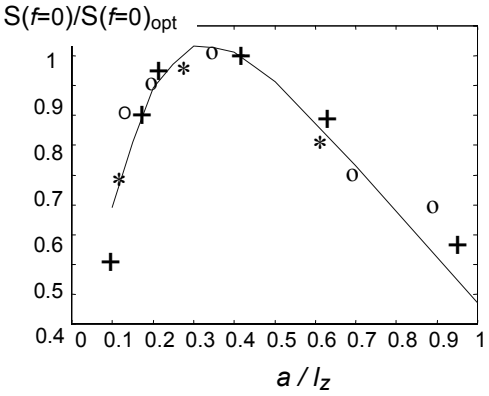

Figure 6-3: Numerically calculated low-frequency sensitivity S(f=0) as a function of the ratio a/l_z (dotted line). The crosses denote experimental results, from device geometries with etch depths l_z=240 μm (+), l_z=300 μm (∗), and l_z=500 μm (o). The vertical scale has been normalised to the optimum value of S(f=0).

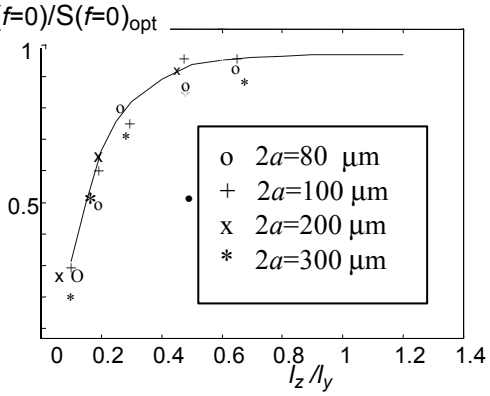

Figure 6-4: Numerically calculated sensitivity S(f=0) as a function of the ratio l_z/l_y (dotted line). The marks indicate experimentally obtained results from devices with l_y=500 μm, l_z=40, 80, 120, 240 or 300 mm, and a=80, 100, 200 or 300 μm. The vertical scale has been normalised to the value of S(f=0) at $l_z=l_y$.

6.5.3 The frequency dependence of the sensitivity

As we know from chapter 3, the mutual wire distance a is directly of influence on the characteristic frequency of the sensitivity curve $S(f)$. A decrease of a increases the bandwidth of this function. The result of a series of measurements (as described in the following section) on a number of sensors with l_z = 240 μm and varying a, is shown in figure 6-5. The experimentally determined sensitivity

curves were approximated by a second order low pass frequency response. The lowest corner frequency f_c of this function is proportional to the thermal diffusion frequency f_D as introduced in chapter 3 and is a characteristic frequency for $S(f)$. It is plotted as a function of a in figure 6-5, on a double logarithmic scale. For the thermal frequency of a sensor with wires in free space, the original analytic model predicted the relationship $f_c \propto a^{-2}$, which is represented by the line.

The experimentally determined corner frequencies have rather large error bars, because the experimentally determined sensitivity functions are approximated by a fit function that is a second order frequency response and thus just an approximation. Besides the fitting is subject to impreciseness. For the corner frequency of the second function, a value of 3 kHz was taken, corresponding to the calculated number for the used wire geometry. This value was not varied.

The line thus represents the analytic model for wires in free space, while the experimental results refer to devices with a channel surface below acting as heat sink. Nevertheless, the behaviour of $f_c \propto a^{-2}$ appears for these sensors. The influence of the channel bottom on the frequency behaviour appears to be small.

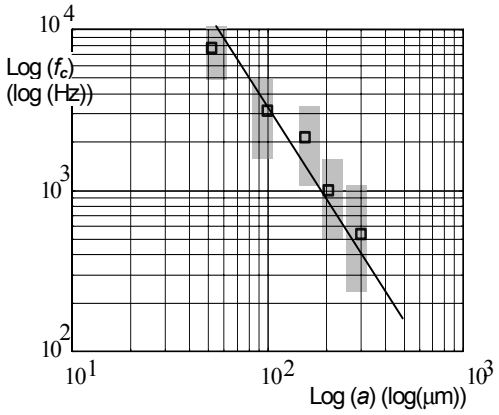

Figure 6-5: Characteristic frequency f_c as a function of the distance between the wires. The acoustically obtained sensitivities were fitted by a second order frequency response with lowest corner frequency f_c. The axes are plotted logarithmically; the line shows the theoretical dependence $f_c \propto a^{-2}$

6.5.4 Comparison to experimental characterisations

To compare the theoretically and the numerically obtained results to the sensitivity curve of the sensor for different geometries, several devices with varying etch depths, mutual wire distances and wire lengths were designed. Since the power to

be dissipated could be varied as well by adjusting the voltage of the wires, many different combinations became possible.

The etch depth l_z of the two-wire sensors was chosen to be 40, 80, 120, 240 and 300 μm, the length l_y was 500 and 1000 mm, while the mutual wire distance varied in the range 50, 80, 100, 200 and 300 μm.

The different sensors were characterised in a standing wave tube with a reference microphone in it, as described in chapter 4. From the thus obtained sensitivity curves the low-frequency sensitivity, the output for $f \rightarrow 0$ in V/Pa or in Vs/m, was determined. We know already that the sensitivity function is characterised by three main parameters: its low-frequency value $S_{f=0}$, a characteristic frequency f_c , and a corner frequency related to the heat capacity of the wires. With the current model calculations we concentrate on the first two. The heat capacity of the wires was not explicitly varied, and the calculated value of the corresponding corner frequency as followed from the analytic model (3 kHz), was taken as a constant in the fitting curves.

First, the low frequency output $S_{f=0}$ of the two-wire sensors is considered, as a function dependent on the mutual wire distance and etch depth. All devices with combinations of a and l_z were calibrated in the standing wave tube. The summary of these results led to the measurement points indicated in the figures 6-3 and 6-4.

In figure 6-3, the low-frequency sensitivity versus the ratio of a and l_z is plotted for a series of measurements with l_z=240 μm and a wire length l_y= 500 μm. For comparison to the model curve, also shown in the figure, the curves are normalised by division through their optimum value $S_{f=0,opt}$. The increase of $S_{f=0}$ with l_z for all a, at constant power P = 55 mW, is seen in figure 6-4.

In figure 6-5 the results of the variation of the wire separation a were already shown, which confirmed the increase of the bandwidth with the decrease of a.

From these results and the figures 6-3 and 6-4, it is concluded that the low-frequency sensitivity has an optimum for a ratio of a and l_z as $a \approx 0.3\ l_z$. Since the signal also increases with l_z, up to $l_y = l_z$, the etch depth l_z should be chosen as $l_z / l_y \approx 0.5$ to 1. With respect to the characteristic frequency however, a should be chosen as small as possible to obtain a broad frequency bandwidth.

6.6 The three-wire configuration

6.6.1 The concept

As stated above, the most relevant quantity to maximise is the so-called is the so-called signal to noise ratio, the quotient *S/N*, with *N* the noise voltage $N = \sqrt{< V_{noise}^2 >}$ in the sensing wires. As a first approximation for this noise voltage, it is assumed that the noise of the heated wires is mainly determined by the Johnson noise level associated with the wire resistance *R*, Eq.(45). We will see in later chapters that this is a justified assumption for frequencies above 300 or 400 Hz. Other sources of noise, in particular low frequency noise with 1/*f* shaped spectral densities, '1/*f* or flicker noise', that are ubiquitous in many systems like thin metal films, metal (-oxide) layers, wires and resistors, and about which much research has been done [e.g. 5-10], are initially not taken into account, although they are certainly manifest in the Microflown situation. Especially for frequencies above approximately 300 Hz, the main contribution to the random voltage fluctuations in the sensor is the Johnson noise, $<V^2_{noise}>_{(f,f+\Delta f)} = (4kTR)\Delta f$. Since the noise is thus temperature dependent, and depends on *R*, which is itself a function of temperature too according to Eq.(40.), an increasing power in a wire leads to an increasing noise voltage. With respect to the noise, a relatively low temperature in the sensing wires is therefore favourable. The signal, however, increases with the total dissipated power. Therefore a new configuration for the Microflown is introduced, based on a separation of the heating and sensing functionality: a three-wire configuration. It consists of three wires, of which the central wire acts as heater and the two outer wires have a sensing function. Most power can be dissipated in the central wire, while the sensing wires have a relatively low temperature (and thus a relatively low noise level). Moreover, the heating wire can be designed such that much power in it can be dissipated, as will be seen its heat capacity is of minor importance.

This concept can simply be implemented in the present model. If we take as a starting point Eq. (20.),

$$\delta T_n(\xi) = sign(\xi)\frac{1}{i\bar{f}}\frac{v_0}{\bar{v}}\frac{\pi}{2}T_0(e^{-\lambda_n|\xi|} - e^{-K_n|\xi|}) \qquad (46.)$$

that expresses the temperature correction at place ξ, due to a wire at $\xi = 0$ heated by a power P/l_y, a generalisation to a configuration of the flow sensor composed of more than two wires is possible. We consider in particular the situation of three wires, located at $\xi = -\xi_1$, $\xi = 0$ and $\xi = \xi_1$. For simplicity the wire at $\xi = 0$ is called heating wire ('H'), the other wires are called sensing wires ('S') (of course all wires are heated and sense too).

Using this expression (20.), the temperature correction at a wire S_1 at $\xi = -\xi_1$, due to a wire H at $\xi = 0$ that is heated by a power P_H, and due to the other wire S_2 at $\xi = \xi_1$ heated by a power P_S, can be calculated. (S_2 is now at a distance $2\xi_1$ from wire S_1) Thus, the temperature difference between wire S_1 and S_2, and therefore the output voltage δu, is found. Since this output signal now depends on both powers P_H and P_S, the ratio between these powers can be varied to find the optimum sensitivity.

Considering thus the low-frequency sensitivity as a function of the relative heater power ($r \equiv P_H/(P_H+2P_S)$), the dashed curve shown in figure 6-6 is found, and it is seen that it has an optimum at approximately $r = 0.8$.

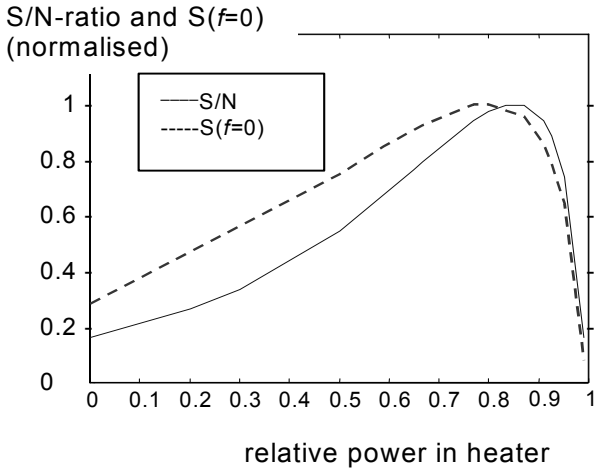

Figure 6-6: Low-frequency sensitivity $S_{f=0}$ as a function of relative heater power $r = P_H/(P_H+2P_S)$, (dotted line) and the signal to noise ratio $S_{f=0}/N$, with N the Nyquist noise level (drawn line).

With respect to the signal-to-noise ratio, defined as the low-frequency sensitivity divided by the noise level due to Nyquist noise, an even higher ratio r is favourable. The curve that shows $S_{f=0}/N$ as a function of the relative heater power r is depicted as the drawn line in figure 6-6. It is seen to have its optimum at $r \approx 0.85$.

For a matter of fact, in the three-wire configuration with a distance between S and H of $a/2$ the characteristic frequency is mainly determined by this distance $a/2$, while in the corresponding situation in the two-wire sensor the characteristic frequency is determined by the separation between the sensing wires, a. Therefore the frequency bandwidth is also increased by the heated wire placed between the two sensing wires. The frequency dependence of a three-wire device of separation a between the sensing wires thus greatly corresponds to that of a two-wire Microflown with wire distance $a/2$.

6.6.2 Experimental characterisation of the three-wire device

Since the output signal increases with the power per unit length, see Eq.(43.), a high power dissipation in the wires is favourable. However, if too much power is dissipated, the wire cannot stand the high temperature. Usually the temperature of the sensing wire, that is designed to be thin, should not increase approximately 650 K. It is found experimentally that the maximum power per unit wire length is about 30 W/m. An advantage of the three-wire configuration is that the heater can be designed such that it can stand a high temperature, currently about 800 K; this wire can be made thick since its heat capacity does not influence the sensitivity function.

To investigate the three-wire configuration, three ‘SHS’-type Microflowns were designed, with wire length 1.5 mm and a distance between the two sensor wires of 100, 200, and 300 μm. The etch depth was 100 μm; $R_{S1} = R_{S2} = 3.47$ kΩ, $R_H = 260$ Ω. The heater voltage was adjusted from 0 to 6 V so that the heater power P_H was equal to subsequently 0, 10, 20, 32, 44, and 58 mW. For each value of P_H, the power in the sensors was varied in six steps from 2 to 21 mW. For each combination, the sensitivity and the signal-to-noise ratio of the three devices were experimentally determined in the standing wave tube. The results are summarized

in figures 6-7 and 6-8. In figure 6-7 results are shown for experiments with several power ratios, calculated for the situations $P_{total} = P_H + 2P_S = 30$ mW and $P_{total} = 21$ mW. These points are compared to the theoretical curve (dotted line). Figure 6-8 shows the thus obtained low frequency sensitivity as a function of the sensor power P_S, with the heater power P_H as a parameter.

Considering the above results, in the first place it can be concluded that the use of the SHS-configuration leads to an improvement of the low-frequency sensitivity at a given total power.

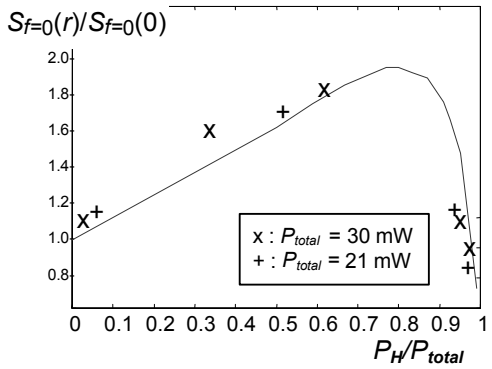

Figure 6-7: Low-frequency sensitivity S(f=0) as a function of relative heater power $r=P_H/(P_H+2P_S)$, (line) according to model calculations, and the experimentally obtained points for $P_{total}=P_H+2P_S$= 21 mW resp. 30 mW.

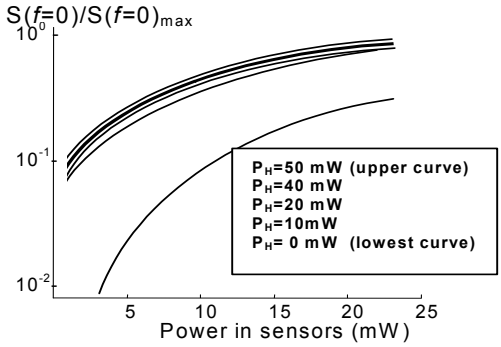

Figure 6-8: Low-frequency sensitivity S(f=0) as a function of power in de sensors, $2P_S$, with the heater power P_H as a parameter, from model calculations. P_H=0 mW (lowest curve); 10 mW; 20 mW; 30 mW; 40 mW; and 50 mW (upper curve).

From figure 6-7 we see that the optimum power ratio $r \approx 0.85$ in the three-wire sensor yields an approximately two times higher low frequency sensitivity than the ratio $r = 0$, which actually represents the two-wire situation. The improvement of the sensitivity in a broad frequency range at this ratio is illustrated by the lowest curve in figure 6-9; the upper curve with $r = 0$ represents the two-wire situation.

6.6.3 An optimally performing device

Comparing the figures 6-3, 6-4 and 6-5, one sees that the requirement of a high low-frequency sensitivity and a high characteristic frequency (large bandwidth)

may lead to conflicting conditions for the wire separation a: for a large bandwidth a should be as small as possible, but if a is very small, the low-frequency sensitivity decreases. As a good compromise, usually a should be chosen relatively small (~100 μm), still without negative consequences for the low-frequency sensitivity, and when the power is set to be more than ~ 50 mW, a satisfying low-frequency sensitivity is measured.

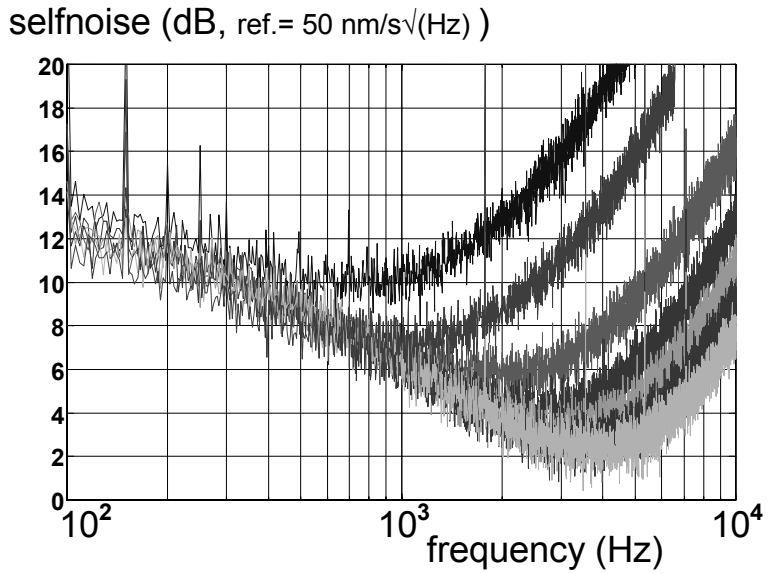

Figure 6-9: Selfnoise levels of the three-wire sensor, for a sensor power P_{S2}+P_{S1}=11.5 mW, and a heater power of resp. P_H=0 mW (upper curve), 5, 10, 20, 32, 44 and 58 mW (lowest curve). R_H=7.90 kΩ, R_{S1}=R_{S2}=256 Ω at room temperature, a=100 μm, l_z=200 μm.

To obtain thus a high characteristic frequency and an optimal signal-to-noise ratio, a good sensor device should have a three-wire configuration with a distance $a \approx$ 100 μm, a large etch depth (preferably about 300 μm, so that $a/l_z \approx 0.3$) and a relative heater power of 0.85.

We designed a rather good performing device from three wires, with R_H = 256 Ω and $R_{S1} = R_{S2}$ = 3.9 kΩ at T = 293 K, a = 50 μm, l_z = 200 μm and P_H = 58.2 mW, $P_{S2} + P_{S1}$ = 11.5 mW. The temperature of the heater, at this power dissipation, reaches approximately 780 K, the sensor wire temperature is 327 K.

The heater power can be relatively large, it is limited by the maximum temperature the heater can stand.

We found a low-frequency sensitivity of 0.57 V/(m/s), a sensitivity at 1 kHz of 0.54 V/(m/s), and an estimated corner frequency of 4.3 kHz. For the estimation of this frequency the approximation procedure as described in section 6.5.2 was applied.

The sensitivity of the sensor together with its noise level leads to the signal-to-noise ratio *S/N*, with *S* in V/(m/s) and *N* in V/√Hz. The inverse, *N/S*, represents the sometimes used quantity 'selfnoise' in m/(s√Hz). It corresponds to a noise level that can be expressed in an equivalent particle velocity. The selfnoise of the described device is seen in figure 6-9. This figure shows the selfnoise levels (in dB with respect to a reference level of 50 nm/(s√Hz)) of the device, for a sensor power $P_{S2} + P_{S1} = 11.5$ mW, and a heater power of respectively $P_H = 0$ mW (the upper curve), 5, 10, 20, 32, 44 and 58 mW (lowest curve).

In the frequency bandwidth of 1 to 4 kHz, an important audible range, the selfnoise is seen to be $6 \cdot 10^{-8}$ to $2 \cdot 10^{-7}$ m/(s√Hz).

6.7 Conclusions

Starting from principal physical equations, the wire temperature and the response signal due to (acoustic or fluid) flow of the thermal flow sensor have been calculated. Since these are expressed as an infinite double series, a good numerical investigation of the sensor behaviour is possible, for varying geometries. Besides this approach allowed to take into account the finite etch depth, contrary to the analytic model of chapter 3 that describes the wires in free space. It is found that for given wire length l_y, the sensitivity increases with etch depth l_z (the depth of the channel), up to $l_z \approx l_y$. The optimum mutual wire distance a at a given l_z, is found to be about $a \approx 0.3\ l_z$. However, to obtain a broadband, flat, frequency response, a has to be chosen as small as possible. Both requirements for a cannot be fully satisfied simultaneously, but a good two-wire device can be made if $a \approx$ 60 μm at a wire length of 500 μm and an etch depth of 200 μm. (A smaller wire length leads to corresponding lower values of a and l_z, but since the total power then also decreases, the sensitivity will decrease). Next it was seen that for l_z larger

than or about as large as l_y, the influence of the channel surfaces acting as heat sink on the sensitivity is negligible.

These dependences of the sensitivity on device geometry, and the dependence on the power, have all been experimentally verified. We found a good correspondence between model and experiment.

Since the signal-to-noise ratio increases with the dissipated power, the power should be as high as possible. The power per unit length is limited by the maximum temperature the thin sensor wire can stand, approximately 650 K.

A significantly better performing device is made of three instead of two wires. The relatively thick central wire, the heater, is heated up to ~780 K, while the other two wires, acting as sensing wires, are relatively cold. The sensor wires thus have a much lower noise level, while the output signal is proportional to the total dissipated power.

This three-wire device, with a relative heater power of 0.85, has a two times higher sensitivity than a two wire sensor of the same dimensions and power. The optimal geometry is found to be near l_y=1 mm, l_z=300 μm, heater-sensor distance a=50 μm and P_{total}
=70 mW. In the frequency bandwidth of 1 to 4 kHz, the selfnoise of this device is about $3 \cdot 10^{-5}$ to $8 \cdot 10^{-5}$ Pa/√Hz.

6.8 References

1 V.B. Svetovoy, I.A. Winter, Model of the μ-flown microphone, Yaroslavl State University, *Sensors and Actuators* A 86 (2000), 171-181.

2 R.W. Fox, A.T. McDonald, 'Introduction to fluid mechanics', 3rd ed., (1985), ISBN 0471821063.

3 R.K. Pathria, 'Statistical Mechanics', University of Waterloo, Canada, (1986).

4 A. van der Ziel, 'Noise', Prentice Hall Electrical Engineering Series, the Netherlands.

5 P. Dutta, P.M. Horn, *Review of Modern Physics*, Vol.53, 3 (1981).

6 G. Grinstein, T. Hwa, H.J. Jensen, *Physical Review A*, Vol.45, 2 (1992).

7 S.H. Liu, *Physical Review B*, Vol.16, 10 (1977).

8 J.H. Scofield, J.V. Mantese, W.W. Webb, *Physical Review B*, Vol.32, 2 (1985).

9 E. Milotti, *Physical Review E*, Vol.51, 4 (1995).

10 M.B. Weissman, *Review of Modern Physics*, Vol.60, 2 (1988).

11 Howe, M.S., 'Acoustics of Fluid –Structure Interactions', New York, NY; Cambridge, UK, Cambridge University Press (1998).

12 Pierce, A.D., 'Acoustics: An Introduction to its Physical Principles and Applications', Woodbury, NY, Acoustical Society of America (1989).

Chapter 7

Noise reduction by means of a cross correlation technique

Abstract

In this chapter a method is presented to reduce the noise level of the particle velocity sensor in certain types of measurements. This method is based on the utilisation of cross-correlation spectra instead of auto-correlation spectra of two of these sensors. The time averaged cross correlation signal of two uncorrelated noise sources is theoretically zero and this principle is used in the measurement of the cross spectrum of two sensors. The larger the measuring time and therefore the number of data points stored, the smaller the variance of the noise power in the cross spectrum. The theoretical dependence of the variance in the power of the cross spectrum on the number of stored data points is compared to theory, for various situations. Dependent on the number of data points used, noise reductions as high as 30 dB have been attained. The noise in the measurements can thus become even considerably lower than the principal resistance noise level (Johnson noise) of the wires. With the described method the signal-to-noise ratio can therefore significantly be increased.

7.1 Introduction

Since the sensor under investigation in the preceding chapters is based on the principle of measuring the acoustic particle velocity instead of pressure, and therefore measures an essentially different physical quantity than conventional microphones do, its performance cannot simply be compared to these pressure sensors. However, for acoustic measurements, particularly for the higher frequencies, the particle velocity sensor is not always favourable due to the decrease of its sensitivity above the two corner frequencies (higher than a few kHz) and its relatively high noise level. A disadvantage of the present sensor is therefore its relatively low signal-to-noise ratio at frequencies above approximately 3 kHz. In this chapter it is endeavoured to reduce the noise level of the sensor, in the entire acoustic frequency spectrum.

One particular application of the particle velocity sensor is the measurement of stationary acoustic signals and stationary sound intensity measurements. Since these signals have the property that their time dependence is well defined, they can be well distinguished from the random and uncorrelated noise signals. The approach to be followed is thus based on the simultaneous use of two nearly identical sensors that each measure the same acoustic signal. The noise both signals are subject to, is mutually uncorrelated. While summing the signals of the two similar sensors, the two uncorrelated noise contributions are reduced by averaging.

7.2 Features of noise sources

So far, with most of the physical descriptions and modelling of the Microflown we concentrated on the frequency characteristics and the sensitivity of the sensor. Purpose in the analysis was, besides the understanding of the behaviour of the sensor, the optimisation of the sensitivity. However, a more relevant parameter than the sensitivity only, is the signal-to-noise (S/N) ratio of a particle velocity sensor.

Since all hot-wire particle velocity sensors consist fundamentally of two or more electronically heated resistors, an inevitable origin of noise is formed by the so-

called resistance noise, which forms thus a theoretical minimum of the noise from one wire. For a resistance R at absolute temperature T, the average voltage variations in a frequency interval Δf are given by the Nyquist formula

$$\langle V_{noise}^2 \rangle_{(f,f+\Delta f)} = (4kTR)\Delta f \qquad (1.)$$

with k the Boltzmann-constant and where the brackets <> denote the averaging over all possible states of the system, which is in our situation equal to the time average ([1]).

It is observed that the noise manifest in the sensor's output signal is, especially for low frequencies, often higher than this Nyquist noise level.

Several explanations for the additional noise can be proposed; it may have an electronic, thermal, (thermo-) acoustic or mechanical origin or a combination of these. One hypothesis describes the noise as originating from 'thermal agitation noise' due to the 'Brownian motion' ([1, 2]) of air molecules or particles of nanometer size present in the air. Next, resistance inhomogeneities or local impurities in the sputtered wire with the corresponding voltage and resistivity oscillations are likely to play a role as well. Apart from any acoustic noise or noisy signals related to the gas or flow, the metal films show low-frequency $1/f$ or flicker noise, which has already been observed very often for thin films [3-8]. These low-frequency fluctuations in thin films and metals show power spectra of the form $1/f^{\alpha}$, with $0.5 < \alpha < 1.5$ and cover a wide range of phenomena about which a lot of studies in literature have been published.

It is not the purpose of this chapter to give an adequate explanation of the precise origin of the measured noise, a more rigorous analysis of these problems is described in the following chapter. Instead, the following method is introduced to reduce significantly the undesirable voltage fluctuations in the output signal of the sensor. The measurement method that will be described now is based on the fact that intrinsic noise sources at two different sensors are mutually uncorrelated (see also [9]). By application of the cross correlation spectrum of the sensors, this noise power can, for long-time averaging, be eliminated.

7.3 Correlation functions of stochastic signals

The noise occurring in the acoustic measurements manifests itself in the form of small, stochastic voltage fluctuations in the output signal of the sensor. The mean value μ of these voltage fluctuations $v(t)$ is given by

$$\mu = E\{v(t)\} =< v(t) >= 0 \tag{2.}$$

where $E\{x(t)\} = \lim_{T\to\infty} \frac{1}{T}\int_0^T x(t)dt$ represents the expectation value of a stationary stochastic time function *x(t)*. With the definition of the corresponding autocorrelation function as

$$\phi_{vv}(\tau) = E\{v(t)v(t+\tau)\} = \lim_{T\to\infty} \frac{1}{T}\int_{-T/2}^{T/2} v(t)v(t+\tau)dt \tag{3.}$$

one sees that the dimension of $\phi_{vv}(t)$ is V^2, so that it can be interpreted as an averaged power P in a 1Ω resistance, in particular $\phi_{vv}(0)=E\{v^2(t)\}=P_{average}=<v^2(t)>$ [1]. For convenience, the quantity V^2 related to the different correlation functions, is in this chapter referred to as 'power', although formally it is power per unit resistance.

The Fourier transform of the autocorrelation function, $\Phi_{vv}(\omega) \equiv F(\phi_{vv}(\tau))$, represents the power density spectrum and shows how the power of the stochastic signal is distributed over the frequency domain. Furthermore, we can define a cross correlation function $\phi_{v_1v_2}(\tau)$, which function indicates the mutual correlation between two signals $v_1(t)$ and $v_2(t)$ [2, 10]. If $v_1(t)$ and $v_2(t)$ are two statistically independent variables, and if one of or both of the signals have expectation value zero (i.e. there is no DC-component), then [11]

$$\begin{aligned}\phi_{v_1v_2}(\tau) &= E\{v_1(t)v_2(t+\tau)\} = E\{v_1(t)\}E\{v_2(t+\tau)\} = \\ &= E\{v_1(t)\}E\{v_2(t)\} = 0\end{aligned} \tag{4.}$$

The autocorrelation function of the sum of two signals $v(t) = v_1(t) + v_2(t)$ follows from

$$\begin{aligned}\phi_{vv}(\tau) &= \lim_{T\to\infty} \int_{-T/2}^{T/2} \{v_1(t)+v_2(t)\}\{v_1(t+\tau)+v_2(t+\tau)\}dt = \\ &= \phi_{v_1v_1}(\tau) + \phi_{v_1v_2}(\tau) + \phi_{v_2v_1}(\tau) + \phi_{v_2v_2}(\tau)\end{aligned} \tag{5.}$$

If $v_1(t)$ and $v_2(t)$ are statistically independent, $\phi_{v_1v_2}(\tau)=\phi_{v_2v_1}(\tau)=0$, so that $\phi_{v\,v}(\tau)=\phi_{v_1v_1}(\tau)+\phi_{v_2v_2}(\tau)$, and therefore for the Fourier transforms yields analogously: $\Phi_{vv}(\omega)=\Phi_{v_1v_1}(\omega)+\Phi_{v_2v_2}(\omega)$.

In measurement techniques, the statistical independence of different noise sources in the cross correlation functions can be applied to reduce the noise [9, 12, 13].

The output signal of the particle velocity sensor is proportional to the vector product $\vec{v}\cdot\vec{n}$, with $\vec{v}$ the local particle velocity and $\vec{n}$ the unit vector in the plane of, and perpendicular to the length of the wires. If now two similar sensors are placed parallel and closely to each other and if the distances between both wires of a sensor and between two different sensors are small compared to the acoustic wavelength, then both output signals are highly correlated. On the other hand, it seems justified to assume that both intrinsic noise sources of the probes, are totally uncorrelated. These noise sources are partially determined by the resistance noise of the resistors, which are independent. If furthermore both sensors are independently powered, the noise associated with the electrical powering should be uncorrelated as well. Other noise sources that occur in the noise spectrum of a particle velocity sensor, that manifest themselves particularly in the low-frequency region, may, depending on their origin, cause either correlated or uncorrelated noisy signals. Of course, acoustic noise will have correlated influences on both acoustic sensors. Strictly spoken, noisy acoustic fluctuations form also a signal to be measured, but since we are interested in stationary, time-independent, signals, these contributions can be distinguished as noise. Besides, electrical interferences (for example frequency components of the electrical powering) may cause correlated disturbances.

Assume that a certain particle velocity leads to an output signal $v_1(t)$ of particle velocity sensor 1, that is contaminated by noise of the form $n_1(t)$. Sensor 2, located closely to the first sensor, then gives an output signal $v_2(t)$, with additional noise $n_2(t)$. Further it is presumed that the original signals $v_i(t)$ contain no 'DC' terms, i.e. $< v_i(t)> = 0$. The cross correlation of $x_1(t) = v_1(t) + n_1(t)$ and $x_2(t) = v_2(t) + n_2(t)$ thus becomes

$$\phi_{x_1x_2}(\tau) = \lim_{T\to\infty} \int_{-T/2}^{T/2} \{v_1(t) + n_1(t)\}\,\{v_2(t+\tau) + n_2(t+\tau)\}dt =$$
$$= \phi_{v_1v_2}(\tau) + \phi_{v_1n_2}(\tau) + \phi_{v_2n_1}(\tau) + \phi_{n_1n_2}(\tau) = \qquad (6.)$$
$$= \phi_{v_1v_2}(\tau)$$

The last step in Eq. (6) follows from the fact that the noise of sensor 1 and that of 2 have no mutual correlation (assuming for a moment there are no acoustic but only electrical or thermal noise sources) and are uncorrelated to the signals as well.

Therefore, the power spectrum of the measured output signals $x_1(t)$ and $x_2(t)$, that are contaminated by uncorrelated noise, is found from this cross correlation;

$$\Phi_{x_1x_2}(\omega) = \Phi_{v_1v_2}(\omega) \qquad (7.)$$

and if both sensors have the same sensitivity (i.e. same proportionality between particle velocity and output voltage),

$$\left|\Phi_{x_1x_2}(\omega)\right| = \Phi_{v_1v_1}(\omega) \qquad (8.)$$

in which noise is not present anymore.

According to this theory, the application of cross spectra leads ideally to a complete removal of the noise spectrum. The two noise sources in the respective signals are assumed to be uncorrelated, so that, the larger the measuring time and therefore the number of data points stored, the more the calculated cross correlation spectrum of the noise can be reduced ([11, 13]).

The mean value of this cross spectrum is zero, but since the integration time is finite, a more relevant parameter to characterise this quantity is its variance, σ^2 The larger the number of points in the time series of the signals, the smaller this variance. Using the Lindeberg-Lévy Theorem, or Central Limit Theorem [11], we illustrate this with the following.

Assume that in the calculation of the auto correlation spectrum and the cross correlation spectrum, a time signal consisting of a series of N data points is used. To get some insight into the behaviour of the calculated quotient of power in cross spectrum and power in auto spectrum as a function of N, the two time signals are simplified to two uncorrelated arbitrary binary series of N points. They are modelled by two time series of which each data point represents a 1 or a –1, similar to the throwing of a coin. Define therefore these series as p_i and q_i ,

consisting only of values 1 and –1. (So p_1, p_2, p_3,..= -1, -1, 1,…) The total power in the autospectrum of the first signal will therefore be proportional to

$$\sum_{i=1}^{N} p_i^2 = N\,, \tag{9.}$$

the power in the autospectrum of the other series is also N, and the power in the cross spectrum of both will be proportional to

$$\sum_{i=1}^{N} p_i\, q_i\,. \tag{10.}$$

Writing $p_i\, q_i \equiv a_i$, the expected or mean value ([11]) of a_i, $E(a_i) = 0$, and its variance σ^2 is Var(a_i) = 1. Now the Lindeberg-Lévy Theorem, or Central Limit Theorem states that for a random variable $\bar{a} = \frac{1}{N}(a_1 + a_2 + ... + a_N)$ that converges in probability to $E(a_i)$, (which is here equal to 0), for which the common variance σ^2 of a_i exist, $\bar{a}$ is asymptotically normal with mean $E(a_i)$ and with a variance σ^2/N. In our calculations we are interested in the ratio (power in cross spectrum/power in auto spectrum), so one should calculate the variance of

$$\frac{\sum_{i=1}^{N} a_i}{\sqrt{\sum_{i=1}^{N} p_i^2 \sum_{i=1}^{N} q_i^2}} = \frac{1}{N}\sum_{i=1}^{N} a_i \;= \bar{a}\,. \tag{11.}$$

We can see now that the variance of this ratio behaves as σ^2/N; inversely proportional to N.

7.4 Measuring the noise spectral densities

To determine the signal-to-noise ratio of the Microflown, both the sensitivity, i.e. the output response of the sensor to a certain particle velocity, and its noise behaviour was measured. For the experiments, we used a two-wire Microflown. The two wires of the used sensor were 1 mm long, 10 μm wide, 0.5 μm thick and had a mutual spacing of 200 μm. The electrically conducting platinum patterns on the silicon nitride carriers was 150 nm thick.

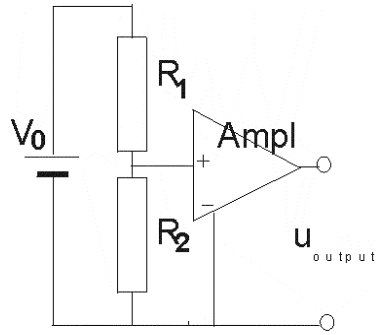

Figure 7-1: Electrical scheme of the set-up to measure the output noise of the Microflown, consisting of the two resistances R_1 and R_2.

The sensitivity of this sensor was determined in a frequency band of about 10 Hz - 4.0 kHz making use of the 'standing wave tube', as described in chapters 3 and 4, by placing the sensor in the tube with at one side a loudspeaker generating a broad frequency spectrum and at the other side a reference microphone. From the ratio between the output signals of both acoustic sensors, we deduced the sensitivity of the particle velocity sensor. The thus obtained sensitivity curve in this frequency range allowed to determine the sensitivity S of the sensor as 0.13 V/(m/s) at f =1 kHz.

To measure the noise spectrum of one particle velocity sensor, consisting of two (equal) resistances R_1 and R_2, a simple set up as shown in figure 7-1 was used. R_1 and R_2 were equal to 1.10 kΩ. The DC-powering was obtained from a 9 V battery as voltage source. The autospectrum of the noise of one sensor thus measured, is plotted in figure 7-2. Additionally a second set-up, identical to the first (figure 7-1) with two perfectly similar amplifiers and an identical but independent voltage source, was used for the noise measurement on sensor 2. Both sensors were placed into two different acoustically isolated boxes to reduce acoustic, and correlated, noise. The boxes were attached by elastic bands to reduce possible low-frequency and correlated noisy influences. In these boxes the probes were additionally sheltered in small tins with a transformer in it to balance the output signal. The two signals were led through shielded, balanced XLR cables and then independently amplified, first by a battery powered amplifier with

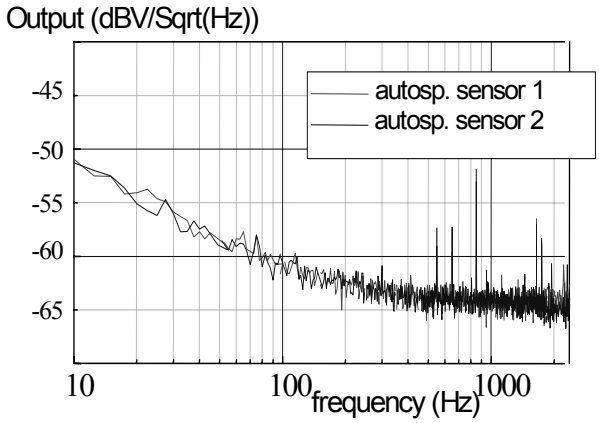

Figure 7-2: Measured autocorrelation spectra of the noise of sensor 1 and 2 (Amplification factor: 100 dB). For frequencies above approx. 600 Hz the spectrum is flat and roughly corresponds to the Nyquist noise level for normal resistances of 1.10 kΩ.

amplification factor 50 dB, then again by a second battery powered amplifier of 50 dB. The signals were recorded by an analyser: a 20 bits AD-converter (with an input impedance of 30 kΩ, and a flat frequency response in the bandwidth 30 Hz - 20 kHz), added to 24 bits PCI digital audio card in a PC. The sample frequency f_s was $44.1 \cdot 10^3$ Hz. The digitised output signals were recorded in the PC using the digital audio card, after which the 50 Hz frequency component and its higher harmonics were filtered out. The two signals were recorded and stored during a total measuring time of 20 minutes.

7.5 Interpretation

The noise levels of these autospectra were compared to the Nyquist noise level of resistances of 1.10 kΩ. Analysing the spectra, it is seen that for frequencies above approximately 600 Hz, the noise spectrum is approximately flat. The value of -163 dBV/√Hz is only slightly higher than the calculated value according to Eq.(1) with

R = 1.10 kΩ; −165 dBV/√ Hz (using the definition dBV = 10 ^{10}log V^2). See figure 7-2.

In the measured autospectra, shown in this figure, one observes also the presence of low frequency noise above the Johnson noise level. To investigate the mutual correlation of especially these low frequency noisy influences, we performed a series of different processes to the recorded signals. The recorded signals were subsequently not filtered (**a**), high-pass filtered above 45 Hz, so frequencies below 45 Hz were filtered out (**b**), high-pass filtered above 80 Hz (**c**), and high-pass filtered above 600 Hz (**d**). For comparison, the method described above to record simultaneously two different sensor signals, was also performed with two normal carbon resistors of 1.10 kΩ in the isolated boxes (**e**).

A mathematical software program, 'Matlab®', was used to calculate the cross correlation function of these pairs of data files. One time series of 20 minutes consisted of $N = 20*60*44100 \approx 5.29 \cdot 10^7$ data points.

The time signal of 20 minutes was subsequently divided into parts of 240 seconds, parts of 60 seconds, 10 seconds and 0.1 second, corresponding to respectively $N = 1.06 \cdot 10^7$, $N = 2.65 \cdot 10^6$, $N = 4.41 \cdot 10^5$ and $N = 4.41 \cdot 10^3$ data points. For each N, we calculated the power in the cross correlation spectrum in the total bandwidth and divided it by the power in the auto spectrum. Since we could thus calculate several values for the same N, the variance of this ratio could be calculated. This variance gives a more representative and reliable measure of the ratio for given N than only one result at that N since we have to do with a stochastically varying variable. The variations in the measured power in the cross correlation function are likely to originate from random errors involved in a sequence of measurements, that have a Gaussian probability distribution [1]. We assume therefore that the variable of interest, the power in the cross correlation spectrum, has a Gaussian (normal) distribution too. The variance of the variable distributed around its mean value was calculated for $N = 4.41 \cdot 10^3$ and $N = 4.41 \cdot 10^5$ different values, yielding the distributions of the variable as seen in figure 7-3. Although the curves are not perfectly smooth due to the finite size of the number N, they tend to a Gaussian (normal) distribution. For $N = 44.1 \cdot 10^5$, the variance is seen to be approximately 10 times smaller than for $N = 44.1 \cdot 10^3$, in correspondence with the theoretical expectation.

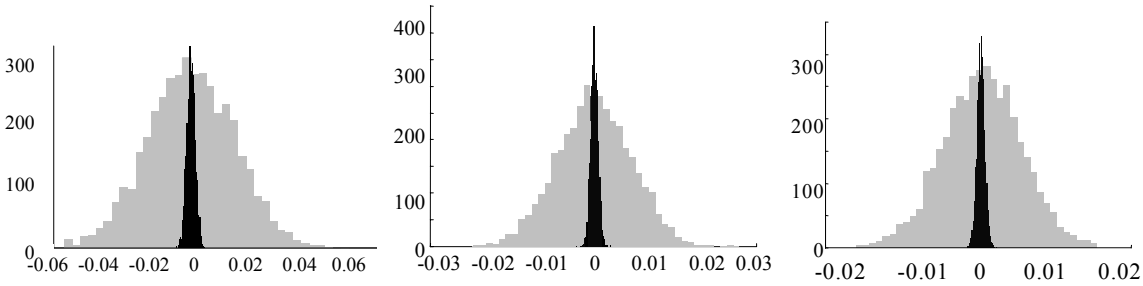

Figure 7-3a. *Figure 7-3b.* *Figure 7- 3c.*

Figure 7-3: Distributions of the calculated ratios (power in cross spectrum/power in auto spectrum), for $N=44.1\cdot10^3$, the broad curves, and for $N=44.1\cdot10^5$; the narrow peaked curves.
a: the cross spectrum of two sensor signals, high-pass filtered from 45 Hz; b: the two sensor signals, high-pass filtered from 600 Hz; c: the unfiltered cross spectrum of the signals of two resistors of 1.10 kΩ.

The estimate of the variance σ^2 of the ratio (power in cross spectrum/power in autospectrum, denoted as x) was determined from

$$\sigma^2 = \frac{\sum_{i=1}^{N}\left(x_i - \frac{1}{N}\sum x_i\right)^2}{N-1} \qquad (12.)$$

The mean value of x, or $E(x)$, in the above expression, should ideally be zero. We might expect that due to some possible correlation in the low-frequency region in the unfiltered signals, this $E(x)$ differs slightly from zero. Therefore, in the above expression the value $\frac{1}{N}\sum x_i$ was evaluated for all situations *a*-*e*, and subsequently used in the calculation of the variances (Eq.12.). The values σ (the square root of the variance) as a function of N are plotted in figure 7-4. The axes of the figure are logarithmically plotted, so that the plotted curve $\sigma = 1/\sqrt{N}$ is a straight line.
Comparing the experimentally found values in figure 7-4 to the theoretical variance $\sigma^2 = 1/N$, they behave as expected. For the signals of the resistors (**e**), the best correspondence to the theoretical dependence of σ^2 on N is seen. Besides it is seen in the figure that the other measured curves, in particular **a**, **b**, and **c**, lie above the theoretical line, although they have the same slope.

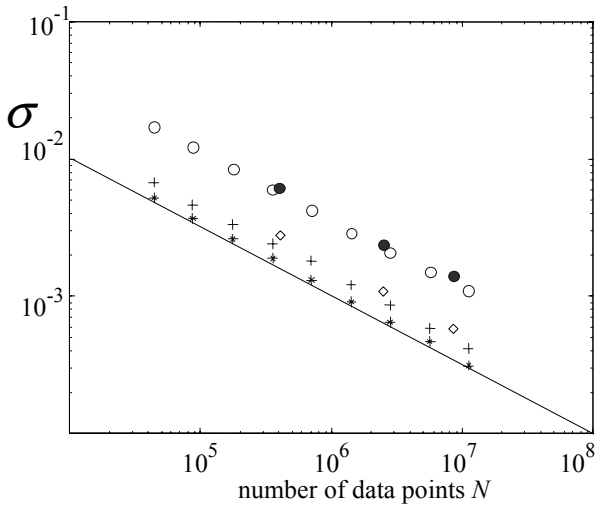

Figure 7-4: Influence of N on the variance of the calculated ratio [*power in the cross spectrum in the whole frequency range / power in the auto spectrum*]. *The variances were calculated for* ***a****:* (•)*, the unfiltered cross spectrum of the two sensor signals;* ***b****:* (o) *the two sensor signals, high-pass filtered from 45 Hz;* ***c****:* (◊) *the two signals, high-pass filtered from 80 Hz;* ***d****:* (+) *the two sensor signals, high-pass filtered from 600 Hz;* ***e****:* (∗) *the unfiltered cross spectrum of the signals of two resistors of 1.10 kΩ.*
The line shows $\sigma = 1/\sqrt{N}$.

The reason for this is that the decrease in the noise of the cross correlation spectrum, the variance, with N, is most effective for flat, broadband, frequency spectra. In cross correlation spectra in which a $1/f$-shaped component is present, there is a correlation between subsequent sample points x_i and x_j, while in a flat spectrum there is no correlation between points x_i and x_j ($i \neq j$) in de series of N points. The variance, which is calculated from a summation over all combinations of x_i and x_j, is therefore higher for $1/f$-spectra than for flat curves.
Although the variances of the obtained cross spectra are somewhat higher than the theoretical value (due to this $1/f$ –component), the deviation of the cross spectra of the unfiltered output signals (**a**) with respect to the theoretical $1/\sqrt{N}$ is only very limited: a reduction of the noise power in the cross spectrum with respect to the power in the auto spectrum of approximately $1.1 \cdot 10^{-3} \approx$ -30dB is attained, while the theoretically maximum reduction for a measurement time of 240 s equals $1/\sqrt{N} \approx$ -35dB (power reduction).

Whereas the variance of the ratio of the auto and cross spectra is most significant, an illustration of one particular measurement may be insightful. The measurement was performed in an anechoic room to eliminate all possible acoustic noise and no acoustic signal was applied. In figure 7-5, the curve of the autospectral density of the measured noise together with the curve representing the cross spectral density, for $N = 4.41 \cdot 10^5$, are plotted as a function of frequency. It is important to note that the cross spectral density has mean value zero and can be both positive and negative. The curve shows for every frequency *f*, the square root of the absolute value $|\Phi_{12}(f)|$ in a small bandwidth *df* around *f*. (*df* was taken to be 1 Hz). It can be seen that the cross spectral density lies indeed almost 25 dB lower than the autospectral density, thus approaching the theoretically expected value $1/\sqrt{N} = 1.51 \cdot 10^{-3}$; or –28 dB. Observing this figure, we must realise that it represents only one particular measurement and that a next determination of the spectra will give a result that slightly deviates from this figure. However, the ratio of the magnitude of the cross correlation spectrum and the auto correlation spectrum, is close to the calculated variance for this number of data points.

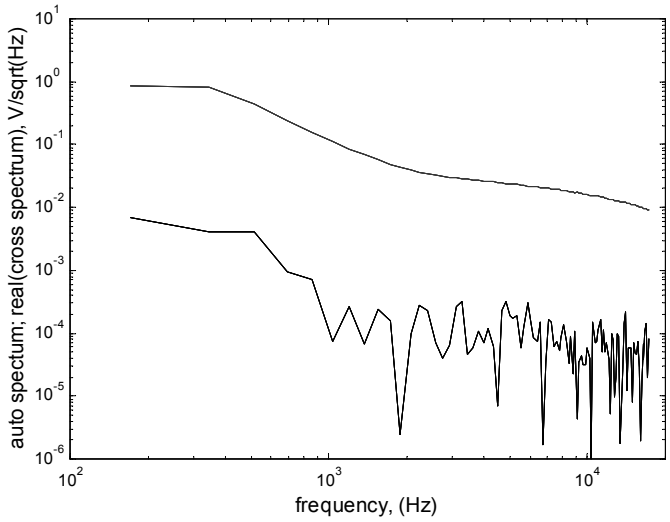

Figure 7-5: One single measurement result of the auto and cross correlation spectrum of the two sensors, for $N = 4.41 \cdot 10^5$ data points (amplification 160 dB).

So, from the figures 7-3, 7-4 and 7-5 it can be concluded that the use of calculating the cross correlation spectrum can reduce the noise level of the sensors considerably; for example if $N = 1.06\ 10^7$ data points are used, a reduction in noise power of 30 dBV/√Hz compared to the auto correlation spectra can be attained. The noise level becomes therefore considerably lower than the Johnson noise for the resistances, $4kTR$, approximately –165 dBV/√Hz for the present wires (without amplification). This implies that the noise level related to the resistance of the two heated wires is no longer a fundamental limit: although the sensor consists of two resistors R (the wires), its average noise power density per bandwidth can be reduced to below $4kTR$.

7.6 An improvement of the signal to noise ratio

Although we have shown that the cross correlation method offers the possibility to decrease the noise level, one should actually demonstrate additionally that a measured acoustic signal S, does not alter due to this procedure. Only then a real improvement of the signal to noise ratio is attained.

Therefore, two identical Microflowns, independently battery powered, were placed very close to each other in a large, acoustically isolated (anechoic) box of about 10 m^3. In the box a loudspeaker was situated and fed with a harmonic signal of exactly 1000 Hz. The two sensor signals were both independently amplified and led through short cables to the AD converter (20 bits, sampling frequency 44.1 kHz). The signals were simultaneously recorded during 20 minutes and post processed in the PC. Figure 7-8 shows the result of the measurement of the two autocorrelation spectra of the sensors (denoted as $P_{11}(f)$ and $P_{22}(f)$) and their cross correlation spectrum ($P_{12}(f)$), for a recording time of 2 minutes. The peak in the spectra at 1000 Hz is well visible; the two auto spectra lie approximately on each other due to the fact that the sensors have an equal sensitivity. Figure 7-8b focuses on the region around 1000 Hz to show an equally high signal peak in the cross correlation spectrum. The power reduction in the cross spectrum, about 20 dB, is not as much as could be expected from a measurement time of 2 minutes ($N = 2{\cdot}60{\cdot}4.41{\cdot}10^3$, so $1/\sqrt{N} = 4.35{\cdot}10^{-4}$; or –33 dB), this is caused by the contribution of

the low-frequency noise. This low frequency noise has not been filtered out as was done in the former measurements.

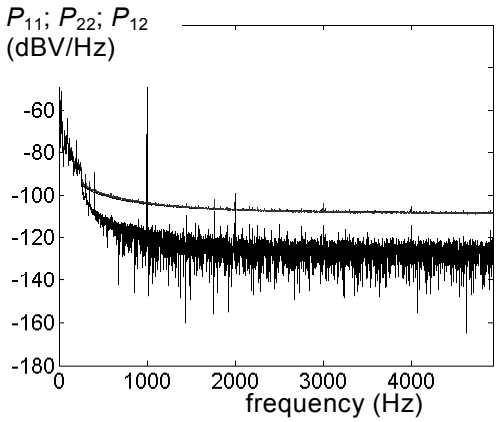

Figure 7-8a: Measurement of the auto spectra of the two sensors ($P_{11}(f)$ and $P_{22}(f)$) and their cross correlation spectrum ($P_{12}(f)$) when an acoustic signal of 1000 Hz is applied. The curves of P_{11} and P_{22} lie approximately on each other; the lower curve shows P_{12}. (measuring time: 120 s)

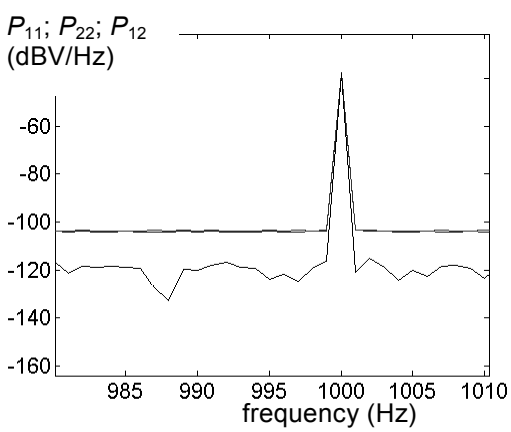

Figure 7-8b: Amplification of the left figure around 1kHz. It is seen that the sharp signal peak is for all spectra equally high, the cross spectrum lies about 20 dB below the auto spectra.

However, a real improvement of the signal to noise ratio has thus been achieved. When the sensor is subject to a signal, in principle modulation noise, or signal related noise, may occur. Since we have not observed any difference in noise level with and without an applied acoustic signal, we may conclude that for the investigated sound levels this signal related noise is negligible. The sensor measures a linear superposition of the acoustic signal and other noise sources. This noise floor can be expressed as an equivalent particle velocity level in (m/s)/√Hz. The noise spectrum (in V/√Hz) divided by the sensitivity then gives the equivalent noise 'particle velocity' level in (m/s)/√Hz. (The noise floor can thus equivalently be defined as the inverse of the signal-to-noise ratio). For a noise power in the cross correlation spectrum of two identical sensors of $5.0 \cdot 10^{-20}$ V^2/Hz, an integration time of 240 s then yields a noise floor of $1.7 \cdot 10^{-9}$ (m/s)/√Hz. This noise power is equivalent to -193 dBV/√Hz, a reduction of 30 dBV/√Hz with respect to the resistance noise level of –163 dBV/√Hz.

It has to be emphasised that in the application of cross correlation spectra, time averages are involved. Therefore, this method of noise reduction is useful for measurement of stationary signals; stationary sound intensity or particle velocity measurements. However, for instantaneous measurements or applications as sound recording, this method cannot be applied.

7.7 Conclusions

In this chapter it was shown that a large reduction of the noise of the Microflown, and of particle velocity sensors in general, in their applications as sensors for stationary sound measurements can be attained. This is achieved by the simultaneous use of two identical sensors closely spaced to each other and recording the cross spectrum of the output signals of both. Since in this cross correlation spectrum the relevant signals add but all the uncorrelated noise sources are eliminated, a significant reduction of the noise can be reached; for an integration time of 240 s this reduction equals 30 dB. The noise level then becomes even lower than the principal resistance noise level of the wire resistors of the sensor. The larger the number of data points used (the larger the measuring time), the larger this reduction becomes. The decrease in noise level as a function of integration time corresponds to theoretically expected values.

7.8 References

1 R. K. Pathria, 'Statistical Mechanics', University of Waterloo, Canada, ISBN 0080189946 (1986).

2 A. v. d. Ziel, 'Noise', Prentice Hall Electrical Engineering Series, the Netherlands.

3 P. Dutta, P. M. Horn: Low-frequency fluctuations in solids: 1/*f* noise, *Review of Modern Physics*, Vol.53, 3 (1981) 497-516.

4 G. Grinstein, T. Hwa, H. J. Jensen: $1/f^{\alpha}$ noise in dissipative transport, *Physical Review* A, Vol.45, 2 (1992) 559-562.

5 S. H. Liu: Theory of 1/f noise in metal films and whiskers, *Physical Review* B, Vol.16, 10 (1977) 4218-4223.

6 J. H. Scofield, J. V. Mantese, W. W. Webb, 1/*f* noise of metals, A case for extrinsic origin, *Physical Review* B, 32, 2 (1985) 736-742.

7 E. Milotti: Linear processes that produce 1/f or flicker noise, *Physical Review* E, Vol.51, 4 (1995) 3087-3103.

8 M. B. Weissman: 1/f noise and other slow, nonexponential kinetics in condensed matter, *Review of Modern Physics*, Vol.60, 2 (1988) 537-571.

9 O. H. Bjor, *Proceedings of Internoise*, Budapest (1997) 1367-1370.

10 W. H. Press, S. A. Teukolsky, W. T. Vetterling, B. P. Flannery, 'Numerical Recipes in C', Cambridge Univ., 2nd Ed. (1992).

11 Korn and Korn, 'Mathematical Handbook for Scientists and Engineers', 2nd Ed., Univ. of Arizona.

12 M. Sampietro, L. Fasoli, G. Ferrari, Spectrum analyzer with noise reduction by cross-correlation technique on two channels, Review of Scientific Instruments, Vol.70, 5 (1999), 2520-2525.

13 A. v. d. Ziel, 'Noise: Sources, Characterization, Measurement', Prentice-Hall, Englewood Cliffs, NJ (1970), 54.

Chapter 8

An investigation of the low frequency noise of the Microflown

Abstract

In this chapter the low-frequency noise in the output signal of the flow sensor is analysed. It is observed that the voltage fluctuations exhibit a spectral density that for low frequencies exceeds the Nyquist noise level (that of a common resistor) and behaves as $1/f^{\alpha}$ with $1 < \alpha < 3$. The influence of small fluctuations in one of the relevant parameters present in the governing heat equation on the fluctuations of the temperature of the wire and therefore on the spectral density of the output voltage, are theoretically analysed. Besides, the dependence of the low-frequency noise on wire temperature and on the electrical power that is dissipated in the metal wire, are investigated experimentally. A difference in the power dependence of this noise between the sensor wires and a common metal film resistor is observed. We propose different possible explanations for this noise behaviour.

8.1 Introduction

Since the thermal flow sensor principally consists of heated wire resistors, the narrow metal films on the silicon nitride beams, an inevitable origin of noise in acoustic measurements is the well-known resistance noise [1, 12]. However, in various noise measurements one observes additionally a contribution to the noise in the output signal of the sensor with a spectral density that exhibits a $1/f^{\alpha}$ behaviour with $\alpha > 1$.

In general, low-frequency $1/f$ noise, that is to say the class of $1/f^{\alpha}$ noises with roughly $0.5 < \alpha < 2$, are ubiquitous in many physical systems. Properties that fluctuate with $1/f$-shaped spectral densities appear in many apparently uncorrelated systems as diverse as metal-oxide-semiconductor (MOS) devices, diffusive systems and ocean currents, and especially in the spectral density of resistance fluctuations of metals. The specific origins of these noise processes are extensively studied and described in literature but not always perfectly understood [2-11, 13].

It is observed that the low frequency noise in the output signal of the flow sensor exhibits a strong dependence on the electrical power that is dissipated in the wire and second, on the wire temperature. To acquire insight in the behaviour and origin of this noise, the spectral density of the voltage fluctuations over the sensor wire is studied experimentally as a function of wire temperature and dissipated electrical power. Next the noise is investigated theoretically. Starting from principal physical equations that describe the wire temperature, it is deduced how tiny fluctuations in one of the parameters in the heat equation, with a certain spectral distribution, will result into small temperature fluctuations and consequently yield fluctuations of the output signal of a single wire.

8.2 Experimental observations

8.2.1 Method of approach

To investigate the noise spectrum, *viz.* the voltage fluctuations in the output signal of the metal wires of the flow sensor, different devices were designed. Sensors with different combinations of metals sputtered on the silicon nitride beams were

fabricated. The motivation for this variation in the thin adhesion layer between the silicon nitride beam and the platinum wire was to investigate the possible influence of the type of adhesion layer on the noise level.
Second, the measured noise level of the wires is expected to depend on the wire temperature and therefore on the dissipated electrical power in the wire. Consequently it is necessary to distinguish between the separate effects of the wire temperature and the power dissipation in the wire on the (low-frequency) noise level. To find out the influence of both individual effects, we will have to heat the wires by electrical dissipation in them, and by external heating without significant power dissipation in the wires.

8.2.2 Variation of the sensors

All sensors consisted of two closely spaced thin silicon nitride beams of 2 μm width, 1.5 mm length and 200 nm height. On these silicon nitride carriers the metal pattern was sputtered. The first type of sensor was made with a 10 nm thick adhesion layer of chromium on the silicon nitride beam with a layer of platinum of 150 nm thickness on it (type A). The second sensor had a 10 nm thick adhesion layer of titanium instead of the chromium (type B), while type C had an adhesion layer of tantalum instead. Finally, one device was realised with only a 150 nm thick platinum layer directly on the silicon nitride (type D). All sensors consisted of two wires (spacing 200 μm), but only one of these was under investigation when the output signal was measured.
The resistance of the investigated wires was measured to be near 270 Ω. As a reference in the experiments, a common metal film resistor of 280 Ω was used.

8.2.3 The electronic measurement set-up

The measurement set-up consisted of the sensor wire (or the resistor) connected in the electrical scheme of figure 8-1a, together with the amplifier of figure 8-1b. The voltage amplification factor of the amplifier was set to be 10^6, corresponding to a multiplication of 10^{12} for $<U^2>$.

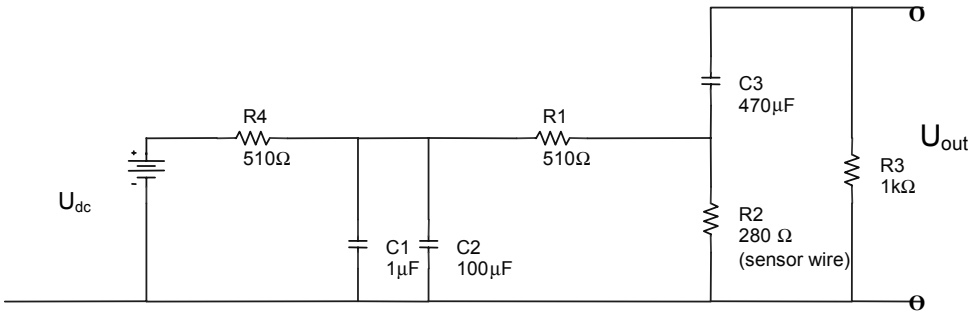

Figure 8-1a: Electrical scheme for adjusting a DC voltage on the sensor wire and measuring the spectrum of the voltage fluctuations of the wire. The amplifier is connected at the right. R_1, R_4, C_1 and C_2 are required to suppress noise from the voltage source.

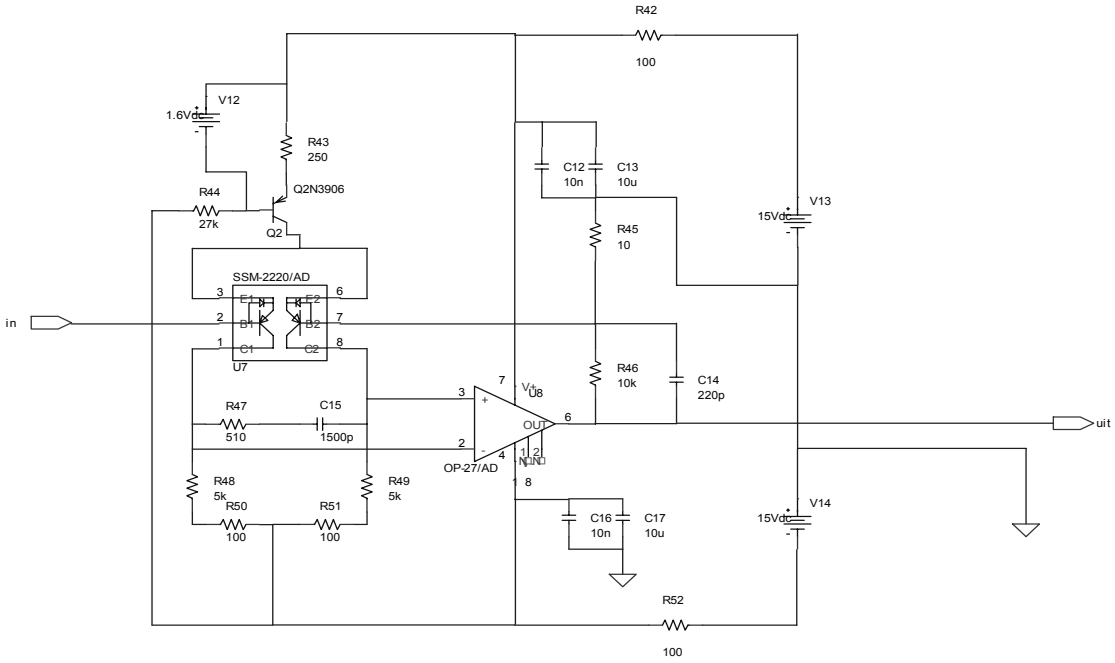

Figure 8-1b: Electrical scheme of the first, and therefore most critical, amplifier for the detected noise signal. Its amplification factor is 10^3. (The total amplification of all amplifiers in series equals 10^6.)

In figure 8-1a we see that not only the noise power of the Microflown (R_2) will contribute to the measured output noise (U_{out}, at the right). The other sources of noise power one has to take into account are those due to the resistance noise of R_1 and R_3, the current noise of the amplifier, i_n, and the voltage noise of the amplifier, u_n. For the voltage fluctuations in a bandwidth (f, $f + df$) of the resistors, the Nyquist theorem [1, 12] gives

$$< u_i^2 >_{(f,f+\Delta f)} = (4k_B T R_i)\Delta f\,, \quad i = 1,2,3 \tag{1.}$$

where the brackets <> denote the averaging over a time scale long compared to that of the fluctuations (see also section 8.4.3).

These voltages give rise to the contributions u_1', u_2'and u_3'at the output signal U_{out}, with $u_i' = f_i(u_i)$ and $f_i(u_i)$ the appropriate transfer function of the network (i = 1, 2, 3). With the notation $R_i \| R_j$ for the equivalent resistance of R_i and R_j parallel, these transfer functions are

$$\begin{aligned} u_1' &= \frac{R_2 \| R_3}{R_1 + R_2 \| R_3} u_1 \\ u_2' &= \frac{R_1 \| R_3}{R_2 + R_1 \| R_3} u_2 \\ u_3' &= \frac{R_1 \| R_2}{R_3 + R_1 \| R_2} u_3 \end{aligned} \tag{2.}$$

The voltage noise of the used amplifier yields, according to its specifications, $\sqrt{< u_n^2 > / \Delta f} \cong 1\,\mathrm{nV}/\sqrt{\mathrm{Hz}}$. The current noise behaves as $\sqrt{< i_n^2 > / \Delta f} \cong 4\,\mathrm{pA}/\sqrt{\mathrm{Hz}}$, leading to a voltage for which $\sqrt{< u_{i_n}^2 >} = \sqrt{< i_n^2 > R_v^2}$ at the output signal, with $R_v = R_1 \| R_2 \| R_3$ the equivalent impedance of the total network observed at the input of the amplifier. The total average noise power (per unit resistance) $< U_{out}^2 >$ then becomes, for the used components

$$\begin{aligned} \tfrac{1}{\Delta f} < U_{out}^2 > &= \tfrac{1}{\Delta f}(< u_1'^2 > + < u_2'^2 > + < u_3'^2 > + < u_n^2 > + < u_{i_n}^2 >) \\ &\approx 3.9 \cdot 10^{-18}\,\mathrm{V}^2/\mathrm{Hz} \end{aligned} \tag{3.}$$

at T = 300 K. An inevitable consequence of the measurement set-up is that this level does not fully correspond to the Nyquist noise level of a Microflown wire of 280 Ω at room temperature, $< u_2^2 > / \Delta f \approx 4.6 \cdot 10^{-18}\,\mathrm{V}^2/\mathrm{Hz}$. In the network the sensor wire is placed in parallel with other resistances, besides noise is added from the amplifier. With Eq. (2.) and the current values, we find $< u_2'^2 > \approx 0.3 < u_2^2 > = 1.4 \cdot 10^{-18}\,\mathrm{V}^2$, so the contribution of the average noise power of the Microflown to the total power is (only!) 36%.

The output signal was led to a PC in which it was digitised to a time series of data points and then 'fast-Fourier' transformed (FFT) in a software program to a frequency spectrum.

8.2.4 A heating cavity

First, the sensor wire was placed into a small cylindrical cavity in a copper bar of about 1 cm diameter and 3 cm length, of which the temperature was gradually increased. The cavity was homogeneously heated by an electrical heating element in the copper. Using an NTC sensing element, the temperature could be adjusted accurately. The power dissipation in the wire, using this electrical set-up, was very small, < 4 nW, so that the self heating due to the electrical dissipation could be neglected. At the initial temperature, T_r = 298 K, the measured noise level showed satisfying correspondence to that of a common metal film resistor with almost the same resistance (R = 280 Ω).

In the figures 8-2a-d, the measured spectra of the different wires at room temperature are shown. For comparison, the spectral density of the resistance was measured and depicted in figure 8-2e. All figures clearly show the flat tendencies of the curves.

The temperature of the cavity was gradually increased in steps of about 25 K, from room temperature up to 445 K. As soon as the cavity had achieved a uniform and constant temperature, the voltage spectrum was measured. Figure 8-2f shows the determined spectral density from wire A at T = 438 K. With the temperature coefficient of resistance of the conducting material of the wire $\beta = 3.0 \cdot 10^{-3}$ K^{-1}, having been determined beforehand by heating the material in a furnace, the wire resistance R_2 and therefore the Nyquist noise level at this temperature can easily be found, approximately $1 \cdot 10^{-17}$ V^2/Hz. This leads to a higher noise level calculated from Eq. (3.) with $\langle u^2 \rangle = 1 \cdot 10^{-17}$ V^2/Hz.

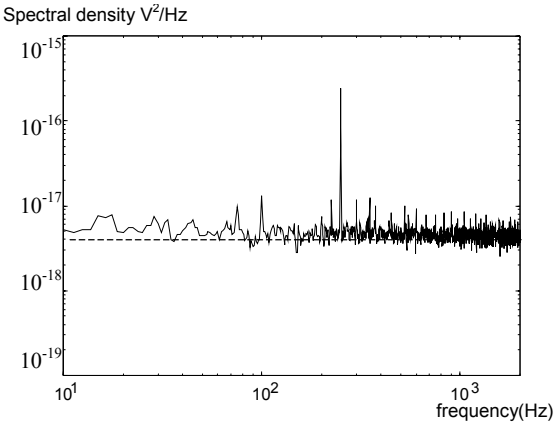

Figure 8-2a: Measured spectral density $<U^2>$/Hz of sensor wire A at T_r =298 K, resistance 270 Ω. The dashed lines in the figures 8-2 a-e show the calculated noise level for R_2=270 Ω, according to Eq. (3.) (that takes all contributions into account): $<u^2>=3.9\cdot10^{-18}V^2/Hz$.

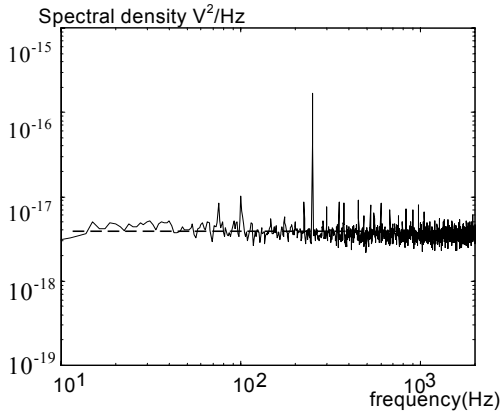

Figure 8-2b: Measured spectral density $<U^2>$/Hz of sensor wire B at T_r=298 K, resistance 270 Ω..

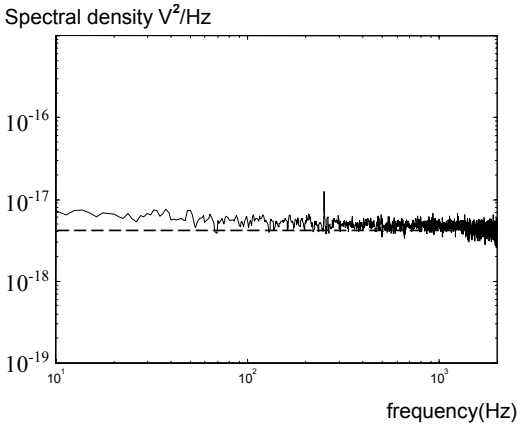

Figure 8-2c: Measured spectral density $<U^2>$/Hz of sensor wire C at T_r=298 K, resistance 270 Ω..

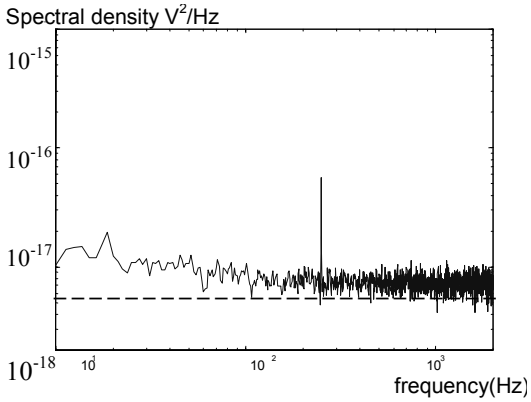

Figure 8-2d: Measured spectral density $<U^2>$/Hz of sensor wire D at T_r = 298 K, resistance 270 Ω..

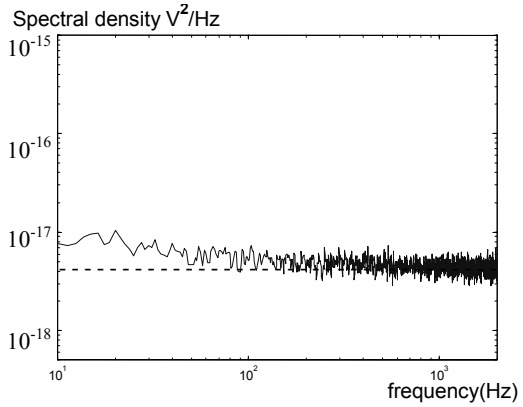

Figure 8-2e: Measured spectral density $<U^2>$/Hz of a common metal film resistor of 280 Ω at T_r=298 K.

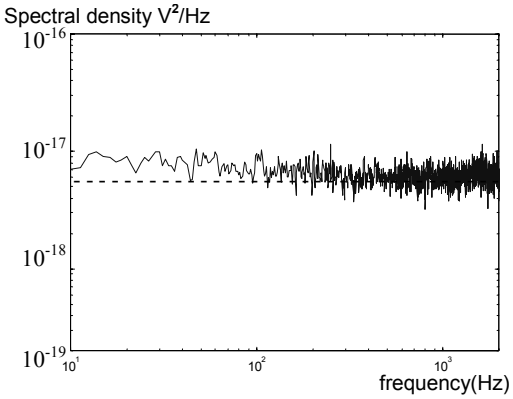

Figure 8-2f: Measured spectral density $<U^2>$/Hz of the sensor wire of figure 8-2b at T = 438 K. At this temperature, the wire resistance was 414 Ω. The dashed line shows the calculated noise level according to Eq.(3.) for R_2=414 Ω, T = 438 K: $<u^2>=5.5\cdot10^{-18}V^2/Hz$.

The increase of the (almost flat) noise level with temperature, in correspondence with the theoretical dependence, is indeed observed in the investigated temperature range for all types of wires and the resistor. The representative spectrum of figure 8-2 f is an illustration of this behaviour.

8.2.5 Heating by electrical power dissipation

In the next series of experiments the temperature of the wire was gradually increased by applying an adjustable voltage over the wire so that it was electrically powered and heated. The adjusted voltage over the sensor leads to additional requirements for the electrical network in which it is connected, since only the fluctuating signals are of interest. Besides, fluctuations in the power source, especially the low-frequency components, have to be suppressed. This is achieved by the combination of the capacitors C_1 and C_2 and the resistors R_1 and R_4, see figure 8-1a. The voltage source in this network provides the required electrical power. The amplification of 10^6 of the detected signal was realised by a chain of

four amplifiers in series. Requirements for the first amplification step in this chain, that is most critical, are most strict. This amplifier, with an amplification factor of 10^3, is depicted in figure 8-1b.

The electrical power that was dissipated in the wire was varied in the range from 0 mW to about 60 mW, the maximum value being determined by the maximum temperature the sensor could stand, approximately 700 K. The measured spectral density of the voltage fluctuations at different temperatures for the titanium-platinum case is shown in figure 8-3. Clearly, the magnitude of the low frequency noise increases with power. Moreover, this noise spectrum shows a frequency dependence as $f^{-\alpha}$ with α ranging roughly between 0 (at $T = T_r$) and 3. For the other types of sensor wires similar behaviour was observed. Comparing the temperature dependence of the low-frequency noise in the case the wire is heated due to the electrical power dissipation in the metal (figure 8-3) with the increase of the low-frequency noise with temperature when the wire is externally heated in an environment of uniform temperature (figure 8-2f), the influences of both P and T can be separated. The self-heating caused by the electrical power dissipation may also cause a temperature profile along the wire that differs from that achieved by external heating in a homogeneously heated environment.

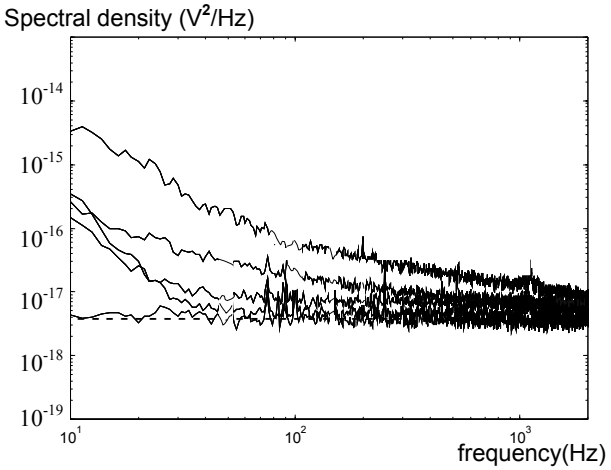

Figure 8-3: Measured spectral density $<U^2>$/Hz of sensor wire B for increasing powers. At increasing power, the wire temperature rises and the low-frequency noise level is seen to increase. See also figure 8-6 for the precise power dependence.

8.3 Processing of the experimental results

The increase of the low-frequency noise due to increasing self-heating (*viz.* the temperature rise as a result from electrical power dissipation) was quantitatively investigated by fitting the curves of the various noise spectra to functions of the form $f^{-\alpha}$. The noise data of the four types of wires for increasing power were analysed using an optimisation method that fitted the data points in a least squares sense. Three degrees of freedom (three parameters, p_1, p_2 and α) were taken so that the general form of the fitting function $S(f)$ was

$$S(f) = \frac{p_1}{(f / f_0)^{\alpha}} + p_2 \qquad (4.)$$

with f_0 = 40 Hz. The first term at the right represents the 1/*f*-noise to be studied, while p_2 corresponds to the Nyquist noise level. For comparison of the low-frequency noise contribution in the different curves both p_1 and α are of interest.

The value $p_1/(f/f_0)^{\alpha}$ was calculated with p_1 and α obtained from the optimisation procedure. At f = 40 Hz, the increase of noise with power appears to be most obvious.

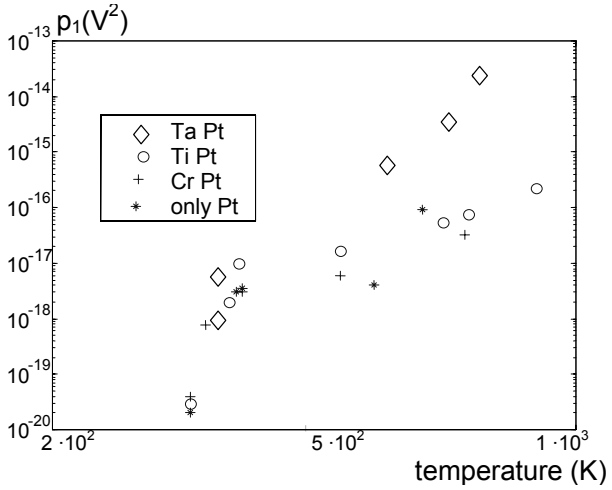

Figure 8-4: The value p_1, representing the contribution of the 1/f noise to $<U^2>$ at f = 40 Hz, as a function of the average wire temperature, that is increased by the electrical power dissipation P. Circles: Pt on Ti, crosses: Pt on Cr, squares: Pt on Ta, stars: Pt only.

At this frequency, $p_1/(f/f_0)^{\alpha} = p_1$, which represents the contribution of the low frequency noise to the value $<U^2>$ at f = 40 Hz. It is plotted as a function of

temperature in figure 8-4. The increase with temperature is evident, but it is clear that the behaviour of the points is not smooth and their error is therefore expected to be large.

The obtained values of the exponent α from the fitted spectra are depicted in figure 8-5 for each wire type, as a function of power. It was observed that the fitted values of p_2, not shown here, were in satisfying correspondence with the expected basic noise level according to Eq.(3.). Figure 8-5 shows an initial strong increase and then a decrease of α with power: for low power dissipation in the wires (about 10-20 mW), α is close to 3 or even higher, whereas it decreases down to 1 for higher powers (90 mW). This behaviour is characteristic for all investigated wire types.

The obtained large values of α at low powers may be partially due to the used fitting procedure: if the frequency spectrum is flat in a broad frequency bandwidth and contains only for very low frequencies a low-frequency noise contribution that dominates only near $f = 0$ Hz, a best fit is found with a small p_1 and large α.

For comparison, the metal film resistor of R = 280 Ω was put in the same set-up (figure 8-1a) with the same amplifier, while the power over the resistance was

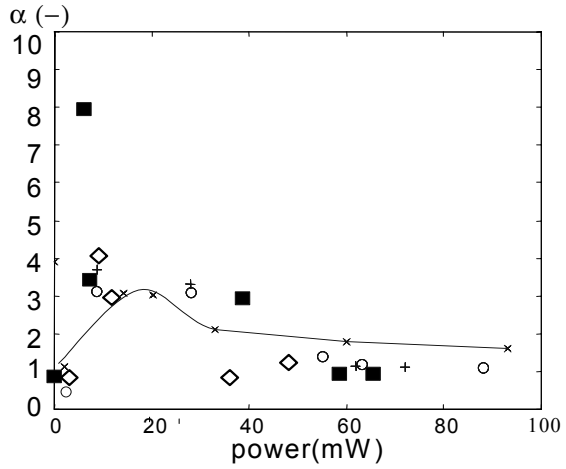

Figure 8-5: Exponent α of de fitted curves ($<U^2>=p_1 f^{-\alpha}+p_2$), circles; Pt on Ti, crosses: Pt on Cr, squares: Pt on Ta, diamonds: Pt only. The fitted α's of the normal resistance are shown on the dotted line.

gradually increased up to 100 mW. The temperature rise of the resistor at this power was measured to be negligibly small compared to that of the powered wires. The measured noise spectra were fitted according to Eq.(4.), resulting in the values of α as a function of power in figure 8-5. As can be observed in the figure, α shows the same tendency as in the heated wire case.

The measured noise spectra of the resistor at the different powers allow a comparison with the sensor wires at these power dissipations. This is illustrated by figure 8-6.

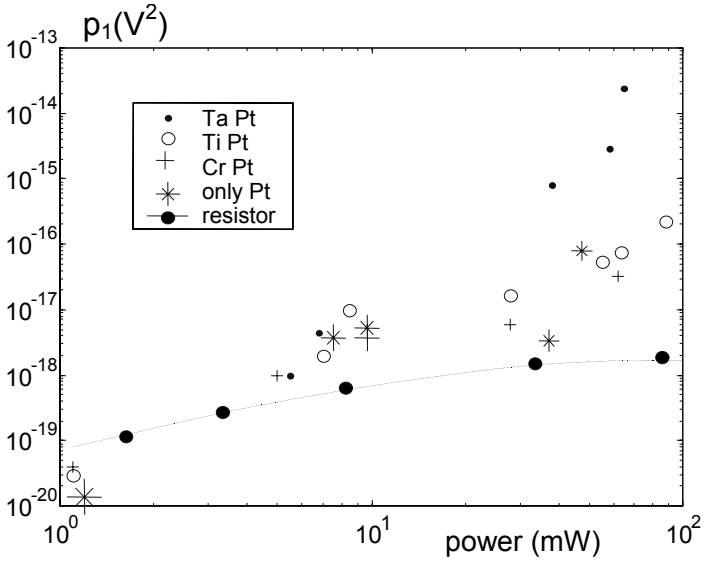

Figure 8-6: The value p_1, representing the contribution of the 1/f noise to $<U^2>$ at f = 40 Hz, as a function of the power dissipation P, for both the sensor wires and the metal film resistor. The dependence on P is different for the wires and the resistor.

Clearly, the dependence on P of the wires differs from that of the resistor. The data points of figure 8-6 were fitted in a least squares sense, resulting in the slopes $\gamma = \frac{\partial \log S_{f=40Hz}}{\partial \log P}$. Table 8-1 shows the values of γ for the different cases.

Table 8-1. The slope $\gamma = \partial \log S_{f=40\,Hz} / \partial \log P$ for the different material combinations of the sensor wire, and the resistor.

	Pt on Ta	Pt on Ti	Pt on Cr	Pt	resistor
γ	3.4 ± 0.6	1.8 ± 0.8	1.8 ± 0.7	1.5 ± 0.5	1.0 ± 0.3

In the theoretic description of section 8.4 we will see that this parameter may be important in finding a possible origin of the noise.

8.4 Theory

8.4.1 Introduction

In the former chapters, chapter 3, 5 and 6, it was seen that the sensor behaviour and the temperature of the wires could well be described by using the stationary heat diffusion equation as a starting point. This equation allowed the deduction of the stationary temperature distribution. To find then the temperature difference of the wires, a small perturbation due to the imposed particle velocity was added. The influence of the introduction of a small perturbation term on the final temperature profile could then be analysed. It formed also the basis for the approach of the electronic characterisation, since then a perturbation term due to the electronic heating was added, which appeared to be valuable to find an analogue between both perturbation effects on the final output signal. This approach, analysing the effect of a small perturbation on the final temperature, may be useful for our noise analysis as well, if we consider a fluctuation of one of the parameters that occur in the heat diffusion equation as a possible origin of the observed noise.

A different physical process in which the observed noise may find its origin, is the thermodynamic noise of the suspended wire. This thin beam, fixed at both ends, has vibration modes in two perpendicular directions. The resonance frequencies of vibration of the wire may lead to an apparent particle velocity.

In the next section the effect of a small perturbation of parameters in the heat diffusion equation is analysed, in 8.4.5 the vibration modes of the wire are considered as a possible origin of the noise.

8.4.2 A small perturbation to the temperature

We have already found (see for example chapter 6, section 6.2) that if the stationary heat diffusion equation is applied to a heater of width *2L* and length l_y in a channel of depth $2l_z$, that produces a power *P*, the temperature in the channel can be written as an expansion in harmonics,

$$T(\xi,\eta,\zeta) = \sum_{n,m=0}^{\infty} T_{n,m}(\xi)\cos(\lambda_n\zeta)\cos(\lambda_m\eta), \qquad \lambda_n = \frac{\pi}{2}(2n+1) \tag{5.}$$

with the normalised variables $\xi = \frac{x}{l_z}; \eta = \frac{2y}{l_y}; \zeta = \frac{z}{l_z}$.

For the coefficients $T_{n,m}(\xi)$ was found:

$$T_{nm}(\xi) = \frac{\pi}{2}\frac{T_0}{\sigma_{nm}}e^{-\sigma_{nm}\xi}, \qquad T_0 = \frac{P}{\pi k l_y}, \sigma_{nm} = \sqrt{\lambda_n^2 + (2l_z/l_y)^2\lambda_m^2} \tag{6.}$$

Imposed on this stationary time distribution, an additional contribution of noisy temperature fluctuations occurs, due to random variations in any of the parameters present in the heat equation. One should therefore investigate now the influence of a certain spectral distribution of small fluctuations in one of these parameters on the spectrum of temperature fluctuations.

In principle, each of the parameters in the heat balance that leads to the constant temperature profile, exhibits noisy variations that introduce small temperature fluctuations. Consequently, the possible candidates for origins of noise that is observed in the output signal are the fluctuations of the electrical power *P* of the source, of the thermal diffusion constant *k* of the gas, and in principle of the parameters ρ en c_p.

With regard to the first, the electrical power P, the assumption can be made that it has an additional small randomly varying component $\delta P(t)$, so that the total value of the dissipated power becomes $P+\delta P(t)$, of which the time dependence is still unknown. The additional perturbation of the temperature this δP will lead to, is called $\delta T(t)$.

Since the temperature now has a time dependence to be taken into account, the original heat diffusion equation contains additionally the time derivative of the temperature and it yields

$$\rho c_p \partial_t T - \nabla(k\nabla T) = Q \tag{7.}$$

The total temperature $T + \delta T$ must be a solution of Eq.(7.) with the term for the power source $P + \delta P$. By subtracting the stationary solution T at constant P, an equation for δT rests. This equation becomes

$$\rho c_p \partial_t \delta T - k\nabla^2 \delta T = \frac{\delta P}{l_y}\delta(x)\delta(z) \tag{8.}$$

Introducing the dimensionless time $\tau = \frac{D}{l_z^2}t$ and frequency $\bar{f} = \frac{2\pi f}{D/l_z^2}$ with $D = k/\rho c_p$, and taking a solution of the form $\delta T = \delta T(\xi,\zeta)e^{i2\pi\bar{f}\tau}$, the equation can be written in normalised variables as

$$(\partial_\xi^2 + \partial_\zeta^2 + \partial_\eta^2)\delta T - \partial_\tau \delta T = -\frac{\delta P}{k l_y}\delta(\xi)\delta(\zeta) \tag{9.}$$

In a fully similar way, it is possible to introduce a fluctuation of the thermal diffusion coefficient, so that its value becomes $k + \delta k(t)$. Neglecting terms of second order, the product of δk and δT, the normalised equation for δT becomes then

$$(\partial_\xi^2 + \partial_\zeta^2 + \partial_\eta^2)\delta T - \partial_\tau \delta T = \frac{\delta k}{k^2}\frac{P}{l_y}\delta(\xi)\delta(\zeta) \tag{10.}$$

Considering small perturbations of the parameters ρ en c_p in the heat equation, $\delta\rho(t)$ en $\delta c_p(t)$, it is seen that these effects are of second order and can therefore be neglected.

For convenience, we continue for the situation in which $\delta P(t)$ is the origin of the temperature fluctuations, the approach for a perturbation of k proceeds analogously.

The perturbation δT is written as an expansion in harmonics

$$\delta T(\xi,\zeta,\eta)=\sum_{n=0}^{\infty}\delta T_{n,m}(\xi)\cos\lambda_n\zeta\cos\lambda_m\eta$$
$$\lambda_n=\frac{\pi}{2}(2n+1) \tag{11.}$$

so that for $\delta T_{n,m}(\xi)$ results

$$\partial_\xi^2\delta T_{n,m}-K_{n,m}^2\delta T_{n,m}=-\frac{\delta P}{kl_y}\delta(\xi)$$
$$\text{with}\quad K_{n,m}=\sqrt{\sigma_{n,m}^2+i\bar{f}} \tag{12.}$$

Using the solution $G_{n,m}(f,\xi-\xi')$ of the following equation,

$$\partial_\xi^2 G_{n,m}(f,\xi-\xi')-K_{n,m}^2 G_{n,m}(f,\xi-\xi')=\delta(\xi-\xi') \tag{13.}$$

the Green's function:

$$G_{n,m}(f,\xi-\xi')=-\frac{1}{2K_{n,m}}e^{-K_{n,m}\lfloor\xi-\xi'\rfloor}, \tag{14.}$$

one finds for $\delta T(f,\xi)$, if the heater is located at $\xi=0$:

$$\sum_{n,m}\delta T_{n,m}(f,\xi)=\sum_{n,m}\frac{\delta P}{2kl_y}\frac{1}{K_{n,m}}e^{-K_{n,m}\lfloor\xi\rfloor} \tag{15.}$$

At the place of the heater, $\xi=0$, the expression for $\delta T(0)$, Eq.(15.), diverges. To avoid this divergence, the finite width of the heater $\xi_0=2L/l_z$ has to be taken into account. Averaging the expression over the width $-\xi_0/2<\xi<\xi_0/2$, one finds

$$\sum_{n,m}\delta T_{n,m}(f,\xi)=\sum_{n,m}\frac{\delta P}{2kl_y}\frac{1-e^{-K_n\xi_0}}{K_n^2\xi_0}e^{-K_n\lfloor\xi\rfloor} \tag{16.}$$

which is convergent for all ξ.

8.4.3 Frequency distribution of the perturbation and of the temperature

In the foregoing section we have found a relation, Eq. (16.), between the temperature perturbation $\delta T(f,\xi)$ of the wire and its origin, a small variation δP (or δk). Point of interest now is how a certain spectral distribution of δP or δk will determine the spectral distribution of the perturbed temperature. The purpose of this section is therefore to find a relation between both spectral densities. Second, the spectral distribution $\delta T(f)$ can be calculated if assumptions about the spectral density of δP, in particular that this can be characterised by a 'flat' spectrum, are made.

The function δP depends in general on t. One can define the autocorrelation function

$$< \delta P(t_1)\delta P(t_2) >= \delta_P^2 w(t_1 - t_2) \tag{17.}$$

where the brackets <> denote the averaging over all possible states of the system, which is in this case equal to the time average [1], and the magnitude $\delta_P = \sqrt{< \delta P(t)^2 >}$ is the 'root mean square value'. The autocorrelation function $<\delta P(t_1)\delta P(t_2)>$ is in principle a function of two variables, t_1 and t_2, but depends only on the difference t_1- t_2. We now make an assumption about the behaviour of $\delta P(t)$: it is presumed that there is no correlation in time, so that function w has a flat, or 'white', frequency spectrum. This corresponds to writing

$$w(\tau) = \delta(\tau) \tag{18.}$$

with $\delta(\tau)$ the Dirac delta function. The Fourier transform of (17.) reads $< \delta P(\omega_1)\delta P(\omega_2) >= \delta_P^2 W(\omega_1,\omega_2)$, with $W(\omega_1,\omega_2)$ the Fourier transform of $w(t_1,t_2)$. Since the autocorrelation function is in principle a function of two variables, it is possible to write w, and the Fourier transform $W(\omega_1,\omega_2)$ as a function of two variables:

$$W(\omega_1,\omega_2) = \frac{1}{(2\pi)^2} \int_{-\infty}^{\infty} dt_1 dt_2 e^{-i(\omega_1 t_1 + \omega_2 t_2)} w(t_1 - t_2) \tag{19.}$$

After the coordinate transform $\tau = t_1$- t_2, $\theta = t_1 + t_2$, this becomes

$$w(\omega_1,\omega_2)=\frac{1}{(2\pi)^2}\frac{1}{2}\int_{-\infty}^{\infty}d\tau d\theta e^{-i\theta(\omega_1+\omega_2)/2}e^{-i\tau(\omega_1-\omega_2)/2}w(\tau)= \\ =\frac{1}{2\pi}\delta(\omega_1+\omega_2)\int_{-\infty}^{\infty}d\tau e^{-i\tau(\omega_1-\omega_2)/2}w(\tau) \tag{20.}$$

Since by definition

$$w(\frac{\omega_1-\omega_2}{2})\equiv\frac{1}{2\pi}\int_{-\infty}^{\infty}d\tau e^{-i\tau(\omega_1-\omega_2)/2}w(\tau) \tag{21.}$$

(here $W(\omega)$ and $w(t)$ both depend only on one variable), one can express W in frequency space as

$$W(\omega_1,\omega_2)=\delta(\omega_1+\omega_2)W(\frac{\omega_1-\omega_2}{2}) \tag{22.}$$

With the assumption for $w(\tau)$, Eq. (18.), its Fourier transform becomes

$$W(\omega)=\frac{1}{2\pi}\int_{-\infty}^{\infty}d\tau e^{-i\tau\omega}\delta(\tau)=\frac{1}{2\pi} \tag{23.}$$

so that for spectral density $<\delta P(\omega_1)\delta P(\omega_2)>$ can be written

$$<\delta P(\omega_1)\delta P(\omega_2)>=\frac{\delta_P^2}{2\pi}\delta(\omega_1+\omega_2) \tag{24.}$$

For the fluctuating signal $\delta T(t)$ we are interested in the autocorrelation function $<\delta T(t_1)\delta T(t_2)>$. With the definitions

$$S=\sum_{n,m}\frac{1-e^{-K_{nm}\xi_0}}{2\xi_0 K_{nm}^2};\qquad T_0=\frac{P}{kl_y} \tag{25.}$$

it follows that

$$<\delta T(t_1)\delta T(t_2)>= \\ =T_0^2\int_{-\infty}^{\infty}d\omega_1 d\omega_2 e^{i(\omega_1 t_1+\omega_2 t_2)}S(\omega_1)S(\omega_2)\frac{<\delta P(\omega_1)\delta P(\omega_2)>}{P^2}= \\ =\frac{\delta_P^2}{P^2}T_0^2\int_{-\infty}^{\infty}d\omega_1 d\omega_2 e^{i(\omega_1 t_1+\omega_2 t_2)}S(\omega_1)S(\omega_2)\delta(\omega_1+\omega_2)W(\frac{\omega_1-\omega_2}{2}) \tag{26.}$$

Making the coordinate transformation $p = \omega_1 + \omega_2$; $q = \omega_1 - \omega_2$, the expression becomes

$$
\begin{aligned}
&< \delta T(t_1)\delta T(t_2) >= \\
&= \frac{\delta_P^2}{P^2} T_0^2 \frac{1}{2} \int_{-\infty}^{\infty} dpdq e^{ip(t_1+t_2)} e^{iq(t_1-t_2)} S(\frac{p+q}{2}) S(\frac{p-q}{2}) \delta(p) W(\frac{q}{2}) = \\
&= \frac{\delta_P^2}{P^2} T_0^2 \int_{-\infty}^{\infty} dq e^{iq(t_1-t_2)} S(q) S(-q) W(q)
\end{aligned}
\tag{27.}
$$

Therefore we can write now

$$
< \delta T(t)\delta T(0) >= \int_{-\infty}^{\infty} dq e^{iqt} C_T(q) \tag{28.}
$$

with $C_T(\omega)$ the measured spectral density of the temperature fluctuations,

$$
C_T(\omega) = \frac{\delta_P^2}{P^2} T_0^2 \left|S(\omega)\right|^2 W(\omega) \tag{29.}
$$

One sees that with the assumption of Eq.(18.), so that Eq.(23.) holds, the spectral density $C_T(\omega)$ becomes simple,

$$
C_T(\omega) = (\frac{\delta_P}{P})^2 T_0^2 \left|S(\omega)\right|^2 \frac{1}{2\pi} \tag{30.}
$$

This approach is similar for fluctuations $\delta k(t)$. If we distinguish between the spectral density due to the power fluctuations $C_T^P(\omega)$, and the spectral density due to a fluctuation of k: $C_T^k(\omega)$, we can write for both

$$
\begin{aligned}
C_T^P(\omega) &= (\frac{\delta_P}{P})^2 T_0^2 \left|S(\omega)\right|^2 \frac{1}{2\pi} \\
C_T^k(\omega) &= (\frac{\delta_k}{k})^2 T_0^2 \left|S(\omega)\right|^2 \frac{1}{2\pi}
\end{aligned}
\tag{31.}
$$

8.4.4 Spectral density of voltage variations

The measured output signal of the wire is a voltage, and the observed noise manifests itself in the form of small voltage variations. From the obtained spectral density of the temperature variations, the spectral density of these voltage fluctuations can be deduced.

The instantaneous temperature of the wire is the sum of the constant time-averaged wire temperature T_w and the small fluctuating part $\delta T(t)$:

$$T(t) = T_w + \delta T(t) \tag{32.}$$

With the room temperature denoted as T_r, and the wire resistance at room temperature as R_0, the measured voltage over the wire becomes

$$U(t) = IR_0(1 + \alpha(T_w - T_r + \delta T(t)) \tag{33.}$$

Consequently, the voltage over the wire $U(t)$ is composed of a constant part, U_w, and a fluctuating part, $u(t)$. The dissipated electrical power P, related to the constant part, equals

$$P = I^2 RT_w = I^2 R_0(1 + \alpha(T_w - T_r)) \tag{34.}$$

and the temperature and voltage fluctuations are related as

$$\delta T(t) = \frac{u(t)}{\alpha I R_0} \tag{35.}$$

so that for the spectral density of the voltage fluctuations, i.e. only those due to the assumed variations in the electrical power P from the power source, yields

$$C_U(\omega) = (\alpha I R_0)^2 C_T^P(\omega) \tag{36.}$$

Additionally, the measured voltage spectral density is determined by the Nyquist noise level of the wire resistance, that exhibits a flat ('white') noise spectrum. Therefore for the total spectral density of the voltage fluctuations, $<u^2>(\omega)$ or $C_U(\omega)$, one finds

$$\begin{aligned} C_U(\omega) = & \frac{PR}{(1+\alpha(T_w - T_r)^2}\left(\frac{\alpha P}{kl_y}\right)^2\left(\frac{\delta_P}{P}\right)^2 \frac{|S(\omega)|^2}{2\pi} \\ & + \frac{PR}{(1+\alpha(T_w - T_r)^2}\left(\frac{\alpha P}{kl_y}\right)^2\left(\frac{\delta_k}{k}\right)^2 \frac{|S(\omega)|^2}{2\pi} \\ & + 4kTR \end{aligned} \tag{37.}$$

The two first terms on the right-hand side of this equation, the two different contributions to the low-frequency noise, except the Nyquist level, find their origin in the fluctuations in power, δP, and in the heat diffusion coefficient, δk, respectively. Assuming the relative variations δ_P/P and δ_k/k to be constant, the dependence on power of both noise sources is as P^3. Note that we have not made yet any estimation of the magnitudes of the relative fluctuations. If, conversely, the magnitude of δ_P itself is constant, the first term will be proportional to P.

8.4.5 Vibrations of the wire as a possible noise origin

It can be assumed that the observed low frequency noise has (partially) a different source and finds its origin in the thermodynamic noise of the suspended wire. This beam, suspended between both clamped ends, has two degrees of freedom leading to possible deflections in both the *x*- and *y*-direction. If there exists at room temperature an axial tensile stress in the beam, the resonance frequencies of vibration are determined by both the flexural rigidity of the wire and the axial stress along it. For the investigated wires, with the current dimensions and materials, and a Young's modulus of approximately $E = 3 \cdot 10^{11}$ N/m^2, these resonance frequencies can be calculated [14,15]. Using an estimation for the tensile stress in the beam, $\sigma = 3 \cdot 10^7$ N/m^2 [14,16], the lowest resonance frequency of vibration at room temperature can be estimated as $\omega_{res} \sim 10 - 100$ kHz.

However, heating the wire causes an increase of its length, δl_y, that in a first order approximation can be described by $\delta l_y = l_{y,0}(1+\alpha \Delta T)$ with $l_{y,0}$ the length at room temperature, ΔT the temperature increase and α the thermal expansion coefficient of the material. We see that for $\alpha_{Pt} = 8.8 \cdot 10^{-6}$ K^{-1} and $\alpha_{SiNi} \sim 3 \cdot 10^{-6}$ K^{-1}, the compressive stresses due to the axial expansion of the materials of the beam become nearly equal to the original axial stress, at temperature rises of roughly $\Delta T \sim 40 - 100$ K. The resultant axial forces in the beam then become therefore small and the related resonance frequencies decrease dramatically [14], down to frequencies below 300 Hz. If the temperature increases further, the compressive stress will dominate. With the present thermal expansion coefficients, these stresses and the related resonance frequencies strongly increase with further increasing temperature.

Thus, in a limited temperature range of about 350-450 K, the resonance frequencies of the vibrations of the suspended wire lie in the low frequency range where the noise is observed. Due to small thermal variations the related spectral peaks are not necessarily very sharp but may have a certain spread. In that case, the described wire vibrations (of thermodynamic origin) can provide a partial explanation for the observed noise, since no well-defined and time-independent peaks are observed in the spectra.

However, the presumed resonance frequencies cannot account for the difference in noise characteristics between electrical powering and external heating of the wire.

8.5 Discussion

8.5.1 Noise due to the measurement set-up

In the measurement of the electronic noise of a thin metal wire, we are confronted with several problems. One of these is that even the pure resistance noise of the resistor is difficult to be detected separately and to be distinguished from other inevitable noise sources due to the electronic network and the amplifiers. This is illustrated by the comparison of expression (3.), that gives for the measured flat noise level a value $< u_{out}^2 > / \Delta f \approx 3.9 \cdot 10^{-18}\,\mathrm{V}^2/\mathrm{Hz}$, with the theoretic noise level of the wire, $4.6 \cdot 10^{-18}\,\mathrm{V}^2/\mathrm{Hz}$. Only about 40 % of the measured flat noise level is determined by the wire under investigation. This rather poor result may be improved by altering the used network of figure 8-1a; and skip R_3 and C_3. (In that case an integration of a capacitor into the amplifier is required). Besides, an improvement would be to increase R_1 in order to realise a better 'current source'. Since this requires a higher voltage provided by the power source to achieve sufficient voltage drop over the sensor wire, a different (larger) voltage source in needed. Although a very low noise amplifier was built for our purpose, the amplifier noise, that will always contribute, cannot be neglected.

However, with respect to the flat noise level, the basic level for frequencies above approximately 1 kHz, the measured and calculated (Eq.(3.)) value correspond within a factor two, see the figures 8-2a-e, which is satisfactory. Second, the increase of wire temperature that causes a higher Nyquist level, is indeed well observed, of which figure 8-2f is an example.

An important conclusion from the above is that the network and the amplifier do not significantly contribute to the low frequency noise of the wire. Possible influences of the power source on the low frequency noise cannot be excluded yet.

8.5.2 The temperature and power dependence

Since a usual observation of the low frequency noise of the Microflown is that it increases with temperature, we separated the effects of the power dissipated in the wire and the temperature of the wire. Besides, a possible dependence on temperature, and the precise relation, might provide useful information about the origin of the noise, as seen in literature [2-9, 13]. When the sensor wire was placed into a cavity of which the temperature was increased, no significant increase of the low frequency noise was observed. Therefore one can conclude that this noise must be due to the fact that power is dissipated in the wire. It is still possible, however, that the voltage source itself adds noise. Besides it cannot be excluded yet that the effect of a temperature gradient, when the hot wire is in a cold environment, contrary to a hot wire due to uniform environmental temperature, may have influence. Second, it is also possible that the fact that the electrically heated wire does not have a uniform temperature along the wire is of importance.

When electrical power is dissipated in the wire, a strong increase of the noise is observed, see figure 8-3. To discover a possible difference in behaviour of designs with different adhesion layers, four types of wires were investigated: a platinum layer on an adhesion layer of titanium, on tantalum, on chromium, or without an adhesion layer directly on the silicon nitride beam. Figure 8-6 shows some of the obtained results. A very large spread exists in the measurement points. Even points from one particular wire are widely spread, which makes it difficult to perceive a clear tendency. One can note, however, that the platinum-tantalum case exhibits a much stronger increase with power than the other wires do.

It is important to compare these power dependences with that of a common metal film resistor. We see in figure 8-6 that the metal film resistor also demonstrates an increase of the low frequency noise with power, although its temperature rise is very small. From this the conclusion can be drawn that the power source considerably contributes to the noise.

Apart from this effect, the sensor wires show power dependent low frequency noise that is not observed for the resistor. To consider the power dependence in more detail, as a measure the slope $\gamma = \frac{\partial \log S_{f=40Hz}}{\partial \log P}$ was determined for the various situations, see table 8-1. The error in the slopes of the fitted curves are

seen to be rather large, which makes a definite statement difficult. From the approach in section 8.4 we know, however, that these slopes may provide information about the noise origin. Two possible origins were particularly considered: a small fluctuation in the heat diffusion coefficient, δk, and perturbations in the power, δP. It followed from Eq. (37.),

$$C_U(\omega) = \frac{PR}{(1+\alpha(T_w - T_r)^2}\left(\frac{\alpha P}{k l_y}\right)^2\left(\frac{\delta_P}{P}\right)^2 \frac{|S(\omega)|^2}{2\pi} + \frac{PR}{(1+\alpha(T_w - T_r)^2}\left(\frac{\alpha P}{k l_y}\right)^2\left(\frac{\delta_k}{k}\right)^2 \frac{|S(\omega)|^2}{2\pi} + 4kTR \qquad (37.)$$

that if the absolute value of the quantity δP is constant, the power dependence of $<U^2>$ is as P^1. For a constant ratio $\delta P/P$, and for a constant ratio $\delta k/k$, it behaves as P^3.

Unfortunately, from the obtained slopes in table 8-1 no definite conclusions can be drawn. For the platinum-tantalum case the slope $\gamma = 3$ fits within the error width of the experimental value, but the curves of the other wires have a slope larger than 1 but smaller than 3.

Let us consider one of the first two terms in the expression for $C_U(\omega)$, and compare quantitatively the measured result with the calculated value for the current situation. We take the (platinum-titanium) wire of l_y=1 mm length, an etch depth of l_z = 250 μm, $\alpha = 3\cdot10^{-3}$ K^{-1}, a resistance at room temperature T_r of 270 Ω, a power dissipation of 10 mW and a temperature T_w = 400 K. Further $D = 1.9\cdot10^{-5}$ m^2 s^{-1}and $k = 2.4\cdot10^{-2}$ W/m K. Calculating $S_0(\omega)$ at 10 Hz and comparing then the calculated value of $C_U(\omega)$ with the experimentally found value at 10 Hz, $C_U(\omega) \approx 2\cdot10^{-16}$ V^2/Hz, one finds

$$\frac{\delta P}{P} \approx 10^{-8} \qquad (38.)$$

or equivalently, if the fluctuations in the heat diffusion coefficient are assumed to be the origin of the noise

$$\frac{\delta k}{k} \approx 10^{-8} \qquad (39.)$$

It demonstrates that only very small relative fluctuations in k or in P are sufficient to account for the observed noise.

8.5.3 The frequency dependence

In deducing Eq.(37.), a flat spectrum for the fluctuations in P or in k was assumed. The result is that the only frequency dependent term in the final expression for $C_U(\omega)$ is $S(\omega)$, a function determined by the stationary temperature profile of a single wire, see its definition Eq. (25.). For l_z = 250 μm and $D = 1.9 \cdot 10^{-5}$ m^2 s^{-1} it has a characteristic frequency of 48 Hz: above this frequency it falls off with a slope –1 on a logarithmic scale. Therefore $|S_0(\omega)|^2$ decreases with slope –2 for frequencies larger than 48 Hz, and is flat below this frequency. From this one may conclude that for low frequencies, but higher than about 50 Hz, the noise can thus be explained. However, the flatness of the spectrum of δP or δk is only an assumption, and other frequency behaviour of δP or δk will lead to different noise spectra. From figure 8-4b we may endeavour to get insight into this frequency dependence. It is seen that for increasing power, the exponent α in $f^{-\alpha}$ initially strongly increases and then decreases from high values (~3 - 5) to 1. A definite statement cannot be made yet.

8.5.4 Thermodynamic noise

The sensor wire is suspended between its two clamped ends and can therefore exhibit small deflections in the two directions perpendicular to its axis. Due to the combination of the elasticity of the wire and its momentum of inertia, certain resonance frequencies for these vibrations occur. The magnitudes of these resonance frequencies depend on the axial stress in the wire. At room temperature, the tensile stress originating from the suspension has been calculated to be too high to account for resonance frequencies in the acoustic spectrum. Due to thermal expansion of the wire while heating, the compressive stresses increase and can become about as large as the original tensile stresses. In this temperature range,

estimated to be 350 – 450 K, the related resonance frequencies thus dramatically decrease, down to the audible frequency range.
Provided that we assume that the sharp resonance peaks are substantially spread due to thermal variations, this effect could account for the observed low-frequency noise. However, it does not provide a fully satisfying explanation for the difference between external heating and self-heating.

8.5.5 Further research

At the moment of the writing of this thesis, it is not possible to draw satisfying conclusions about the origin of the noise. It is clear that much more measurements have to be done. Currently, many other sensor wires with other types of adhesion layers are under investigation. A point of interest is the platinum tantalum wire. New and reproducible measurements on tantalum have to be performed. Other material combinations for which Microflowns have been designed recently are tantalum-rhodium and rhodium-platinum.
Moreover, if a substantial part of the low-frequency noise finds its origin in the power fluctuations δP while electrical power is dissipated in the wire, this effect still has to be explained in more detail. Therefore, the wire surfaces are currently analysed using an SEM (scanning electron microscope). Figure 8-7 shows a SEM-photograph of the platinum surface that has been sputtered on a chromium adhesion layer. It reveals the presence of grains in the sputtered material, with a characteristic size of about 20 nm. A hypothesis is that with their effect on the scattering of electrons, these grains may cause small fluctuations in the dissipated power in the platinum wire. Definite conclusions still have to be drawn.

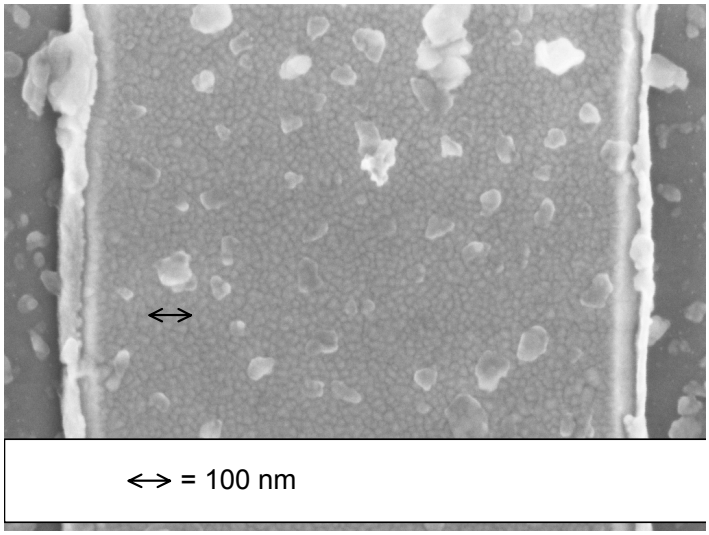

Figure 8-7: SEM photograph of a platinum wire sputtered on a chromium adhesion layer. (magnification $6 \cdot 10^4$). Grains in the structure are clearly visible, with an average size seen to be near 20 nm.

8.6 References

1 R.K. Pathria, Statistical Mechanics, University of Waterloo, Canada, (1986).

2 M.B. Weissman, *Physical Review Letters*, Vol. 41, 1 (1978).

3 M.B. Weissman, *Review of Modern Physics*, Vol. 60, 2 (1988).

4 P.Dutta, P.M. Horn, *Review of Modern Physics*, Vol.53, 3 (1981).

5 G. Grinstein, T. Hwa, H.J. Jensen, *Physical Review A*, Vol.45, 2 (1992).

6 S.H. Liu, *Physical Review B*, Vol.16, 10 (1977).

7 J.H. Scofield, J.V. Mantese, W.W. Webb, *Physical Review B*, Vol. 32, 2 (1985).

8 J.H. Scofield, J.V. Mantese, W.W. Webb, *Physical Review B*, Vol. 34, 2 (1986).

9 J.H. Scofield, W.W.Webb, *Physical Review Letters*, Vol. 54, 4 (1985).

10 E. Milotti, *Physical Review E*, Vol. 51, 4 (1995).

11 M. DiBattista, J.W. Schwank, *Journal of Applied Physics*, Vol. 86, 9 (1999).

12 A. van der Ziel, Noise, Prentice Hall Electrical Engineering Series, the Netherlands.

13 A.A. Balandin, Noise and Fluctuations Control in Electronic Devices, California, USA, ISBN 1588830055 (2002).

14 S. Bouwstra, Resonating Microbridge Mass Flow Sensor, Ph.D.-thesis, University of Twente (1990) ISBN 9090033289

15 L.D. Landau, E.M. Lifschitz, Lehrbuch der Theoretischen Physik, Band 7, Akademie Verlag, Berlin.

16 S. Bouwstra, R. Legtenberg, Th.J.A. Popma, Silicon-rich LPCVD Silicon Nitride Films for Micromechanical Devices, *Technical Digest Eurosensors II*, Enschede, The Netherlands (1988), 167.

Chapter 9

Discussion

Abstract

In this final chapter a short summary of this thesis is given, the obtained results are presented and discussed and some general conclusions are drawn. Besides, some recommendations for further developments are presented, and current and future applications of the Microflown are described.

9.1 Summary

In this thesis a particular thermal flow sensor, the Microflown, is studied. By virtue of its property to be sensitive to particle velocity, the physical quantity associated with sound, the sensor is especially used for sound intensity measurements.

It is endeavoured to physically understand the behaviour of the Microflown and to give an adequate description of its sensitivity. The purpose of the presented analytic model is to deduce an explicit expression for the temperature difference between the two heated wires of the sensor due to an imposed particle velocity, to which the output signal is proportional. This is achieved by finding first the temperature distribution around the heated wires from the heat diffusion equation. This stationary temperature profile is altered slightly, asymmetrically, due to the forced convection of an acoustic wave. It is shown that this particle velocity can be described by a small perturbation term added to the heat equation to obtain an expression for the resulting temperature difference of the wires. The thus obtained sensitivity function is seen to be well characterised by two important characteristic frequencies, a ‘thermal’ frequency, and a second corner frequency related to the heat capacity of the wires. Another important property of this function is its value at zero frequency. An explicit expression for this low frequency sensitivity is found, allowing a good description and consequently optimisation of the sensor for the measurement of steady flows.

The model is verified by acoustic measurements on many sensors of varying geometries and a satisfying correspondence between theory and measurement is found.

Since the Microflown is mainly used for sound intensity measurements, an overview of the different principles that can be applied to measure sound intensity is given, methods based on particle velocity sensors, pressure microphones or a combination of them. The measurement principle that seems to be most favourable makes use of one pressure microphone and one particle velocity sensor. The advantage of this principle is that no pressure gradients or spatial derivatives of the particle velocity are involved. This so-called p-u probe is an affordable and

practical measuring device for measuring several acoustic parameters and can easily be extended to a three-dimensional probe.

The calibration method of the sensor that is most common, the standing wave tube, is described next. It considers particularly the limits of validity of this method by analysing the effects of the viscous and thermal properties of the gas in the tube. These viscothermal effects on the calibration are shown to be small. Nevertheless, they should be considered in the design of a standing wave tube; by proper design the viscothermal effects can be made negligible.

Then it is shown that the sensor's sensitivity and frequency behaviour can be determined electronically as well, and an electronic method for determination of the device output response, which is more convenient, is therefore presented. The previous approach, the introduction of a small perturbation to the heat diffusion equation, is applied to the electronic case: the small additional electrical heating of one of the two wires can be described by a perturbation term. Using a specific property of Green's functions, the electrical response of the other wire can be translated to the acoustic response. The principle is shown to be geometry independent, it can be applied for a wide range of thermal flow sensors, even for those consisting of more than two wires. The method is not only less complicated, it also makes it possible to cover easily the entire acoustic frequency spectral range. The theory is experimentally verified for various thermal flow sensors of different geometries.

The model developed in the second chapter is the basis for further optimisation. Since the theory is now implemented into a numeric program, several assumptions and restrictions for the deduction of the analytic model can be dropped. The implementation of the numeric model into a software program allows for an investigation of the influence of varying sensor dimensions on the sensitivity. Thus, improved devices could be fabricated, among which Microflowns with a new geometry consisting of three, instead of two, wires of which the central wire is most heated. These three-wire sensors have a significantly improved signal-to-noise ratio and a larger frequency bandwidth.

The last two chapters deal with the noise that is present in the output signal. First a method to reduce the noise level of the particle velocity sensor is described. This method is based on the utilisation of cross-correlation spectra instead of auto-

correlation spectra of two of these sensors. The underlying principle is that the time averaged cross correlation signal of two uncorrelated noise sources is theoretically zero. The larger the measuring time and therefore the number of data points stored, the smaller the variance of the noise power in the cross spectrum.
Finally, the characteristics and origins of the noise are investigated in detail. Especially the low-frequency noise is analysed and it is observed that the voltage fluctuations exhibit a spectral density that for low frequencies behaves as $1/f^{\alpha}$ with $1 < \alpha < 3$. The approach of introducing a perturbation that has shown to be useful in the former chapters, is applied to analyse the influence of small fluctuations of external physical quantities on the fluctuations of the wire temperature and consequently on the spectral density of the output voltage. Besides, the dependence of the low-frequency noise on wire temperature and on the dissipated power are investigated experimentally. It is found that the electrical power dissipation and the related self-heating of the wire play an important role in the observed noise behaviour, although this phenomenon is not well understood yet. A difference in the power dependence of this noise between the sensor wires and a common metal film resistor is observed. We propose different possible explanations for this noise behaviour.

9.2 Discussion and conclusions

In the description of the Microflown the approach of the introduction of a small perturbation representing the convection term in the heat diffusion equation, has shown to be a strong tool. Justification of this approach lies in the fact that the involved flow velocities or particle velocities are generally very small. One of the main purposes of the physical analysis was to find a compact and well applicable expression for the sensor sensitivity, and this has become possible using this description: the output signal can be written as an explicit function of the material and fluid parameters, sensor dimensions and frequency. By virtue of its compactness, the function is not only very useful for engineering purposes, the analytic deduction also allows a much better understanding of the behaviour of the sensor and the physical phenomena that play a role. For the assumed small velocities, it reveals in particular the antisymmetry in space of the function for the

output signal, as follows from merely physical principals, which entails no temperature change of a single wire due to the particle velocity. That is, if there would be only one wire, the temperature distribution around the wire will be altered due to convection, but the temperature at the wire itself does not change. The Microflown works by virtue of the presence of more than one wire. In this respect the sensor is essentially different from an anemometer, that operates in a regime of larger velocities, for which King's law applies.

The sensitivity function has been deduced using a two-dimensional model of the sensor that describes its behaviour well for all practical applications. For frequencies down to zero one will be confronted with the finite dimensions of the sensor, the wires are not infinitely long, which leads to a diverging function. It has been shown that if the finite length of the wire is taken into account, this problem can be solved and the thus modified sensitivity function behaves properly for all frequencies. The behaviour of a thermal two–wire flow sensor due to small velocities, even that for the situation of DC (steady) flows, can thus be considered as completely described.

The perturbation approach is also the foundation of the description of the electrical characterisation. Since it has been shown that the sensor's sensitivity and its frequency behaviour can be determined electronically instead of acoustically, and a proof of principle of the electronic set up has been realised, an advanced calibration method has become possible. Not only the entire acoustic frequency bandwidth can be determined, it also implies that a characterisation of the sensor without the influences of the package on its sensitivity becomes possible. Besides it is a promising method for characterising the different aspects of the recently designed three wire configurations, like the influence of the power ratio and heat capacity.

From the obtained insight it has become possible to optimise the sensor for the different acoustic applications. With the obtained design guidelines it has become possible to find the favourable dimensions for an optimum performance. The largest improvement is obtained by the three wire configuration. We have seen that realising a device with a relative power dissipation of 0.85 in the central heater increases the low frequency sensitivity by a factor 3 (*ca.* 10 dB), and that the frequency bandwidth is increased by more than a factor of two, even more than

what theoretically is expected. This still not well understood increase of the bandwidth is a challenge for future research and may allow even further optimisation.

In the central wire, the heater, most of the electrical power is dissipated so that this wire is relatively hot, while the two sensing wires are on a relative low temperature and thus have a lower noise level. The central wire can be optimised for high powers and can have a high thermal mass while the sensing wires have a small heat capacity. A small heat capacity of the sensors increases the bandwidth, and a large thermal mass for the heater is not only favourable for a high power dissipation, it also filters (reduces) its noise level. Since the design of the device with respect to these heat capacity effects has not yet been concentrated on, it is to be expected that the performance and especially the signal to noise ratio, of future devices, can even be augmented.

In figure 9-1 an overview is given of the development of the performance of the different Microflowns in the last years. It can be seen that during these years a considerable improvement of the sensor performance has been attained (see also the next section).

An important subject of investigation has been the noise that is observed in the output signal, especially for low frequencies. No matter what the precise origins of these measured voltage fluctuations are, it can relatively easily be shown that for stationary signals, a technique based on the utilisation of cross-instead of autocorrelation spectra of two identical sensors can reduce the noise. Although the principle is not new (see for example [8, 13]), it is seen to be a very useful tool for the Microflown. Since it was also experimentally confirmed that the signal is not influenced by the cross correlation technique, significant improvements of the signal to noise ratios can be attained for the measurement of steady state sound sources; improvements of almost 30 dB have been achieved. For sound intensity measurements of stationary signals, an important application of the Microflown, the method is a promising technique, since not only uncorrelated noise but also time dependent acoustic signals that are not of interest, are filtered out. Besides it might be useful to obtain more insight into the origin of the low frequency noise, that is still not well apprehended.

The physical origins and behaviour of the noise itself have been an important point of interest, and still are, since they are not understood yet at the moment of writing this thesis. In the theoretical investigation, again the perturbation theory is applied to analyse the influence of small fluctuations of the parameters that are present in the heat equation on the fluctuations of the wire temperature and therefore on the spectral density of the voltage. With this approach, the experimental results can partially be explained, if fluctuations in the electrical power dissipated in the metal wire are assumed to be an origin of the noise. Besides, the self-heating due to power dissipation in the wire, that results in an inhomogeneous temperature distribution along the wire and in a temperature gradient in the environment, seems to play a role. A Microflown wire exhibits a considerably higher noise level than a metal film resistor of equal temperature, resistance, and dissipated power. A sufficient explanation for this behaviour has not been found up till now, and further research with respect to this subject is certainly required.

9.3 Outlook

9.3.1 Future research

During the last years, a significant improvement of the performance of the Microflown has been achieved, illustrated by figure 9-1. Both the low frequency sensitivity, the measurable frequency bandwidth and the signal to noise ratio for a broad frequency range have increased. The main reason for this is that a better understanding of the sensor and a reliable description have allowed an optimisation of the device with respect to its dimensions. Moreover, the proposed different geometry consisting of three wires, currently in use already, has led to a significantly improved performance. Figure 9-1 illustrates the development of the Microflown by dint of the selfnoise of the sensor in the course of time[1]. The three-

[1] The selfnoise, the ratio between sensitivity and noise, can be considered as the equivalent noise level of the sensor, in (m/s)/√Hz. Here it has also been scaled with a frequency dependent weighing curve, taking into account the human ear sensitivity, the 'A-weighing curve' [12]. The selfnoise R (in m/s) can then be defined as $R = \{\int_0^\infty N^2(f)/S^2(f)W^2(f)df\}^{1/2}$, with $N(f)$ and $S(f)$ the frequency dependent noise level and sensitivity respectively, and $W(f)$ the 'A-weighing curve'. The unit dB represents $20\ ^{10}\log(R/R_{ref})$, with $R_{ref} = 50$ nm/s.

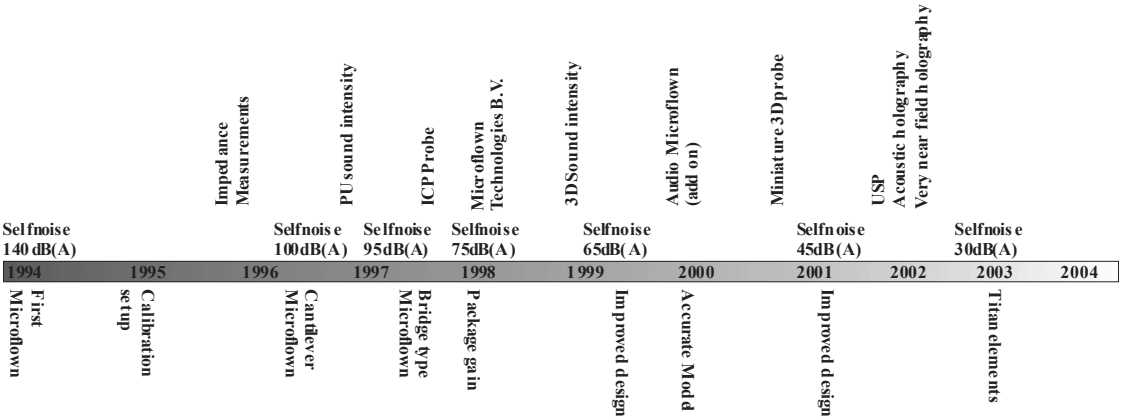

Fig. 9.1: Developments of the Microflown. The selfnoise in dB(A) has been calculated for a 20 kHz bandwidth and an operating power of 40 mW. For telecom purposes the bandwidth is limited to 3.4 kHz and the power dissipation to 10 mW, the selfnoise is then approximately 14 dB lower. For sound reinforcement the operating power can be chosen higher, resulting in a lower selfnoise.

wire configuration is called here ‘Titan’.

The fact that the sensor sensitivity can be fully and satisfactory described and its behaviour is considered to be understood now, does not mean that the research on the sensor has finished. The main subject to be investigated in more detail is without doubt the low frequency noise of the electrically heated wire. Although various experiments have been performed, with respect to different materials, influence of temperature and influence of power, many questions still rest, and advanced experiments have to be done. This leads to requirements for the measurement set-up, especially with a very low noise power source or a construction in which this noise is eliminated, and an electrical network in which only the noise of interest is amplified. Besides, new devices with different materials, for example the combinations tantalum-rhodium and rhodium-platinum, have to be investigated in order to understand the possible influence of the metal properties. As proposed at the end of the former chapter, the structure of the used material that is sputtered on the silicon carrier may be of influence on the noise spectrum. This assumption requires a more detailed examination of the metal surfaces.

Different propositions for an improvement of the sensor performance have been suggested. Some are mentioned here.

- The signal-to-noise ratio of the Microflown is proportional to the square root of the applied heating power, so in principle this signal-to-noise ratio can be improved by increasing the power. However, this is not an option for battery powered equipment like hearing aids and mobile telecom equipment. In fact, these applications need a reduction of the power consumption. A significant improvement can be obtained by improving the sensor structure by using a material with a much higher temperature coefficient of resistivity than the currently used platinum. Since the operating principle is based principally on the measurement of a relative resistance difference due to a temperature change, this is the most fundamental and effective way to improve the performance. Amorphous germanium has a temperature coefficient of resistivity of $2.6 \cdot 10^{-2}\ K^{-1}$, which is ten times higher than that of platinum with chromium. Replacing the platinum wires by wires from germanium will thus result in an improvement of the sensitivity and signal-to-noise ratio by more than a factor of 10 or a reduction of the power consumption by a factor of 100.
  The resistivity of germanium is very high compared to metallic conductors (approximately 6 Ωm compared to the resistivity of platinum of $1 \cdot 10^{-7}$ Ωm). This implies that a Microflown with germanium as sensing material cannot be processed with the currently used one mask fabrication method. To fabricate sensors with germanium as sensing material a layout with metal contact arrays on a beam, with additionally germanium in between, can be used. It has been demonstrated [1] that this is well feasible. It is seen that this can lead to an increase of the sensitivity of 20 dB.
  The high temperature coefficient of resistivity of germanium can be explained by the conduction mechanism of the germanium being an amorphous semiconductor. Since the operating temperature range for the working of the sensor should be taken narrow, the sensor has to operate in an electronic feedback loop, keeping the temperature of the two wires close to each other. Additionally, a feedback loop has the advantage of increasing the bandwidth of the sensor, and can often provide a digital output signal, which is convenient for high-end audio applications.

- One of the two corner frequencies of the particle velocity sensor is caused by the thermal mass (heat capacity) of the wire. If a single hot wire, for example an anemometer, is kept at a constant temperature, the corner frequency goes up to several hundreds of kilohertz, see e.g. [2]. This principle can be extended to two-wire flow sensors like the Microflown. An example of a control system for two-wire flow sensors was developed at the University of Twente [3]. The corner frequency related to the thermal mass of the wires of the Microflown is currently in the order of 3 kHz. A feedback control system could easily shift this frequency to 20 kHz or higher, which is sufficient for audio applications.
- It has appeared that the three-wire sensor is a promising design, favourable compared to the two-wire device. The underlying principle of separation of sensing and heating may be used in other compositions. Designs with four or even more wires, or realisations in which the wires are composed in a different formation may turn out to be promising and should be studied further. Separation of the functions of sensing and heating imposes new requirements on the different wires, for example with respect to their thermal mass, resistivity and thickness.

9.3.2 Latest developments

After the invention of the Microflown and its well-known applications developed since then, mainly the acoustic measurement purposes like one- and three-dimensional sound intensity measurements and measurements of particle velocity, apparent pressure and specific impedance, the sensor and likewise its applications have made a considerable development during the last few years. Not only the sensor sensitivity itself has increased, new applications for the particle velocity sensor have emerged too. Some of these are

Near field and very near field sound source localisation

The availability of particle velocity sensors offers new ways for solving numerical inverse methods for the calculation and localisation of a near field source [4, 5, 6, 7]. For a sound source of characteristic length L emitting waves with wave number

k_0, wavelength $\lambda_0 >> L$, the regions 'near field' and 'very near field' can be defined. A place r is said to be located in the near field of the source, if $k_0 r << 1$, while in the very near field both $k_0 r << 1$ and $2\pi r_n / L << 1$ (r_n is the distance normal to the vibrating surface of the source). In the (very) near field, pressure p and particle velocity u are $\pi/2$ out of phase, and the ratio pressure/particle velocity is small; $p \approx -i(\rho c)u\frac{L}{\lambda}$ (with ρc the specific acoustic impedance).

Near field acoustic holography has always been a compromise between the intrinsic properties of pressure transducers on the one hand, and the numerical inverse calculation methods on the other hand. Until recently, pressure transducers were the only sensor category available for acquiring input signals. In the proximity of an object however, the pressure level of a sound wave is low, gradually building up as it leaves the object. Measuring at a distance sufficiently far from the source is preferred. On the other hand, the computational power required for solving the inverse problem increases with the distance to the object, which makes a small distance to the source preferable. Consequently, numerical measurement methods based upon pressure transducers are always a compromise.

If, however, particle velocity sensors are used, the intrinsic requirements of the sensor itself and the numerical routines are no longer conflicting: the particle velocity level is high near the sound source. Another advantage is that, measuring closer to the object, the contribution of reflections distorting the observations, is reduced. By measuring in the near field, more information can be obtained and less computational power is required.

In the ultimate case, near field acoustic holographic problems become very near field holographic problems. These very near field source localisation problems are easy to solve, since close to a vibrating object, the particle velocity as measured approaches the surface velocity of the object under investigation. When the particle velocity is measured in the very near field of the surface, it becomes equal to the velocity of the vibrating surface and the need for mathematic modelling even vanishes. These effects were demonstrated at The University of Twente [4, 5, 6].

Measurement of structural vibrations of materials

The Microflown, or even better an array of Microflowns, is suitable for the measurement of vibrations of various kinds of materials. An important advantage of the application of a particle velocity sensor for this measurement is the absence of contact between sensor and vibrating surface. Usually applied sensors in this field are in particular pressure transducers, (mini) accelerometers and laser vibrometers. Especially for the measurements on materials that are difficult to analyse optically, like damping materials, foam, rubber or black surfaces, for the analysis of scattering surfaces and for obtaining a real time and three dimensional image of the particle velocity around the surface, the Microflown may be preferable compared to a laser vibrometer.

In comparison with an accelerometer, the sensor is often favourable, since accelerometers are contact based sensors and thus affect the behaviour of the vibrating object. The output of an accelerometer is acceleration, requiring the time integration of data, a step that can be avoided with the particle velocity sensor.

A specific application in this field is the study of the modes of a small vibrating silicon beam (5 mm × 17.5 mm), piezo-electrically excited at 10 kHz [9]. A 'Microflown scanning probe' scans the object in normal and in lateral direction, and since the probe is in the very near field, the measured particle velocity coincides with the surface velocity. See the figures 9-2a and b. In figure 9-2b it is seen that the lateral velocity is minimal where the normal (surface) velocity is at most, and vice versa. The figure has been determined for a sensor sample distance of 1 mm, so that the near field condition is fulfilled and the measured particle velocity equals the surface velocity.

Other applications that were recently demonstrated are the determination of the modes of a vibrating plate and the measurements of the sound fields of a hole in a rigid plate [6, 7, 10, 11].

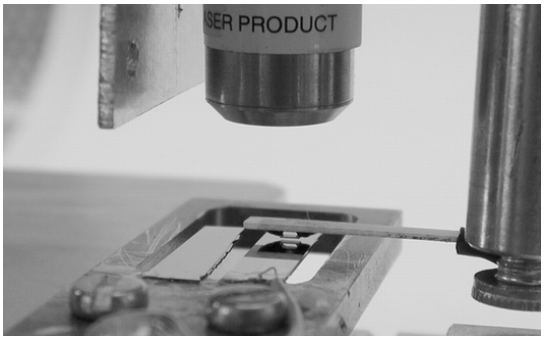

Figure 9-2a. A 'Microflown scanning probe' actuated by a robot scans a small vibrating silicon beam (5 mm × 17.5 mm), to find the vibration modes [9, 10].

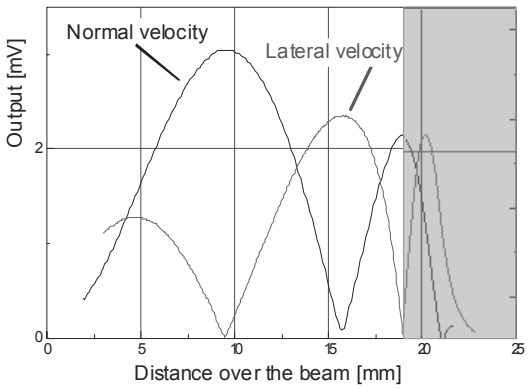

Figure 9-2b. Normal and lateral velocity as a function of the distance along the beam. The grey part shows the signals beyond the beam, caused by the sound field generated by the tip of the beam [9, 10].

Various acoustic applications

Apart from the original, noted applications of the Microflown, new utilisations of the sensor have been discovered and investigated. One of them is the *in situ* determination of the specific acoustic impedance of materials, for which the material under study does not have to be placed into a standing wave tube, which is sometimes inconvenient or even impossible. The particle velocity sensor is placed close to the sample and from the measured particle velocity its reflection coefficient is deduced. Alternatively, a combination of the sensor and a microphone measures both acoustic energy and sound intensity, providing the required information.

Another application is the possibility to make a representation of the sound field around a sound source, like a loudspeaker. With a three dimensional p-u probe (a 'USP', see [4]) two dimensional representations were recently obtained at the University of Twente, showing the iso-intensity regions and the intensity streamlines around a sound source, and three dimensional images of the wave fronts and of the involved sound intensity streamlines. Related to this, near field and far field source localisation are still studied in detail and further developed.

For most of these acoustic applications, an array of sensors instead of only one is favourable, providing simultaneously more measurement data. Besides, the signal to noise ratio increases with the number of sensors in the array.

Finally, the combination of three particle velocity sensors and a microphone, the p-u probe, is applied for three dimensional impulse response determination and the identification of spatial reflections, allowing the design of for example music halls.

9.4 References

1 P. Ekkels, Microflown improvement; various means to improve the signal-to-noise ratio of the Microflown, *M.Sc. Thesis*, University of Twente (2002).

2 M. Elwenspoek, R.J. Wiegerink, Mechanical Microsensors, Springer Verlag (2000).

3 T.S.J. Lammerink, N.R. Tas, G.J.M. Krijnen, M.C. Elwenspoek, A new class of temperature flow sensors using $\delta t = 0$ as control signal, *Proceedings of MEMS*, Japan (2000) 525-530.

4 www.microflown.com ('Applications')

5 R. Visser, Acoustic Source Localization based on Pressure and Particle Velocity Measurements, *Proceedings of Internoise*, Korea (2003).

6 R. Visser, Inverse Source Identification based on Acoustic Particle Velocity Measurements, *Proceedings of Internoise*, Dearborn, USA (2002).

7 R. Visser, Regularization in nearfield acoustic source identification, *Proceedings of the Eighth International Congress on Sound and Vibration*, Hong Kong, China (2001), 1637-1644.

8 O. H. Bjor, *Proceedings of Internoise*, Budapest (1997) 1367-1370.

9 B. de Jong, private communications, (2004).

10 www.microflown.com

11 H.-E. de Bree, private communications, (2004).

12 H.-E. de Bree, 'The Microflown', ISBN 9036515793, Amsterdam, The Netherlands (2001).

13 M. Sampietro, L. Fasoli, G. Ferrari, Spectrum analyzer with noise reduction by cross-correlation technique on two channels, Review of Scientific Instruments, Vol.70, 5 (1999), 2520-2525.

Dankwoord

Ongetwijfeld is het dankwoord het meest en tevens vaak het eerst gelezen onderdeel van het proefschrift, door iedereen die graag wil zien of zijn of haar naam erin genoemd wordt. En bovendien, het is het enige stuk in het Nederlands. Mij dat realiserende, is het des te belangrijker niemand te vergeten. Om het me daarom niet al te moeilijk te maken, wil ik allereerst, voordat ik een aantal mensen persoonlijk noem, mijn dank uitspreken naar alle collega's van de Micmec, met wie ik de afgelopen jaren zo prettig heb samengewerkt en die met zijn allen een gezellige en ontspannen vakgroep vormen waarin je je snel op je gemak voelt.
Ik kan niet bij het begin beginnen zonder Hans-Elias te noemen, door wie ik in contact ben gekomen met de Microflown. Zijn open, ontspannen en spontane karakter maakten het contact heel gemakkelijk en prettig. In het bijzonder dankzij hem heb ik gekozen voor een promotie met betrekking tot de Microflown. Ook tijdens de afgelopen jaren heeft hij het werken altijd op een ontspannen, gemakkelijke en toch eigenlijk heel verstandige manier opgevat en leuk gemaakt. Daar heb ik niet alleen van geleerd, maar vooral ook van genoten en daarvoor wil ik hem hartelijk danken.
Natuurlijk wil ik veel dank uitspreken naar mijn promotoren Miko Elwenspoek en Erik Druyvesteyn. Miko is in staat op een totaal niet-autoritaire manier een zeer ontspannen onderzoeksklimaat te creëren en de vakgroep tot een voor iedereen prettige omgeving te maken, met volop plaats voor wetenschappelijke creativiteit. Altijd kon ik bij hem binnenlopen voor een vraag, en bovendien heb ik aan hem te danken dat ik op zo'n leuke manier bij het geven van onderwijs betrokken ben geraakt.
En ik wil Erik bedanken, voor zijn enthousiasme en enorme betrokkenheid bij mijn project, waarmee hij het onderzoek steeds een nieuwe impuls heeft gegeven. Ook gaat mijn dank uit naar Gijs, voor zijn nauw betrokken begeleiding, de altijd opbouwende kritiek en de vele interessante en vaak heel gezellige gesprekken die we samen hebben gevoerd. And I would like to thank Vitaly, from whom I have learned so much about physics and who was not only some teacher but also a kind of a friend for me.
En het hele onderzoek was niet mogelijk geweest zonder de hulpvaardigheid van Doekle en zijn bereidheid Microflowns af te monteren, een versterkertje te maken of aanverwante werkzaamheden te verrichten, en zonder Phillip, die met alle plezier nog aanvullende metingen aan zijn 'prioriteitenlijstje' toevoegde. Ook de technologische hulp en de adviezen van Erwin en Meint, naast het feit dat het erg leuke collega's zijn, was altijd heel waardevol en daar wil ik ze graag hartelijk voor bedanken.

Voor de hulp bij alle akoestische metingen en de metingen aan het ruisgedrag van de Microflown ben ik veel dank verschuldigd aan Henny, altijd bereid een nieuwe electrische schakeling te maken, en aan Ron, met zijn kennis van de akoestiek.
De conferenties die ik bezocht heb in onder meer Parijs, München, Cork (Ierland), Guimarães (Portugal), Sevilla en Orlando, waren een succes vooral ook dankzij Hans-Elias, Henk Wensink, Theo, Remco, John, Regina, Gijs, Bart, Edin, Toon, Erik en Petra. En voor de gezelligheid op de beurzen over akoestiek in Nice en Sevilla bedank ik graag tevens Alex, Tjeerd-Hans en Doekle.
Voor zijn sfeerverhogende aanwezigheid en vaak noodzakelijke handigheid (die ik nog wel eens ontbeer) bedank ik Pino, en vanzelfsprekend ook Henk van Wolferen. Wat ik mis aan vaardigheid met betrekking tot de PC en het computernetwerk wist hij op een subtiele maar zinvolle manier aan te vullen, en daar heb ik veel aan gehad.
Ook de secretaresses waren van onschatbare waarde en in het bijzonder bedank ik Ingrid voor haar enorme bereidwilligheid, en Judith, Marieke, Simone en José.
En aan Marko, bovendien, heb ik veel gehad bij de uiteindelijke vormgeving van het proefschrift, bedankt!
Tot slot wil ik mijn zusje, Mariëlle, bedanken voor het aanvaarden van het paranimfschap, en vooral ook mijn ouders, voor hun mentale steun, meeleven en interesse en zonder wie dit resultaat zeker niet bereikt was.

Biografie

Joost van Honschoten werd geboren op 3 januari 1972 in Deventer, en verhuisde twee jaar later naar Raalte, waar hij opgroeide. Hij doorliep er aan het Florens Radewijn College het atheneum en ging in 1991 op kamers in Enschede om technische natuurkunde te gaan studeren aan de Universiteit Twente. Deze studie rondde hij in 1996 af met een afstudeeropdracht aan de vakgroep biofysica/technische optica, waar hij zich bezighield met onderzoek aan laser-Doppler bloedperfusiemetingen. Het onderzoek richtte zich op de grootte van de coherentieoppervlakken waarmee de 'speckle'patronen van het verstrooide laserlicht kunnen worden gekarakteriseerd.
Daarna werkte hij enkele maanden bij de leerstoel theoretische natuurkunde aan de beschrijving van solitaire golven, solitonen, in optische schakelaars. Hij kwam in contact met Hans-Elias de Bree, en de toenmalige vakgroep transductietechniek (de 'MicMec') onder leiding van professor Miko Elwenspoek. Daar begon hij in 1999 zijn promotieonderzoek aan de Microflown, waarin het accent lag op de fysische modellering van het gedrag van de sensor, aangevuld met experimenteel onderzoek. Gedurende die periode kwam hij in contact met dr. Vitaly Svetovoy, een Russische wetenschapper die samen met een collega eveneens onderzoek aan de Microflown deed en daarover een eerste artikel had gepubliceerd. Het daaropvolgende contact met Svetovoy en de vele discussies over de modelvorming gaven een krachtige impuls aan het onderzoek. Ook het verblijf van Svetovoy van enkele maanden aan de universiteit Twente was voor Joost een heel leerzame periode.
Tevens raakte hij tijdens zijn promotie betrokken bij het geven van onderwijs, door Miko zo nu en dan te assisteren bij de colleges electrodynamica, hetgeen hij met veel plezier deed.
Daarnaast is Joost een groot liefhebber van wandelen, tekenen en schilderen (aquarelleren), hardlopen, en vooral de Franse taal. Tevens geeft hij met veel plezier bijlessen wiskunde, natuur- en scheikunde aan scholieren van het middelbaar onderwijs.